



HAL
open science

Application and development of dissolution dynamic nuclear polarization techniques for kinetic studies of metabolic reactions

David Guarin

► **To cite this version:**

David Guarin. Application and development of dissolution dynamic nuclear polarization techniques for kinetic studies of metabolic reactions. Chemical Sciences. Ecole normale supérieure - ENS PARIS, 2021. English. NNT: . tel-03985370

HAL Id: tel-03985370

<https://hal.science/tel-03985370v1>

Submitted on 13 Feb 2023

HAL is a multi-disciplinary open access archive for the deposit and dissemination of scientific research documents, whether they are published or not. The documents may come from teaching and research institutions in France or abroad, or from public or private research centers.

L'archive ouverte pluridisciplinaire **HAL**, est destinée au dépôt et à la diffusion de documents scientifiques de niveau recherche, publiés ou non, émanant des établissements d'enseignement et de recherche français ou étrangers, des laboratoires publics ou privés.



Distributed under a Creative Commons Attribution 4.0 International License



École Normale Supérieure

Doctoral school n° 388 : Chimie Physique et Chimie Analytique de Paris Centre

Laboratoire des Biomolécules (LBM), UMR 7203

Application and development of dissolution dynamic nuclear polarization techniques for kinetic studies of metabolic reactions.

DAVID O. GUARIN

Thesis presented for the degree of Doctor of Philosophy

Directed and supervised by **DANIEL ABERGEL**

Co-supervised by **DENNIS KURZBACH**

Jury members

Daniel Abergel	Professor, Sorbonne Université	Thesis director
Mathilde Lerche	Senior Researcher, Technical University of Denmark	Reviewer
Patrick Giraudeau	Professor, Université de Nantes	Reviewer
Konstantin Ivanov	Professor, Novosibirsk State University	Examinator
Sami Jannin	Professor, Université de Lyon 1	Examinator
Rachel Katz-Brull	Professor, Hebrew University of Jerusalem	Examinator
Dennis Kurzbach	Professor, Universität Wien	Co-supervisor

Abstract

Cellular metabolism involves regulatory mechanisms that allow the cell to adapt to its environment, thus modifying its phenotype accordingly. Understanding how this metabolism adapts provides fundamental information to develop and improve diagnostic and treatment methodologies for several diseases. However, growing evidence suggests that even the quantification of a complete set of metabolites is not sufficient to predict cell's phenotype. On the contrary, knowledge of metabolic fluxes is necessary to understand how cells adapt to their environment.

NMR is a unique observation tool that relies on the interaction between nuclear spins and magnetic fields, and is therefore non-invasive and non-destructive. However, NMR spectroscopy suffers from its intrinsic lack of sensitivity, which can be compensated to some extent by signal averaging, which in turn decreases the sampling rate of the reactions. To circumvent this constraint, Dissolution Dynamic Nuclear Polarization (DDNP) methods were introduced at the beginning of the century. Indeed, this technology allows real-time monitoring of dynamic processes by allowing NMR sampling rates < 1 Hz, while capitalizing on the intrinsic atomic resolution of NMR spectroscopy. The objective of this Ph.D. work is to implement and optimize a DDNP-based methodology to perform kinetic studies of metabolic reactions in both in vitro samples and in living cells.

Initially, we focused on the study of the oxidative stage of the PPP (oxPPP). The objective was to characterize the enzyme kinetics of glucose-6-phosphate dehydrogenase. We have therefore performed experiments by monitoring the NMR signals of the different metabolites involved in the transformation. The analysis of these experiments allowed us to extract the different kinetic parameters of the reaction. The consistency of the values obtained was

evaluated using statistical tools, by comparison with independently measured references and with bibliography. Between the extracted parameters, we were able to characterize the anomerization kinetics of G6P, which seems to be a contribution to the current knowledge of the system.

In a second approach, we set up a procedure to perform DDNP experiments on living cells. We focused however on the study of glucose consumption and metabolism by *E.coli* K12. The characterization of the phenotypic response by *E.coli* was made possible by analyzing the real-time kinetics of hyperpolarized [U - ^{13}C ; U - 2H]glucose and its metabolic products. Analyses of these experiments allowed us to relate the extracellular ^{13}C anomeric signals of glucose to the relative glucose uptake of each anomer by *E. coli*, and so, to the relative activities of glycolysis and the pentose phosphate (PPP) pathway in the cell. Moreover, the analysis of the real-time evolution of a couple of products' signal intensities showed to depend on cellular growth stages and hence also provided an intrinsic marker of the *E.coli* metabolic response to a sudden (hyperpolarized) glucose exposure. As proof of concept, additional experiments were performed with multiple substrates on different cell systems. The results suggests that different metabolic characteristics can be observed on such systems using DDNP techniques.

Keywords

Nuclear Magnetic Resonance, Metabolism, Dynamic Nuclear Polarization, Enzyme kinetics,

Résumé en Français

Dans le métabolisme cellulaire interviennent des mécanismes de régulation qui permettent à la cellule de s'adapter à son environnement, donc de modifier son phénotype en conséquence. Comprendre la façon dont ce métabolisme s'adapte fournit des informations fondamentales pour développer et améliorer les méthodologies de diagnostic et de traitement pour plusieurs maladies. Cependant, de plus en plus de preuves suggèrent que même la quantification d'un ensemble complet de métabolites ne suffit pas pour prédire le phénotype cellulaire. Au contraire, la connaissance des flux métaboliques est nécessaire pour comprendre comment les cellules s'adaptent à leur environnement.

La RMN est un outil d'observation unique qui repose sur l'interaction entre les spins nucléaires et les champs magnétiques, et est donc non invasive et non destructive. Cependant, la spectroscopie RMN souffre de son manque intrinsèque de sensibilité, qui peut être compensé dans une certaine mesure par la moyenne des signaux, qui à son tour diminue le taux d'échantillonnage des réactions. Pour contourner cette contrainte, les méthodes de polarisation nucléaire dynamique par dissolution (DDNP) ont été introduites. En effet, cette technologie permet de suivre en temps réel des processus dynamiques en permettant des taux d'échantillonnage RMN < 1 Hz, tout en capitalisant sur la résolution atomique intrinsèque de la spectroscopie RMN. L'objectif de ce travail de doctorat est de mettre en œuvre et d'optimiser une méthodologie basée sur la DDNP pour réaliser des études cinétiques des flux métaboliques à la fois dans des échantillons *in vitro* et par observation de cellules vivantes.

Dans un premier temps, nous nous sommes focalisés sur l'étude de l'étape oxydative de la PPP (oxPPP). L'objectif étant de pouvoir caractériser la cinétique enzymatique de l'enzyme glucose-6-phosphate déshydrogénase. Nous avons donc réalisé des expériences en suivant

les signaux RMN des métabolites impliqués dans la réaction. L'analyse de ces expériences nous a permis de caractériser les différents paramètres décrivant la cinétique de la réaction. La cohérence des valeurs obtenues a été évaluée au moyen d'outils statistiques, par comparaison avec des références mesurées de manière indépendante et par comparaison avec les valeurs documentées. Entre les paramètres extraits, nous avons pu caractériser les cinétiques d'anomérisation du G6P, ce qui semble être une contribution à la connaissance actuelle du système.

Dans un deuxième temps, nous avons mis en place une procédure permettant de réaliser des expériences de DDNP sur des cellules vivantes. Cependant, nous nous sommes concentrés sur l'étude de l'absorption et du métabolisme du glucose par *E. coli* K12. La caractérisation de la réponse phénotypique par *E. coli* a été rendue possible par l'analyse de la cinétique en temps réel de traces de glucose [$U\text{-}^{13}\text{C}$; $U\text{-}^2\text{H}$] hyperpolarisé et de ses métabolites. Les analyses de ces expériences nous ont permis de relier les signaux ^{13}C anomériques extracellulaires à l'absorption relative de glucose de chaque anomère par *E. coli*, et aux activités relatives de la glycolyse et de la (PPP) dans la cellule. En outre, l'analyse de l'évolution en temps réel de l'intensité des signaux de quelques produits métaboliques a montré que ceux-ci fournissent un marqueur intrinsèque de la réponse métabolique du glucose à l'exposition soudaine au glucose hyperpolarisé. Comme preuve de concept, des expériences supplémentaires ont été réalisées avec de multiples substrats sur différents systèmes cellulaires. Les résultats suggèrent que différentes caractéristiques du métabolisme peuvent être observées sur de tels systèmes au moyen des techniques DDNP.

Mots Clés

Resonance Magnétique Nucléaire, Métabolisme, Polarisation Dynamique Nucléaire, Cinétique Enzymatique

Contents

Abstract	I
Résumé en Français	III
Physical and Chemical Constants	XI
Physical and chemical constants	XIII
Introduction	1
I Metabolism studies and NMR	7
1 Overview of the studies on metabolism	8
1.1 Metabolism	8
1.1.1 Presentation of some fundamental metabolic pathways	10
1.1.1.1 Glycolysis	12
1.1.1.2 The Pentose Phosphate Pathway	15
1.2 Study of metabolome, a functional approach	17
1.2.1 Metabolomics	17
1.2.2 Fluxomics	19
2 NMR	23

2.1	NMR in metabolomics and fluxomics	25
2.1.1	<i>In vitro</i> and <i>ex vivo</i> studies	25
2.1.1.1	NMR spectroscopy to study enzyme kinetics in real-time	25
2.1.1.2	<i>Ex vivo</i> metabolomics by NMR	27
2.1.2	In vivo studies	29
2.1.2.1	NMR in vivo assignment with bioreactor	30
2.1.2.2	NMR in cell kinetic study	31
2.2	The Dissolution DNP technique	33
2.2.0.1	The invention of Dissolution DNP	34
2.2.1	Advantages and known limitations of DDNP methodology	35
2.2.1.1	Fast sampling technique ideal for fluxomic studies	35
2.2.1.2	Reproducibility problems of a complex experiment	36
II	A review of the basics of DNP and DDNP	39
3	Short review of DNP	41
3.1	Polarization	41
3.1.1	Density Matrix	43
3.1.1.1	Boltzmann distribution	45
3.1.2	Spin polarizations at cryogenics temperatures	46
3.2	Polarization Transfer	46
3.2.1	EPR spectrum	47
3.2.2	DNP mechanisms	50
4	The Dissolution DNP system	52
4.1	DNP Hardware	52
4.1.1	Bruker, 6.7 T polarizer	52
4.1.1.1	Magnetic field and cryogenics	52
4.1.1.2	Probe, RF circuit and μ -wave irradiation	54

4.1.2	Cryogen-free 9.4 T Polarizer	55
4.1.2.1	Magnetic field and cryogenics	55
4.1.2.2	Probe, RF circuit and μ -wave irradiation	57
4.2	Dissolution DNP experiment	58
4.2.1	Sample preparation	58
4.2.2	Dissolution experiment	59
4.2.3	NMR sequences	62
4.2.3.1	Liquid-state NMR sequences	62
4.2.3.2	Cross-polarization sequences	64
III	In-vitro studies of enzymatic reactions by DDNP	67
5	Enzymatic cascade with glucose as substrate	69
5.1	Context of the experiment	69
5.2	The reaction scheme	71
5.3	Materials and methods	73
5.3.1	Sample preparation and DNP experiment	73
5.3.2	Reaction medium and NMR	74
5.4	Results and Analysis	75
5.4.1	Individual analysis of the experiments	77
5.4.2	Simultaneous fit	80
6	Characterization of G6PDH with labeled G6P	85
6.1	Production and purification of [U- ¹³ C; U- ² H]G6P.	85
6.2	Kinetic analysis	94
6.2.1	Characterizing G6PDH activity and G6P anomerization rate	96
6.2.2	Pseudo-first order, complete reaction scheme	99

IV	In cell fluxomic studies by DDNP	105
7	Glucose metabolism in <i>E.coli</i> K12	106
7.1	A brief background overview	106
7.2	Materials and methods	108
7.2.1	Cell culture	108
7.2.2	DNP setup and NMR	108
7.3	DDNP study of glucose metabolism in <i>E.coli</i> K12	110
7.3.1	The decay rates of the α/β -glucose anomeric signals are markers of the cellular metabolic response to a glucose pulse	113
7.3.2	Quantitative kinetic analysis of metabolite signals	118
	Conclusion	124
A	DNP mechanisms	127
A.1	Dipolar interactions and spectral diffusion	127
A.1.0.1	Spectral diffusion	128
A.1.0.2	Hyperfine coupling	131
A.1.1	Solid Effect	132
A.2	Thermal Mixing mechanism	134
A.2.1	Triple spin flips	134
A.2.1.1	Cross effect	136
A.2.2	Spin temperature exchange and μ -wave irradiation	138
A.3	Characterizing TM via cross-talk between spin reservoirs	143
A.3.0.1	Reaching a common spin temperature	145
A.3.0.2	Heat transfer between the nuclear Zeeman reservoirs	145
B	Pyruvate into Ecoli ATCC and 2,4-DNP	149
B.0.1	Experiment n ^o 1, no cell treatment	150
B.0.2	Experiment n ^o 2, addition of 2,4-dinitrophenol	152

C	Glucose into Macrophages	155
C.0.1	Cell culture and DDNP setup	156
C.0.2	Glucose metabolism in macrophages	157
	References	160

Physical and chemical constants

Planck Constant	k_B	$6.62607004 \times 10^{-34}$	$\text{m}^2.\text{kg}.\text{s}^{-1}$
Boltzman Constant	k_B	$1.38064852 \times 10^{-23}$	$\text{J}.\text{K}^{-1}$
Bohr Magneton	μ_B	$9.274009994 \times 10^{-24}$	$\text{J}.\text{T}^{-1}$
Vacuum Permeability	μ_0	$1.256637062 \times 10^{-6}$	$\text{H}.\text{m}^{-1}$
Gyromagnetic ratios	γ_i		$\text{rad}.\text{s}^{-1}.\text{T}^{-1}$
e^-		176.085×10^8	
^1H		267.522×10^6	
^2H		41.065×10^6	
^{13}C		67.282×10^6	
^{15}N		-27.116×10^6	
^{31}P		108.291×10^6	

Acronyms and Notations

2,4-DNP	- 2,4-dinitrophenol
6PGA	- 6-Phosphogluconic acid
6PGL	- 6-phosphogluconolactonase
ATP	- Adenosine triphosphate
ADP	- Adenosine diphosphate
AMP	- Adenosine monophosphate
BIRD	- Bilinear rotation decoupling
CP	- Cross polarization
CE	- Cross effect
CEp	- Capillary electrophoresis
DNP	- Dynamic nuclear polarization
DDNP	- Dissolution dynamic nuclear polarization
DE	- Differential Evolution
EPR	- Electron Paramagnetic Resonance
FPLC	- Fast protein liquid chromatography
G6P	- Glucose-6-phosphate
G6PDH	- Glucose-6-phosphate dehydrogenase
GC	- Gas chromatography
HGP	- Human Genome Project
HPLC	- High performance liquid chromatography
LB	- Lysogeny broth
LC	- Liquid chromatography
MC	- Monte Carlo
MG	- Micro wave guide
MS	- Mass spectrometry
MFA	- Metabolic flux analysis

NMR - Nuclear magnetic resonance
oxPPP - Oxydative phase of the penthose phosphate pathway
PEP - Phosphoenolpyruvate
PPP - Penthose phosphate pathway
PS - Phase Separator
PTS - Phosphotransferase system
R5P - Ribose 5-phosphate
RF - Radio frequency
SE - Solid effect
SEC - Size exclusion chromatography
SNR - Signal to noise ratio
TM - Thermal mixing
VTI - Variable Temperature Insert

Introduction

Living organisms display exceptional attributes that allow them to adapt to and replicate in changing environments. To this end, they evolutionary developed complex reaction networks that enable energy production by consumption of nutrients and respiration (chapter 13 [1])[2, 3, 4]. The French chemist Antoine Lavoisier already noticed this phenomenon in the 18th century by realizing that animals transform chemical fuels into heat. He wrote: "[...] respiration is nothing but a slow combustion of carbon and hydrogen, which is entirely similar to that which occurs in a lighted lamp or candle [...]"[5]. Evidently, when trying to understand the chemistry of life, it is of major importance to understand the biochemical processes that determine the conversion of nutrients consumed by living organisms. Although studies of the conversion of starch into sugar were already undertaken in the early 1800s [6], the first description of biochemical degradation of nutrients was given by Pasteur only by 1850. Indeed, he initially documented the conversion of sugar into alcohol by yeast and the catalysis of the conversion by "ferments". Molecules with related catalytic functions, i.e. enzymes, were later identified and named by Buchner [4] and Kühne [7] in 1897. Today, thousands of enzymes have been isolated and studied, and their structure, reactions and mechanisms elucidated. These reactions form the metabolic network, the complete set of enzymatic reactions at the center of cell adaptability is called metabolism [8, 9, 1]. The term 'metabolism' denotes the complete ensemble of enzymatic and non-enzymatic reactions occurring in an organism. Etymologically (from greek *metabolê*, "change") the "metabolism" defines a system that undergoes constant changes [10]. Interestingly, one of the first uses of the word 'metabolism' (in the chapter *History of metabolism* written by Graham Lusk [11, 10]), all the different appearances of the word "metabolism" (in German *Stoffwech-*

sel) were systematically translated from German to English as "metamorphosis"[8]. Indeed, chemical reactions involved in the metabolic network are under constant change, their variability enables cellular adaptability and survival [1, 12].

In this thesis, I focus on the use of nuclear magnetic resonance (NMR) spectroscopy to study metabolic networks and reactions. To this end, several particularities render NMR a unique tool. One of its main advantages is based on the fact that NMR makes use of interactions between nuclear spins and magnetic fields, and is therefore non-invasive and non-destructive.

The versatility of this observation technique enabled its use in a wide range of applications, ranging from material science[13, 14], to the study of intact cells[15, 16], or the conformational analysis study of biological macromolecules [17, 18]. From the early years of NMR, studies on biochemistry research were developed. Mildred Cohn developed the first enzymology NMR based studies in 1962 [19]. Moreover, in the end of the 1960s, applications focusing on the study of amino acids and peptides were published by Oleg Jardetzky [20, 21]. Contributions to the study of the metabolism had also been given in the early stages of NMR by Robert G. Shulman and coworkers [22].

Biology and NMR have decades of common history [23]. During these years, the use of NMR has contributed to the characterization of a wide set of intermediate molecules in the metabolism i.e., metabolites [24, 25, 26]. Although having a description of the set of metabolites involved in metabolism can give fundamental information about the cells' conditions [27, 12], the mere identification of a complete set of metabolites does not suffice to predict the cellular phenotype. The complexity of the reaction network operating in the ensemble of metabolic processes requires the direct monitoring of metabolic reactions. This is necessary to provide a quantitative analysis of the fluxes of metabolites, and to directly establish the relations between metabolic changes and variations in the environment. NMR has proven to be well suited for this purpose, as it is able to observe in a non-invasive manner multiple metabolites simultaneously[25, 27]. However, NMR spectroscopy suffers from its intrinsic lack of sensitivity, which can be compensated to some extent by signal averaging, which in

turn increases the duration of each detection, i.e. decreases the sampling rate of the reactions. Various strategies have been developed to circumvent this issue in order to study the evolution of metabolic reactions, with conventional NMR, and without the need of a real-time observation [28, 29, 30]. The studies of metabolic transformations, or metabolic fluxes, are mainly based on stoichiometric analyses of ^{13}C labeled substrates to determine reaction rates [31]. Since the 1990s, a vast field focusing on the study of such fluxes have developed [32]. However, this technique relies mostly on the analysis of the isotopomer distribution of labeled metabolites, which at the same time depends on an untangled network of multiple metabolic processes. Other strategies slow down reactions to the scale of the NMR sampling rate [33, 29] Performing direct observations of fast metabolic reactions near physiological conditions often remains a challenge with conventional NMR.

Increasing NMR sensitivity has been one of the main motivations for the development of NMR methodology and instrumentation over the years [34, 35, 36, 37]. Some years ago, Dissolution Dynamic Nuclear Polarization (DDNP) technique was developed. The technique was able to provide tremendous sensitivity enhancements, by several orders of magnitude (up to four) [38], to conventional NMR experiments. Such a methodological leap forward has stimulated a wealth of possible applications, among which the study of metabolism [39, 40, 41, 42, 43]. Indeed, in 2003, it was demonstrated that the polarization gain achieved by DNP at cryogenics temperature could be transferred to ambient temperature to perform liquid-state NMR. With such a high signal enhancement DDNP enables one to monitor reactions with a time resolution on the order of the second or lower. It therefore becomes possible to study the various metabolites' time evolution, with high-spatial and high-temporal resolutions. [44, 45, 46, 47]. DDNP has found applications in the study of the metabolism, mainly in the characterization of metabolic fluxes and in the kinetic study of enzymatic reactions [48, 49, 50, 51, 52]. The interest in this technique has grown in recent years, several studies have been performed on different biological systems, and the methodology keeps being optimized [47, 45, 53, 54].

The objective of this Ph.D. work was to implement and optimize a methodology based on DDNP to perform kinetic studies of metabolic reactions. To perform this study two main approaches were undertaken.

The first approach relied on the study of a metabolic reaction or a series thereof. The strategy consists of performing enzymatic reactions *in vitro*, while using DDNP to monitor their evolution in time. The principal objective is to quantitatively characterize the kinetics of enzymatic reactions.

The second approach aims to perform a global observation of the metabolism by monitoring the uptake and transformation of a hyperpolarized substrate in living cells. The objective is to implement the DDNP methodology to the study of living systems in real-time and, if possible, identify biological markers to elucidate correlations between changes in metabolism and variations in cellular conditions. Hence, both approaches aim to perform quantitative kinetic studies of metabolic reactions.

The DDNP experiment is rather complex and requires the combination of multiple techniques. To start with, the hyperpolarization of the sample has to be optimized which requires an understanding of the fundamental processes giving rise to DNP phenomena. The hyperpolarization process has to be coordinated with liquid-state NMR, and with the preparation of the samples containing the biological and biochemical systems to be studied. The experiments thus require to define a protocol to prepare the *in vitro* samples or the cell cultures. Moreover, the objective is to perform a quantitative analysis of kinetic reactions. The latter implies that models reproducing the chemical reactions have to be defined and numerical tools have to be implemented in order to extract the relevant information present in the resulting NMR data.

The results obtained in my Ph.D. work and the methodologies used will be presented in this manuscript in four principal parts.

The first part is an introduction to metabolism and to the use of NMR in the study of metabolism, it includes a presentation of the strategies used to study the metabolome and

the fluxome.

A theoretical description of DNP phenomena is of fundamental importance for the understanding of DDNP methodology. Thus, in the second part, we will give a quick overview of the DNP phenomenon. The subject is further developed in Annex A, together with a study of thermal mixing mechanism. The experimental setup for dissolution DDNP will also be presented in the second part.

The third and fourth parts deal with DDNP metabolic studies performed in the course of this work. It includes the results obtained with both approaches to the kinetic study of the metabolism.

Part I

Metabolism studies and NMR

Chapter 1

Overview of the studies on metabolism

A fundamental characteristic of living organisms is their ability to adapt to the environment. In order to better understand the mechanisms underlying cellular adaptability, it is of major importance to characterize the metabolic pathways involved. These complex networks of chemical reactions enable living organisms to extract and transform chemical energy from the environment, to adapt to variations in their surroundings, and to replicate and assemble [1, 55, 9]. This is true for the simplest living organism, the cell. Both prokaryotic cells (that do not possess a nuclear membrane [1]), and eukaryotic cells [56] exhibit many differences, yet share many common metabolic pathways.

1.1 Metabolism

The complex networks of enzymatic reactions composing the metabolism is regulated by the homeostasis principle, according to which, in the cell, some quantities are maintained in a defined range (pH, osmolality, ...)[57, 58, 59]. Different metabolic processes allow the cell to uptake nutrients from the environment, and ensure their transformation and use for multiple purposes (energy production, nucleic acid synthesis, and synthesis of bigger macromolecules). This is in general achieved by cross-regulations of various coupled enzymatic reaction pathways[60, 61, 62].

The complete set of metabolites present in a system is defined as the metabolome[63].

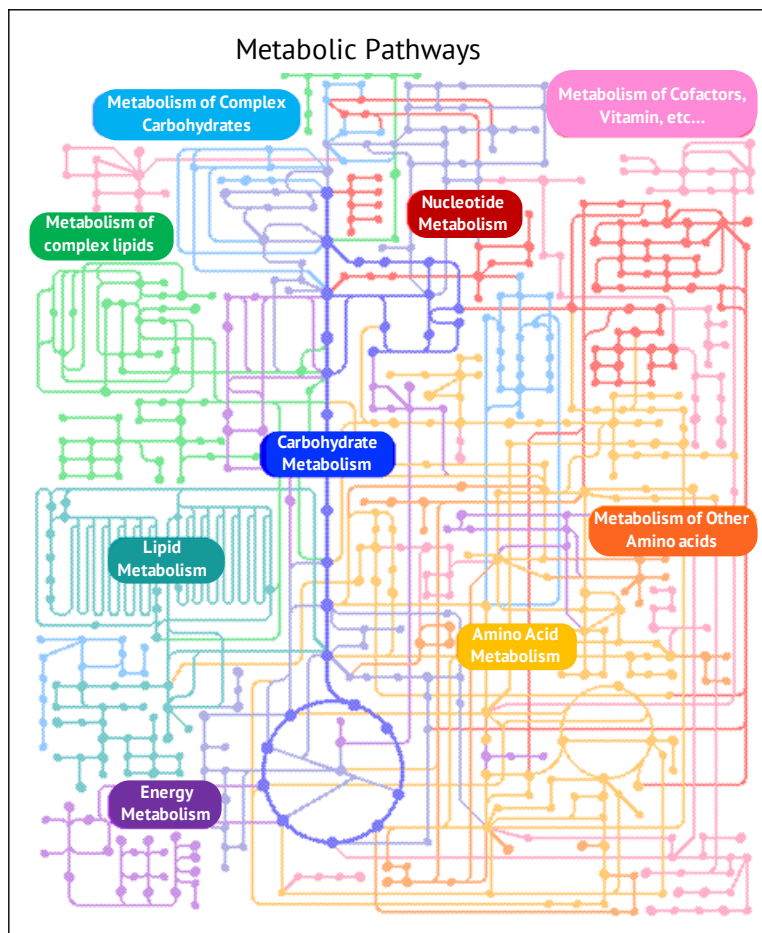


Figure 1.1: Scheme representing a part of the metabolism of an eucaryotik cell. Each dot is a metabolite, each line is an enzymatic reaction and each color is a metabolic pathway. In this scheme, the complexity of the reaction network involved in metabolism can be observed.

The metabolism of an organism is a very complex system to study, it is estimated that the number of metabolites associated with enzymatic reactions range from ~ 600 in yeast metabolism, to approximately 200 000 in humans and plants[64, 1].The extreme complexity of this reaction network is illustrated in figure1.1 for a eukaryotic cell (reproduced from reference [1]). A typical eukaryotic cell can produce up to 30 000 proteins involved in thousands of catalyzed reactions, organized in metabolic pathways[1]. The reduced representation of metabolism, displayed in figure 1.1, shows how multiple metabolites (each dot) are involved in different metabolic pathways (in different colors). A number of metabolic pathways are common or similar for all types of cells whilst others are specific to some cellular organisms[65, 66, 1]. In the following paragraph, some of the more general metabolic pathways that are related to the studies presented in this work will be briefly introduced.

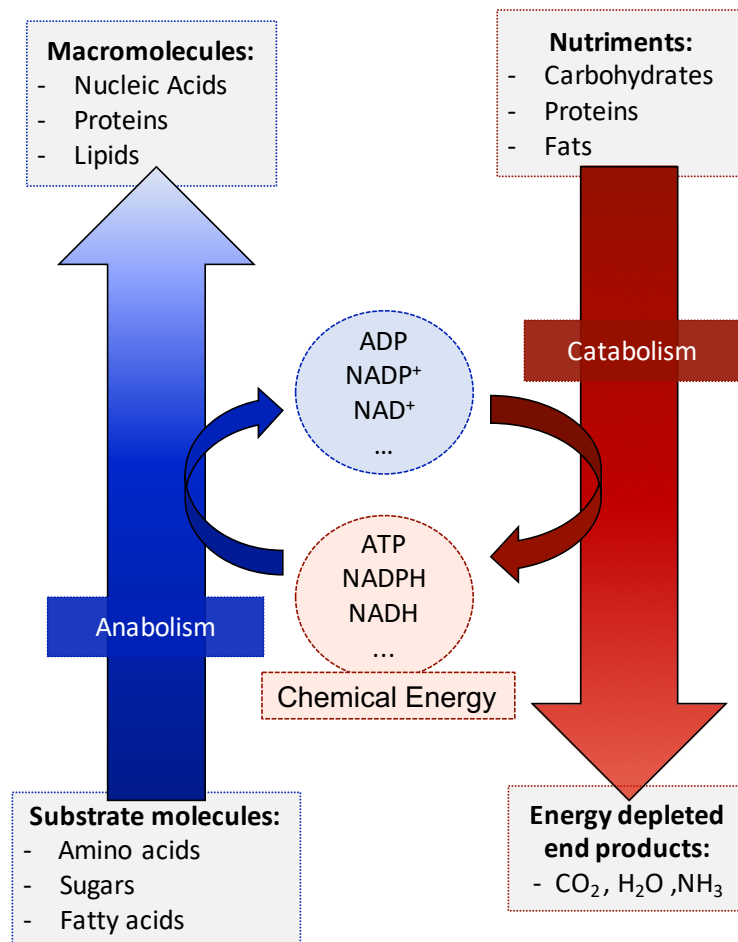


Figure 1.2: Scheme of the metabolism cycle. The catabolism that stocks chemical energy under the form of different small molecules (in red) and the anabolism that consumes chemical energy for synthesis of larger molecules (in blue).

1.1.1 Presentation of some fundamental metabolic pathways

Cells can be categorized according to the types of energy sources and nutrients they use. Autotrophs, such as photosynthetic bacteria, vascular plants, and green algae, use CO₂ from the atmosphere as their only source of carbon, energy is provided by the sun through photosynthesis [67, 1]. Alternatively, most microorganisms are heterotrophic, as they use nutrients found in the environment (sugars, fatty acids, etc...) as carbon sources [67, 1].

The chemical energy obtained from different sources is then stored and used in the different metabolic processes as free energy and is therefore converted into heat. In catabolic reactions, organic nutrients are converted into smaller molecules, a process associated with a conversion of energy that is stored in the form of ATP, or molecules with a reducing power

such as NADH and NADPH (see chapter 14 of [1]). Alternatively, anabolic reactions contribute to the biosynthesis of various biomolecules such as lipids, proteins, nucleic acids, etc...) from smaller-sized precursors. These processes consume chemical energy stored in the form of ATP, NADH, NADPH, etc... [1]. Figure 1.2 displays a summarized scheme of the anabolic-catabolic cycle.

For many heterotrophs, glucose is a fundamental nutriment [3, 68, 60]. Its degradation produces high quantities of free energy (for a general reference, see chapter 13 of [1]) and can also be stored as a polymer (glycogen) and be released in case of increased energy demand[69, 70].

Glucose uptake in *E.coli*

Multiple cellular systems have different glucose uptake mechanisms. For *E.coli*, the mechanism has been repeatedly studied and described [71, 72, 73]. The phosphoenolpyruvate-carbohydrate phosphotransferase system (PTS) is at the origin of transport and phosphorylation of different sugars in *E.coli*, namely glucose[71, 73, 72, 30]. PTS activity controls the preferential uptake of glucose over other sources of carbon[71]. The phosphoryl group transferred to glucose by the PTS originates from phosphoenolpyruvate (PEP), an intermediate product of glycolysis [73]. This transfer occurs through a series of enzyme-catalyzed reactions that result in the production of glucose-6-phosphate (G6P). Interestingly, glucose phosphorylation takes place within the membrane, upon translocation of the sugar towards the cell interior, so that it reaches the cytoplasm as G6P[72, 73, 30]. Moreover, studies have pointed to the anomeric selectivity of the glucose transfer through the membrane in *E.coli* [72, 30]. The work of *S. Benthin et al.* [30] suggested that glucose transfer by PTS relied on two independent anomer specific transport systems (see figure 1.3). Both glucose and G6P undergo spontaneous anomerization processes at particular rates to reach an anomeric equilibrium. This equilibrium depends on the conditions of the system (pH, temperature, etc.) [74, 75].

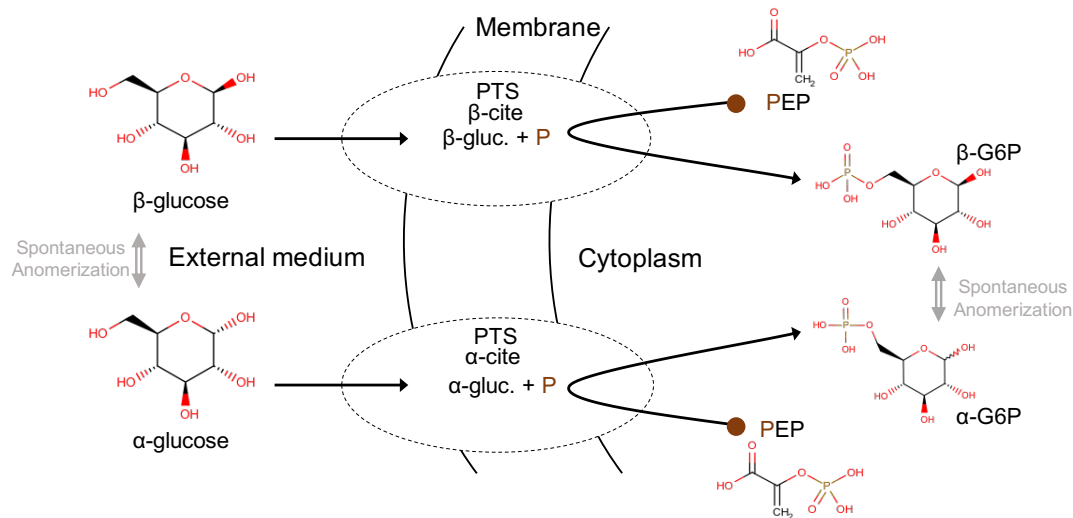


Figure 1.3: Glucose anomer selective uptake in *E. coli*. Both uptake and phosphorylation of glucose are done by the Phosphotransferase system. The phosphoryl group is provided by phosphoenolpyruvate metabolite in order to produce G6P. Both glucose and G6P can anomerize spontaneously.

1.1.1.1 Glycolysis

The main glucose catabolic pathway is glycolysis, it was discovered in 1897 on yeast fermentation [4] and was completely described for yeast by Otto Warburg [76]. This metabolic pathway was the first discovered metabolic pathway and probably the most studied one [68, 65, 76]. Through glycolysis, a molecule of glucose is degraded to produce two molecules of pyruvate. Part of the released energy is stored in the form of ATP and NADH. Glycolysis comprises two phases. In the first phase, glucose is phosphorylated into glucose-6-phosphate (G6P) (step 1 in fig. 1.4), 2 molecules of ATP are consumed and one hexose is cleaved into two molecules of 3 carbons each (step 5 in fig. 1.4). In the remainder of the glycolytic sequence, the *payoff phase* [1], four molecules of ADP are phosphorylated into four molecules of ATP (steps 7 and 8), two molecules of NADH are produced (step 6), such as two molecules of pyruvate (step 8). For the complete scheme of glycolysis see figure 1.4. During complete glycolysis, considering both phases, two molecules of ATP and two molecules of pyruvate are thus produced, and two molecules of NADH are reduced.

After glycolysis, pyruvate is catabolized along three different routes [1, 65]. For most cellular systems (most bacteria [77], mammalian cells [60, 78] and multiple plants [68]), while

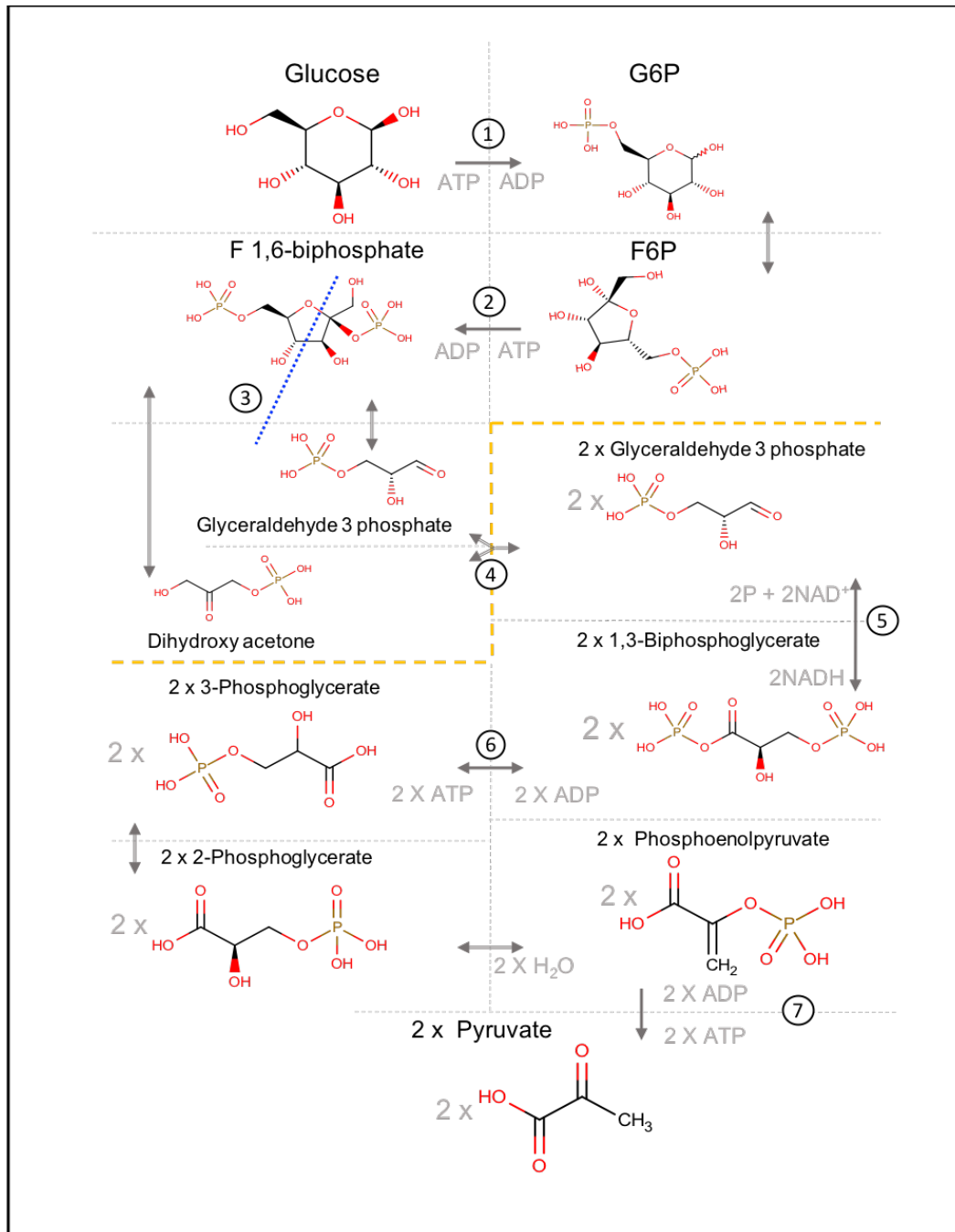


Figure 1.4: Transformation of glucose into pyruvate through glycolysis. The yellow dotted line separates the "preparatory phase" and the "payoff phase" of glycolysis (see chapter 14 of [1]). 1 Phosphorylation of glucose by *hexokinase* enzyme with consumption of one molecule of ATP and subsequent transformation into fructose 6-phosphate (F6P) by *phosphoexose isomerase* catalytic activity. 2 Phosphorylation of F6P into fructose 1,6-bisphosphate by consumption of a second molecule of ATP, catalyzed by *phosphofruktokinase-1*. 3 6-carbon structure divided into two 3-carbon structures. 4 Beginning of the payoff phase, production of two glyceraldehyde 3-phosphate molecules. 5 Transformation catalyzed by *glyceraldehyde 3-phosphate dehydrogenase* and yields two molecules of NADH. 6 Transformation catalyzed by *phosphoglycerate kinase*, where two molecules of ADP are transformed into ATP. 7 The final reaction of glycolysis produces two molecules of pyruvate and two molecules of ATP. The reaction is catalyzed by the enzyme *pyruvate kinase*.

in aerobic conditions, pyruvate produces acetyl-coenzyme A which is then completely catabolized into multiple molecules of CO_2 by the transformations occurring in the citric acid cycle [1, 79]. These transformations yield multiple molecules of ATP. On the other hand, under anaerobic conditions, pyruvate follows either degradation into lactic acid or degradation into ethanol (and CO_2) after fermentation [78, 76]. In 1861, Pasteur discovered that the consumption rate of glucose in Yeast was increased in anaerobic conditions [3], which evidenced the regulation of the metabolism according to the cell environment. The "Pasteur Effect" was later understood as a metabolic control mechanism to ensure a constant ATP level both in aerobic and anaerobic conditions, i.e., to maintain homeostasis [2]. Under anaerobic conditions, glycolysis yields two molecules of ATP, whereas in aerobic conditions, the total oxidation of glucose through the citric acid cycle produces 30 up to 32 molecules of ATP (ref. [1], chap. 14), which represents a ~ 15 fold increase of ATP production.

For *E.coli* in aerobic conditions, pyruvate is converted to acetyl-CoA and CO_2 by the pyruvate dehydrogenase complex. This enzyme is regulated under anaerobic conditions depending on the NAD^+/NADH ratio [80]. Acetyl-CoA is further processed within the citric acid cycle to produce additional ATP and reducing equivalents.

In anaerobic conditions, *E.coli* uses a wide variety of substances (since no oxygen available) as electron acceptors [81]. However, the absence of oxygen leads to the inactivation of the citric acid cycle that causes an increased production of acetate and formate [62]. Under such conditions, the production of succinate, formate, acetate, lactate, and ethanol is enhanced, which maintain the oxido-reduction balance [62], through the *mixed acid fermentation* pathway.

As has been mentioned, glucose is a fundamental nutrient for a majority of cellular systems. Since glucose supply is not always sufficient, there is a pathway through which glucose can be synthesized called gluconeogenesis. Gluconeogenesis is an anabolic pathway that transforms pyruvate, lactate, and oxaloacetate (or any compound that can be converted into one of these three) back into glucose. In the glycolytic pathway, seven enzymatic reactions are reversible and three reactions are not (steps 1, 2, and 8 in figure 1.4). Gluconeoge-

nesis follows the seven reversible enzymatic reactions of glycolysis, and replaces the three non reversible reactions by introducing new enzymes. Although gluconeogenesis requires the consumption of 4 molecules of ATP and 2 of NADH, the total energetic rendering is positive. The latter is true since in different conditions, without gluconeogenesis, pyruvate would be excreted from the cell and the production of multiple molecules of ATP (by the degradation of pyruvate in aerobic conditions) would not happen[82, 1]. Moreover, both glycolysis and gluconeogenesis are regulated allosterically or by phosphorylation of an enzyme so that when one is activated the other one is inhibited and conversely[82, 1].

1.1.1.2 The Pentose Phosphate Pathway

A second catabolic route for glucose after phosphorylation into glucose-6-phosphate (G6P) is the Pentose Phosphate Pathway (PPP). This pathway is composed by two consecutive stages. The first, the oxidative stage (OxPPP) represents the main source of NADPH, a major reductive agent in the cell [1, 83, 84]. In non photosynthetic cells, the oxPPP is a major source of NADPH, that is used in fatty-acid synthesis and in the uptake of inorganic nitrogen[85], for instance. The production of NADPH through the PPP, a main source of reductive power in the cell, maintains the redox potential necessary to protect the cellular system against oxidative stress [84]. In figure 1.5, a scheme depicting the oxPPP is presented. During the oxPPP two molecules of NADPH are produced in a chain of reactions that also yields a molecule of ribose 5-phosphate (R5P) and a molecule of CO₂. R5P can then be used as a precursor for other cellular processes like nucleic acid synthesis.

However, for some organisms that primarily require NADPH (like cellular systems in tissues) and that have a mechanism to regenerate NADP⁺, the ribose-5-phosphate is recycled to produce hexose phosphates again, namely G6P[61, 66, 1]. As a matter of fact, one of the last steps of the PPP in such systems produces fructose-6-phosphate which is converted into G6P, thus closing the cycle. For the structure of 6 carbons to be recovered, six molecules of pentose phosphates (R5P and xylulose 5-phosphate) are transformed into five molecules of hexose phosphates (G6P), after which the cycle starts again[83, 61].

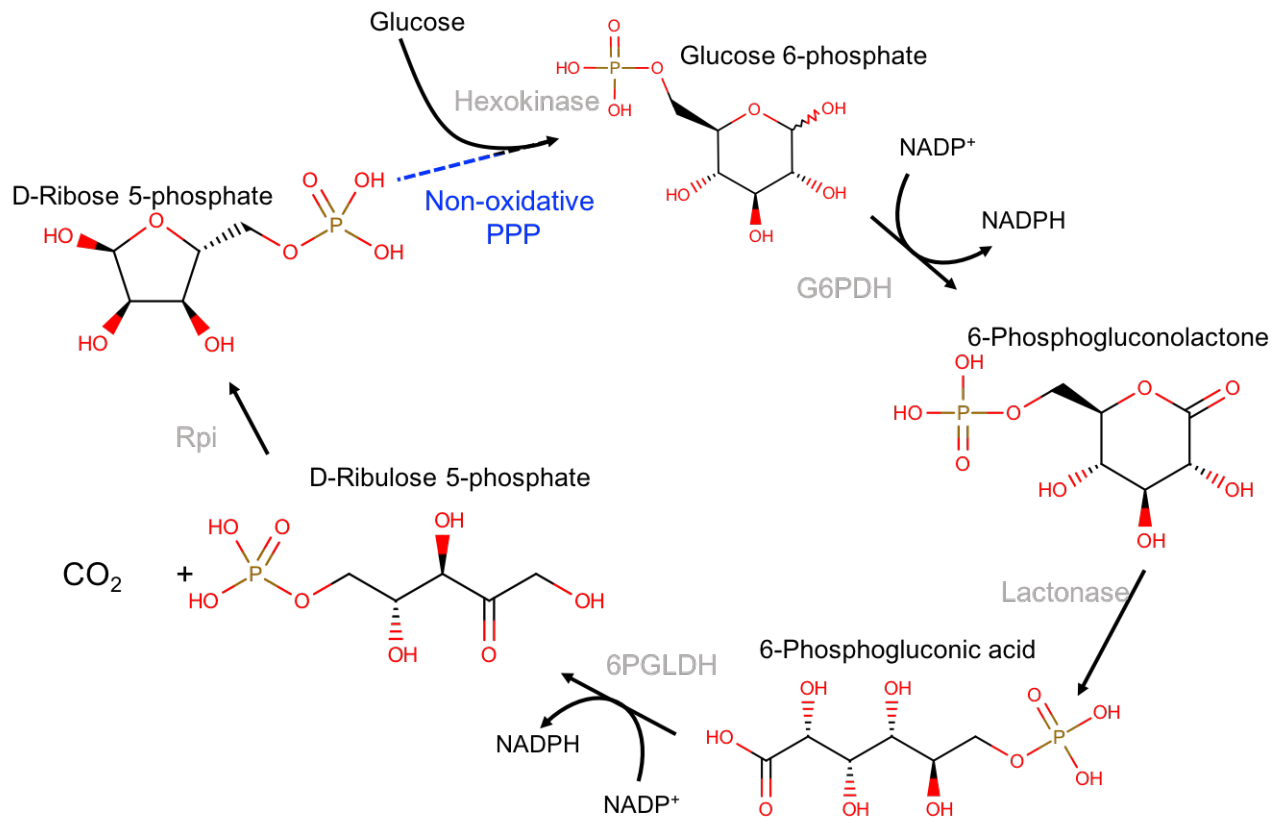


Figure 1.5: oxPPP. The PPP starts with phosphorylated glucose (produced by hexokinase). The complete oxidative phase renders a molecule of CO_2 , two molecules of NADPH and a molecule of D-ribose 5-phosphate (R5P). Although R5P can be used as precursor in multiple cellular processes, the cycle can also continue after producing R5P through the non oxidative PPP, after which G6P is produced again (blue dotted line). [66]

Glucose-6-phosphate is the common precursor of glycolysis and PPP, its respective use for both pathways is under the control of various regulatory mechanisms[80, 68, 62, 83, 61]. In the first place, NADP^+ is needed for the first reaction of the oxPPP, the dehydrogenation of G6P by the enzyme G6PDH. Similarly for glycolysis, two molecules of ATP are required in the preparatory phase. The availability of both NADP^+ and ATP is a form of metabolic regulation. Moreover, the relative concentrations of $\text{NADP}^+/\text{NADPH}$ have an allosteric effect on the first enzyme of the PPP, G6PDH. Hence, if the cell produces large quantities of NADP^+ , the high concentration allosterically stimulates G6PDH activity, increasing the flux of G6P through the PPP [61]. Other alterations of the PPP activity can be induced by several diseases. For instance, in human cells, decreased activity of G6PDH has been related to the presence of diabetes and hypertension [86]. Additionally, for cancer cells, the

reduction of pyruvate into lactate is prioritized over its aerobic degradation through the citric acid cycle. This phenomenon is called the Warburg effect [78, 76].

PPP and glycolysis regulations are dependent on the conditions of the organism, the availability of nutrients, etc... The cellular processes depending on these metabolic pathways are therefore dependent on cellular conditions in such a way that the observation of these pathways' activities could lead one to identify nutrient deficiencies or the presence of diseases.

1.2 Study of metabolome, a functional approach

Since, metabolic processes originate in enzymatic reactions, characterizing these reactions is expected to shed light on the cell phenotypic response to external stimuli or genetic variations. Such knowledge of metabolism can lead to advances in diagnosis and in the treatment of multiple diseases[87].

1.2.1 Metabolomics

Metabolomics (a term first introduced by O. Fiehn in 2002 [12]), i.e. the metabolome analysis, designates the ensemble of studies aiming at the identification and quantification of all the metabolites of an organism [12, 88, 89]. The suffix "-omics" has been recently used to characterize multiple fields of research in biology. Genomics (illustrated in particular by the Human Genome Project (HGP) [90]), transcriptomics [91], proteomics[92] and metabolomics [88, 64], each point to an important aspect of the cell function. Importantly, variations on the transcriptome or the proteome alone do not necessarily imply changes in the phenotype [64]. In this perspective, metabolomics is of particular relevance, as it can bridge the phenotype-genotype gap [12].

Multiple metabolomic strategies have been categorized by Nelsen and coworkers [93] into two main approaches. In the first approach metabolites are identified to define metabolic profiles of the studied samples, *metabolic profiling*. In the second approach quantitative

analysis is performed on a set of metabolites of a known system, "targeted metabolomics". For both approaches, multiple observation techniques are used. However, the most popular are NMR and Mass Spectrometry (MS) [94, 88, 95, 27]. The latter can be coupled to multiple separation techniques such as CEp (capillary electrophoresis) or, GC and LC (gas chromatography and liquid chromatography), which have found widespread applications [96, 97, 98, 99, 100, 101].

For LC techniques, the separation of the sample components is done in liquid-state and so, samples need minimal pretreatment [102]. LC-MS have been recently used for multiple applications in metabolomics [98, 99, 57]. The metabolite profiles obtained with this technique, typically contain hundreds of components and their analyses require the use of advanced statistical tools[103]. Another separation method that has been combined with MS is capillary electrophoresis. In this technique only small amounts of sample are needed and is well suited to polar, ionizable, molecules [104, 99]. CEp-MS has been used to perform quantitative metabolome analysis on *B. subtilis*[96]. In *Soga et al.*, a CEp-MS method was proposed, it enabled the identification and quantification of a large set of metabolites of *B. subtilis*. CEp-MS technique has however proven multiple drawbacks related to sample sticking to the capillary wall, lack of separation, or decreased species stability, which leads to problems in the quantitative aspects of the method[105]. Alternatively, Fourier transforms infrared spectroscopy (FT-IR) has also been used in metabolomics. The advantages related to FT-IR technique are the small amount of sample needed, the rapidity of the analysis, and the lack of long and time-consuming pre-treatment of the sample [106, 107]. The technique has been used in multiple studies of metabolism [107, 108]. The resulting profiles obtained with this technique are nevertheless composed of overlapping signals, difficult to disentangle[107, 109]. To date, the measurement and identification of the total set of metabolites and the complete network of metabolic pathways have not been possible. The latter is not surprising since no single methodology enables the observation and determination of all metabolites in a sample[64]. Since no single technique can be used for all metabolic studies, it is difficult to define databases with complete spectral information and

identification of metabolites. Recently, efforts have been made to develop databases containing metabolomic spectral analyses combining several observational techniques. The Human Metabolome Database (HMDB) [110](<https://hmdb.ca/>) and the Spectral Database for Organic Compounds (SDBS) of the National Institute of Advanced Industrial Science and Technology, Japan, (<https://sdfs.db.aist.go.jp>), are good examples of such efforts. They recompile information of the metabolome obtained by means of several techniques.

Although metabolomic applications of the previously introduced techniques are still being developed, their combination has nevertheless enabled partial descriptions of the metabolome, hence elucidating multiple features of metabolism [111, 99, 88]. Still, the multiple intricate metabolic pathways are dynamic processes, their evolution in time determine the concentration of the different metabolites involved in the different cellular functions. Hence, a way to observe metabolisms evolution in time is fundamental, especially since for cells the distinct metabolic processes are regulated and strongly interconnected. Quantitative analysis of the fluxes of metabolites and metabolic reactions is necessary to get a better understanding of the regulation of the metabolic pathways, it would also evidence correlations between regulatory mechanisms and cellular functions. The study of these fluxes is also an "-omics" field of research and is called fluxomics.

1.2.2 Fluxomics

The study of metabolic fluxes to better understand variations of the phenotype adds complexity to what was already a very complicated system. Novel approaches to biology have been developed to construct a more holistic way of describing biological systems and living organisms. An example of such is systems biology which aims to predict the possible behavior of a biological system based on its different components. Systems biology relies on an interdisciplinary approach to characterize biological systems of multiple scales (cells, tissues, organs) by using the molecular components, the physiological functions, and the complete phenotype to create thorough quantitative computational models that can be tested with high technology observation techniques [112]. System biology has been used in

the characterization of both the fluxome and the metabolome [64, 113, 114].

Fluxomic studies depend on observation techniques able to track the fate of a set of metabolites. To the date, the most frequently employed techniques depend on the use of ^{13}C labeled substrates[32, 28, 114]. This approach consists of feeding the studied organisms (tissues, cells, etc...) with ^{13}C labeled substrates to trace the transformation of the substrate into new metabolites. Different strategies implement the selective labeling of substrates in order to better identify what kind of transformation is taking place (what carbon structure is being transferred). As mentioned in the previous section, glucose is a fundamental nutrient in a majority of living organisms and is therefore one of the most commonly used labeled substrates in fluxomic studies [64, 28].

A major drawback of ^{13}C labeled fluxomic analysis is that, even with selective labeling of the substrate, the contribution of several metabolic pathways acting simultaneously on the substrate is hard to differentiate. The analysis is then limited to substrates intervening on the central carbon metabolism following metabolic transformations that are already known and can therefore be identified and traced in the sample[64].

Metabolic flux analysis (MFA) is another name given to the characterization of fluxes[32, 28]. Different methods have been developed to analyze metabolic fluxes and to describe their role in metabolic processes[64]. The first approach consists of a comparative analysis of metabolic fluxes. The system is studied under varying conditions and compared to reference samples. It does not give precise quantitative information about the evolution of metabolic reactions but helps to establish the impact of different fluxes in a cell's phenotype, sometimes called MIDA (mass isotopomer distribution analysis). Other approaches develop integrative methodologies to follow the transformations of the labeled substrates and reconstruct, through mathematical models, metabolic processes. For both approaches, practical examples will be given later in this chapter. A complementary approach to the analysis of the fluxome is to characterize individual reactions by studying enzyme kinetics and their impact on the metabolic pathways. In this respect, the characterization of inhibitions, regulations, and variations of enzyme activities are clearly important ingredients for

the description of the fluxome and contributes to the elucidation of the cell phenotype.

The different methodologies mentioned above have been used individually or simultaneously to characterize the fluxome of a big diversity of organisms, some examples are :

- **1998 L. Agius** : Description of the activity of produced and purified glucokinase enzyme from rat hepatocytes. Study of the enzyme activity in presence of different inhibitors and precursors. The activities of glucokinase were assayed following different methodologies adapted to experimental conditions. Activities were extracted from samples with: varying concentrations of glucose as substrate, with different glucose analogs as substrate, in presence of different glucokinase inhibitors. From the extracted enzyme activities multiple features of the enzyme were deduced, features directly related to phenotypic changes of the cell. For example the translocation of glucokinase from the nucleus of the cell to the cytoplasm due to an increase in glucose phosphorylation. [115]
- **2001 - M. Dauner et al.** : First combined study using NMR and MS observation techniques among others. Evaluation of the energy consumption and dissipation on [U-¹³C]-glucose metabolism of *Bacillus subtilis* bacteria. The system was tested under various conditions: carbon in excess, carbon limitations, nitrogen limitations and phosphorus limitations. The metabolic reaction of the bacteria was assayed to determine the concentration evolution of multiple products, the consumption of oxygen and glucose, and the relative concentrations of intracellular ATP/ADP. They observed that for cultures with carbon excess at big dilution rates (low cellular concentrations) there are no mechanisms that dissipate ATP different from the principal metabolic pathways (gluconeogenesis, etc..). On the other hand, for low dilution rates, almost 20% of the energy is dissipated through alternative mechanisms. It was also the case for samples with phosphorus or nitrogen deprivation [31]. Description of the alternative ATP dissipating mechanisms are given.
- **2001 - W. Wiechert et al.** : Proof of concept, use of a quantitative methodology to study different anaplerotic reactions in *Corynebacterium*. Labeled glucose was used

as a substrate, with different labeling strategies. In this work, they use ^{13}C -FLUX methodology, a strategy to make quantitative studies of fluxes. It follows a series of optimization steps: giving a biological description of the system, define a mathematical model to characterize flux evolution, perform statistical analysis, optimize the experimental design for observation and evaluation of the biological system [28].

- **2004 - S. Marin et al.** : Study of glucose metabolic network in rat hepatocytes. It uses MIDA and $[1,2-^{13}\text{C}]$ labeled glucose. Cell samples were prepared with variations in the incubation conditions, different metabolites were added to the incubation medium in addition to selectively labeled glucose. For some samples, the metabolites added to the medium are substrates of the gluconeogenesis pathway. At the end of incubation, samples were frozen and subsequently processed to extract metabolites. After mass spectroscopy analysis, the isotopomer distribution showed a different flux of glucose through the glycolytic/gluconeogenetic pathways depending on the metabolites available in the sample. This example is a comparative study that gives a description of rat hepatocytes phenotypic variations related to substrate conditions [116].

Multiple methodologies rely on different observation techniques to describe the fluxome of an organism [32, 64, 28]. However, few techniques defined fluxes in terms of kinetic parameters and time domain observations. For the majority of strategies, the fluxes are determined by analysis of the isotopomer distribution after metabolism of ^{13}C -labeled substrates [116, 32, 31]. Fluxes were inferred from analytical models of metabolic pathways or comparative approaches. Direct observation of metabolic reactions would require an efficient high-throughput, quantitative technique, or an alteration of the sample to slow down metabolic processes. Having a technique that allows fast sampling (ideally larger than 1 Hz) would simplify quantitative approaches and elucidate the reactions involved in metabolic processes.

Chapter 2

NMR

The purpose of the work presented in this manuscript is to develop a technique to perform kinetic studies of metabolic reactions. We aim therefore to develop a methodology focused on the characterization of the fluxome. For this purpose, NMR presents multiple advantages as an observation technique. The non-destructive nature of the technique, the capability of defining structures [17, 117], and the option for quantification [118, 119, 120], are characteristic features of NMR. Moreover, there is no need of isolating the analytes which implies that samples can be easily prepared [121]. Finally, NMR allows the simultaneous observation of several analytes in a mixture [120, 121]. All of the previously mentioned features have made this technique a fundamental tool in multiple domains like material science [13, 14], pharmacy [122, 123], food industry [124, 125] etc. NMR has also contributed to the metabolomics and fluxomics fields of research and is, with MS, one of the two main observation techniques [111, 126, 32]. However, it seems that for these two '-omics' fields of research, MS has been more frequently used [127, 128, 111]. The characteristic features of both techniques have been repeatedly compared and discussed [99, 32, 129, 130, 64, 111]. The benefits of both techniques have even been combined in metabolomics and fluxomics studies [31, 126].

However, major drawbacks in NMR related to the low sensitivity [64, 128, 32], low resolution [131, 132, 111] or hardware cost [133, 32] seem to reduce the use of NMR technique in these fields of research. This problematic was addressed in a recent review by Patrick

Giraudeau [128]. It seems that the previously mentioned limitations as well as a lack of historical collaboration between both scientific communities are at the origin of the limited use of NMR in metabolomics and fluxomics fields. Moreover, W. Wiechert, in a review about MFA and fluxomics, claims that "The optimization of NMR measurement parameters and the proper interpretation of all the peak fine structures in a spectrum require a skilled NMR specialist" [32]. The latter implies that the technicalities of NMR method limit its use in groups in which NMR is not a usual tool. P. Giraudeau also mentions that the limited use of NMR in metabolomics also originates from the lack of collaboration between researchers in both fields, "limited connections between the historical NMR groups [...] and the large community of NMR users who are involved in practical metabolomics studies[...]"[128].

NMR field is nonetheless experiencing major developments to address multiple of its major limitations. For the study of samples heavily charged with different metabolites, techniques have been developed to avoid or disentangle the signal overlapping. Although increasing the magnetic field [35, 128] or relying on alternative nuclei (namely ^{13}C or ^{31}P)[134, 32, 135, 136] have been focused to circumvent this issue, other new strategies have been recently implemented. These new strategies rely on decoupling techniques[137, 138] and multi-dimensional NMR [139, 140, 141, 142] to spread and differentiate overlapping resonances.

To overcome the high budget related to NMR hardware, companies have developed low field, benchtop NMR spectrometers [143, 133, 128]. The new devices not only are less expensive ($< 100\,000$ €) but also are less heavy and have smaller dimensions (< 100 kg) than conventional spectrometers[128]. Although the low field related to such devices implies a loss of sensitivity and resolution, these spectrometers can still be used in metabolomics. As a matter of fact, benchtop NMR spectrometers have already been used in metabolomics to make metabolic profiles of urine samples for patients with type II diabetes [144].

Finally, multiple strategies to increase NMR sensitivity have been addressed in recent years. Not only NMR hardware has advanced [34, 35], but also techniques relying on increasing nuclear polarization have been developed and implemented [36, 145, 146] to over-

come NMR sensitivity problems. Between these techniques, Dynamic Nuclear Polarization (DNP) has had a big impact in the NMR community and will be further developed in the remaining of this manuscript.

2.1 NMR in metabolomics and fluxomics

The major advances presented in the previous paragraph have brought the fields of metabolomics and fluxomics closer to NMR. Multiple NMR based strategies have been used to contribute the characterization of metabolism.

2.1.1 *In vitro* and *ex vivo* studies

The study of metabolic processes sometimes depend on the *in vitro* reproduction of the phenomenon. Multiple reasons make living organisms not suited for direct observation. Living organisms are complex systems that cannot always be adapted to the experimental conditions of the observation method, namely destructive methods. Additionally, during detection, the observed system has to be static. For long-duration observations, the evolution of living systems can therefore be problematic. However, reactions in metabolism can be reproduced *in vitro* [19, 75, 72] or analyzed *ex vivo* to characterize a particular metabolic process or to assess the impact of an organism on its environment [147, 148, 149].

2.1.1.1 NMR spectroscopy to study enzyme kinetics in real-time

The easy preparation of samples in NMR, its quantitative nature, and the simultaneous observation of multiple analytes, are ideal features for the study of enzyme kinetics. The first applications of NMR in the study of enzymatic reactions date from the late 1960s [19, 150]. The quantitative aspect of NMR has been used to characterize different enzymatic reactions [115, 75]. The analysis has not been restricted to ^1H NMR, studies relying on ^{31}P and ^{13}C (between others) [135, 151, 152], together with multi dimensional NMR [75] have contributed to these metabolic characterizations. Most studies are based on deducing enzyme activi-

ties from analytical models [153, 30], and by comparison with reference reactions at known rates. However, real-time monitoring of the reactions remains scarce due to the low time resolution of the NMR technique. To overcome this issue, some approaches have focused on slowing down the observed enzymatic reaction artificially, thus enabling its screening [33, 30, 29]. This approach was used to characterize the second reaction of the oxPPP [33]. When this work was published, there was a debate over the role of the second enzyme of

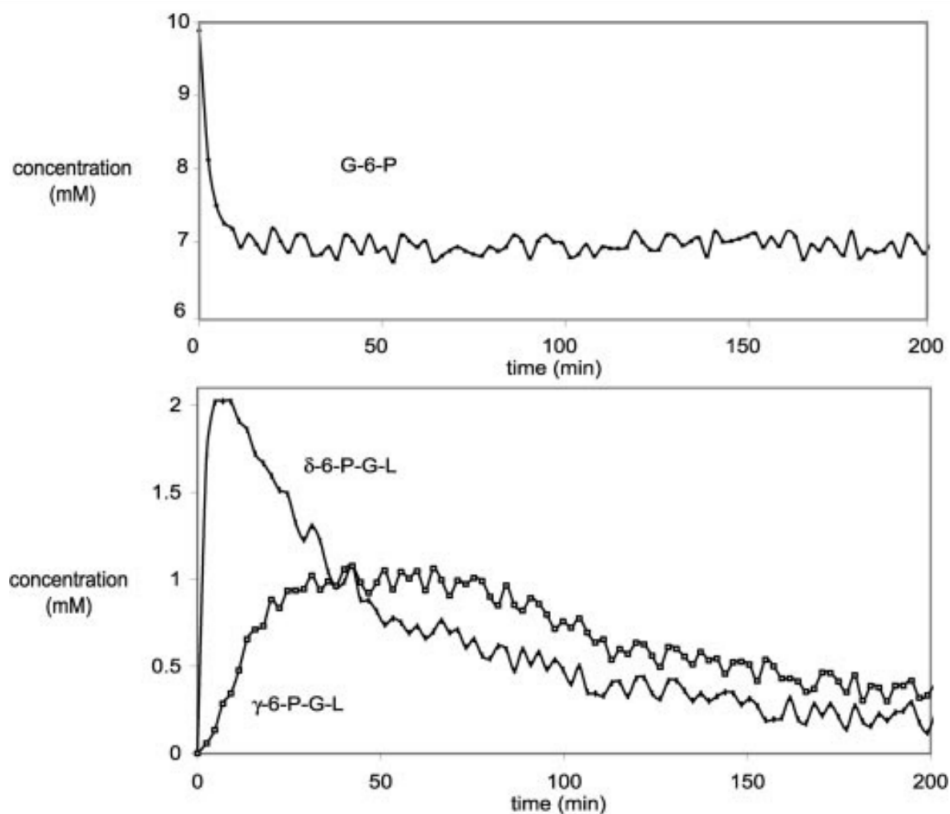


Figure 2.1: Figure taken from [33], concentration evolution of G6P δ -PGL and γ -PGL. Concentration values were deduced from ^{31}P NMR signal. The reactions were performed at 5°C to slow down the process.

the PPP, 6-phosphogluconolactonase (6PGL) enzyme. Supposedly 6PGL enzyme catalyzed the hydrolysis of the two isomer forms of 6-phosphogluconolactones, δ -PGL and γ -PGL. In that study, the first 2 enzymatic reactions of the oxPPP were reproduced *in vitro*, in a sample containing the labeled substrate, $[\text{U-}^{13}\text{C}]$ G6P. A sample without the second enzyme was also used to assess the spontaneous hydrolysis of δ and γ isomers. Samples were cooled to 5°C to slow down the enzymatic reaction so as to monitor them in real-time. A two-minute time resolution was achieved with ^{31}P NMR (an averaging of 80 scans was required for each

spectrum).

The ^{13}C carbon labeling was used only to identify the reaction products of the G6P dehydrogenation by G6PDH. The curves of the peak intensities versus time provided the kinetics of the different metabolites involved in the reaction (figure 2.1). These experiments demonstrated that the oxidation of G6P by G6PDH yielded only one isomer, δ -PGL. The γ -PGL isomer is mainly observed after all G6P is consumed. A second conclusion was that the only substrate of 6PGL enzyme is δ -PGL. In a subsequent experiment, a sample with both isomers at the same concentration was stabilized (5 °C , pH 6.7). 6PGL enzyme was then added, its activity transformed δ -PGL into phosphogluconic acid (6PGA) and let γ -PGL unchanged proving that only δ -PGL isomer is a substrate for 6PGL enzyme.

The work cited here is an example of how the screening of metabolic reactions can provide direct qualitative information of enzymatic reactions with simplified models. Moreover, quantitative information can be easily extracted from the data since the relation between precursor and product can be directly observed. However, to better reproduce metabolism, the *in vitro* systems need to be prepared near physiological conditions. The latter implies that an increased time resolution is required to be able to monitor enzymatic reactions in real-time.

2.1.1.2 *Ex vivo* metabolomics by NMR

The adaptation of a cellular system to its environment causes variations in the excreted metabolites. Depending on the organism, the nutrients available, and the active metabolic processes, different metabolic products can be released to the external medium[148, 149]. Metabolomics has also relied on the characterization of the external medium to evidence variations in cells phenotype [149, 154]. *Ex vivo* NMR methodology has been optimized for different samples like plasma and urine [147, 155, 149]. This *ex vivo* characterization relies on the observation of samples heavily charged with metabolites. The peak attribution of such samples can thus be very challenging due to the multiple overlapping resonances, analyses therefore use statistical tools for data treatment to overcome this issue[156, 157]. *Ex vivo*

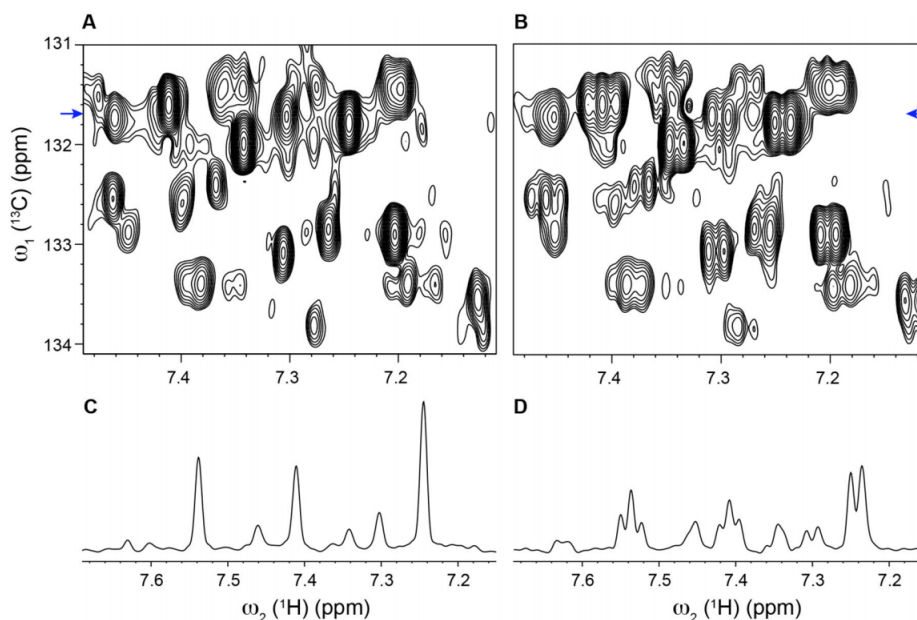


Figure 2.2: Figure taken from [?]. Spectrum on the aromatic region of a sample of mouse urine. 2D ^1H - ^{13}C pure shift HSQC spectrum (A), compared to a standard HSQC (B).

samples are normally stable for longer periods than living organisms, multi-dimensional NMR experiments can thus be used to facilitate peak attribution [141, 158].

However, in some cases, the scalar coupling of the different nuclei causes the apparition of additional resonances. Hetero-nuclear decoupling standard techniques are commonly employed in NMR[159] and can be used to reduce the sample's resonances overpopulation. Moreover, recent developments use "pure shift NMR" methodologies to perform homonuclear decoupling.

In the work published in *I. Timari et al. 2019*, they use pure shift NMR to perform homonuclear decoupling on mouse urine samples. The metabolomic characterization is simplified since the spectra become better resolved if the resonances related to the scalar coupling are removed. In figure 2.2, a conventional HSQC spectrum (B) is compared to a pure shift HSQC spectrum (A). The spectra displayed in the aromatic region shows how there are multiple overlaps of different resonances when no decoupling is applied, even at high magnetic fields. One of the particularities of their work is that the optimization of the pulse sequence, gives HSQC spectra with no loss of sensitivity and with the improved

resolution of pure shift.

Hence, *ex vivo* samples are stable for longer periods than living cells or *in vitro* reproductions of enzymatic reactions. Multiple NMR techniques with enhanced spectral resolutions can thus be used to characterize metabolic profiles. However, *ex vivo* samples have been isolated from the studied organisms and so the organism's evolution cannot be observed.

2.1.2 In vivo studies

In this manuscript, when NMR is said to study *in vivo* systems, it also considers samples of isolated cells (in-cell) and isolated tissues. Other magnetic resonance (MR) based techniques, namely magnetic resonance imaging (MRI), has been used to perform *in vivo* studies of the metabolism of living animals and humans [160, 161, 162].

The non destructive characteristic of MR techniques enables the study of *in vivo* systems. Additionally NMR is very versatile with temperature regulation and so, samples can be studied near physiological conditions. Nevertheless, there is a drawback, NMR spectrometry requires a certain time to make a detection, duration in which the sample must be stable. As has been mentioned multiple times in this manuscript, living organisms evolve and adapt to the environment. In order to use NMR as an observation method for *in vivo* applications, the living organism must be put in a steady state or the reactions have to be quenched during the detection time[163, 164, 165].

Moreover, the observation of living cells results in heavily charged spectra. As for *ex vivo*, the presence of a very large set of metabolites makes peak attribution a difficult process. Multiple strategies have been developed in NMR to analyze complex systems and facilitate the attribution of peaks, namely 2D NMR [132, 142]. Heteronuclear MR has been also used for this purpose, in the study of multiple cellular systems [166, 30, 164, 72, 16].

2.1.2.1 NMR in vivo assignment with bioreactor

NMR probes have been adapted to the study of living system by developing mechanisms to distribute nutrients and oxygen to the cells, present in the NMR tube[167, 142, 168]. These bioprobes or bioreactors, subminister nutrients at constant intervals and uses the self-regulation of a cellular system to imitate a metabolic steady state in which NMR is used to characterize the metabolome.

In the work presented in *M.T. Anaraki et al.* [142] the use of a bioprobe (or bioreactor), constructed in their group, is used to stabilize the metabolism of a living organism. The bioreactor used in this work is called *Low-volume flow-system*, a complete description is given on [169]. The studied system is *Daphnia Magna* a small crustacean (1.5 - 5 mm) that consumes algae and is eaten by fish. The organism is small enough to be studied with NMR spectrometers in 5 mm NMR tubes and is constantly fed with nutrients and oxygen through the bioreactor. The only food source used was another living organism, algae *Chlamydomonas reinhardtii* which was previously fed with ^{13}C enriched nutrients.

The principal objective of this work was to make a complete characterization of the metabolome of a living organism. The NMR spectrometry based description can subsequently be used to characterize the metabolome of other organisms. Multiple NMR strategies were used to identify the very big amount of metabolites present in such a complex biological system. In figure 2.3 we see an HSQC in vivo spectra of ^{13}C enriched *Daphnia Magna* with a color coded metabolite attribution. The attribution was made based on supplementary NMR experiments and by comparison with multiple databases and with literature. The peak attribution was very challenging because of the overpopulation of all spectra recorded, as for the majority of *in vivo* metabolomic experiments. In [142], it was mentioned that the attribution "required a laborious manual approach that required checking on a peak by peak basis across numerous spectra and the literature, which was important to avoid misassigning components due to overlap". The multitude of different 2D and even 3D NMR experiments were then used to relate 1D simple ^1H experiments to a complex and

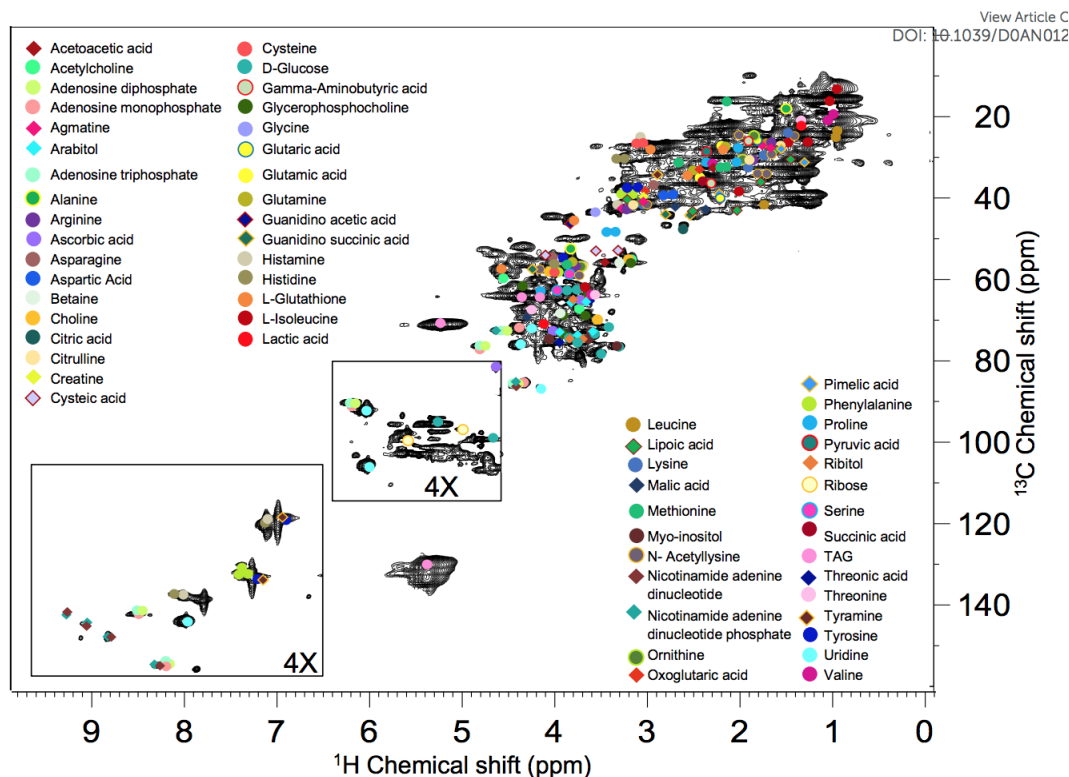


Figure 2.3: *In vivo* 2D HSQC (^1H - ^{13}C) spectrum of ^{13}C -enriched *Daphnia magna* with color coded metabolites assigned. Figure taken from [142]

complete peak attribution. This effort constitutes a big contribution to the metabolomics field, feeding databases with a spectral description of a living organism's metabolome and making it accessible to studies with less NMR complexity and without the need of ^{13}C labeling. In my opinion, this work is a great example of what is metabolomics true objective as a holistic approach.

2.1.2.2 NMR in cell kinetic study

As mentioned above, multiple in-cell studies have been performed with NMR in metabolomics [15, 132, 16]. However, kinetic in cell studies remain scarce due to the low temporal resolution achievable with NMR. NMR has nevertheless been used to perform kinetic studies of metabolism focusing on slow reactions (time scales in the order of tens of minutes to multiple hours) [163, 170, 168]. ^{31}P MR has been widely used in-cell to characterize the kinetics of multiple features related to cells' metabolism like substrates consumption, production of

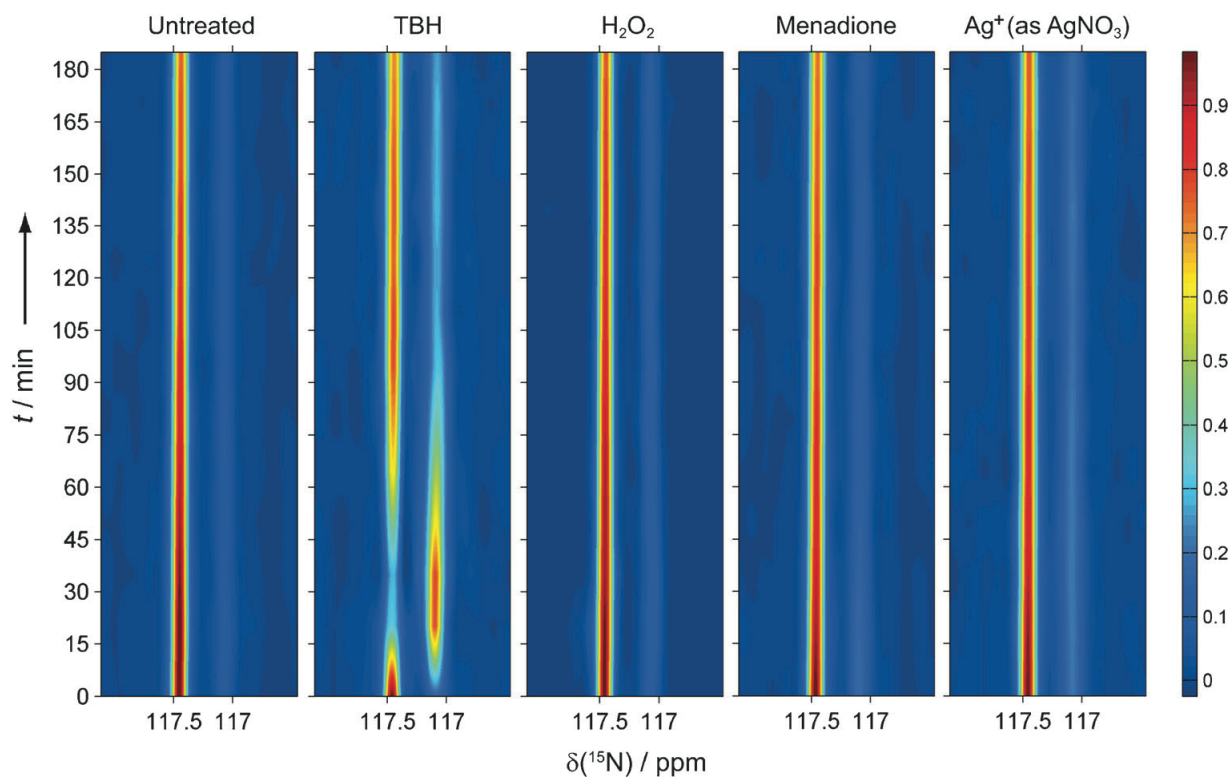


Figure 2.4: Figure taken from [170]. Time-course analysis of glutathione redox homeostasis in living *S. cerevisiae* cells upon oxidative stress. The cellular response to oxidative stress was monitored over the course of the experiment by using in-cell NMR spectroscopy, shown here as filled contours from 1D ^{15}N projections summed over $\delta(^1\text{H})=8.0\text{--}8.3$ ppm of the $^1\text{H}\text{--}^{15}\text{N}$ HSQC spectra

energy, or internal pH regulation [163, 171, 172, 173]. Other work based on in-cell ^{13}C NMR has been documented [72, 174]. ^{13}C Isotope labeling is often used to increase signal intensities, enabling also faster NMR detections. ^{13}C labeling techniques have also been combined with 2D-NMR in the characterization of dynamic, and interaction properties of proteins in living cells with time resolutions in the order of tens of minutes [175, 176].

In [170], multi-dimensional NMR is used to study the oxidation of ^{15}N labeled glutathione with a real-time fluxomic approach. Selective pulses were used to reduce the sampling window and so, reduce the time needed for each detection. 2D NMR allowed to separate peaks that overlapped in the ^1H dimension whereas remained well separated in ^{15}N dimension. The technique was used on *Saccharomyces cerevisiae*, which has a specific high-affinity uptake system for glutathione. Pulses were calibrated to allow the quantitative monitoring of the evolution of the different signals. The system was studied under various conditions, to this end cells were treated by the addition of different compounds

($\text{H}_2\text{O}_2, \text{AgNO}_3, \dots$) and compared to reference control experiments, see figure ??.

In this work, they were able to study the flux of a metabolic reaction in a living organism. They used non disruptive and quantitative characteristics of NMR, mixed with the increased spectral resolution of 2D NMR and selective isotope labeling to that end. Although the method allowed to successfully identify variations of the glutathione flux in different cellular environments, the reactions observed had characteristic time scales in the order of multiple tens of minutes. Hence, this method is an effective way to perform real-time studies on living cells provided that the reaction observed is a slow process (tens of minutes). However, a vast majority of metabolic reactions in living organisms are characterized by times scales inferior to a second.

Although NMR seems to present multiple advantages to the study of living systems, its time resolution limits the study of fluxes to slow reactions or artificially slowed reactions. In order to develop a more general technique to monitor real-time metabolic reactions, for both in cell and *in vitro* systems, the time resolution of NMR need to be increased, i.e. NMR sensitivity needs to be enhanced.

2.2 The Dissolution DNP technique

Developing methodologies for signal enhancement on NMR is of primary importance to overcome the weak sensitivity of NMR, its principal limitation. One of the principal hyperpolarization techniques used to date is dynamic nuclear polarization (DNP), a technique that originated with Overhauser's idea to use electron polarization to increase nuclear polarization [177]. The term dynamic nuclear polarization was given by Abragam, in 1958, while performing experiments on diamagnetic insulators using paramagnetic impurities, the polarization donor system [146]. A review of DNP mechanisms will be given in the next chapter.

Although DNP constituted a methodology that successfully enhanced NMR signal, multiple features of the technique strongly limited the range of applications. The main problem of DNP for a solution state spectroscopist is to use a hyperpolarized sample at ambient

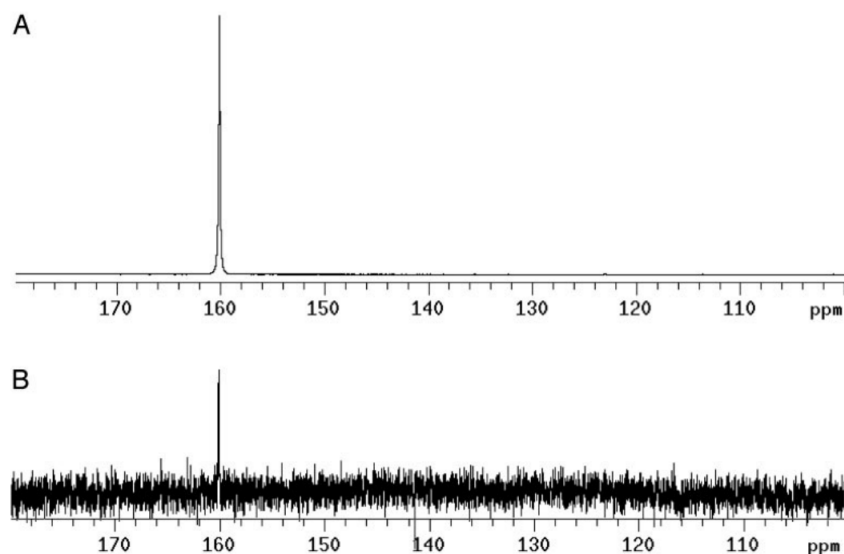


Figure 2.5: Figure taken from [178], both spectra acquired on the same sample of Urea at 59.6 mM in the same 9.4 T spectrometer. **A:** DDNP experiment. **B:** Urea in thermal equilibrium, averaging over 65 h, 232128 transients. Estimated signal enhancement of $\epsilon = 44\ 400$.

temperature whilst it is prepared at cryogenic temperatures.

2.2.0.1 The invention of Dissolution DNP

In this perspective, a major technical development was achieved in 2003. When in *J.H. Ardenkjær-Larsen et al.* a frozen DNP sample was dissolved and transferred to a conventional liquid-state NMR spectrometer [178]. The sample remained hyperpolarized for a duration in which NMR signal was strongly enhanced. Since the hyperpolarized state is not an equilibrium state, when a sample leave DNP conditions the polarization enhancement starts decaying following longitudinal relaxation, characteristic to each nuclear system (proportional to T_1 time constant). Experiments were carried on both ^{13}C -labeled urea and urea in natural abundance. The spectra displayed on figure 2.5 was acquired with urea in natural abundance, the upper spectrum uses dissolution DNP. Signal enhancement was on the order of 44 400 between hyperpolarized ^{13}C and thermally polarized spectra. A

In figure 2.5, the spectrum with no hyperpolarization (i.e. at thermal equilibrium) was averaged over 65 h, 232128 scans compared to 1 scan for the experiment with hyperpolarization. Since the signal intensity determines the time resolution achievable for the monitoring of dynamical processes, hyperpolarization represents a most useful way to observe reactions

with small time scales, on the order of the acquisition time ($\sim T_2^*$). Typically experiments performed with DDNP have a time resolution on the order of a second or less. Hence, DDNP technique has enough time resolution to make real-time studies of metabolic reactions. The labeling strategies used in the multiple fluxomic methodologies can be combined with DDNP or replaced by the contrast between hyperpolarized and thermally polarized compounds[46, 45, 44, 128]. Dissolution DNP technique appears as a very promising technique that has led to a wide range of potential applications, in metabolomics or fluxomics, both *in vitro* and *in vivo* [179, 49, 50, 53, 180].

2.2.1 Advantages and known limitations of DDNP methodology

2.2.1.1 Fast sampling technique ideal for fluxomic studies

In DDNP, the analytes' signal can be monitored for the duration in which the hyperpolarization remains. However, each NMR pulse generates a polarization loss proportional to $1 - \cos \theta$, where θ is the flip angle. Thus, in DDNP, time sampling of metabolic reactions is achieved using the smallest possible flip angles. The simple NMR pulse sequences used in DDNP provide spectra that can be analyzed quantitatively.

Relying on nuclear species with characteristically long relaxation times has been prioritized in DDNP experiments to avoid the complete relaxation of the hyperpolarized signal. ^{13}C MR is thus frequently used, which represents also an increase in spectral resolution compared to ^1H MR [47, 45]. Such a technique thus allow the simultaneous screening of a substrate and its metabolic products. It can thus be used to perform kinetic studies of metabolic reactions or to elucidate the reaction schemes of different metabolic processes.

Although DDNP methodology seems to be very promising for applications in multiple domains, some of the major concerns have to be addressed. To start with, as mentioned above, hyperpolarization is not an equilibrium state. When the DNP sample leaves the polarizer (DNP hardware), longitudinal relaxation causes the sample to go back to equilibrium i.e. to thermal polarization. Hence, during the transfer, a part of the polarization enhancement is lost. Naturally, to reduce enhancement loss one can, reduce the duration of the

transfer, slow the relaxation process, or use substrates with characteristic long T_1 . Different DDNP setups rely on the manual injections of the dissolved sample, characterized by long transfer times (5-10 s duration)[38, 53, 181]. Other setups with automatic injection systems normally push the sample with gas through pipes connected to the NMR tube inside the spectrometer[182, 183]. These systems, have other problems related to the mechanical shock of the injection, which can damage the sample (such as living cells). Pressure regulated injectors are being developed for DDNP applications, to prevent the mechanical shock of the automatized dissolution systems[45, 184, 54, 185]. The usual strategies to increment hyperpolarized signal in DDNP are thus often based on choosing substrates with characteristically long T_1 and diminishing the transfer duration. Being forced to choose molecules with functional groups having long T_1 is clearly a strong limitation for metabolomic and fluxomic studies since some metabolic pathways are therefore not accessible to DDNP methodology.

2.2.1.2 Reproducibility problems of a complex experiment

As will be detailed in the next chapter, DDNP experiments depend on a very complicated set-up. The time needed for the polarization of the sample to attain a maximum hyperpolarization level can vary from tens of minutes to several hours. After reaching maximum polarization, the sample, which is frozen in a bath of liquid helium, has to be dissolved to be transferred to the NMR spectrometer. Thus, samples have to be extracted from chambers filled with cryogenic liquids, where any air leakage would provoke the complete freezing of the system, causing the failure of the DDNP experiment and in most cases the loss of the DNP sample. Moreover, during the dissolution experiment, for a big majority of DDNP systems[182, 185, 183], the dissolution procedure is done manually and so the duration of the dissolution step changes between experiments. The polarization of the sample transferred to the NMR spectrometer is therefore dependent on the experiment and so is not completely repeatable.

Solvents used for the dissolution of the frozen DNP sample are warmed to very high

temperatures ($\sim 140^\circ\text{C}$) to optimize the amount of sample liquefied and transferred. Hence, the dissolution implies that the DNP sample has to be exposed to extreme thermal conditions which limit the nature of the hyperpolarized compounds that can be used.

As mentioned in the introduction, the principal purpose of my Ph.D. work is to optimize the experimental procedure both technically, by adapting the DNP technique and the hardware to the study of biological and biochemical systems; and analytically, by developing methods to characterize the kinetics of the observed reactions. In the next chapters, after properly introducing DNP and DDNP, the fluxomics projects undertaken during my Ph.D. will be presented, the results serving as an additional proof of concept of the potential contributions of DDNP to the study of metabolism.

Part II

A review of the basics of DNP and DDNP

Chapter 3

Short review of DNP

As mentioned in the last chapter, DNP is able to increase NMR signal by several orders of magnitude. It was discussed that the enhancement depends on reducing the temperature to cryogenic levels which implies that the studied system must be frozen and so, in solid-state. The Dissolution DNP experiment bridges the gap between DNP hyperpolarization and conventional liquid-state NMR, where *in vivo* and in-cell biological systems, as well as *in-vitro* biochemical systems can be studied. DDNP experiments are complex, as many different issues are encountered, especially regarding the loss of polarisation during transfer of the solution with the hyperpolarized spins. Optimizing the different steps of the experiment is therefore of primary practical interest.

In this chapter, we will review the main mechanisms of DNP hyperpolarization, and some recent aspects of thermal mixing will be discussed.

3.1 Polarization

The spin momentum of the electron, $\hbar\mathbf{S}$, is associated to the magnetic moment $\boldsymbol{\mu}_S = \hbar\gamma_S\mathbf{S}$, where \hbar is the reduced Planck constant and γ_S is the electron spin gyromagnetic ratio: $\gamma_S = \frac{\mu_B}{\hbar}g_S$; μ_B is the Bohr magneton and g_S is the g-tensor (isotropic for the free electron). Electrons have half odd spin, and so $|\mathbf{S}| = S = \frac{1}{2}$. Similarly, the nuclear magnetic moment will be noted $\boldsymbol{\mu}_I = \hbar\gamma_I\mathbf{I}$. In the following, we will assume $I = \frac{1}{2}$ as is the case for protons.

In the presence of a magnetic field, the degeneracy of the spin energy levels is lifted, which leads, by virtue of the Boltzmann law, to a population imbalance between the upper and lower states, therefore a spin polarization. It will be shown below that reducing thermal motion can be described by a cooling of the spin system. As a matter of fact, nuclei are difficult to polarize. Efficiently increasing their polarization cannot be undertaken by simply imposing a strong magnetic field, hence the originality of DNP. The qualitative idea of DNP is to achieve a similar orientation for a large population of nuclear spins i.e. to increase the polarization of the nuclear spin system. Hence, polarization is the relative difference of populations in the two states of energy. To quantify the polarization enhancement achievable via DNP, the interactions between the particles and the field need to be introduced.

The Zeeman interaction between the electron spin magnetic moments and the external constant magnetic field \mathbf{B} is:

$$\mathcal{H} = -\hbar\mathbf{B}\cdot\boldsymbol{\gamma}_S\cdot\mathbf{S} = \hbar\boldsymbol{\omega}_S\cdot\mathbf{S} = \hbar(\omega_S^x S_x + \omega_S^y S_y + \omega_S^z S_z), \quad (3.1)$$

where $\boldsymbol{\omega}_S$ is the frequency vector $\boldsymbol{\omega}_S = -\mathbf{B}\cdot\boldsymbol{\gamma}_S$. The spin state vector can be represented by a two-dimensional state vector $\boldsymbol{\psi}_S = \begin{pmatrix} a \\ b \end{pmatrix}$ in the basis of states $\{|m_S\rangle\} = \{|\frac{1}{2}\rangle, |-\frac{1}{2}\rangle\}$

$$|m_S\rangle = |\frac{1}{2}\rangle = \begin{pmatrix} 1 \\ 0 \end{pmatrix} \quad \text{and} \quad |m_S\rangle = |-\frac{1}{2}\rangle = \begin{pmatrix} 0 \\ 1 \end{pmatrix} \quad (3.2)$$

where the three spin operators are represented by the Pauli matrices:

$$S_x = \frac{1}{2} \begin{pmatrix} 0 & 1 \\ 1 & 0 \end{pmatrix}, \quad S_y = \frac{1}{2} \begin{pmatrix} 0 & -i \\ i & 0 \end{pmatrix}, \quad S_z = \frac{1}{2} \begin{pmatrix} 1 & 0 \\ 0 & -1 \end{pmatrix} \quad (3.3)$$

Next, we want to determine the energy related to the electron spin interacting with the field \mathbf{B} . An externally applied static magnetic field \mathbf{B}_0 orients the space and defines z-axis

of a Cartesian coordinate system. In this reference frame, $\omega_{0S} = -\mathbf{B}_0 \cdot \boldsymbol{\gamma}_S$, and the Zeeman hamiltonian writes:

$$\mathcal{H}_{0S} = \frac{1}{2}\hbar \begin{pmatrix} \omega_{0S} & 0 \\ 0 & -\omega_{0S} \end{pmatrix} \quad (3.4)$$

For nuclei, the frequency vector is actually $\omega_{0I} = \gamma_I \mathbf{B}_0$ since γ_I is positive and not negative like γ_S and:

$$\mathcal{H}_{0I} = -\frac{1}{2}\hbar \begin{pmatrix} \omega_{0I} & 0 \\ 0 & -\omega_{0I} \end{pmatrix} \quad (3.5)$$

3.1.1 Density Matrix

The description of a statistical ensemble of spins requires the use of the density matrix. For an isolated particle described by its wave function $|\psi\rangle$, the density matrix is defined as the projection operator $|\psi\rangle\langle\psi|$, which, for a single spin 1/2, takes the form:

$$|\psi\rangle\langle\psi| = \begin{pmatrix} a \\ b \end{pmatrix} (a^* b^*) = \begin{pmatrix} aa^* & ab^* \\ ba^* & bb^* \end{pmatrix} \quad (3.6)$$

For a statistical ensemble of spins where N copies of the particle occurs with some probability, the density matrix is the average of the projectors over the ensemble:

$$\rho = \overline{|\psi\rangle\langle\psi|} = \begin{pmatrix} \overline{aa^*} & \overline{ab^*} \\ \overline{ba^*} & \overline{bb^*} \end{pmatrix} = \begin{pmatrix} \rho_+ & \rho_{\perp} \\ \rho_{\perp}^* & \rho_- \end{pmatrix} \quad (3.7)$$

Then, the polarization vector $\mathbf{P}_S = (P_S^x, P_S^y, P_S^z)$ is defined as:

$$\begin{aligned}
P_S^x &= -\frac{1}{S} \frac{\text{Tr}\{\rho S_x\}}{\text{Tr}\{\rho\}} \\
&= -\text{Tr} \left\{ \begin{pmatrix} \rho_+ & \rho_\perp \\ \rho_\perp^* & \rho_- \end{pmatrix} \begin{pmatrix} 0 & 1 \\ 1 & 0 \end{pmatrix} \right\} / \left\{ \text{Tr} \begin{pmatrix} \rho_+ & \rho_\perp \\ \rho_\perp^* & \rho_- \end{pmatrix} \right\} = -\frac{\rho_\perp + \rho_\perp^*}{\rho_+ + \rho_-}, \\
P_S^y &= -\frac{1}{S} \frac{\text{Tr}\{\rho S_y\}}{\text{Tr}\{\rho\}} \\
&= -\text{Tr} \left\{ \begin{pmatrix} \rho_+ & \rho_\perp \\ \rho_\perp^* & \rho_- \end{pmatrix} \begin{pmatrix} 0 & -i \\ i & 0 \end{pmatrix} \right\} / \left\{ \text{Tr} \begin{pmatrix} \rho_+ & \rho_\perp \\ \rho_\perp^* & \rho_- \end{pmatrix} \right\} = -i \frac{\rho_\perp - \rho_\perp^*}{\rho_+ + \rho_-}, \\
P_S^z &= -\frac{1}{S} \frac{\text{Tr}\{\rho S_z\}}{\text{Tr}\{\rho\}} \\
&= -\text{Tr} \left\{ \begin{pmatrix} \rho_+ & \rho_\perp \\ \rho_\perp^* & \rho_- \end{pmatrix} \begin{pmatrix} 1 & 0 \\ 0 & -1 \end{pmatrix} \right\} / \left\{ \text{Tr} \begin{pmatrix} \rho_+ & \rho_\perp \\ \rho_\perp^* & \rho_- \end{pmatrix} \right\} = -\frac{\rho_+ - \rho_-}{\rho_+ + \rho_-},
\end{aligned}$$

Now, since the components a and b of $|\psi\rangle$ are complex numbers: $a = a_0 e^{i\phi_a}$, and $b = b_0 e^{i\phi_b}$.

The variation of the phase ϕ is restricted to $0 \leq \phi_a \leq 2\pi$, $0 \leq \phi_b \leq 2\pi$. We can thus express the density operator (in eq. 3.7) as:

$$\rho = \begin{pmatrix} \overline{aa^*} & \overline{ab^*} \\ \overline{ba^*} & \overline{bb^*} \end{pmatrix} = \begin{pmatrix} a_0^2 & a_0 b_0 e^{i(\phi_a - \phi_b)} \\ a_0 b_0 e^{-i(\phi_a - \phi_b)} & b_0^2 \end{pmatrix} \quad (3.8)$$

And by computing the averages we find that:

$$\overline{e^{\pm i(\phi_a - \phi_b)}} = \frac{1}{(2\pi)^2} \int_0^{2\pi} d\phi_a \int_0^{2\pi} d\phi_b e^{\pm i(\phi_a - \phi_b)} = 0 \quad (3.9)$$

so that the density matrix therefore adopts the following form:

$$\rho = \begin{pmatrix} \rho_+ & 0 \\ 0 & \rho_- \end{pmatrix} = \begin{pmatrix} a_0^2 & 0 \\ 0 & b_0^2 \end{pmatrix} \quad (3.10)$$

Therefore, $\rho_{\perp} = 0$ and $\rho_{\perp}^* = 0$, hence $P_S^x = P_S^y = 0$ and $\mathbf{P}_S = (0, 0, P_S^z)$. As expected, the polarization is thus defined by its component along \mathbf{B}_0 . Now we have, $|\mathbf{P}_S| = P_S = P_S^z = -\frac{\rho_+ - \rho_-}{\rho_+ + \rho_-}$ where P_S is the polarization of the electrons.

3.1.1.1 Boltzmann distribution

Following the quantum mechanical definition, the probability to find the particle in one of those states is, respectively:

$$p_{+\frac{1}{2}} = \frac{aa^*}{aa^* + bb^*} = \frac{a_0^2}{a_0^2 + b_0^2}, \quad \text{and} \quad p_{-\frac{1}{2}} = \frac{bb^*}{aa^* + bb^*} = \frac{b_0^2}{a_0^2 + b_0^2}, \quad (3.11)$$

According to the Boltzmann statistics, and by introducing eq. 3.11, the probability of the spin being in one of either states is:

$$p_{+\frac{1}{2}} = \frac{1}{Z} e^{-\frac{1}{2}\beta_S \hbar \omega_{0S}} = \frac{a_0^2}{a_0^2 + b_0^2} \quad \text{and} \quad p_{-\frac{1}{2}} = \frac{1}{Z} e^{+\frac{1}{2}\beta_S \hbar \omega_{0S}} = \frac{b_0^2}{a_0^2 + b_0^2} \quad (3.12)$$

Here, $\beta_S = \frac{\hbar}{k_B T_S}$, where k_B is Boltzmann constant and T_S is the spin temperature (the concept of spin temperature is defined in [Appendix A](#)) here given for electrons. In these expressions, $Z = e^{+\frac{1}{2}\beta_S \hbar \omega_{0S}} + e^{-\frac{1}{2}\beta_S \hbar \omega_{0S}}$ is the partition function. From equations 3.11 and 3.12, we obtain for the electron Polarization:

$$P_S = -\frac{\rho_+ - \rho_-}{\rho_+ + \rho_-} = -\frac{a_0^2 - b_0^2}{a_0^2 + b_0^2} = \frac{e^{+\frac{1}{2}\beta_S \hbar \omega_{0S}} - e^{-\frac{1}{2}\beta_S \hbar \omega_{0S}}}{e^{+\frac{1}{2}\beta_S \hbar \omega_{0S}} + e^{-\frac{1}{2}\beta_S \hbar \omega_{0S}}} = \tanh\left(\frac{1}{2}\beta_S \omega_{0S}\right) \quad (3.13)$$

The expression for the nuclear polarization is defined in a similar fashion. In conclusion, electron and nucleus polarizations under a static magnetic field \mathbf{B}_0 at the sample temperature T_{sample} is defined as follows:

$$P_S = \tanh\left(\frac{1}{2}\beta_S \omega_{0S}\right) = \tanh\left(\frac{\hbar \omega_{0S}}{2k_B T_S}\right) \quad (3.14)$$

$$P_I = \tanh\left(\frac{1}{2}\beta_I \omega_{0I}\right) = \tanh\left(\frac{\hbar \omega_{0I}}{2k_B T_S}\right) \quad (3.15)$$

Where both spin temperatures $T_S^S = T_S^I = T_{sample}$, the spin system is said to be at *thermal polarization*.

3.1.2 Spin polarizations at cryogenics temperatures

The expression of polarization given by equation 3.14 defines the relation between P_S (or P_I) and the external magnetic field B_0 , the spin temperature T_S and the nature of the particle γ_S or γ_I . Boltzmann distribution is defined for a spin system at constant sample temperature T_{sample} and constant B_0 , the system is considered at equilibrium. Under these conditions the spin temperature equals the sample temperature: $T_S = T_{sample}$. For a sample at $T = 1.2 K$ and $B_0 = 6.7 T$ the electron and nuclear polarizations are:

$$P_S = 0.99 \quad (3.16)$$

$$P_I = 0.0016 \quad (3.17)$$

This shows that, even though the samples are cooled to cryogenic temperatures the polarization obtained for protons is still very weak. On the other hand, in the exact same conditions, the polarization for electrons is almost of 100 %. DNP mechanism relies on transferring the polarization of the electronic spins at cryogenic temperatures to the nuclear spins. This transfer is achieved by means of a set of multiple dipolar interactions that will be detailed in the next section.

3.2 Polarization Transfer

DNP nuclear polarization enhancement depends on the transfer of polarization from electron spins to nuclear spins by means of microwave (μ -wave) irradiation. The electron and nuclear spins are coupled through dipolar interactions that induce transitions, spin flips. Spin flips also occur within the populations of both electronic and nuclear spins. The phenomenon of diffusion of spin flips is called spectral diffusion.

3.2.1 EPR spectrum

In order to understand the polarization transfer processes, it is necessary to describe the interactions of the electron spins with their environment. In DDNP experiments, the paramagnetic impurities are unpaired electrons of the stable radicals used as polarizing agents. As a matter of fact, unpaired electrons act as paramagnetic centers that have an orientation with respect to the magnetic field B_0 . Although this interaction has a fundamental precession frequency, defined by the frequency vector $\omega_{0S} = \mathbf{B}_0 \gamma_S$ (introduced in the precedent chapter), some frequency shifts can be induced by the interactions with the environment and by the particular orientation of each paramagnetic center with respect to the magnetic field. The interactions of an electron with the external magnetic field, and with the local magnetic fields created by the magnetic moment of the surrounding particles, gives rise to the Electron Paramagnetic Resonance (EPR) spectrum.

Depending on symmetry properties of the radical, different orientations of the paramagnetic centers can induce variations in its Zeeman response to the external magnetic field. Variations of the Zeeman response related to the orientation of the paramagnetic centers describe an anisotropy of the g-tensor. Moreover, unpaired electrons are affected by the interaction with nearby nuclear spins (intra-molecular), additional electronic spins, and remote nuclear spins. Frequency shifts caused by the g-tensor anisotropy and by the interactions with nearby nuclear spins are responsible for "inhomogeneous broadening". This type of broadening does not fluctuate and hence is time independent. The frequency shifts induced by interactions with other electron spins and more remote nuclear spins lead to "homogeneous broadening". The frequency shifts related to this broadening is fluctuating and so is time dependent. Consequently, the EPR spectrum is affected by the nature of the radical, its interaction with the static magnetic field, and its coupling with other surrounding particles. The EPR spectrum is thus a convolution of both homogeneous and inhomogeneous broadening. The interactions related to the inhomogeneous broadening are larger (up to several orders of magnitude, depending on the sample) and hence cause larger frequency shifts than

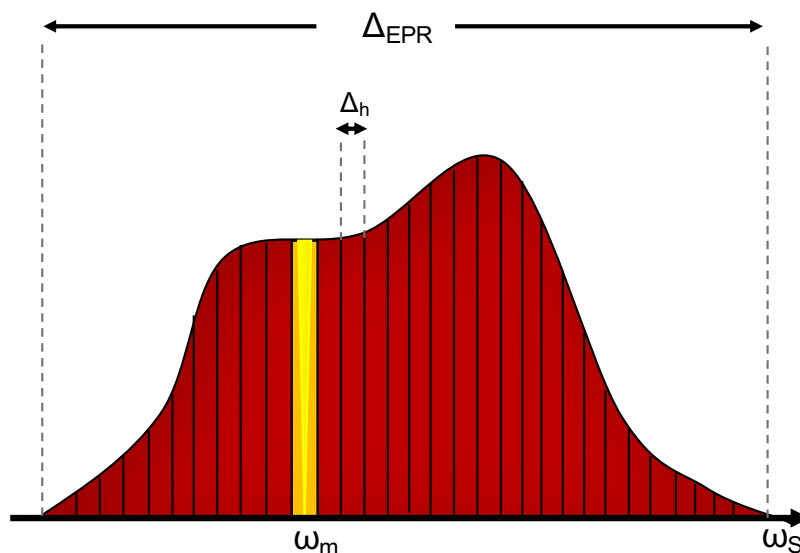


Figure 3.1: Schematic drawing of an arbitrary EPR spectrum. Here, Δ_{EPR} is the total width of the EPR spectrum, it is determined by the *inhomogeneous broadening* of the radical. Δ_h is the width of the so called "spin packets"[186, 187] determined by the *homogeneous broadening* that creates a time-dependent fluctuating field i.e. ω_S varies in time in a frequency range of Δ_h . Slow spin diffusion is responsible of a "Hole Burning"[186, 187], whereby saturation of the EPR line remains local at the μ -wave irradiation frequency.

homogeneous broadening. This is illustrated in figure 3.1, where the maximum width of the EPR line Δ_{EPR} depends on the "inhomogeneous broadening", and the time dependent shift Δ_h due to the fluctuating interactions at the origin of the "homogenous broadening", are depicted. The shape of the EPR line of the radical is of major importance for the presence and efficiency of the different DNP mechanisms.

The μ -wave irradiation used for DNP alters the electronic polarization because of the absorption of energy by the electron spins, and thus saturation occurs at the irradiation frequency. Depending on the efficiency of homogeneous broadening the saturation of the μ -wave irradiation can be diffused in the range Δ_h , thus saturating a band of the EPR spectrum and not just a discrete frequency [188, 187].

The Hamiltonian representing the contribution of the μ -wave irradiation along the x-axis has the following expression,

$$\mathcal{H}_m = 2\mathbf{B}_1 \cos(\omega_m t) = 2\hbar\omega_{1S} S_x \cos(\omega_m t) \quad (3.18)$$

where $\mathbf{B}_1(t)$ is the magnetic field created by the microwave, ω_m is the carrier frequency

of the μ -wave and $\omega_{1S} = -\gamma_S B_1$.

The energy absorbed by the electron spins can be expressed in terms of the thermodynamic potentials. Indeed, for an electron spin with a Zeeman angular frequency ω_S , the free energy is given by:

$$F_S = -\frac{\hbar}{\beta_S} \ln(Z) = -\frac{\hbar}{\beta_S} \ln(e^{+\frac{1}{2}\beta_S \omega_S} + e^{-\frac{1}{2}\beta_S \omega_S}) \quad (3.19)$$

where Z is the partition function. From this expression the entropy S_S and the energy U_S can be derived as:

$$S_S = -\frac{\partial F_S}{\partial T_S} = -\frac{\partial F_S}{\partial \beta_S} \cdot \frac{\partial \beta_S}{\partial T_S} \quad (3.20)$$

$$U_S = F_S + T_S S_S = -\frac{1}{2} \hbar \omega_{0S} \tanh\left(\frac{1}{2} \beta_S \omega_{0S}\right) \quad (3.21)$$

Ans so, by introducing the expression of polarization derived in the past section, and given in eq. 3.14:

$$U_S = -\frac{1}{2} \hbar \omega_{0S} P_S \quad (3.22)$$

Hence, variations of the polarization are thus related to variations of the internal energy of the spin system. When the μ -wave saturates a band of the EPR spectrum, if no other mechanisms can build up the thermal polarization in the saturated band, it is then said that the irradiation *burns a hole* in the EPR line, in yellow in figure 3.1, (see chapter 3 of [187]). The energy related to the μ -wave irradiation is at the origin of the polarization transfer in DNP. Hyperpolarization phenomena is competing with nuclear relaxation mechanisms. Although normally, at DNP temperatures, nuclear spin-lattice relaxation is very slow compared to DNP polarization transfer, nuclear species can relax through its dipolar coupling with electron spins, sometimes called nuclear relaxation by paramagnetic impurities [189, 190, 191]. Hence, in order to get the nuclear-spin system out of the Boltzman equilibrium state and to enhance its polarization, the rate at which the polarization is transferred from electron to nuclear spins has to be bigger than the nuclear relaxation rate [189, 188, 187].

3.2.2 DNP mechanisms

The μ -wave irradiation of the EPR spectrum triggers a transfer of polarization from the almost fully polarized electron-spin system to the nuclear-spin system. The transfer is done through a series of dipolar interactions that define the mechanism of polarization transfer. These transfer mechanisms strongly depend on the shape and width of the EPR spectrum [189, 187, 190, 192, 186] and thus depend on the sample composition, magnetic field, etc. In a given sample, DNP mechanisms determine the achievable nuclear polarization enhancement. Hence, a thorough understanding of the underlying mechanisms is a prerequisite for the optimization of DNP and DDNP experiments. In this section we briefly present these DNP mechanisms, a more detailed introduction is given in [Appendix A](#).

The principal documented DNP mechanisms in solid-state samples are, the Solid Effect (SE)[146, 189, 190, 187], the Cross Effect (CE) [193, 194, 192, 195, 186, 187] and Thermal Mixing (TM)[196, 197, 189, 188, 198, 199, 187].

The SE mechanism, discovered in 1958 [146], relies on the dipolar coupling of an electron spin and a nuclear spin. In this mechanism, the μ -wave irradiation provides energy to the coupled spin system, enabling transitions that otherwise would not be energy-conservative. These μ -wave induced transitions are responsible for the transfer of polarization from the electron spins to the nuclear spins, that under irradiation is more efficient than the nuclear relaxation by paramagnetic impurities [189, 190]. SE mechanism is predominant when the inhomogeneous spectral breath Δ_{EPR} is smaller than the nuclear Larmor frequency ω_{0I} [189, 200] (and see [Appendix A](#)).

Both CE and TM mechanisms depend on the coupling of three spins, two electron spins, and one nuclear spin. The coupling between the three-spin system can induce transitions (triple spin flips) provided that the difference between the two electron Larmor frequencies matches the nuclear Larmor frequency ($|\omega_S^i - \omega_S^j| = \omega_{0I}$). Triple spin flips thus occur when the inhomogeneous breath of the EPR spectrum is larger than the nuclear Larmor frequency ($\omega_{0I} < \Delta_{EPR}$).

The differences between CE and TM mechanisms have been the subject of discussion

[186, 192]. However, it has been generally agreed that the predominance of one of these two mechanisms relies on the homogeneous broadening linewidth (Δ_h) of the EPR spectrum [186, 195, 192]. For systems with weak mutual interactions between electron spins (and hence weak homogeneous broadening), where $\Delta_h < \omega_{0I}$, CE is the predominant mechanism [186, 195, 201]. On the other hand, for systems with strong mutual interactions between electron spins, where electron spectral diffusion is therefore also enhanced, and $\Delta_h > \omega_{0I}$, TM is assumed to be the predominant mechanism [186, 195, 188, 202].

In TM conditions, μ -wave irradiation is diffused throughout the EPR spectrum. The triple spin-flip conditions are therefore matched for different nuclear species simultaneously, provided that $\omega_{0I} < \Delta_{EPR}$ [187]. Surprisingly, under these conditions, transfers of polarization were observed between different nuclear-spin systems [196]. TM mechanism presents multiple particularities that have been largely studied and documented [196, 189, 186, 202, 187]. During my master's internship (also at the LBM, in the team *Paris en Résonance*), and during a part of my thesis, I worked on the characterization of TM regime in DNP samples. The results obtained in my master's are presented in [Appendix A](#) together with a more detailed introduction to the different DNP mechanisms, namely TM.

Chapter 4

The Dissolution DNP system

Performing DDNP experiments remains challenging and requires a complex instrumentation. The dissolution system has been under constant evolution and optimization, aiming to increase the efficiency and reproducibility of the experiments, and to simplify what is a complex procedure. In this chapter, I will describe the complete set-up with which I performed the different experiments presented in this thesis.

4.1 DNP Hardware

In our laboratory, two polarizers based on different technologies were used and will be introduced in this chapter.

4.1.1 Bruker, 6.7 T polarizer

The main DNP instrument used was a Bruker 6.7 T polarizer. This hardware prototype developed by the Bruker company was installed 5 years ago with the help of Daniel Abergel, Dennis Kurzbach and Dr. Emanuelle Weber - Ph.D. student at the time.

4.1.1.1 Magnetic field and cryogenics

This polarizer is composed of a cryo-magnet and a cryostat. The cryostat, where the NMR probe and the sample are introduced for experiments, is brought to cryogenic temperatures

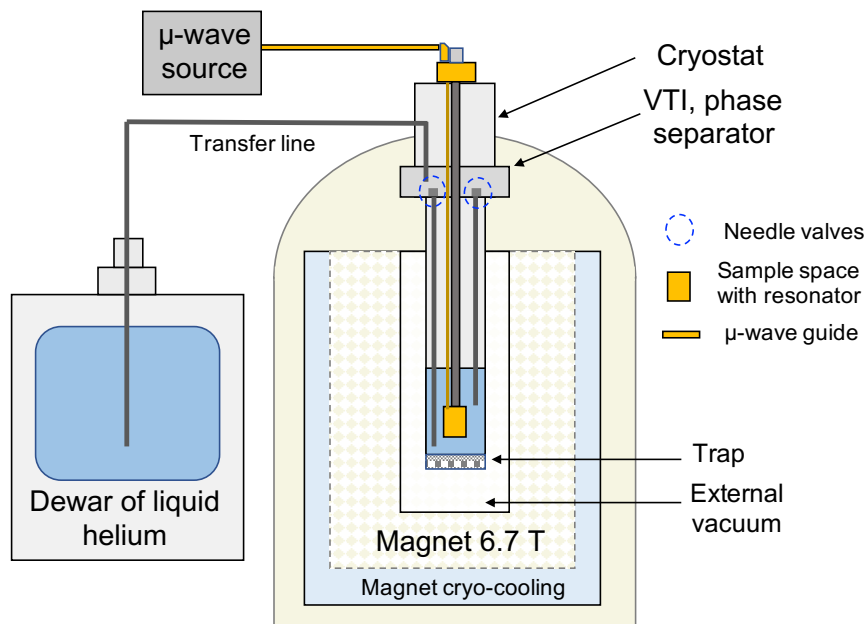


Figure 4.1: Complete scheme of the Bruker 6.7. polarizer with the exchangeable dewar of liquid helium (~ 100 L) connected to the cryostat. The μ wave source (and frequency doubler) emitting the irradiation going to the sample through the μ wave guide. We can also see the cryostat with the phase separator allowing the filling of liquid helium in the sample space, the transfer of liquid helium is regulated by two needle valves releasing helium at different heights in the cryostat. The magnet is isolated from the cryostat by a chamber that is pumped to create void, the external vacuum. When the polarizer is warm, the trap between the cryostat and the external vacuum becomes porous allowing the pumping of impurities in the cryostat. Finally we see the cryo-magnet that is cooled down by a chamber with liquid helium, then in a subsequent chamber liquid nitrogen and ultimately a last chamber pumped to create void isolating the previous chambers from the outside.

by filling it with liquid helium, 1He . The liquid helium is stored in an external dewar that is connected to the cryostat by means of a transfer line (see figure 4.1). Liquid helium is introduced in the sample area of the polarizer through the so-called phase separator (PS) in which the liquid and the gaseous Helium are separated. Two needle valves are used to control the amount of helium flowing into the remaining part of the cryostat where the sample is located (figure 4.1). The evaporated helium gas goes to a recovery line and is re-liquefied by the Cryogenics Department at the ENS. This service aims to reduce the cost generated by the constant need for liquid helium in DNP experiments.

The typical temperature inside the cryostat, in the sample space is ~ 4.2 K. However, pumping on the cryostat permits to reach temperatures as low as ~ 1.2 K by using a pumping system that comprise a forevacuum pump and a Roots pump. The magnetic field of 6.7 T is achieved by a Bruker kind magnet. A number of features are automatized to increase

the reproducibility of DNP and to make it more user friendly. For information, the typical helium consumption on a week of DDNP experiments amounts to $\sim 80 - 100$ L of liquid helium.

4.1.1.2 Probe, RF circuit and μ -wave irradiation

The probe includes the Radio Frequency (RF) circuit and the Microwave Guide (MG). The MG connects the microwave source with the system, allowing at its terminus the irradiation of the sample. The microwave source is an ELVA1 emitting at ~ 94 GHz (93800-94200 MHz) which is coupled to a Virginia Diodes frequency doubler so that the output signal is in the range 187.6 - 188.4 GHz. The ELVA1 source maximum power is of 350 mW. Experiments typically used a saw-tooth modulated microwave irradiation with a 100 MHz frequency span. In figure 4.2 a picture of a Proton/Deuterium probe is shown. Most DNP probes have

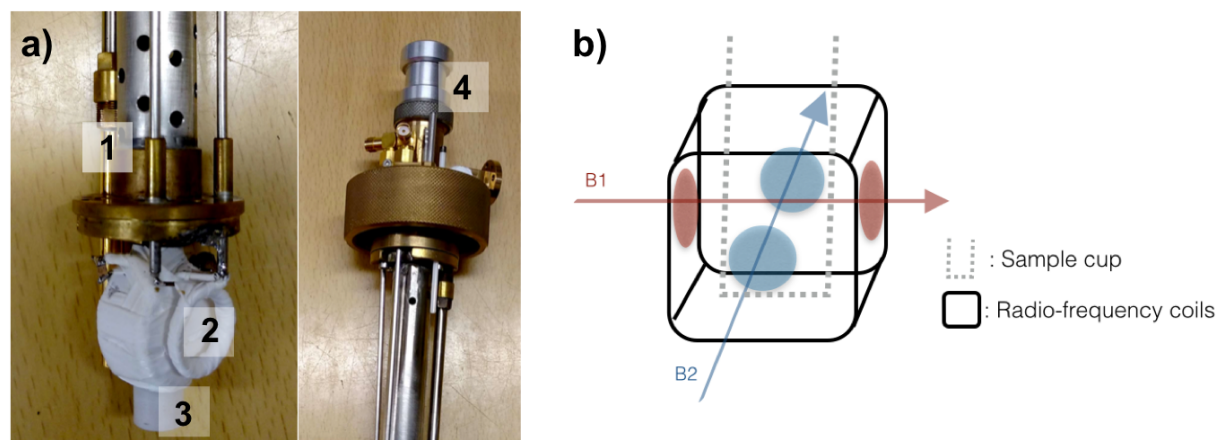


Figure 4.2: a) Bottom and Head of a Proton/Deuterium DNP probe. In the bottom part (left side) we see a Helmholtz resonator built in the laboratory. In the structure we see: 1 μ -wave guide, 2 induction coil for one of the two channels, 3 teflon sample holder and 4 airtight cap, this is the entry of the sample stick that holds the sample and introduce it inside the resonator immersed in a bath of liquid helium. b) Scheme showing the perpendicular distribution of the coils for perpendicular directions of the two induced magnetic fields (related to each channel). The perpendicular distribution reduces the possible coupling of the fields induced by the two RLC systems.

two channels, one for protons and a second for an X nuclei. So are the probes we use in the laboratory, which are able to excite simultaneously the magnetization of two different nuclei. Four different radio-frequency coils are arranged in a perpendicular array. The currents circulating in each RLC (Resistor (R), inductor (L), capacitor (C)) circuit creates two

mutually orthogonal magnetic fields, each circuit at a different resonance frequency. Thus, RF fields tuned at two different frequencies are generated at the Larmor frequencies each nuclei $\omega_L = \gamma_{nuc} \times B_0$.

4.1.2 Cryogen-free 9.4 T Polarizer

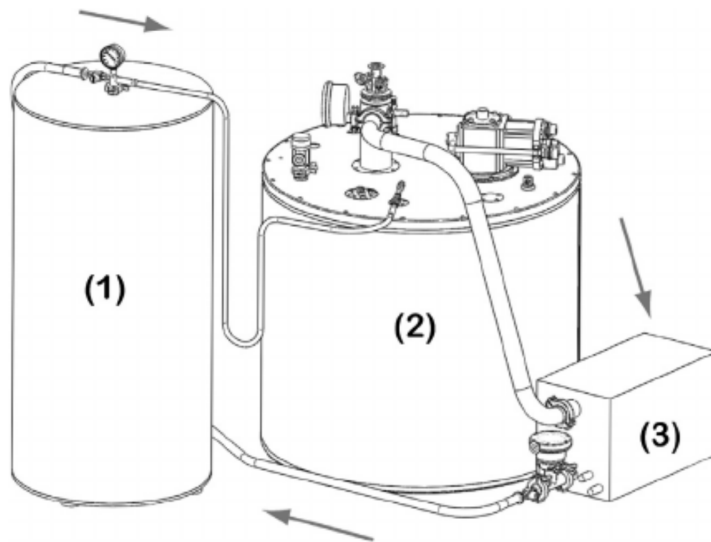


Figure 4.3: Image taken from [203], depicting an external view of the Cryogen-free Polarizer. **1** Helium gaz storage tank with a maximum capacity of 200 L. DNP system with the dry magnet, the VTI system and the DNP probe. **3** Dry pump allowing the flow of helium through the entire system. The arrows indicate the helium circuit involved in the cool-down of the polarizer.

The second polarizer used in this work, mounted by M. Baudin [203], is based on a different design and uses a dry magnet and cryostat, which avoids the need for liquid helium, a system inspired on recently developed hardware [204, 205]. Since both the magnet and the VTI (Variable Temperature Insert, the cryostat) are cooled with a recycling loop of helium, the cost related to the consumption of Helium is strongly reduced.

4.1.2.1 Magnetic field and cryogenics

In these “cryogen-free” or “dry” superconducting magnets, liquid helium is provided by “built-in” liquefiers. In our setup, a cryo-cooler (Sumitomo Heavy Industries - RDK-415D cold head and F50H compressor) is used to cool the magnet. This kind of magnets can be set at different fields B_0 with a principal drawback regarding the homogeneity of the magnetic

field, which is not problematic for these DNP experiments performed on non rotating solids. In the ENS *cryo-free* polarizer, the magnet is usually ramped up to 9.4 T although it could be also energized at 3.35 T and 6.7 T. The whole process of cooling down the magnet takes around 30 h (starting at room temperature). It is important to note that even though the electronic polarization P_e is stronger at higher fields, some of the mechanisms of polarization transfer (from electron spins to nuclear spins) may be less efficient.

After the system reaches its base temperature (2.5 K), a circuit of helium is set to cool-down the cryostat, in green in figure 4.4. The circuit starts with a 200 L storage tank containing helium gas connected to the cryostat. The helium is then cryo-pumped into a chamber with a volume of 0.5 L in which it is liquefied, called the helium pot. The liquid helium is then filled into the VTI space that contains the probe. The volume of liquid helium flowing in the VTI is regulated by a manually operated needle valve. The circuit goes through two charcoal traps that filter helium preventing blockages of the circuit due to water or nitrogen impurities.

Temperatures down to 1.4 K can be reached in this cryostat. The evaporated helium goes to the storage tank waiting to be re-liquefied starting again the cycle. The system is depicted in figure 4.3, where the arrows indicate the flow of helium through the circuit. Although the VTI and the probe are in contact, the probe is designed to avoid any leakage of superfluid helium. Thus, the circuit flowing through the VTI is a closed system with no loss of helium. The helium gas inserted inside the probe, i.e. in the sample space, is liquefied through thermal contact with the VTI. Since it is leak-tight the volume of gas entering the probe can be easily controlled. For a conventional experiment, the sample space is filled with ~ 50 L of helium gas. The circuit of helium going to the probe (in blue in figure 4.4) is independent of the other circuits. Any excess of helium gas or evaporation can be recuperated into airtight bags connected to the probe and eventually re-liquefied into the sample space.

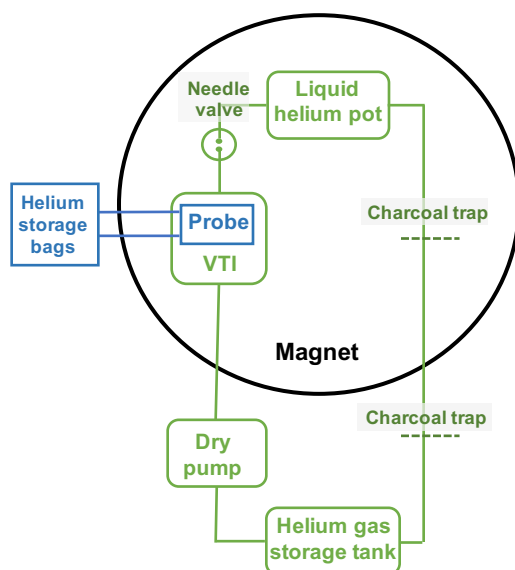


Figure 4.4: Scheme of the different and independent helium circuits of the polarizer. In green, the VTI cooling closed system. In blue, the sample space system refilled with helium gas that liquefies due to the thermal contact with the VTI.

4.1.2.2 Probe, RF circuit and μ -wave irradiation

The design of the RF probe used in this set up is very similar to the one described for the 6.7 T Bruker polarizer, based on a Helmholtz design (see figure 4.2) with two RF saddle coils tuned at ^1H and X resonance frequencies.

The μ -wave irradiation is achieved through a Virginia Diodes source, with an output power between 0 and 75 mW and a frequency between 262-264 GHz after several multiplication steps ($\times 3, \times 2, \times 2, \times 2$), generated from an output frequency of ~ 11 GHz. The μ -wave is modulated using a saw-tooth modulation function, typically in a range of 100 MHz. The μ -wave is guided to the sample through a μ -wave guide fixed to the probe structure.

This cryogen-free polarizer introduces a major improvement for DNP applications, as the liquid helium autonomy in the sample space increases the maximum duration of a DNP experiment, as helium is constantly re-liquefied. Even though the constant pumping of the different helium circuits represents a cost, the very low helium consumption is highly valuable in view of its scarcity. Although there are major improvements for this new generation of "Cryo-free" polarizers, some models need still to be optimized and automatized to improve the accessibility of the user to the complete system.

4.2 Dissolution DNP experiment

The DDNP experiment involves the transfer of a hyperpolarized sample in solid-state, inside the polarizer at cryogenic temperatures, to a solution-state NMR spectrometer operating at ambient temperature. The challenge of keeping the maximum possible polarization throughout requires optimizations and improvements at each stage of the experiment, including sample preparation.

4.2.1 Sample preparation

The composition (pH, nature of the substrate, nature of the radicals, ...) of the DNP samples is of major importance for the DDNP experiment, as the level of hyperpolarization, and the relaxation of the hyperpolarization during the transfer depends on it.[206, 207, 208, 46, 209]

DNP samples used for dissolution experiments avoid the complete crystallization of the sample. To this end, the sample is designed to solidify as solid glass. The complete crystallization of the sample has an impact on multiple aspects of DNP. First of all, the separation of the sample in different phases disrupts the homogeneity of the sample and destroys the contact between the radicals and different nuclear species [206, 207] which get separated. Furthermore, the different mechanisms of DNP depend on the environment of the electrons (as explained in the previous chapter) and the rotational freedom of the radicals, a complete crystallization of the sample would extremely influence the latter. In order to prevent complete crystallization, glass forming solvents (or colloquially, glassing agents) are added to the sample. Glycerol, DMSO, ethylene glycol and ethanol are some of the most common for DDNP applications. We prioritize water-soluble solvents and we aim for the most homogeneous samples[210, 206].

Clearly, the optimization of the DNP sample depends on the particular application, on the substrate and the radical used. Nevertheless, the experimental setup (magnetic field, sample transfer) present features that also have to be considered while preparing the sample [207, 201, 206, 211]. The magnetic field, for instance, has an impact on the mechanisms of

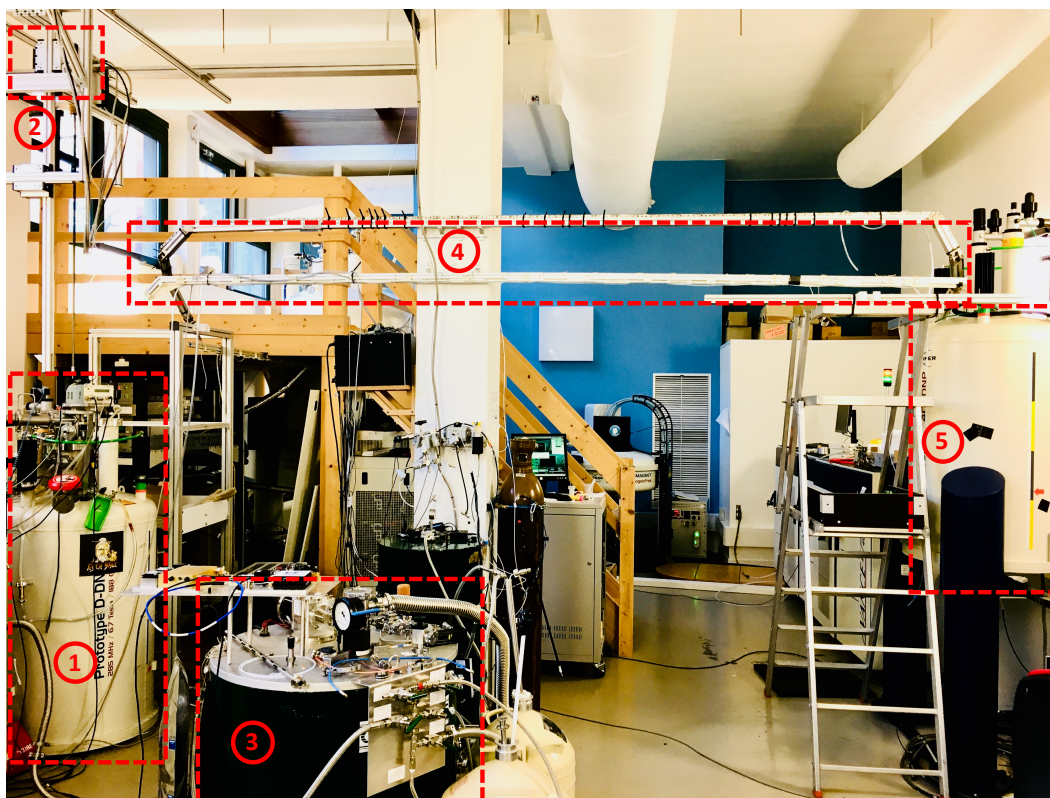


Figure 4.5: Laboratory picture at Paris en Resonance, LBM, framed in red are the different parts of the dissolution system. 1) Bruker 6.7 T polarizer. 2) Dissolution box for Bruker polarizer. 3) Cryo-free 9.4 T polarizer. 4) 0.9 T magnetic tunnel. 5) 400 MHz Bruker NMR spectrometer.

polarization transfer in DNP. The radical nature and concentration are parameters that have therefore to be optimized in function of B_0 [203, 195, 211].

4.2.2 Dissolution experiment

DDNP experiments rely on a sequence of steps, each of which is related to a piece of hardware as seen in figure 4.5 and must be optimized to yield satisfactory experiments. There is also a scheme presented in figure 4.6 with the different steps of a conventional DDNP experiment. Both figures represent the DDNP setup presently operating at the ENS, *Paris en Resonance* team. The different steps of the DDNP experiment (fig. 4.6) are:

- **1) Hyperpolarization of the sample:** The DNP sample is inserted in the polarizer. The polarizer is then filled with liquid helium and cooled down to 1.2 K, the μ -wave is set on. Depending on the hyperpolarized nuclei, the DNP sample, and the hyperpolarization strategy, the duration required to reach maximum nuclear polarization can

vary from some tens of minutes to several hours.

- **2) Dissolution:** After reaching the maximum of polarization the frozen sample is dissolved and transferred. To this end, a solvent inside the dissolution box (number 2 in figures 4.6 and 4.5) is warmed up and pressurized minutes before the dissolution. Additionally, an overpressure is set inside the cryostat with a flow of helium gas. The overpressure prevents any air leakage that would immediately freeze inside the cryostat. When the cryostat is over atmospheric pressure and the solvent is warm and pressurized (~ 140 °C and 10.5 bar), the cryostat is opened, the dissolution-cane is inserted in the central cavity of a cane leading to the sample holder, connecting the warm solvent with the frozen DNP sample. Subsequently, the warm and pressurized solvent is pushed towards the sample-holder containing the frozen DNP sample which is instantly dissolved. A constant flow of helium gas pushes the dissolved and diluted DNP sample through a magnetic tunnel, inside the NMR spectrometer, and finally injects it inside the NMR tube. The total transfer takes around 3 s.
- **3) Sample mixing and NMR detection:** Although the total transfer takes 3 s, the sample reaches the NMR tube 1 second after dissolution step starts. In many applications, the NMR tube is prepared with a solution containing reactants awaiting the dissolved DNP sample. The incoming DNP sample, diluted in the dissolution solvent, mixes with the solution inside the NMR tube. The NMR detection is automatically triggered by the dissolution system upon dissolution, which allows for the observation of hyperpolarized spectra.

The previous description of the dissolution DNP methodology shows the complexity of the experiment. After the dissolution of the sample, it is normally advantageous to maintain a magnetic field during the transfer to minimize relaxation and therefore reduce polarization losses. Avoiding regions of zero magnetic field, where the Zeeman interaction vanishes and the energy levels become degenerate is critical. Zero field regions are very often induced by the shielding of NMR magnets.[208, 212]. For these reasons, a magnetic tunnel was added

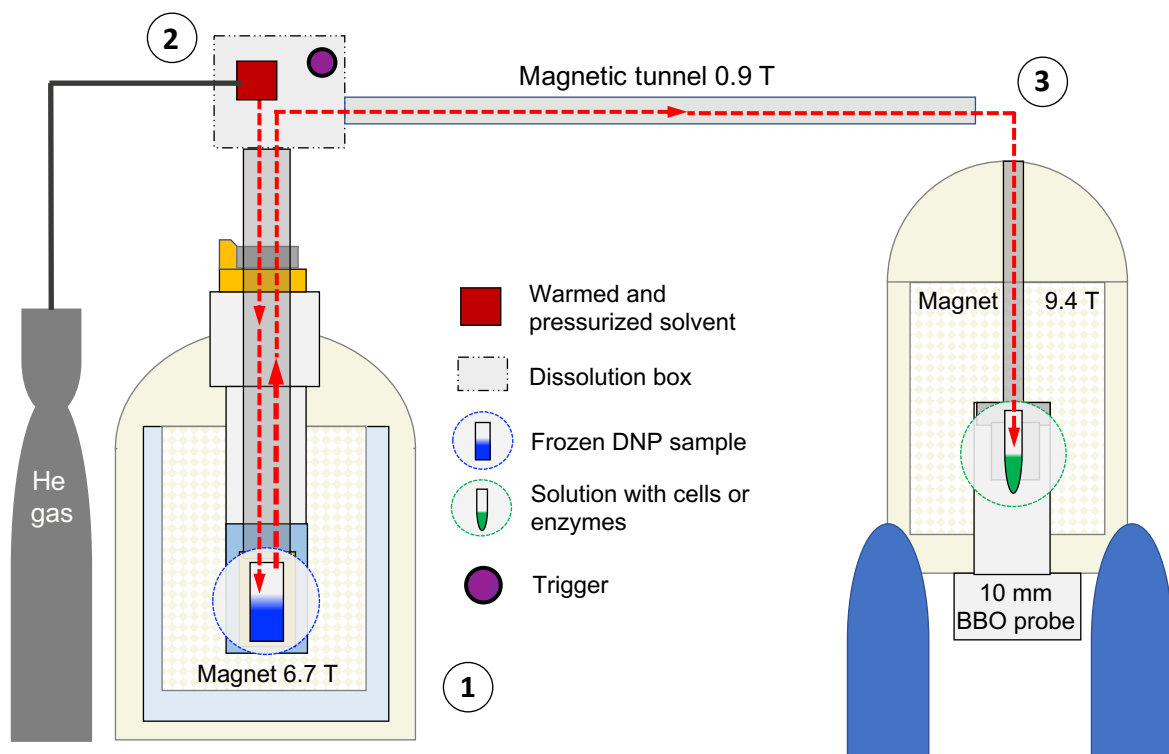


Figure 4.6: Scheme of the DDNP system at *Paris En Resonance* laboratory. The red dotted line indicates the path followed by the heated and pressurized solvent during the dissolution. The solvent is pressurized and pushed through the circuit with a continuous flow of He gas. When the solvent is ejected from the box to the circuit, a trigger starts the NMR detection after a 0.5 s delay. The different steps of the experiment are detailed in the text.

to the dissolution system in our setup[212]. This magnetic tunnel covers a distance of ≈ 4 m, with a magnetic field of 0.9 T (number 4 in picture of figure ??).

Although the major problems of this technique are related to the conception of the NMR experiment and the DNP sample, some of the issues one often encounters during the dissolution experiment are:

- Complete consumption of the liquid helium before maximum polarization is achieved, the experiment has to be started again.
- Air leakages or misregulation of the helium gas pressure can cause complete freezing of the system during the dissolution. The DNP sample is usually lost.
- Slow pressurization of the dissolution box (with the dissolution solvent) can cause overheating and burning of the resistance responsible for warming up the solvent.

- Misconfiguration of the 'triggers' causing the NMR sequence not to launch. The hyperpolarized signal is then lost.

Additionally, the amount of sample that is actually transferred to the NMR tube, as well as its polarization, vary depending on the configuration of the DDNP experiment. The composition and volume of the DDNP sample, the temperature and volume of the dissolution solvent, the pressure of the He gas bottle, the duration of the continuous flow of helium during the transfer are, among others, parameters that define the transferred volume of the DNP sample. Although the transferred volume can be calibrated, small variations on the setup can change its value. However, the lost volume can be estimated to vary between zero losses and a third of the DNP sample.

Many efforts are being done towards automatizing the system to ensure better stability and reproducibility of DDNP technique [54, 213, 214, 215, 185, 184].

4.2.3 NMR sequences

4.2.3.1 Liquid-state NMR sequences

As has already been mentioned, excitation pulses in NMR kill a part of the hyperpolarization. The amount of magnetization destroyed by each excitation pulse is proportional to $1 - \cos \theta$, where θ is the flip angle. In the absence of relaxation, the signal after n experiments is written as:

$$S_{Hyp}(t) = S_{Hyp}^0 \times \cos^n(\theta)$$

Where S_{NMR}^0 is the initial hyperpolarized signal. Thus, in DDNP, time sampling of metabolic reactions is achieved using the smallest possible flip angles. Hence, a $\theta = 30^\circ$ pulse would destroy $\sim 13\%$ of hyperpolarization in one scan. Therefore, in DDNP, the most common sequences are simple 1D detections that use low angle squared pulses in the relevant spectral window. Each single scan is taken with a time interval (that determines the time resolution), the final sequence of 1D scans composes a 2D experiment in which the second dimension

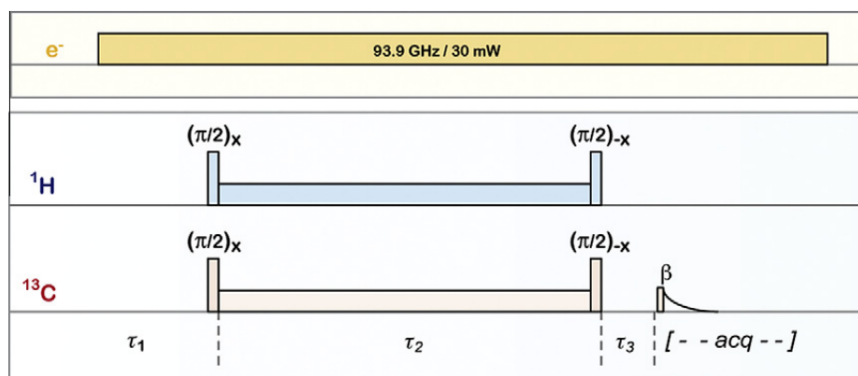


Figure 4.7: Figure taken from [218]. Cross polarization pulse sequence performed on ^1H and ^{13}C during μ -wave irradiation. After CP, ^{13}C signal is acquired. For more information go to [218].

is time. These experiments are said to be pseudo-2 dimensional. DDNP-NMR can be used to observe different nuclei, the most common are ^{13}C , ^1H , ^{15}N and ^{31}P . Normally ^{13}C is prioritized due to its characteristically long T_1 and its fundamental role in organic molecules. ^1H has shorter T_1 relaxation times that, depending on the dissolution setup, can cause the complete relaxation of the hyperpolarization during the transfer. [46, 44, 45]

However, the versatility of NMR can be used to make slightly more complex experiments in which protons are hyperpolarized and subsequently detected in NMR. A strategy has been to use hyperpolarized water to transfer hyperpolarized protons to particular molecules through chemical exchanges. This technique has been used to study protein structures and protein-ligand interactions, between others [41, 40, 216]. DDNP with hyperpolarized water has also been used to transfer hyperpolarization to alternative nuclei through conventional cross-relaxation [209, 217]. Other NMR strategies have been developed to optimize DDNP and widen the range of applications. The use of gradients has also contributed on the field of DDNP. In recent years a new technique called *Ultra Fast* based on spatial data encoding, allows one to perform multidimensional detections on a single scan. The technique was first proposed in *Frydman et al.* in 2002 [219], today is a technique commonly used in multiple domains. Since 2-dimensional experiments can be recorded on a single scan, the hyperpolarization of the nuclear species can be used. In multiple teams, DNP and ultra-fast techniques have been combined to profit the signal enhancement and the fast acquisition in multidimensional NMR [220, 221].

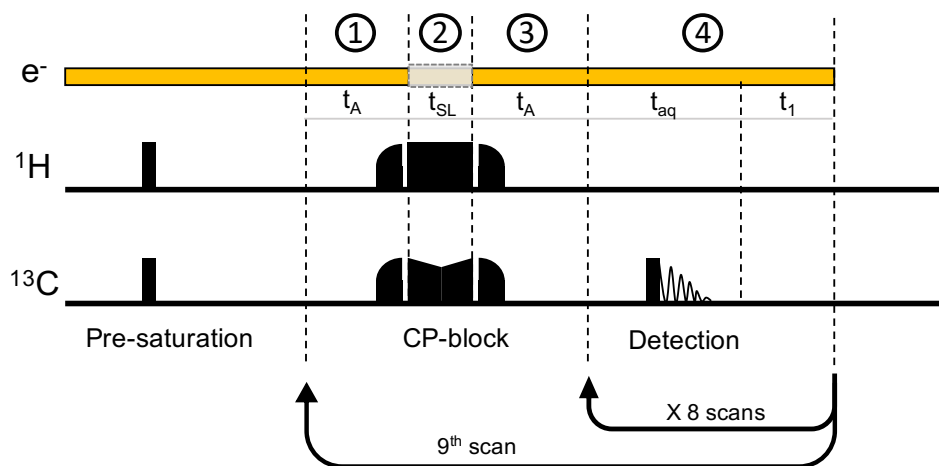


Figure 4.8: CP pulse sequence used in all experiments presented in this manuscript. The pulse starts with a series of 90° pulses to destroy any previous polarization called pre-saturation (not needed for CP). **1)** Adiabatic pulse of t_A duration set to align spins in the x-axis, both nuclear magnetization is transferred from z-component to the x-component. **2)** Spin lock to transfer polarization. The optimal t_{SL} duration depends on the strength of ^1H , ^{13}C dipolar coupling. For ^{13}C , the pulse is ramped-up and down to efficiently find Hartmann-Hahn match, it has been empirically tested in the lab. **3)** Magnetization is brought back to the z-axis with an adiabatic pulse that lasts for t_A . **4)** 10° squared excitation pulse and acquisition on ^{13}C channel to monitor the evolution. After acquisition, a duration t_1 of 30-90 s for the spins to relax. The 4th step is repeated 8 times (4-12 min), in the 9th scan the CP is repeated and the sequence starts again.

4.2.3.2 Cross-polarization sequences

Two principal strategies are used in DNP to hyperpolarize a sample, "direct hyperpolarization" and "cross polarization" (CP).

CP is used to transfer polarization between different nuclear species. With this technique, the polarization build-up of lower gamma nuclei can be accelerated, and higher polarizations can be achieved. ^1H direct hyperpolarization is usually significantly faster and higher than that of other nuclei (see for instance [section A.3](#)), and is therefore commonly used in CP as polarization donor.

The use of CP technique in DNP was introduced in *Jannin et al.* 2011 [218]. In this publication a pulse sequence is used to transfer polarization from ^1H to ^{13}C nuclei. CP transfers magnetization through dipolar coupling from the high- γ nuclei (^1H) to the low- γ nuclei (^{13}C) during a "spin-lock" period in which the Hartmann-Hahn condition is met [222]. The CP pulse sequence used in our experiment is based on the reference [218] which is displayed in figure 4.7.

The CP pulse program used consists of 4 steps, 3 of which are simultaneous for both

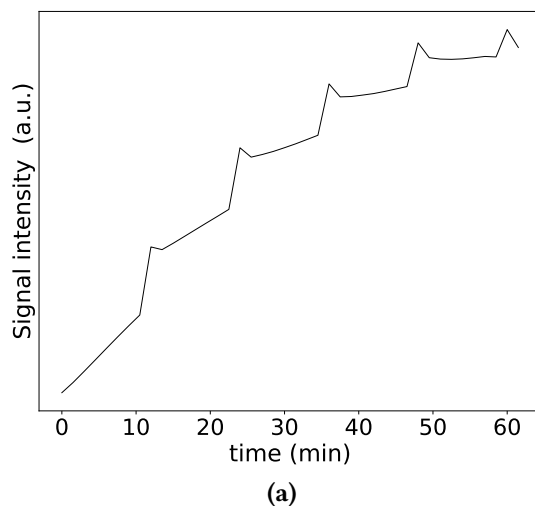


Figure 4.9: 4.9a Typical CP profile. The time interval between every scan is 90 s, each CP step is done every 8 scans, i.e. 14 min. This duration is chosen in function of the time needed for protons to polarize, characteristic of the sample.

channels ^1H and ^{13}C (depending on the probe, the second channel could be set to ^{31}P or ^{15}N frequencies). In the first step a 90° adiabatic pulse is set for both channels. It is followed by a "spin-lock" pulse that creates a thermal contact (Hartmann-Hahn) between the two nuclei and during which magnetization is transferred. During the spin lock, for one nucleus, the amplitude of the field is swept in order to optimize the Hartmann-Hahn match. The optimal duration for the spin-lock pulse depends on the strength of the dipolar coupling. During the contact period, the μ -wave irradiation is stopped by means of μ -wave gating. In the third step spin magnetization is brought back to the z -axis by a second adiabatic pulse. On the fourth step, a low angle excitation pulse (usually 10° in our experiments) is set on the ^{13}C channel to monitor the evolution of the signal. The CP block (first 3 steps) is repeated every 8 scans, between each scan there is a time lapse that can vary between 30 and 90 seconds. During this period ^1H polarization builds up until transfer during CP. In figure 4.9a, the signal evolution of a sample under CP is depicted. Each signal 'jump' corresponds to Hartmann-Hahn transfer between ^1H and ^{13}C . For each experiment, pulse powers and durations are optimized empirically. The CP is repeatedly tested on the sample, each parameter's value is progressively varied.

Part III

In-vitro studies of enzymatic reactions by DDNP

Chapter 5

Enzymatic cascade with glucose as substrate

5.1 Context of the experiment

The study of metabolic fluxes requires the characterization of enzymatic reactions taking place in a living organism, which requires the knowledge of the role and the functional characteristics of each enzyme, as well as their regulation, an essential aspect to understand the organisms phenotype. Over the past few years, dissolution DNP has been used to monitor the kinetics of fast enzymatic reactions *in vitro* by recording simultaneously the time resolved NMR signal of an hyperpolarized substrate and its reaction products[48, 49, 223, 52]. A brief summary of such investigations is given below, as an overview of the state of the art of DDNP applications to enzyme kinetics. In *A.W. Barb et al.* the transformation of pyruvate into alanine by the catalysis of alanine transaminase was studied *in vitro* by means of DDNP [179]. In this study, both ^{13}C NMR and ^1H NMR were used to monitor the signal evolution of labeled pyruvate, the catalytic effect of alanine transaminase was detected and the protonation induced by the enzyme was characterized. However, quantitative kinetic analysis was not performed.

As a proof of concept, the hydrolysis of Na-benzoyl-L-arginine catalyzed by trypsin was studied in reference [49]. In this study the system of reactions was monitored by NMR

for a total of 3 s, during which the reaction rates were characterized. Relaxation of the hyperpolarized sample was considered and measured independently. For these experiments, the substrate concentration was chosen so that the reaction kinetics evolved linearly with time (0 order). Although the kinetic rate of the reaction could be extracted, the method was tested in a very simplified reaction system consisting of a linear evolution in time of a single reaction.

DDNP and ^{13}C NMR have been compared with ^{19}F NMR as method to monitor the evolution of enzymatic reactions. In *Eykin and coworkers*, the catalytic activity of carboxypeptidase G2 is studied [48]. The single-step reaction is monitored by ^{13}C NMR for the complete duration of hyperpolarization, with 3,5-difluorobenzoyl-L-glutamic acid in natural abundance as substrate. Subsequently, the same reaction is studied by means of ^{19}F NMR. However, activities are only extracted with the second method, without DNP. A discussion of the pertinence of both techniques is given.

A more complex system involving two successive reactions has been studied by DDNP. The successive transformation of choline into betaine aldehyde, and betaine aldehyde into betain, was monitored in [224]. This reaction is catalyzed by choline oxidase enzyme and was modeled by two subsequent pseudo first order reactions. Kinetic rates characterizing the reactions were extracted and their values were evaluated by comparison with bibliography. The obtained values were in the same order of magnitude than the documented ones. Some possible inconsistencies of the resulting values were discussed. However, no further statistical assessment of the validity of the parameters was done.

In this work, real-time DDNP studies on the enzyme kinetics of the oxPPP ([subsubsection 1.1.1.2](#)) were undertaken. This studies are performed on *in vitro* samples, i.e. enzyme solutions containing a single or a combination of successive enzymes of this metabolic pathway. Some aspects of this particular metabolic pathway have been previously studied by means of DDNP technique[225, 226, 50].

Phosphorylation of glucose into G6P catalyzed by hexokinase enzyme was monitored in *Miclet et al.*[50]. The evolution of $[\text{U-}^{13}\text{C}; \text{U-}^2\text{H}]$ glucose signal and its $[\text{U-}^{13}\text{C}; \text{U-}^2\text{H}]$ G6P

were recorded for the complete duration of the hyperpolarized signal (~ 20 s). The resulting data was fitted with a simple model to extract the kinetic rates of the enzymatic reaction. The reaction was independently analyzed for both α and β anomers which catalytic rates were successfully determined. The results suggested that hexokinase activity has no anomeric specificity.

A continuation of this work was presented in *Sadet et al.*, where two consecutive reactions catalyzed by hexokinase enzyme and G6PDH enzyme were studied. The experiments were performed with $[U-^{13}C; U-^2H]$ glucose to produce $[U-^{13}C; U-^2H]G6P$ and subsequently $[U-^{13}C; U-^2H]$ δ -PGL. The reactions were reproduced *in vitro* with high enzyme activities in order to force a fast production of δ -PGL. Although the reaction was monitored from the injection of the dissolved hyperpolarized sample of glucose, only the data obtained after complete consumption of the G6P was analyzed (~ 10 s after injection). A kinetic analysis was performed on the spontaneous degradation of δ -PGL and kinetic rates were extracted. Hence, only one-step non-enzymatic reactions were studied.

Kinetic studies of the first steps of the oxPPP remains a challenge. To start with, glucose and G6P resonances have to be identified and integrated, which becomes difficult due to the overlap of their C_1 peaks. Also, multiple spontaneous reactions must be considered in the kinetic study, which adds complexity to the reaction scheme, and makes its numerical analysis more demanding. Here, we undertake a complex study of a cascade of enzymatic reactions while considering multiple additional spontaneous reactions. A first approach we used to the study of this system relied on the direct observation and analysis of the cascade of enzymatic reactions. A second approach will be presented in the next chapter where G6P is hyperpolarized and used as substrate. We therefore bypass the glucose phosphorylation stage and so avoid resonance overlap, as well as simplify the kinetic model.

5.2 The reaction scheme

The phosphorylation of glucose and the first reaction of the PPP are enzyme catalyzed reactions in which additional spontaneous reactions are involved. In the first reaction of the

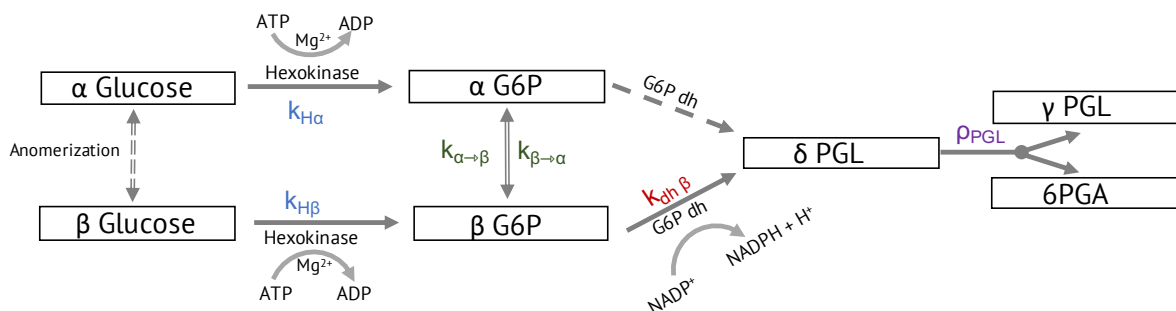


Figure 5.1: Cascade of enzymatic reactions. The cofactors involved in the two enzymatic reactions are also represented. In dotted lines are represented the reactions that will not be considered in our model. The anomerization rates of G6P are represented in green. Hexokinase enzyme activity rate is represented in blue and G6PDH activity rate in red. ρ_{PGL} in violet represents the rate of δ -PGL degradation due to both hydrolysis and isomerization.

enzymatic cascade, glucose is phosphorylated into G6P by the catalysis of hexokinase enzyme. The second reaction is catalyzed by G6PDH enzyme and transforms a molecule of G6P into a molecule of δ -PGL. More information about this pathway is given in [subsection 1.1.1.2](#).

Glucose and G6P populations have two anomers α and β , and G6PDH has an anomer specific activity towards β -G6P [74, 33]. This specificity is taken into account in our analysis. The transformation of α -G6P into δ -PGL is therefore disregarded. Several non enzymatically catalyzed reactions have also been included in this scheme. The kinetic rate of the spontaneous α/β anomerization determines the evolution of both anomers' concentrations towards a thermodynamic equilibrium. For glucose, this rate has been shown to be on the order of several minutes [74, 227]. Since our DDNP experiments allow us to observe the hyperpolarized analytes for only some tenths of seconds, glucose anomerization may not be considered. Alternatively, the anomerization rate of G6P is much faster ($\leq \text{min}$) and was therefore taken into account in our model [227]. Besides, δ -PGL is known to isomerize into γ -PGL and hydrolyzed into 6PGA. [226, 33, 75]. Both isomerization and hydrolysis reactions occur spontaneously on the time scale of the studied enzymatic reactions and were therefore considered. The complete reaction scheme is presented in figure 5.1. In these experiments the dependence of the enzymatic reactions on the cofactor concentrations was avoided by using them in large excess with respect to the substrate. Also, the spontaneous

degradation of δ -PGL and its hydrolysis into 6PGA were accounted empirically by a simple exponential "leakage" term 5.1. Under these conditions, the hexokinase enzymatic reaction rate depends solely on the available concentration of glucose, and is therefore considered as a pseudo-first order reaction. Similarly, the G6PDH catalyzed reaction β -G6P \rightarrow δ -PGL, is assumed to depend only on the concentration of β G6P. The set of coupled pseudo-first order reactions, the anomerization of G6P, and the degradation of δ - PGL determine the concentration evolution of the different metabolites in the reaction cascade.

5.3 Materials and methods

5.3.1 Sample preparation and DNP experiment

All experiments were performed with the same DNP sample composition. Glucose samples were prepared with a solution of D₂O:Eth-Gly at 50:50% volume composition, in which the polarizing agent TEMPOL (4-Hydroxy-TEMPO) was dissolved to reach a final concentration of 40 mM. [U-¹³C; U-²H]glucose was added to the sample to attain a concentration of 400 mM. For each experiment a sample of 75 μ L was transferred to a PEEK sample holder and was inserted inside the cryostat, in contact with a bath of liquid helium where it solidifies as a solid glass (DNP system described in subsection 4.1.1). Each DNP sample contains 30 μ mol of [U-¹³C; U-²H]glucose. A CP sequence was used to hyperpolarize the sample. A maximum of polarization was achieved after \sim 60 min, with the sample at 1.2 K and under μ -wave irradiation at 187.9 GHz frequency and 350 mW power.

Dissolution was achieved by flushing 5 mL of D₂O previously heated to 403 K at 10.5 bar onto the frozen hyperpolarized sample. The hyperpolarized solutions were transferred from the polarizer to the 400 MHz spectrometer (distant by \sim 5-6 m from each other) upon Helium gas flow. Mixing of the hyperpolarized sample with the solution of enzymes takes place in a 10 mm NMR tube sitting inside the NMR spectrometer, typically began less than one second after dissolution and was complete after 3 seconds.

5.3.2 Reaction medium and NMR

A common buffer solution containing the cofactors (ATP and NADP⁺) was prepared for both experiments. The cofactor solution containing both enzyme cofactors consisted on 2 mL of HEPES buffer 200 mM at pH = 7.2, to which 180 μmol of ATP and 180 μmol of NADP⁺ (90 μmol per experiment) and 46 μL of a stock solution at 1 M of MgCl (23 μmol per manip) were added. 400 μL of a solution of NaOH 1 M were added to the mixture to reach a pH of 7.4; 54 μL of HEPES completed a total volume of 2.5 mL which was splitted into two samples of 1.25 mL per experiment.

The concentration of the cofactors was three times larger than the maximum expected substrate concentration in the NMR tube to match pseudo-first order conditions of the experiments. Enzymes were added in a subsequent step. Commercially available (*Merck*) yeast (*saccharomyces cerevisiae*) hexokinase and G6PDH enzymes were used. Experiments were performed with two different hexokinase activities. In one experiment, 1.26 mg of Hexokinase with a specific activity of 83 $\text{u}\cdot\text{mg}^{-1}$, and 0.35 mg of G6PDH with an specific activity of 165 $\text{u}\cdot\text{mg}^{-1}$ were used. The experiment contained a total of 104 ± 8.3 u of hexokinase and 57.8 ± 16.5 u of G6PDH. For a second experiment, 50.6 ± 8.3 u of hexokinase and 57 ± 16.5 u of G6PDH were weighted and added to the second sample. Thus, hexokinase activity was approximately half for the second experiment. In both experiments the sample containing both cofactors and enzymes was transferred to a 10mm NMR tube and inserted inside the NMR spectrometer some minutes before the dissolution experiment. NMR spectra was recorded at $T = 310$ K on a 9.4 T *Avance III* Bruker spectrometer with a 10 mm BBO probe. Each DDNP experiment consisted in a series of 1D ¹³C spectra with 10° read pulses. ²H and ¹H decoupling was performed in all experiments using a WALTZ16 pulse sequence.[159]

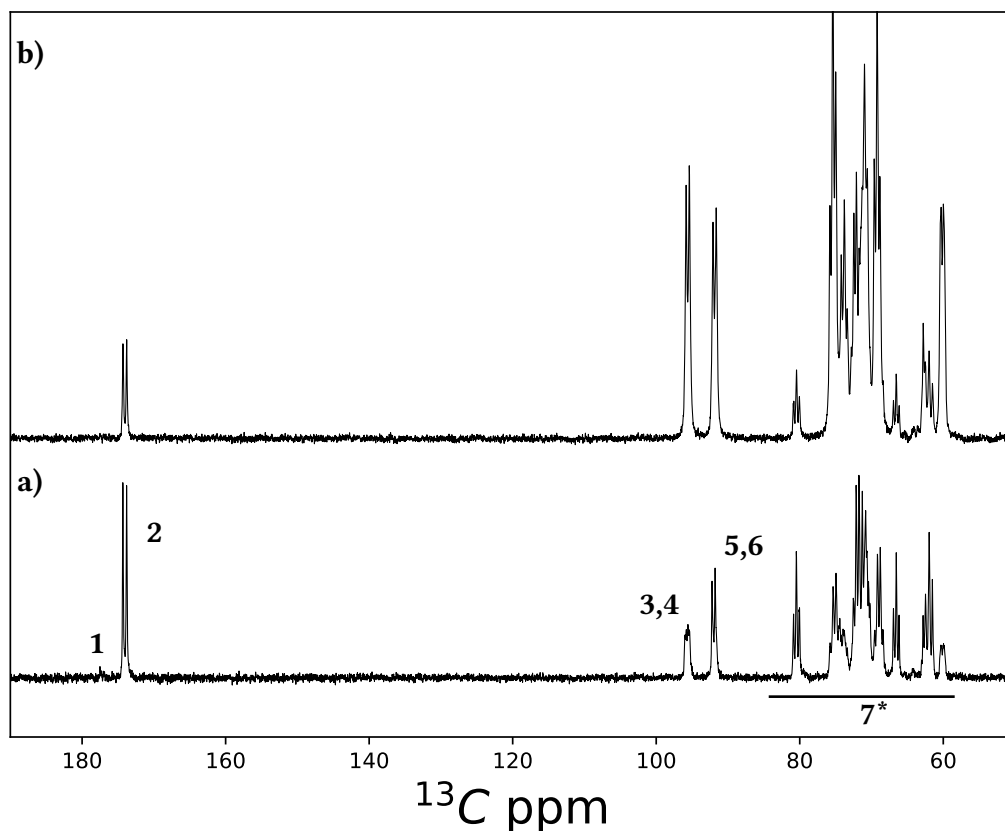


Figure 5.2: ^{13}C NMR, superposition of the first 10 scans, for both experiments. **a)** Experiment 1, u hexokinase and u G6PDH. **b)** Experiment 2, u hexokinase and u G6PDH. For both experiments the different resonances are: **1** γ -PGL C₁; **2** δ -PGL C₁; **3,4** β -gluc. and β -G6P C₁; **5,6** α -gluc. and α -G6P C₁; and **7*** and overlay of all other carbon resonance from Gluc., G6P, and PGL species, both carbons of ethylene-glycol also appear in 7*.

5.4 Results and Analysis

^{13}C 1D spectra extracted from the pseudo-2D experiments 5 s after injection (5th scan) are displayed in figure 5.2. The carbonyl region exhibit the ^{13}C ₁ resonance signal of δ -PGL, which therefore attests for the presence of the reaction cascade. For experiment 1, glucose signals have a faster decay, which is consistent with the experimental conditions, since the activity of hexokinase is twice the one used for experiment 2. Also, for experiment 1, a faster production of δ -PGL, as well as γ -PGL, is observed, as attested by the stronger signals. Although the G6PDH activities in both experiments were approximately identical, the kinetics of the reaction cascade seems to be faster than for experiment 1, which points

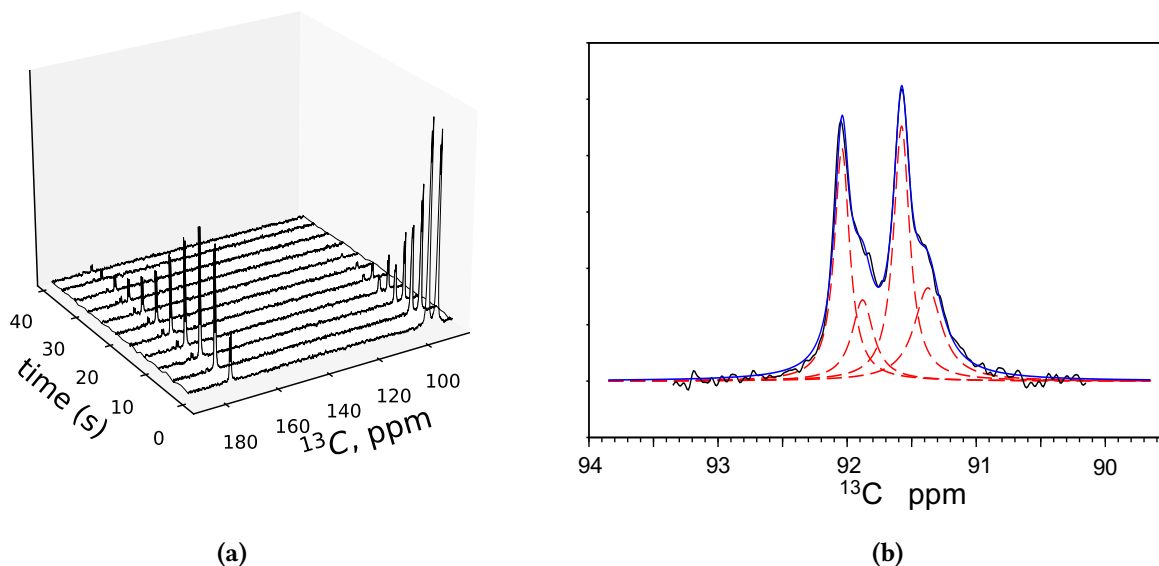


Figure 5.3: Figures taken from experiment 1.5.3a Stackplot of the first 40 scans in which we see the signal evolution of both anomers of G6P and glucose C_1 in the right side. In the left we see the signal evolution of δ -PGL's C_1 and, a weak signal of its isomer γ -PGL.5.3b Deconvolution of α -glucose and α -G6P C_1 . The deconvolution was achieved by fitting a summation of 4 lorentzian functions, centered in each peak's position, to the NMR data. The experimental data is represented in black, each lorentzian is represented in red, and the convolution of the four lorentzians is represented in blue.

to the fact that the different reactions are coupled. Both anomers of glucose and G6P C_1 resonances are doublets (due to J_{CC}^1 coupling) and overlap, so that, in order to determine glucose and G6P C_1 signal intensities, both signals must be deconvoluted. However, it is interesting to note that ratios of the relative intensities of both anomer signals are inverse in both experiments, which is likely a consequence of the anomeric specificity of G6PDH towards β G6P.

The time evolution of the different metabolite signals is illustrated in a stacked plot of DDNP 1D spectra, in figure 5.3a. The signals of glucose and G6P C_1 were deconvoluted with Lorentzian functions centered on the chemical shift of the peak maxima, with a tolerance of 3 points (~ 3 Hz, each spectrum contained a total of 16384 points corresponding to 150 ppm) for both resonances. An example is displayed in figure 5.3b. The time evolution of the signal intensity was then reconstructed for each metabolite. Through the reaction pathway described above, the magnetization of the various metabolites obeys the following set of

equations:

$$\frac{d}{dt} \begin{pmatrix} M_{G\alpha} \\ M_{G\beta} \\ M_{G6P\alpha} \\ M_{G6P\beta} \\ M_L \end{pmatrix} = \begin{pmatrix} -k_{H\alpha} - r_{G\alpha} & 0 & 0 & 0 & 0 \\ 0 & -k_{H\beta} - r_{G\beta} & 0 & 0 & 0 \\ k_{H\alpha} & 0 & -k_{\alpha \rightarrow \beta} - r_{G6P\alpha} & k_{\beta \rightarrow \alpha} & 0 \\ 0 & k_{H\beta} & k_{\alpha \rightarrow \beta} & -k_{dh\beta} - r_{G6P\beta} - k_{\beta \rightarrow \alpha} & 0 \\ 0 & 0 & 0 & k_{dh\beta} & -d_L \end{pmatrix} \begin{pmatrix} M_{G\alpha} \\ M_{G\beta} \\ M_{G6P\alpha} \\ M_{G6P\beta} \\ M_L \end{pmatrix} \quad (5.1)$$

(the colors used match those in figure 5.1). The parameters $r_x = 1/T_{1,x}$ are the spin-lattice relaxation rates (in s^{-1}) of the x metabolite. Parameter d_l corresponds to the lumped decay rate of the δ -PGL signal, which includes both its relaxation and chemical transformations $d_L = r_L + \rho_{PGL}$.

5.4.1 Individual analysis of the experiments

We used the model of equation 5.1 to fit both experiments independently. In our model 5 kinetic rates, 5 relaxation parameters and 5 initial signal values, i.e., a total of 15 parameters are fitted. The algorithm chosen for the fit is called Differential Evolution (DE) [228]. DE is an evolutionary kind of algorithm, and thus use a metaheuristic approach in which no assumptions about the system have to be made, i.e. no initial values have to be given. This minimization algorithm thus avoids the target function to be trapped in a local minimum due to its dependence on initial conditions. Note, however, that there is no proof of convergence, unlike strategies based on gradient minimization [228]. Results of the fitting are displayed in figure 5.4 for both experiments, which show that data are well reproduced by the model. The fitted lines (continuous lines) reproduce well the evolution of the experimental NMR signal (dotted lines) for the different metabolites. However, the output parameters display multiple inconsistencies. To start with, some parameters values converge to zero. Some of the model parameters seem to be underdetermined, and so their values cannot be determined independently. This suggests that the system of differential equations is not constrained enough by the data, which therefore suggests that we need to introduce addi-

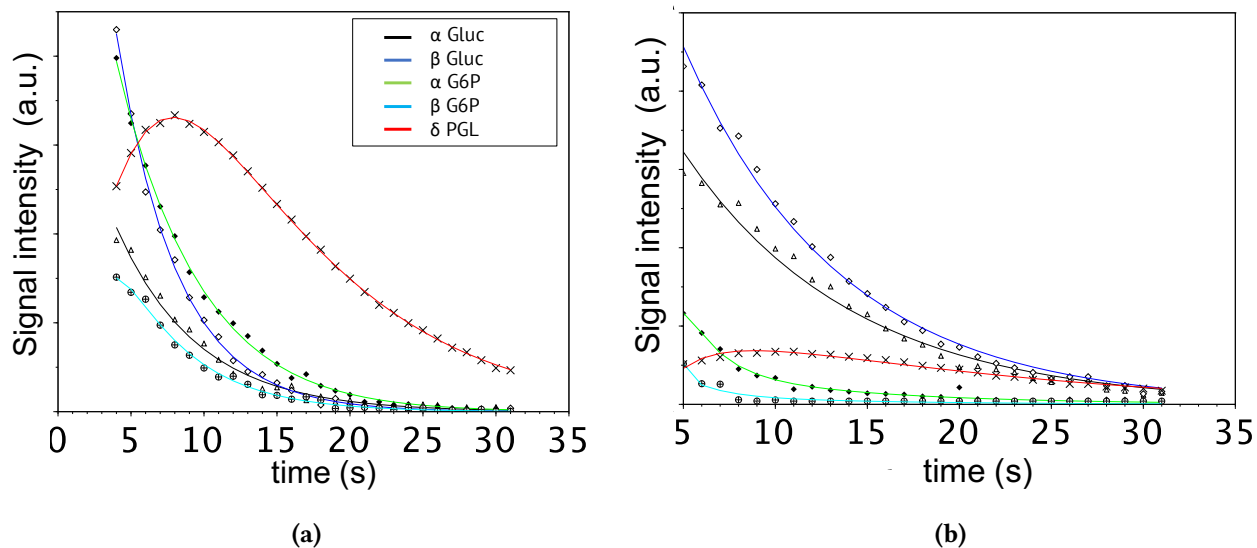


Figure 5.4: Independent fit of the data resulting from experiment 1 (in **a**) and experiment 2 (in **b**). The data was fitted individually for each experiment with the model presented in equation 5.1.

tional constraints for the analysis.

A Monte Carlo (MC) simulation to mimic experimental noise (due to NMR detection) was used to evidence potential correlations between parameters. According to standard practice, experimental noise was estimated for each experiment by computing the standard deviation of the signal in a region without resonances. It was then randomly added to each point of each 1D spectrum and the analysis was performed on these new pseudo-experimental data. It is important to precise that with the MC simulation only the error related to the detection noise can be determined, other sources of experimental are thus not estimated.

The MC showed that not all parameters converged to the same values for each realization of the noise. Moreover, significant correlations between some parameters obtained, as illustrated in figure 5.5 for experiment 1. In contrast, the kinetic eigenmodes of the reaction pathway (5.1) were well constrained and consistently extracted from the data. These are:

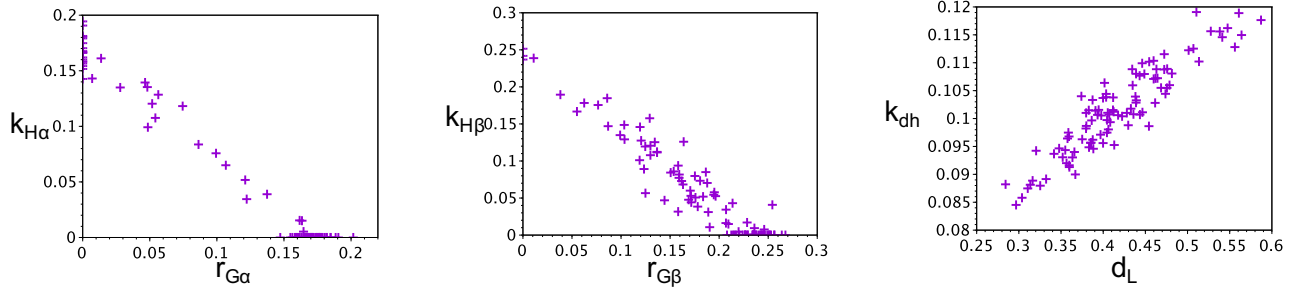


Figure 5.5: Example of scatter plots evidencing correlations found for some parameters obtained from experiment 1. Results obtained after 150 MC iterations. See text for more details about the MC. The same correlations are observed for experiment 2.

$$\left\{ \begin{array}{l}
 x_1 = -k_{H\alpha} - r_{G\alpha} \\
 x_2 = -k_{H\beta} - r_{G\beta} \\
 x_3 = -\frac{1}{2}(k_{\alpha \rightarrow \beta} + k_{dh\beta} + k_{\beta \rightarrow \alpha} + r_{G6P\alpha} + r_{G6P\beta} + \\
 \quad (k_{\alpha \rightarrow \beta}^2 + 2k_{\alpha \rightarrow \beta}(-k_{dh\beta} + k_{\beta \rightarrow \alpha} + r_{G6P\alpha} - r_{G6P\beta}) \\
 \quad + k_{dh\beta}^2 + 2k_{dh\beta}(k_{\beta \rightarrow \alpha} - r_{G6P\alpha} + r_{G6P\beta}) \\
 \quad + k_{\beta \rightarrow \alpha}^2 + 2k_{\beta \rightarrow \alpha}(r_{G6P\alpha} + r_{G6P\beta}) + r_{G6P\alpha}^2 - 2r_{G6P\alpha}r_{G6P\beta} + r_{G6P\beta}^2)^{\frac{1}{2}} \\
 x_4 = -\frac{1}{2}(k_{\alpha \rightarrow \beta} + k_{dh\beta} + k_{\beta \rightarrow \alpha} + r_{G6P\alpha} + r_{G6P\beta} - \\
 \quad (k_{\alpha \rightarrow \beta}^2 + 2k_{\alpha \rightarrow \beta}(-k_{dh\beta} + k_{\beta \rightarrow \alpha} + r_{G6P\alpha} - r_{G6P\beta}) \\
 \quad + k_{dh\beta}^2 + 2k_{G6P\beta \rightarrow 6PGL}(k_{\beta \rightarrow \alpha} - r_{G6P\alpha} + r_{G6P\beta}) \\
 \quad + k_{\beta \rightarrow \alpha}^2 + 2k_{\beta \rightarrow \alpha}(r_{G6P\alpha} + r_{G6P\beta}) + r_{G6P\alpha}^2 - 2r_{G6P\alpha}r_{G6P\beta} + r_{G6P\beta}^2)^{\frac{1}{2}} \\
 x_5 = -d_L
 \end{array} \right. \quad (5.2)$$

, which shows the various parameters dependencies. These complex relationships between eigenvalues and kinetic parameters suggest that additional constraints may be needed to exactly extract all of the model parameters. In particular, independent measurements of spin lattice relaxation times of glucose relaxation may be used to extract hexokinase kinetic parameters from eigenvalues x_1 and x_2 . However, for the third and fourth eigenvalues there is no external measurement we can perform to extract the kinetic parameters involved.

5.4.2 Simultaneous fit

To try and overcome the underdetermination of the model, both experiments were fitted simultaneously. In this case, relaxation and anomerization parameters are common to both experiments. This is not a strong assumption, as both experiments were performed in the same conditions (temperature and pH of the sample, magnetic field, etc...). Since the two experiments exhibit different kinetics, we could expect the fitting problem to be less degenerated. Moreover, one can expect that, with this strategy, no independent measurements of anomeric rates, or G6P relaxation rates (that could not be measured) should be required, since the data sets are mutually constraining.

For the simultaneous fits we imposed that the parameters, $r_{G\alpha}$, $r_{G\beta}$, $r_{G6P\alpha}$, $r_{G6P\beta}$ and d_L ; and $k_{\beta\rightarrow\alpha}$, $k_{\alpha\rightarrow\beta}$ are identical in both experiments. Alternatively, the G6PDH and hexokinase activities were kept as independent parameters in both experiments.

Results of this simultaneous fit are displayed in figure 5.6. It is seen that the data are well reproduced. Here, although individual parameters seem to be better determined, some inconsistencies remained. The MC consisted on 500 iterations with addition of noise, and unconverged trials (82), as attested by significantly larger values of the target function, were discarded. Following this procedure, most of the eigenvalues were well defined, although x_3 exhibited a bimodal distribution 5.7. The histograms of the eigenvalues obtained from the Monte Carlo simulation (representing a total of 320 MC iterations) are shown in figure 5.7. For x_3 , one of the two modes has no physical meaning, the resulting parameter values are many orders of magnitude bigger than what is documented in bibliography or what was prepared during the experiment. The iterations converging to this mode could thus be discarded. The obtained set of parameters are displayed in table 5.1. We can see that, for 7 of the 10 parameters, the distributions have standard deviations of 3% to 10% of the average value of the parameter, and could thus be considered well-defined. Three other parameters, $r_{G6P\beta}$, $k_{\alpha\rightarrow\beta}$ and $k_{\beta\rightarrow\alpha}$, were less well-defined. Their standard deviation is of $\sim 50\%$ or larger than the average value of the parameter, and exhibited mutual correlations as shown in figure 5.8. It turns out that, for $k_{\beta\rightarrow\alpha}$ and $r_{G6P\beta}$, in 222 and 226 iterations of the MC the

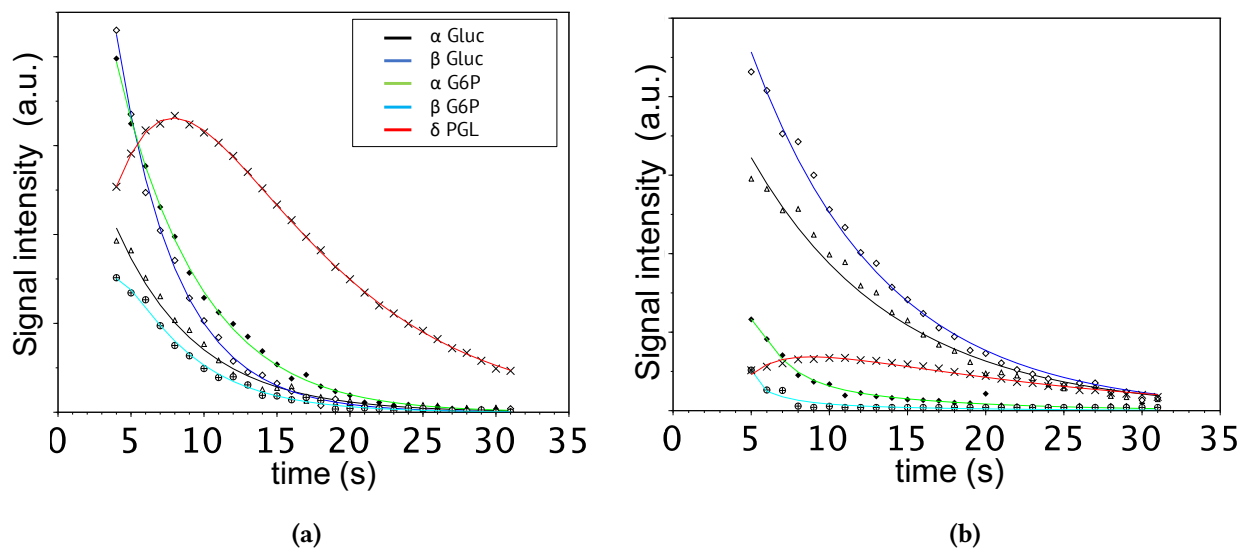


Figure 5.6: Simultaneous fit of the data resulting from experiment 1 (in a) and experiment 2 (in b). Only the parameters related to enzyme activities in the model (eq. 5.1) were consider different for each experiment, i.e. all other parameters were consider equivalent for both experiments during the simultaneous fit.

resulting values are lower than 0.001, respectively. For this reason, their histograms seem to be empty. Strategies to further constrain the model in order to extract these parameters will be discussed later. Although the complete set of parameters could not be determined, some parameters could be estimated with an error lower to 10%. The parameters defining glucose relaxation for both anomers are almost equivalent, which is realistic. These values are also similar to documented values of glucose in similar experimental conditions[226] [51]. Regarding the activity of hexokinase, the kinetics of the enzyme are found slightly faster

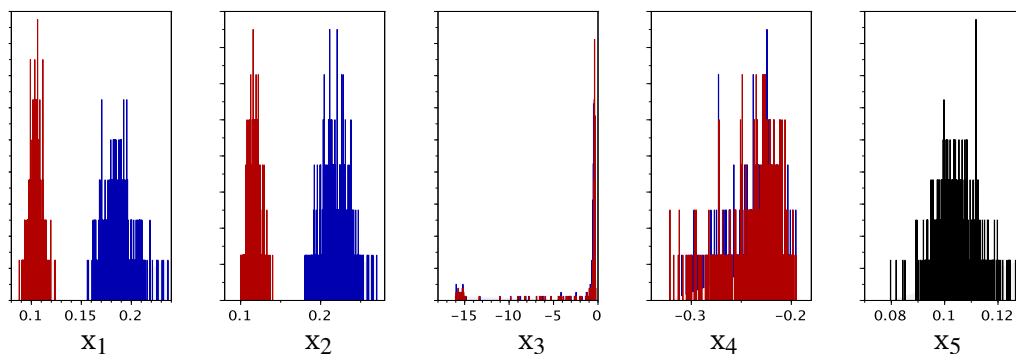


Figure 5.7: Histograms of the eigenvalues obtained for experiment 1 (in blue) and experiment 2 (in red). The distributions resulted from an MC simulation consisting of 500 iterations. X_5 is defined as equivalent for both experiments and therefore has no color code.

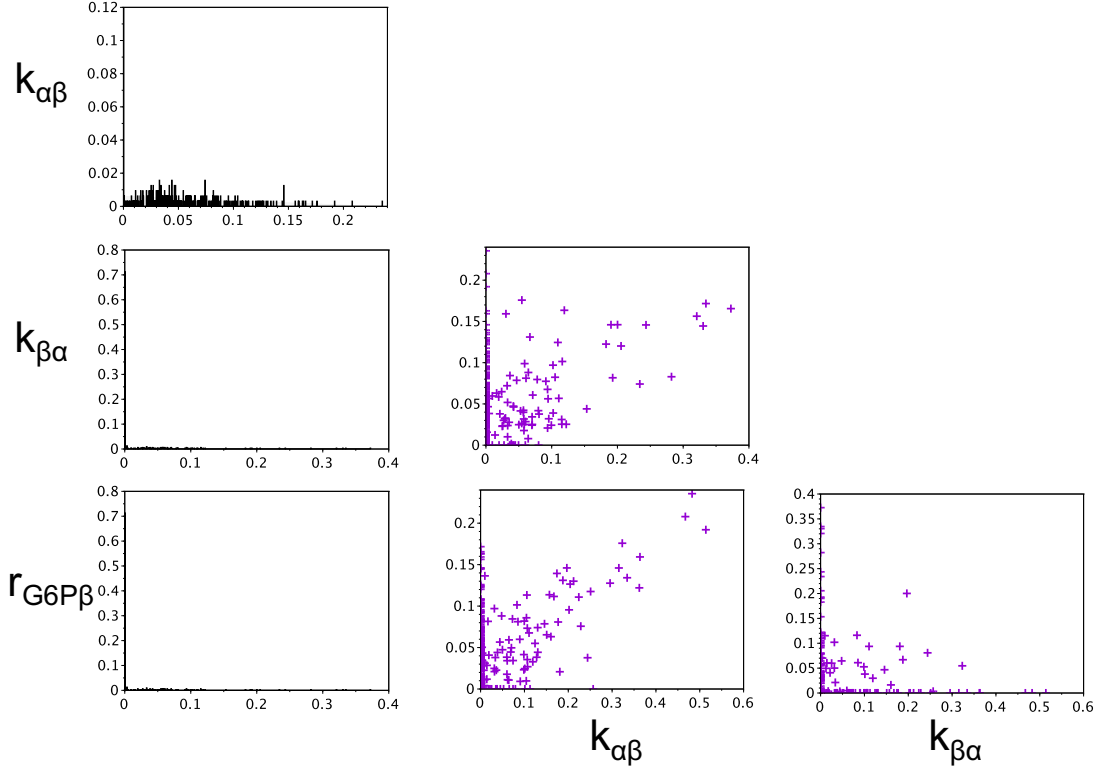


Figure 5.8: In the first column are displayed the histograms obtained with the MC simulations of the 3 undefined parameters. For both $k_{\beta\alpha}$ and $r_{G6P\beta}$ more than 70% of the values are < 0.0001 , their values can be thus neglected. Parameter correlations are displayed on the other 2 columns.

towards the β transformation in both experiments, i.e. $\frac{k_{H\beta}^{exp1}}{k_{H\alpha}^{exp1}} = 1.4$ and $\frac{k_{H\beta}^{exp2}}{k_{H\alpha}^{exp2}} = 1.27$, note that the ratio is very similar for both experiments. Finding such similar ratios is reasonable since we used the same enzyme in the same experimental conditions. Moreover, this value is similar to a value of $\frac{k_{H\beta}}{k_{H\alpha}} = 1.58$ measured in [50].

The kinetic rates for G6PDH catalysis seems to be approximately equal in both experiments, with a value $k_{dh\beta} \sim 0.4$, which is consistent with the fact that samples were prepared with the same G6PDH activities. In addition, the ratios of the hexokinase rate constants for the two anomers vary in a similar fashion between experiments, i.e., $\frac{k_{H\alpha}^{exp1}}{k_{H\alpha}^{exp2}} = 5.5$ and $\frac{k_{H\beta}^{exp1}}{k_{H\beta}^{exp2}} = 5.3$. This is realistic, as both rates $k_{H\beta}$ and $k_{H\alpha}$ reflect the same enzyme kinetics. However, the values of these experimental ratios was larger than the expected value of ~ 2 , conditions in which the experiments were prepared.

The latter inconsistency can be related either to errors in the preparation of the samples

or to the presence of non-considered transformations. As a matter of fact, multiple regulation mechanisms have been identified for this chain of reactions. To start with, it has been shown that glucose can be a low-affinity substrate of G6PDH enzyme [74]. Additionally, the ratio between NADPH/NADP⁺ has a regulatory effect on G6PDH activity [61]. Finally, the accumulation of G6P has been documented to have an inhibitory effect on hexokinase activity [50]. In order to properly extract the enzyme activities, these additional reactions have to be considered in the model. However, the model as defined for this experiments does not allow to extract the complete set of kinetic parameters. Adding new parameters is hence not conceivable.

Improving and extending the strategy described in this chapter should involve the combination of additional experiments with different enzyme activities. This implies that all experiments must be done within a short time to avoid enzyme degradation and activity losses, which occurs once in solution. However, in practice, the time required to perform one such DDNP experiment - sample preparation and hyperpolarization ($\sim 1h$) - amounts to about 2 h with the current instrumentation. Therefore, a set of 3 experiments with different enzyme activities, and a calibration experiment, would then need a total time of 8 h if no setback occurs.

The strategy presented in this section can nevertheless be advanced to a versatile and useful tool for more complex systems in which enzymatic cascades need to be characterized, provided that the different reactions involved in the system, and the relevant regulatory

	Parameter	$k_{H\alpha}$	$k_{H\beta}$	$k_{dh\beta}$	$k_{\alpha\rightarrow\beta}$	$k_{\beta\rightarrow\alpha}$
Exp. 1	Average	0.095	0.126	0.434	0.052	0.023
	St. deviation	0.009	0.011	0.042	0.022	0.028
Exp. 2	Average	0.018	0.023	0.376		
	St. deviation	0.002	0.003	0.26		

Parameter	$r_{G\alpha}$	$r_{G\beta}$	$r_{G6P\alpha}$	$r_{G6P\beta}$	d_L
Average	0.091	0.092	0.171	0.035	0.104
St. deviation	0.0054	0.0063	0.062	0.08	0.003

Table 5.1: Resulting parameters of the simultaneous fit. Average over 352 MC iterations after filtering.

mechanism are considered.

Chapter 6

Characterization of G6PDH with labeled G6P

It is clear that studying the kinetics of each enzyme individually is much simpler than the complete cascade of events. We therefore decided to focus on the kinetics of G6PDH only. We produced and purified G6P to this aim.

6.1 Production and purification of [U-¹³C; U-²H]G6P.

For this study, we optimized a technique previously used in the lab to produce and purify [U-¹³C; U-²H]G6P [229]. Labeled G6P was enzymatically produced from [U-¹³C; U-²H]glucose. To this aim, labelled glucose is simply added to a buffer solution containing Hexokinase, ATP (cofactor) and MgCl₂ [229]. Formerly, a *fast protein liquid chromatography* (FPLC) with an anion exchange column was used to separate the different sample components and to extract the substrate from the reaction medium. Although an effective way to purify labeled G6P, the above strategy is very time consuming. Indeed, due to the saturation of the column, only a limited amount of molecules can be retained, which limits the flow and volume to be processed. The various anionic components of the reaction medium can be adsorbed on the column (ATP, ADP, AMP, buffer, G6P) and therefore contribute to its saturation, where AMP is produced by the spontaneous dephosphorylation of ATP and ADP.

In the work presented in chapter 3 of [229], after optimization of the method a maximum of $\sim 347 \mu\text{mol}$ of [U-¹³C; U-²H]G6P, could be purified during a total of 17 purifications by FPLC, implying that the complete process lasted for $\sim 11 \text{ h } 20 \text{ min}$ to obtain 94.458 mg of [U¹³C-U²H]G6P.

Another purification strategy developed during this work is presented below. We used size-exclusion (or molecular-sieve) chromatography (SEC)[230]. Here, the separation is based on the differing ability of molecules, depending on their sizes, to go through the pores of the gel-filtration medium, present in a column. Thus molecules at the exit of the column are separated according to their size. Labeled G6P was obtained from the following reaction medium:

- 500 mg [U-¹³C; U-²H]glucose, 2,6 mmol.
- 45 mL of Phosphate Buffer, 100 mM, pH = 7,25.
- 1,71 g ATP, 3.37 mmol.
- 3,1 mL of a 1M MgCl₂ solution corresponding to a final concentration of 3,1 mmol.
- 1,8 mL of a 1M NaOH solution for a final pH of 7,1.
- 200 U of Hexokinase enzyme from *saccharomyces cerevisiae*, representing 5,37 mg.

The enzymatic reaction took place during 48 H at ambient temperature and was subsequently frozen at (-20 C°) once glucose phosphorylation was complete. The masses of these different molecules and of hexokinase (water excluded) add up to $m_{init} = 4,355 \text{ g}$. After production, the pH was raised to 10.5 to precipitate the magnesium as magnesium hydroxide and magnesium phosphates. Subsequent centrifugation of the reaction medium was used to remove the Mg(OH)₂ and (MgHPO₄) precipitates. The resulting solution was then lyophilized and weighted. The obtained solid has a total mass of 3,9 g suggesting we filtered 455 mg of magnesium salts. The solid was dissolved again in 15 mL of H₂O close to solubility limit to be deposited on the SEC column. We used a column filled with a Sephadex® G25

gel filtration resin (Diameter: 35 mm; Length: 150cm). After being cleaned by a solution of 200 mM NaOH and extensively washed with water, the reaction medium was inserted into the column. Fractions were collected every 5 min (10-12 mL per fraction) with a flow of 2-2,4 mL.min⁻¹. A dehydration reaction was used to identify the fractions containing

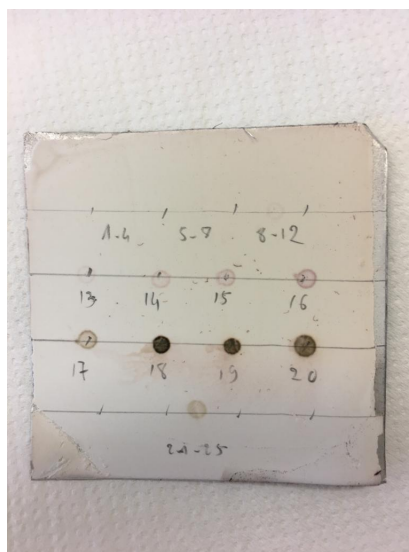


Figure 6.1: Colorimetric test used to reveal the presence of carbohydrates. After spotting each fraction on a TLC silica gel plate, the plate is plunged in a H₂SO₄ solution and heated. The apparition of brown marks confirms the presence of sugars in the different fractions.

sugars (ATP, ADP, AMP and G6P). In figure 6.1, we see that most of the sugars present in the reaction medium are found in fractions #16 to #20. In order to assess the efficiency of the purification method we measured the amount of G6P obtained in each fraction and its purity. The amounts of ATP, ADP and Phosphate buffer were also quantified in order to evaluate the purity of the [U-¹³C; U-²H]G6P obtained. As a first quantification, fractions #16 to #25 were lyophilized and weighted. The resulting masses are presented in table 6.1. Since the TLC plates showed absence or very weak presence of sugar in fractions \geq #20, we pooled the five fractions #21 to #25(named fraction #21*). The total mass collected within these fractions was 2.8 g, which corresponds to 70% of the total mass deposited on the SEC column. The remaining 30% (1, 1 g) mg accounts for non-sugar compounds. The HK protein that could be eluted in earlier fractions and in contrast, salts (phosphate, Na, Cl, Mg) could be present in fractions \geq #25. Subsequently, the solids were dissolved in pure D₂O (in 500 μ L for fractions #16 and #17, and in 1 mL for fractions #18-#21), and the amounts of [U¹³C-

Fractions	16	17	18	19	20	21*	total
mass (mg)	9	75	504	768	643	829	2828

Table 6.1: Mass of solid obtained after purification by gel filtration of the reaction medium and subsequent lyophilization.

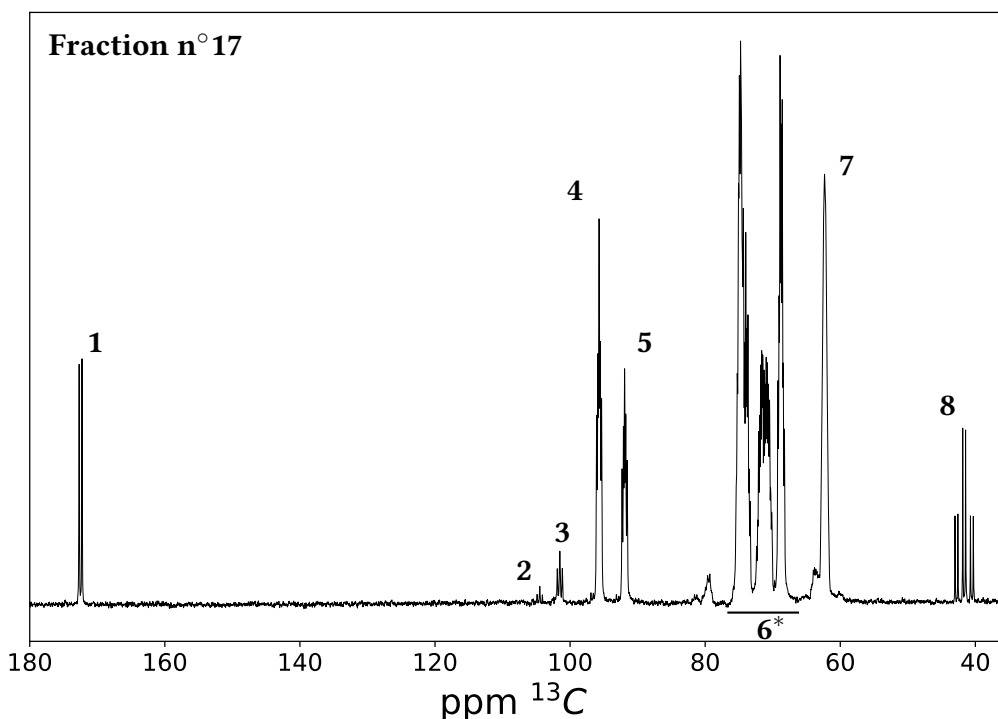


Figure 6.2: ¹³C NMR spectrum for the peak attribution of fraction n° 17. The lyophilized fraction was dissolved in 500 μL of pure D₂O. 1 glycine C₁, 2 β-G6P C₁ furanose, 3 α-G6P C₁ furanose, 4 β-G6P C₁ 5 α-G6P C₁, 6* C₂₋₅ of both anomers of G6P, peak overlay, 7 G6P C₆, 8 Glycine C₂.

[U-²H]G6P in these samples were measured by means of ¹³C NMR. The peak assignment is presented in figure 6.2. In the resulting ¹³C spectra we can also identify the furanose form of the G6P, which is a spontaneous transformation of the G6P molecule. The cyclic structure of the sugar consists of a cycle of 4 carbons in the furanose form compared to a 5 carbons cycle in the pyranose form, the most common form for G6P. In this manuscript, when we refer to G6P, we thus refer to G6P in the pyranose form.

We acquired a ¹³C spectra of each fraction in presence of [U-¹³C]glycine sample contained in a capillary inside the NMR tube, to serve as a reference for quantitation. The relation between G6P concentration and glycine's ¹³C signal intensity was calibrated by comparison with a reference solution containing a known concentration of [U-¹³C; U-²H]glucose.

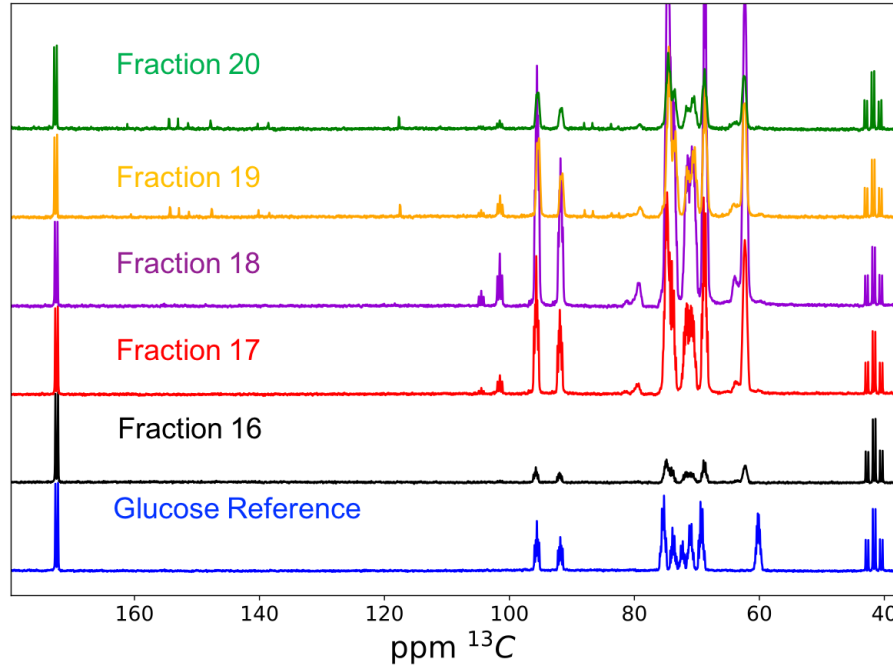


Figure 6.3: ^{13}C spectra for quantification of the different fractions collected after purification. Reference used for quantification was $[U-^{13}C]$ glycine, peak in the carbonyle region

The relation is given by:

$$\frac{S'_{Gly}}{S_{Gref}} = \frac{[Gly]}{[Gref]}, \quad \text{and} \quad \frac{S_{G6P}}{S_{Gly}} = \frac{[G6P]}{[Gly]} \quad (6.1)$$

$$[G6P] = \frac{S_{G6P}}{S_{Gly}} \times \frac{S'_{Gly}}{S_{Gref}} [Gref]$$

Hence, the concentration obtained in each fraction $[G6P]$ can be determined in function of the signal ratios in each NMR spectra $\frac{S_{G6P}}{S_{Gly}}$, the signal ratios obtained in the reference experiment with glucose $\frac{S'_{Gly}}{S_{Gref}}$, and the known concentration of glucose $[Gref]$. After measuring $[G6P]$, the amount of materia N_{G6P} can be determined in function of the volume in which the lyophilized fraction was diluted, $N_{G6P} = [G6P] \times V_{samp}$. The ^{13}C spectra acquired for the different fractions are displayed in figure6.3. Since the C1 and C6 resonances of G6P can be integrated separately, we performed three independent quantifications using the un-

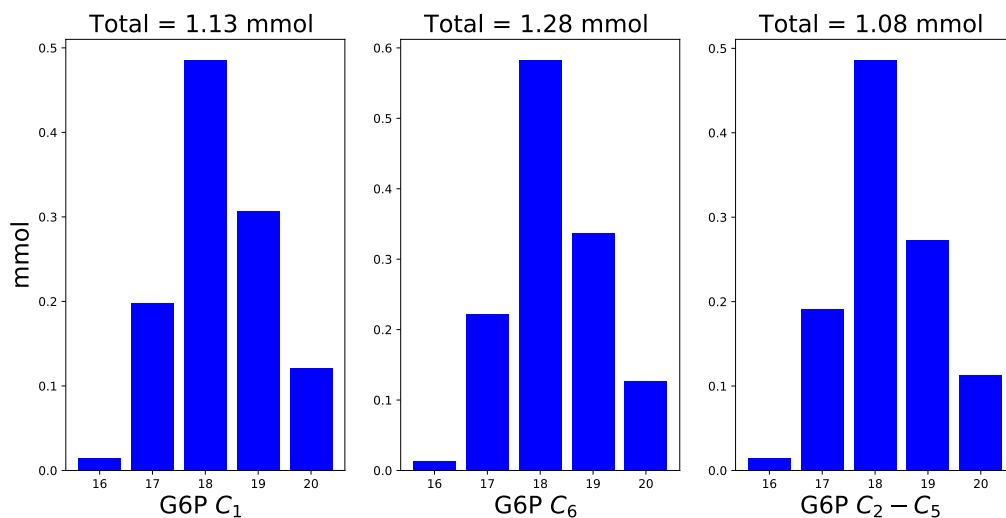


Figure 6.4: Multiple quantifications of G6P's amount of substance, performed with different ^{13}C resonances

shielded C1 peaks, the most shielded C6 resonance and lastly the C2-C5 zone. We can thus cross-check the resulting values.

The signal attributed to G6P C₁ was obtained by integrating the resonances of both α and β G6P C₁, the intensities obtained were then added. For the second quantification, we integrated the region 66-77 ppm, in which C₂₋₅ resonances of G6P are located. The total signal intensity was then divided by 4. The third quantification was performed by directly integrating C₆ resonance of G6P. The results obtained in the different measurements are displayed in the histograms of figure 6.4. The results presented in the histograms of figure 6.4 show similar values for the quantifications performed with different ^{13}C resonances, 1.08-1.28 mmol. Results suggest a loss of 1,32-1,52 mmol, representing 50% to 58% of the original transformed substrate, since the G6P was produced from 2.6 mmol of glucose . Part of the G6P is however present in the furanose form, characterized by higher chemical shifts for the C1 as seen in the ^{13}C spectra (see figure 6.3). However, after quantification, the furanose conformers only represent a total of 0.126 mmol. Hence, a significant amount of $[U^{13}C-U^2H]G6P$ is retained in the remaining fractions or lost during the purification procedure. Since ATP and ADP are not ^{13}C labeled, their quantification was performed by means of 1H NMR. We followed the same strategy to quantify the amount of substance of these two compounds in the different fractions. Glycine was not a good reference in 1H

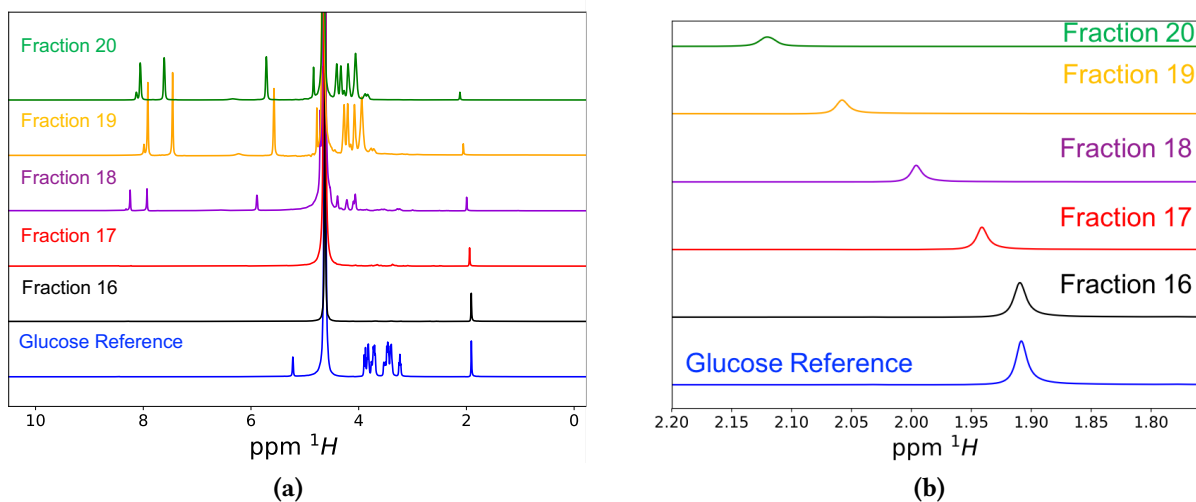


Figure 6.5: 6.5a 1H spectra for quantification of the different fractions collected after purification. The molecule used as reference for quantification was acetic acid and the peak used for the analysis is the one around 2 ppm. 6.5b Possible variation in susceptibility due to changes in the concentration of the different molecules on each fraction.

NMR because of resonances overlaps with the ribose moities. Therefore, we used acetic acid as the reference compound inside the capillary. The amounts of ATP and ADP were measured together. The resulting 1H NMR spectra are displayed in figure 6.5. We used the resonances of ATP/ADP in the aromatic region to perform the quantification.

Although all 1H NMR spectra were acquired at the same temperature, we can however observe a frequency shift for the different fractions. The shift, more evident in the aromatic region ($\sim 7-9$ PPM), could be related to a variation in pH. The pH in each fraction is mainly regulated by the concentration of phosphate buffer. It is therefore normal to see different shifts in each spectrum due to the different compositions of each fraction. The frequency shift was considered in the determination of the signal intensities used in the quantification. Moreover, there seems to be an smaller frequency shift in the acetic acid peak (~ 1 ppm). Since the acetic acid is inside a capillary, the pH should not change between fractions. A variation in the magnetic susceptibility can cause a frequency shift for the reference resonance, and a modification of its shape, see figure 6.5b. The significant changes in composition, density and viscosity, between fractions may account for this magnetic susceptibility shift which, however, have no impact on the quantification. The results

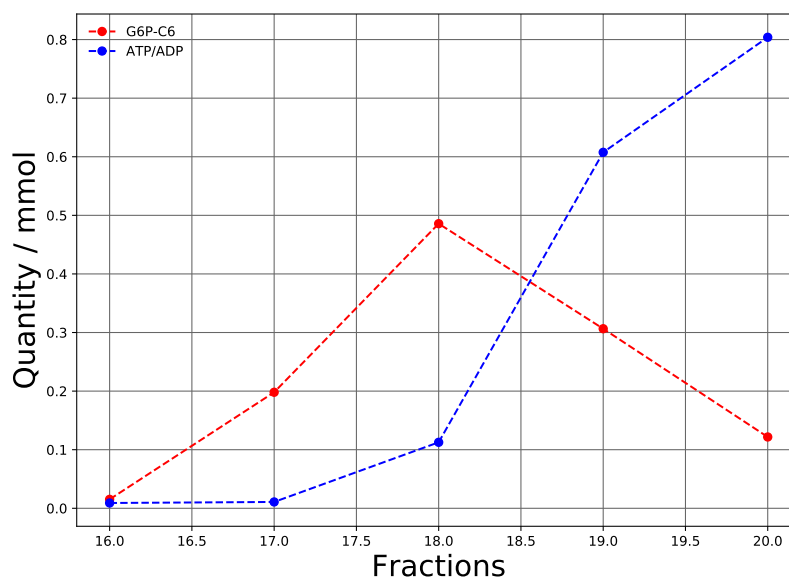


Figure 6.6: Comparison of the quantity of ATP/ADP vs G6P per fraction. G6P plot results from the quantifications done with the $^{13}C_6$ peak.

of the measurements of ATP/ADP quantities are displayed in table 6.2 together with the results of the quantification of G6P. Originally, we added 3.37 mol of ATP and at the end we only recover a total of ATP and ADP of 1,54 mol. These results suggest that a only the half of ATP/ADP was present in the fractions 18-20. Figure 6.6 suggests that a remaining mass should be present in later fractions (after #20). We can already observe that the fractions #17 and #18 have bigger concentrations of G6P, the presence of ATP/ADP seems to be not significant. For later fractions, the quantity of ATP/ADP overtakes G6P and these fractions have to be further purified. A summary of these observations is presented in figure 6.6.

To evaluate the presence of the phosphate buffer in these fractions we use ^{31}P NMR. The spectra obtained for the different fractions is displayed in figure 6.7b. On this figure we can also observe the resonances related to ATP, ADP and even AMP 6.7 along with the phosphate

Fractions	16	17	18	19	20	Total
G6P-C ₁	0.015	0.2	0.49	0.31	0.12	1.13
G6P-C ₂ – 5	0.015	0.2	0.49	0.27	0.11	1.08
G6P-C ₆	0.013	0.22	0.58	0.34	0.13	1.28
ATP/ADP	0.01	0.01	0.11	0.61	0.80	1.54

Table 6.2: Quantification in 10^{-3} moles of G6P and ATP/ADP for the different fractions.

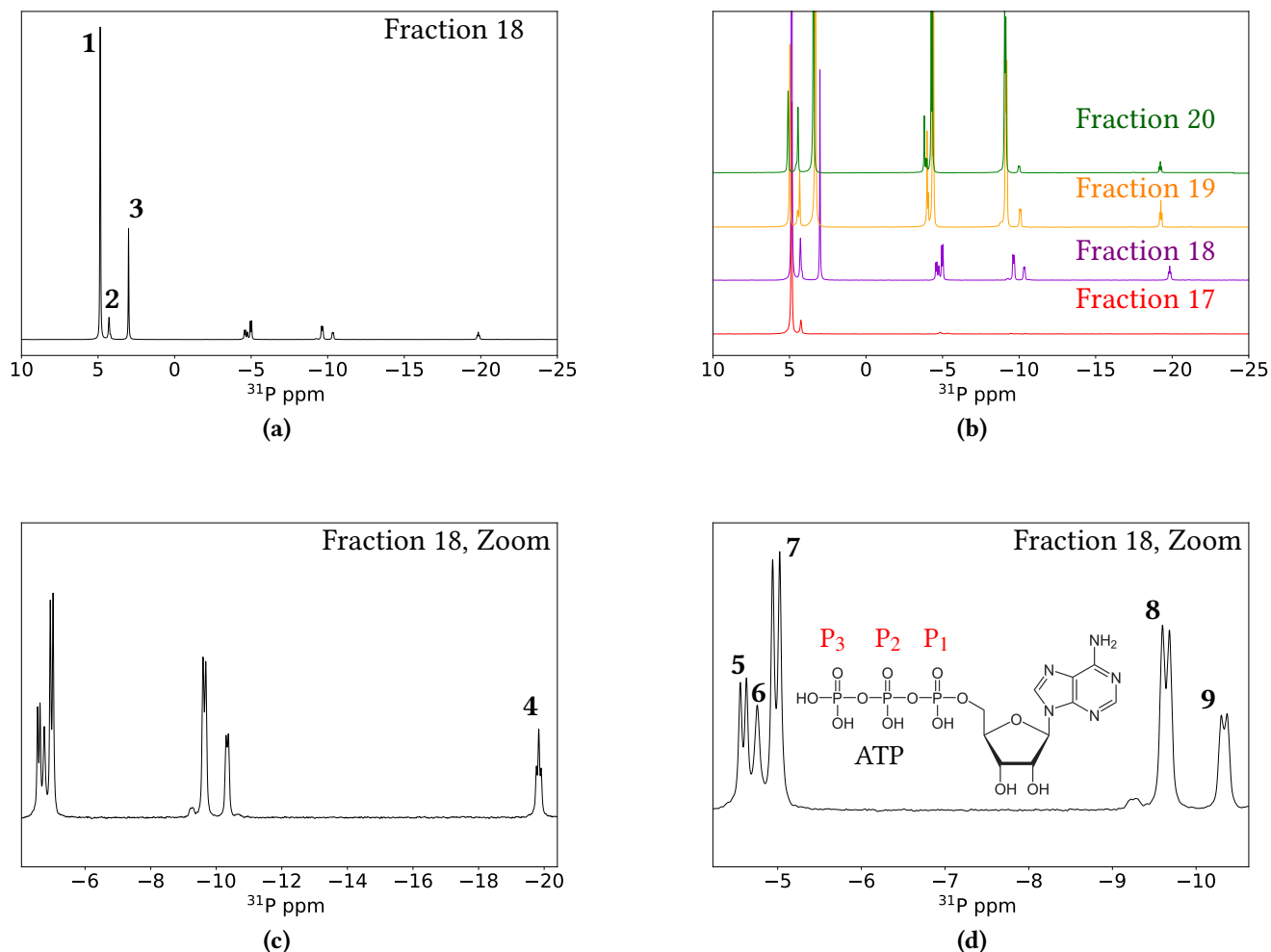


Figure 6.7: ^{31}P NMR spectra with peak attribution. **a)** Spectrum obtained for fraction 18 complete spectra, with in **c)** a zoom over -4 -20 ppm region and in **d)** a zoom over -4 -11 ppm region. In **b)** are displayed the spectrum obtained for fractions 17-20. Assignments of phosphate groups have been deduced from the integration of the signals and the observed manifolds : **1** α -G6P, **2** β -G6P, **3** Phosphate buffer, **4** P₂ ATP, **5** P₃ ATP, **6** AMP, **7** P₂ ADP, **8** P₁ ADP, **9** P₁ ATP .

resonance of G6P. In the spectra given in 6.7 we can see that for fraction 17, no resonances different to G6P can be observed. This fraction is $\sim 93\%$ pure (measured with the relative signal intensities of all peaks in ^{31}P spectrum). For fraction 18, G6P is still the predominant compound with higher concentration, however the concentration of Phosphate buffer, ATP and ADP cannot be neglected. For the other fractions G6P concentration is not predominant anymore. After quantification, the final production of $[U^{13}C, U^2H]G6P$ was of 60 mg in fraction 17, and 158 mg in fraction 18. If both fractions are conserved 218 mg of $[U^{13}C, U^2H]G6P$ were produced. Since fractions were collected every 5 min, collecting 25 fractions

imply a final duration of 2 h 5 min for the complete purification process. Compared to the FPLC purification method developed in [229] where 94.5 mg of $[U^{13}C, U^2H]G6P$ were purified in a process that took ~ 11 h.

For future purifications, we plan to make successive passages through the column. Hence, the fractions that were not highly pure ($>80\%$) and not conserved after the first passage could be filtered again, to retain the almost completely pure fraction, increasing rendered $[U^{13}C, U^2H]G6P$. However, the amount of purified G6P was half of the expected amount. The profile displayed in figure 6.2 suggest that most of G6P should be present in the fractions analysed, (16-20). The latter implies that half of the G6P was lost during the production/purification process. In this scope, it would be interesting to identify the main origins of G6P losses.

6.2 Kinetic analysis

The first experiments performed with the produced and purified $[U-^{13}C; U-^2H]$ G6P focused on both confirming the anomeric specificity of G6PDH by DDNP as a proof of concept, and on determining the kinetics of the spontaneous anomerization of G6P. A simplified representation reaction pathway relative to the system under study is depicted in figure 6.8, where the approximations that were used for this study are indicated. The first approximation is to assume that, as shown in [74], G6PDH has a specific activity towards the β anomer of G6P. Secondly, since for the different experiments the cofactors are present in excess (~ 10 -fold with respect to the substrate), their concentration is assumed constant and is discarded from the kinetic analysis. Both of these approximations were already used in the previous chapter.

The first DNP sample used in this round of experiments was prepared with nearly pure $[U-^{13}C, U-^2H]G6P$ (according to the quantification procedure described previously - purification fraction #17). The DNP sample was a mixture of 10%:40%:50% $H_2O:D_2O$:Glycerol- d_8 in volume. The final G6P concentration of the sample was 500 mM and the radical chosen was TEMPOL (4-hydroxy-TEMPO). The concentration of radical chosen for the experiment

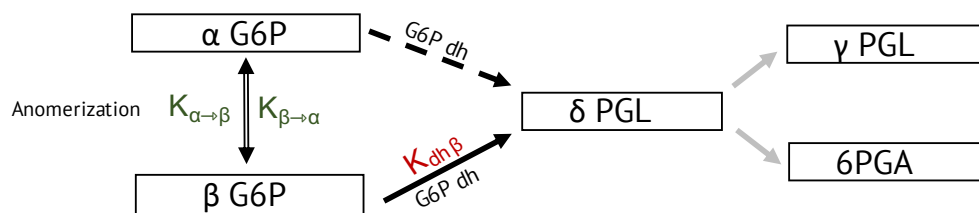


Figure 6.8: Simplified scheme of the observed system for the series of experiments using G6P as the substrate. There are two kinetic parameters determining the anomerization of the substrate and one kinetic parameter related to the G6PDH activity on the β -G6P anomer. The dotted arrow represents the discarded transformation due to the enzyme specificity [33]. Gray arrows represent non studied reactions related to the spontaneous hydrolysis and isomerization of the δ -PGL.

was 50 mM, concentration optimized for the static magnetic field (9.4 T, cryo-free polarizer) and the CP sequence used during the hyperpolarization of the substrate, [subsubsection 4.2.3.2](#). 75 μ L of the formerly presented sample were introduced in the polarizer for a total of 37.5 μ mol of G6P. Two experiments were performed. Experiment A served as a reference to observe the conventional decay of G6P signal without any enzyme activity, and experiment B was performed with a high enzyme G6PDH activity (400 u). The G6PDH used (Merck), was extracted from *Saccharomyces cerevisiae* and packaged with an specific activity of 319 $u.mg^{-1}$

Both experiments were performed on our 9.4 T polarizer and followed the usual steps of DDNP. Maximum polarization was reached after ~ 6 CP steps (\sim one hour) at 1.2 K and under μ -wave irradiation. The μ wave power was set to 75 mW and irradiation was performed at 263 ± 1 GHz, modulated with a saw-tooth function over a range of 100 MHz. The DNP sample was dissolved in 5 mL of D_2O heated at 403 K and pressurized at 10.5 bar, and transferred to the NMR spectrometer, into a 10 mm NMR tube containing the solution with cofactors and, depending on the experiment, enzymes. The total transfer lasted 3 s although the G6P arrive to the NMR tube from the first scan, 1 s after the dissolution.

In experiment A, no enzymes were added to the solution sitting in the NMR tube. On the other hand, the cofactor, $NADP^+$, was added so that the density and viscosity conditions would match as closely as possible in both experiments. The $NADP^+$ concentration was a tenfold larger than substrate concentration in order to neglect its variation during the course of the experiment, and consider it constant for the reaction kinetics. Thus, 375 μ mol

of NADP^+ were added to a solution of HEPES buffer 200 mM, pH = 7.4. After mixing with the dissolved sample, the final sample volume was ~ 3 mL.

For experiment B, the same procedure was used, where 400 u of *glucose-6-phosphate dehydrogenase* yeast enzyme were added. After mixing with the dissolved sample, the final sample volume was ~ 3 mL .

Both experiments were acquired in the same 400 MHz bruker spectrometer, in a 10 mm BBO dual channel probe tuned to ^{13}C and ^1H . Both ^1H and ^2H decoupling were preformed using a Waltz-16 sequence during the acquisitions. The excitation pulses consisted on a series of subsequent squared pulses of 10° with a 1 s interval between each other.

6.2.1 Characterizing G6PDH activity and G6P anomerization rate

The summed spectra obtained for both cases (experiments A and B) are shown in figure 6.9. In experiment B, the production of δ -PGL (label 2) shows that the dehydrogenation reaction of G6P actually took place and that the enzyme was therefore active. In addition, a small resonance signal in the vicinity of δ -PGL, in the carbonyl region of the ^{13}C spectrum can be assigned to γ -PGL, the isomerisation product of δ -PGL [226]. The spectra displayed in figure 6.9 is actually the superposition of 256 scan, hence 256 seconds. The large peak intensity ratio between the two isomers δ – PGL/ γ – PGL suggests that the spontaneous isomerization process is slow compared to the production of the δ -PGL by the enzyme. Note also that, in the absence of glucose in the sample, no peak deconvolution is needed to analyze the anomeric signals, and the signal intensities of each metabolite were simply obtained by direct peak integration.

Both experiments were performed in the same pH and temperature conditions in order to avoid variations of the T_1 relaxation times. Hence, the differences in the signal decays of the two anomers only depended on the activity of the enzyme. In figure 6.10a, the anomeric $^{13}\text{C}_1$ signal intensities over time of the two anomers in experiments A (red) and B (blue) are depicted. For both experiments the α - and β -G6P signals are respectively represented by

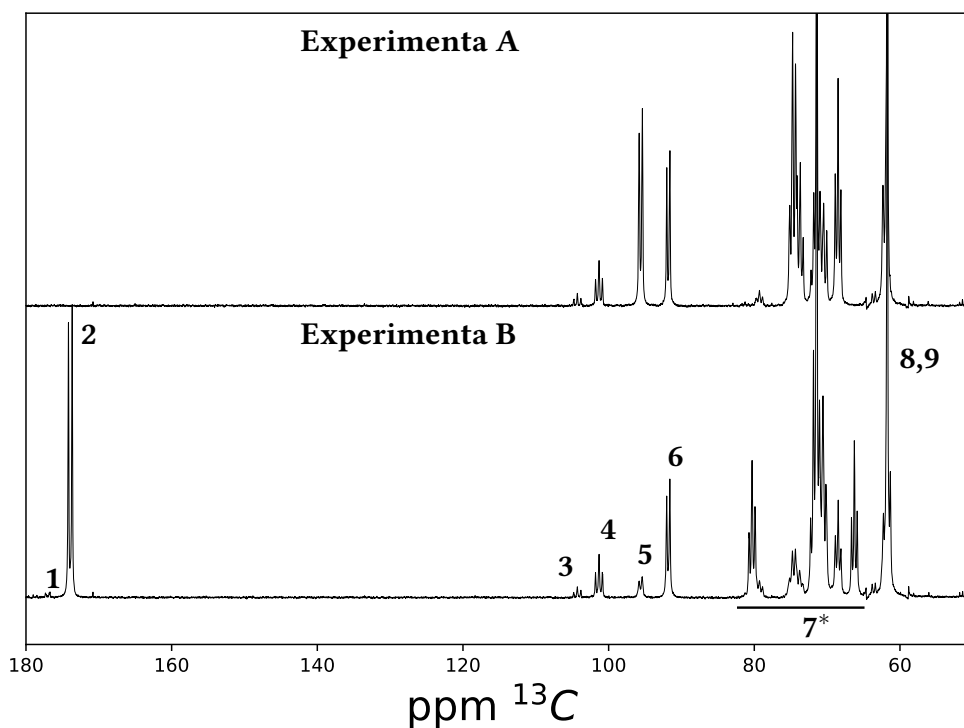


Figure 6.9: Superposition of 256 scans for the two different experiments. For the peak attribution we have for the relevant molecules: **1** γ -PGL C₁, **2** δ -PGL C₁, **3** furanos C₁, **4** furanos C₁, **5** β G6P C₁, **6** α -G6P C₁, **7*** resonances overlay containing G6P C₁₋₅, PGL C₁₋₅, and glycerol c₂, **8** G6P C₆, and **9** glycerol-d8 C_{1,3}. We can see in experiment B that the enzyme is active and producing δ -PGL. Additionally, a difference in the signal intensity ratio of both anomers (in the C₁ of α and β anomers) in the different experiments. Induction decay signals were processed using the NMRPipe software[231] and the Python library NMRglue[232] in the following way. A 2 Hz exponential apodization was used, and zero filling was applied prior to Fourier transformation.

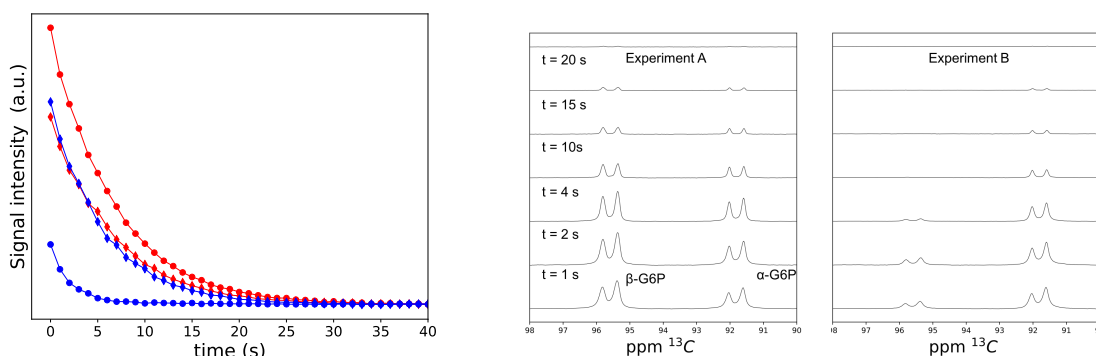


Figure 6.10: 6.10a Signal evolution of both G6P anomers for the different experiments. In this experiment A is in red and experiment B is in blue and we have \blacklozenge and \bullet that represent respectively the α -G6P and β -G6P signals. 6.10b 1D spectra of the two experiments at different times. We see that for the experiment with enzymes the signal of the β anomer disappear much faster.

filled diamonds and circles. A simple inspection of this graph shows qualitative information about the differential kinetics of both anomers in both experiments. First, it appears that the β -G6P to α -G6P intensity ratios are larger in the reference experiment A than in experiment B. Moreover, α -G6P in both experiments and β -G6P for experiment A have apparent similar decay curves, in contrast to the β -G6P signal intensities that decay faster and disappear roughly 5 times faster in experiment B, see figure 6.10b. This seems to indicate an accelerated decay, therefore kinetics, of the β -anomer signal due to the selective consumption of the anomer in the enzymatic reaction.

The decay curve of each signal was fitted to an exponential decay to extract the rate at which the molecule relax and transforms. For experiment A, assuming that the G6P is initially at anomeric equilibrium, the concentration ratio should be constant over the duration of the experiment, and the signal should decay exponentially with T_1 . For the first $n = 20$ scans, where the signal to noise ratio (SNR) is high enough, we computed the signal ratio between the two anomers of experiment A and obtain an average:

$$\sum_{t=i}^n \frac{S_{\alpha i}^A / S_{\beta i}^A}{n} = 1.48 \pm 0.047 \quad (6.2)$$

where the error was given by computing the associated standard deviation. The ratios at each time point of the anomeric signals are practically constant in time for experiment A. This confirmed the assumption that the experiment started at anomeric equilibrium. The intensities of both anomers versus time in experiment A are displayed in figure 6.11. Curves were fitted to a mono-exponential function to extract the relaxation rates of both anomers.

Thus, the following equation was used for the independent fit of both anomers in experiment A:

$$S_{\alpha,\beta}^A(t) = S_0 e^{-r_{\alpha,\beta} t} \times \cos(\theta)^n \quad (6.3)$$

Where θ is the flip angle of the detection pulses (10°), n is the scan number at time t and S_0 represent initial signal. The extracted relaxation parameters were nearly equivalent, $r_{\alpha}^A = 0.1330$ and $r_{\beta}^A = 0.1338$,

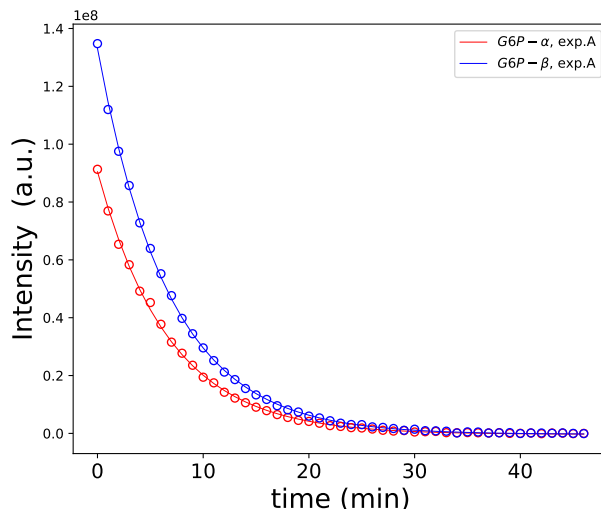


Figure 6.11: Fit of the exponential decay (equation 6.3) for both anomers of G6P in experiment A. The extracted relaxation parameters seem to be almost equivalent $r_{\alpha}^A = 0.1330$ and $r_{\beta}^A = 0.1338$

In a recent paper G6P anomeric ratio was measured at 309 K in pure D₂O, and was found to be ~ 1.7 [226]. To confirm the anomeric rate equilibrium value, obtained before and displayed in equation 6.2, we perform a new measurement of the anomeric ratio in the same experimental conditions.

To do so, a reference NMR spectrum was recorded with the sample recovered long after (\sim day) experiment A, in the same temperature conditions. The reference spectrum was obtained by averaging 1024 scans, with squared excitation pulses of 30° at 20 s interval for a total duration of more than 5 hours. The resonance peaks of β -G6P and α -G6P $^{13}\text{C}_1$ were integrated and the ratio of the signals gave:

$$\frac{S_{\alpha}^{ref}}{S_{\beta}^{ref}} = \frac{k_{\alpha\beta}}{k_{\beta\alpha}} = 1.44 \quad (6.4)$$

which is consistent with the result obtained in eq. 6.2.

6.2.2 Pseudo-first order, complete reaction scheme

A more detailed and quantitative analysis of both the G6P anomerization and enzyme kinetics was performed by combining the observations of both experiments A and B, and by

taking into account the kinetics of the chemical reactions and the longitudinal relaxation rates $r_i = \frac{1}{T_1^i}$ of the different nuclei. The model used thus included relaxation times of the $^{13}\text{C}_1$ of both anomers of G6P, together with the anomerization rate constants $k_{\alpha\beta}$ and $k_{\beta\alpha}$. As explained above, owing to identical experimental conditions, these parameters were considered identical in both experiments A and B. Moreover, in experiment B, and because of the large excess of NADP^+ cofactors, the kinetics of the enzymatic reaction was simplified and assumed a pseudo-first order reaction in [G6P]. Finally, the evolution of the δ -PGL signal was represented by a leakage term d_L that encompasses relaxation and consumption of the latter into 6PGA and isomerization with γ -PGL. Both experiments were fitted together in order to better constraint the definition of the output parameters by the fit.

$$\frac{d}{dt} \begin{pmatrix} M_{G\alpha}^B \\ M_{G\beta}^B \\ M_L \end{pmatrix} = \begin{pmatrix} -k_{\alpha\beta} - r_G & k_{\beta\alpha} & 0 \\ k_{\alpha\beta} & -k_{dh} - r_G - k_{\beta\alpha} & 0 \\ 0 & k_{dh} & -d_L \end{pmatrix} \begin{pmatrix} M_{G\alpha}^B \\ M_{G\beta}^B \\ M_L \end{pmatrix} \quad (6.5)$$

Obviously, for experiment A, since no enzyme was present in the sample, no oxidation of G6P occurred so that only the parameters related to the anomerization (in blue in equations 6.6 and 6.5) and to the relaxation of G6P were considered. Therefore, the model simplified to:

$$\frac{d}{dt} \begin{pmatrix} M_{G\alpha}^A \\ M_{G\beta}^A \end{pmatrix} = \begin{pmatrix} -k_{\alpha\beta} - r_G & k_{\beta\alpha} \\ k_{\alpha\beta} & -r_G - k_{\beta\alpha} \end{pmatrix} \begin{pmatrix} M_{G\alpha}^A \\ M_{G\beta}^A \end{pmatrix} \quad (6.6)$$

Fitting of the model parameters to the data was achieved through the Differential Evolution (DE) algorithm[228], which adjusted a set of 10 different parameters including 3 kinetic parameters ($k_{\alpha\beta}$, $k_{\beta\alpha}$, k_{dh}), 1 relaxation parameters (r_G) and d_L which has both a relaxation component and a kinetic component, and 5 parameters related to the initial values of the monitored signals (S_i at time $t = 0$) in both experiments.

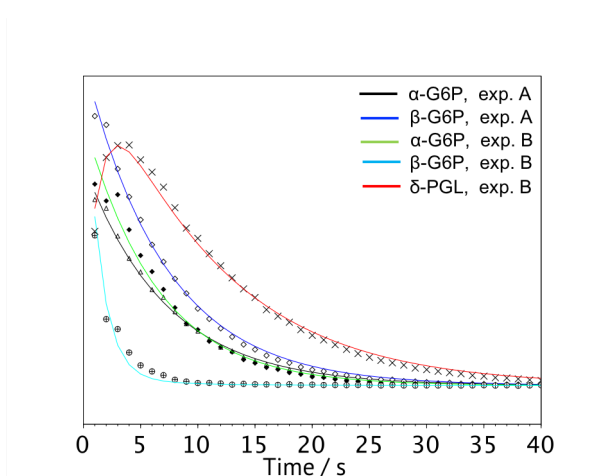


Figure 6.12: Data of experiments A and B simultaneously fitted with the model introduced in equations 6.6 and 6.5.

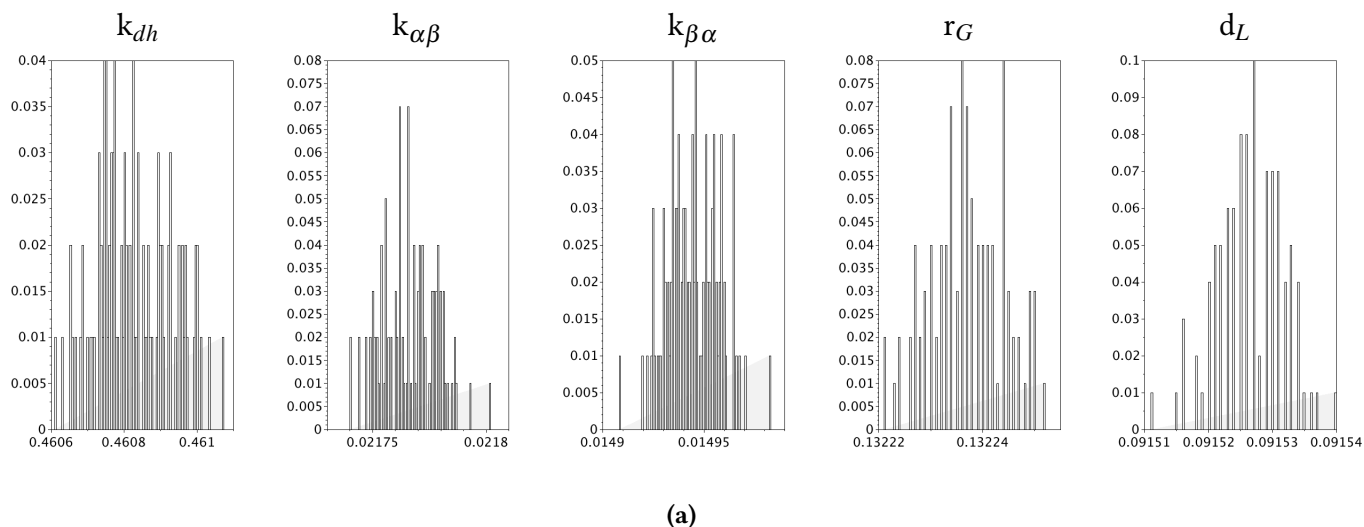
Parameters	Value (s^{-1})
k_{dh}	0.460
$k_{\alpha\beta}$	0.02
$k_{\beta\alpha}$	0.015
r_G	0.132
d_L	0.092

Table 6.3: Output parameters of the simultaneous fit of experiments A and B. This parameters were injected to the model previously introduced in this paragraph to reproduce the signal evolution displayed in figure 6.12.

In figure 6.12, the resulting fitted signals are displayed, which reproduce well the experimental observations. The obtained parameter values are displayed in table 6.3. The relaxation value for β -G6P and α -G6P is $r_G = 0.1338$, hence $T_1 = 7.47$ s found similar to the values documented in bibliography [226, 225], which can be explained by the resembling temperature conditions. The kinetic constant of the G6P oxidation has the value $k_{dh} = 0.46$ s^{-1} . In a first order kinetics, this is the initial slope of the G6P exponential decay curve. It also represents the maximum transformation rate of β -G6P, from which the enzyme activity can in principle be determined. Enzymes activities are given in units *unit* (u), 1 *unit* = 1 $\mu\text{mol} \cdot \text{min}^{-1}$, and defined as the amount of transformed substrate (in μmoles) per minute (note that the enzyme specific activity is in units and per mg of enzyme, $\mu\text{mol} \cdot \text{min}^{-1} \text{mg}^{-1}$). Thus, the maximum enzyme activity can be calculated from the kinetic rate k_{dh} , using the amount of G6P N_{G6P}^0 (in μmoles) and a time period of 60 s :

$$A_{dh}^{max} = k_{dh} \times N_{G6P}^0 \times 60 \quad (6.7)$$

Assuming that the complete hyperpolarized G6P is transferred from the polarizer to the NMR spectrometer, so that $N_{G6P}^0 = 37.5$ μmol , the maximum activity is then: $A_{dh}^{max} = 0.46 \times 37.5 \times 60 = 1024u$.



Parameters	k_{dh}	$k_{\alpha\beta}$	$k_{\beta\alpha}$	r_G	d_L
Average	0.461	0.022	0.015	0.132	0.092
St. Deviation	1.10^{-4}	$1,2.10^{-5}$	$1,3.10^{-5}$	7.10^{-6}	$5,3.10^{-7}$

(b)

Table 6.4: 6.4a Distribution of values obtained with a MC algorithm (100 iterations) for the different kinetic parameters in the model. 6.4b Average values and standard deviations resulting from the distributions obtained with the MC.

The latter estimate is ~ 2.5 times larger than the expected value, based on the specific activity of the enzyme and the amount used in the experiment (400 u). However, it should be noted that the determination of the activity depends in the amount of G6P transferred during the dissolution (see subsection 4.2.2) Considering that 3 mL out of the 5 mL dissolution sample typically reaches the NMR tube in our experiments, this value of A_{dh}^{max} can be significantly overestimated. Besides, the specific enzyme activity indicated by the supplier is measured at 20 °C, whereas our DDNP experiment were performed at 37 °C, which may increase enzyme activity [233]. For these reasons, despite an apparent discrepancy, the obtained enzyme activity seems to be consistent with the experimental conditions. The analysis of the above experiments led to values of the G6P anomerization rates. These show that the $k_{\alpha\beta}$ rate is faster than the $k_{\beta\alpha}$ rate, which is consistent with the knowledge that at equilibrium, there is a population excess of the G6P β over the α anomer. The associated equilibrium constant K is given by $:K = \frac{k_{\alpha\beta}}{k_{\beta\alpha}} = \frac{p_{\beta}}{p_{\alpha}}$, the populations of both anomers. The experiments give the resulting value $K = \frac{k_{\alpha\beta}}{k_{\beta\alpha}} = 1.42$, which is consistent with the ratio

extracted in a direct manner from the reference NMR experiment, using equation 6.4. Additionally, the constant is in agreement with documented values of the anomeric equilibrium [75, 226].

The impact of the detection noise on the resulting values was estimated with a MC algorithm. Experimental noise was again estimated for each experiment by computing the standard deviation of the signal in a region without resonances. The averages and standard deviations of the resulting distributions are presented in table 6.4b. As we can see, all parameters are well defined with errors inferior to 0.1% of the resulting values.

In conclusion, when we assess the validity of the fit results by analyzing the pertinence of the different parameters we found that:

- Both measures of the relaxation parameters, which are equivalent as expected, are consistent with values in literature.
- Anomerization parameters tend to an equilibrium value that is consistent with the one found in a separate measurement and document in bibliography.
- The obtained G6PDH activity is consistent with the preparation of the experiment.
- The noise did not affect the values obtained for the extracted parameters.

Hence the methodology seems to provide a reliable approach to characterize the kinetics of such complex system of reactions.

Part IV

In cell fluxomic studies by DDNP

Chapter 7

Glucose metabolism in *E.coli* K12

7.1 A brief background overview

DDNP-NMR has been used as a targeted method to monitor the fate of (hyperpolarized) substrates and their metabolites, giving access to the kinetic study of selected metabolic pathways under various circumstances. Both *in vivo* [43, 234, 234, 42, 235] and in-cell studies of metabolism [53, 236, 237, 238, 51, 239] have benefited from the high sensitivity, therefore temporal resolution, afforded by DDNP. The combination of DDNP and MRI have enabled the observation of metabolism in isolated tissues [240, 241], living animals [235, 242] and in humans [234, 42, 243]. DDNP has been applied to various cell types, such as bacteria [236, 244, 245], yeast [180, 236, 246] and eukaryotic cells, including macrophages or parasites [51, 239, 247]. A number of studies have focused on cancer metabolism by monitoring the uptake of [1-¹³C]pyruvate and its transformation into [1-¹³C]lactate [234, 51, 238]. The particularly long relaxation time of pyruvate C_1 and its role in metabolism make it a natural choice as hyperpolarized substrate for such studies [238, 234]. Requested in particular for *in vivo* spectroscopy and imaging in clinical trials [42, 234].

Although [1-¹³C] pyruvate has also been widely used for in-cell DDNP [248, 239, 246, 247, 244], several studies using ¹³C-labeled glucose [51, 236, 245], or alternative ¹³C labeled substrates have been proposed [249, 47]. DDNP has been used to monitor the evolution of [U¹³C, U²H]-glucose and of its metabolites in *E.coli* [236], for different growth conditions.

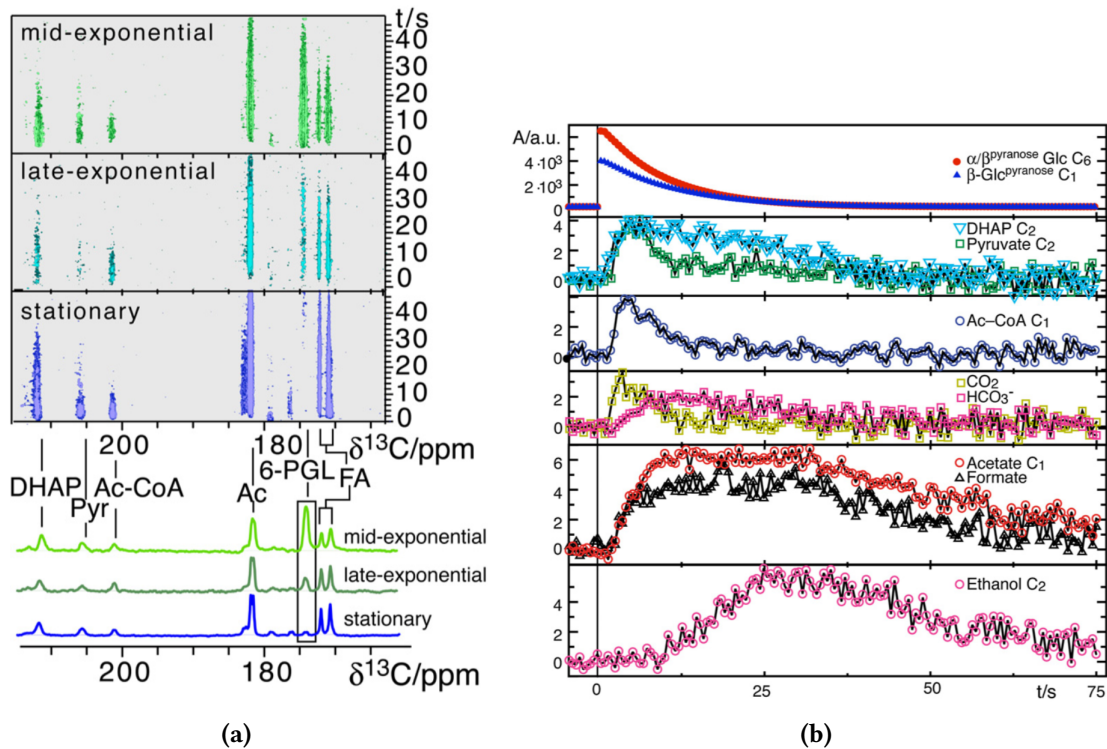


Figure 7.1: Figures taken from [236]. **7.1a** Comparison of glucose metabolism of *e.coli* BL21 in different growth conditions. The production of 6PGL seems reduce with the growth phase. **7.1a** Signal evolution of different detected metabolites.

A qualitative assessment of the metabolic state at the different growth phases was made (figure 7.1 adapted from ref. [236]).

In a similar perspective, we tried and improved our DDNP methodology to make it a tool able to assess the metabolic response of living cells prepared in various metabolic states to a rapidly changing environment, in the present case, a sudden glucose injection into the cell suspension. This involves performing and analyzing real-time kinetics of hyperpolarized substrates, such as $[\text{U-}^{13}\text{C}, \text{U-}^2\text{H}]$ -glucose and its metabolic products, in different cellular systems. Experiments were mainly performed on *E. coli* cells grown to different states, in order to study the adaptation of the metabolic response.

7.2 Materials and methods

7.2.1 Cell culture

E. coli K12 (DH10B) were stored in stock solutions of 30% glycerol at -80°C . When needed, frozen stock solutions were scrapped with sterile pipet cones to add bacteria to a 250 ml erlenmeyer flask containing 25 ml of rich lysogeny broth (LB) medium, they were grown over night at 37°C and 230 rpm shaker speed. Precultures were inoculated in 50 ml of LB medium contained in 500 ml erlenmeyer flasks to an optical density (OD) $\text{OD}_{600} < 0.4$, and grown at 37°C and 230 rpm shaker speed to the desired OD_{600} , which is proportional to the cell concentration in the culture, and is used to monitor the growth stage. For *E. coli*, OD_{600} of 1.0 corresponds to 8×10^8 cells/mL. Cells were harvested at different stages of the growth phase, immediately (\sim minutes) before the DDNP experiment is performed. The results presented in this chapter are from experiments performed on cell suspensions that were harvested at ODs ranging from 0.8 (early exponential growth phase, $\approx 6.4 \times 10^8$ cell/mL) to 2.8 (stationary phase, $\approx 2.24 \times 10^9$ cell/mL). Cells were harvested after centrifugation (3850 G-force for 5 minutes) and supernatants were discarded. Cell pellets were then washed in 2 mL of a 100 mM HEPES buffer pH 7.4, and resuspended in 0.5 mL of the same HEPES buffer and 35 μM EDTA. The cell suspension was then transferred into a 10 mm NMR tube moments before the DDNP experiment.

7.2.2 DNP setup and NMR

Glucose samples were prepared for DNP following a usual procedure [226]. A solution of $\text{H}_2\text{O}:\text{DMSO}:\text{D}_2\text{O}$ with a 15%:35%:50% volume composition was prepared, in which the polarizing agent TEMPOL (4-Hydroxy-TEMPO) was dissolved to reach a final concentration of 40 mM. $[\text{U}-^{13}\text{C}, \text{U}-^2\text{H}]$ -glucose was added to the sample to attain near-saturation conditions at a concentration of 5 M. Doubly ^2H , ^{13}C , labelled glucose was used in order to avoid too fast relaxation following dissolution. A $[\text{U}-^{13}\text{C}, \text{U}-^2\text{H}]$ -glucose stock solution with a concentra-

tion of 5 M was prepared for multiple DNP experiments. For each experiment a sample of 50 μL transferred to a PEEK sample holder was inserted in the cryostat, as described above (subsection 4.1.1 and ??), in contact with a bath of liquid helium where it solidifies as a glass.

DNP experiments were performed alternatively with two DNP polarizers operating at 6.7 T (Bruker prototype operating at 1.2 K and μwave irradiation at 187.9 GHz, and 350mW W of power) and 9.4 T (cryogen-free system with μwave frequency 263 ± 1 GHz and power=75 mW). The sample was hyperpolarized at ~ 1.27 K using a cross-polarization sequence to accelerate polarization buildup and to increase the steady-state polarization (see subsubsection 4.2.3.2). Steady-state polarization was typically reached in 50 min.

In both cases, μwave irradiation was modulated with a saw-tooth function over a range of 100 MHz with a modulation frequency of 1-2 kHz, in order to increase the saturation region of the EPR spectrum of the radicals, and thereby enhance the DNP efficiency.[250] Dissolution was achieved by flushing 5 mL of D_2O previously heated to 403 K at 10.5 bar onto the frozen hyperpolarized sample. The hyperpolarized solutions were transferred from the polarizer to the 400 MHz spectrometer (distant by ~ 5 -6 m from each other) upon Helium gas flow. Mixing of the hyperpolarized solution with the cell suspension takes place in a 10 mm NMR tube sitting inside the NMR spectrometer, typically began less than one second after dissolution and was complete after 3 seconds.

NMR spectra were recorded at $T = 310$ K on a 9.4 T *Avance III* Bruker spectrometer with a 10 mm BBO probe. Each DDNP experiment consisted in a series of 1D ^{13}C spectra with 10° read pulses. ^2H decoupling was performed in all experiments. Alternatively, ^1H decoupling was not used during acquisition in the post-DDNP (thermalized), but only in the reference samples used for the identification of the metabolites. In both cases, decoupling was achieved using a WALTZ16 pulse sequence.[159]

NMR FIDs were apodized with an 10-Hz exponential window, and zero filling was applied prior to Fourier transformation. Processing of the NMR data was performed using the NMRPipe software,[231] and the obtained spectra were exported to ascii format for peak integration using the Python library NMRglue.[232]

Exp	1	2	3	4	5	6	7	8*
OD ₆₀₀	0.8	0.9	1	1.4	2.4	2.5	2.8	1.7
	Early exponential			Late exp. & stationary				

Table 7.1: Experiments list - OD, optical density, and growth phase in the last line. *: an acidic jump stress factor was applied in this experiment.

7.3 DDNP study of glucose metabolism in *E. coli* K12

For the present study, eight DDNP experiments were performed, using cells grown along the same protocol, albeit harvested at different growth stages. The criterion used to distinguish between the growth stages was the measured OD₆₀₀ value of the culture medium. Thus, *E. coli* samples with OD₆₀₀ between 0.8 and 2.8 were used for 8 different experiments (see Table 7.1). In an additional experiment, an acidic jump to pH = 4 was applied to the cell suspension ~ 2 min before the dissolution experiment.

Our DDNP experiments typically yielded time-resolved series of hyperpolarized ¹³C spectra as shown in Figs. 7.2b and 7.2c. The most intense peaks originate from [U-¹³C, U-²H]-glucose, and were *ca.* two orders of magnitude larger than the remaining hyperpolarized ¹³C signals. The α and β anomers were monitored through the resonance frequencies of their anomeric carbons ¹³C₁ ($\delta(^{13}\text{C}_{1\alpha}) \approx 93$ ppm, $\delta(^{13}\text{C}_{1\beta}) \approx 95.5$ ppm). Additional resonances originating from various moieties present in the sample, and observed in these ¹³C DDNP spectra, were assigned in a rather straightforward manner thanks to the knowledge of the species involved in the glucose metabolism in *E. coli*, and their referenced chemical shifts: [33, 245] ethanol ($\delta(^{13}\text{C}_1) \approx 58$ ppm), acetate ($\delta(^{13}\text{C}_1) \approx 181.5$ ppm and $\delta(^{13}\text{C}_2) \approx 24$ ppm). These were consistently observed within seconds after complete in-situ mixing of the hyperpolarized glucose with the cell suspension in the NMR tube. Moreover, for acetate, ¹³C₁ and ¹³C₂ resonances were doublets with characteristic ¹J_{CC} carbon-carbon splittings. Comparison with spectra acquired on the same samples several minutes (~ 10 min) after each DDNP experiment, i.e. on spins at thermal equilibrium (TE), provided confirmation of the previous signal assignments and allowed one to identify additional resonances originating from metabolites that were not present yet in the DDNP experiments, thereby

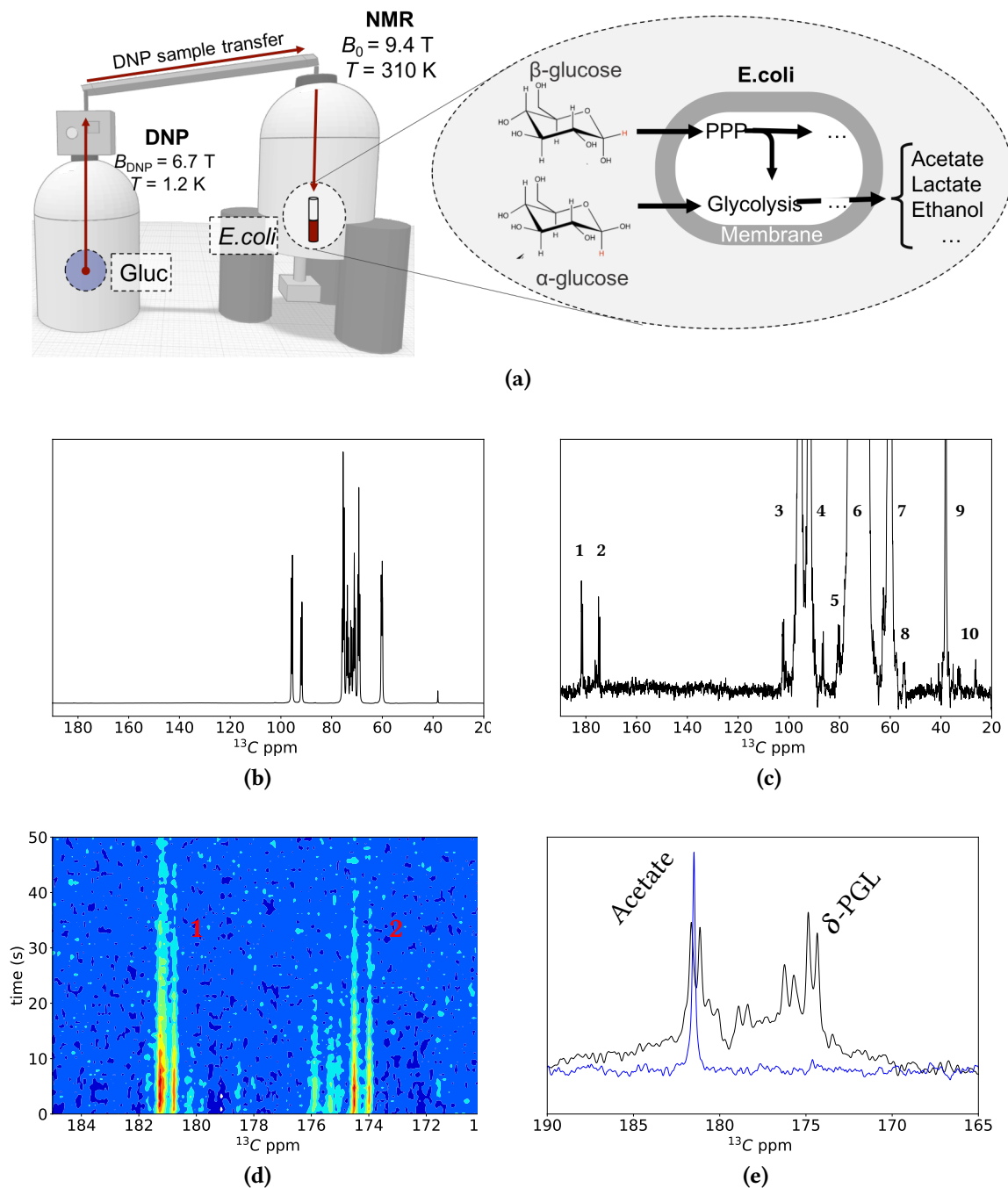


Figure 7.2: **7.2a:** Schematics of the set up used for the DDNP experiments (see text for details). **7.2b:** Typical ^{13}C DDNP spectrum experiment, third scan taken from experiment # 3 in Table 7.1. The signal originates principally from hyperpolarized glucose, whilst signals from metabolites are \sim two orders of magnitude smaller. **7.2c:** Peak assignment of the DDNP spectrum of exp # 3 in Table 7.1, the superposition of the first 20 scans in the DDNP experiment is displayed. Resonances 1 and 10 were assigned to $^{13}\text{C}_1$ and $^{13}\text{C}_2$ resonances of acetate. Peaks 3 and 4 correspond to the β and α $^{13}\text{C}_1$ anomeric carbon resonances of glucose, whilst labels 6 and 7 indicate the $^{13}\text{C}_{3-5}$ and $^{13}\text{C}_6$ atoms of glucose. Signals labeled 2 and 5 were tentatively assigned respectively δ -PGL which is the first product in the PPP and whereas the very weak unassigned doublets upfield by 1ppm and 4 ppm could correspond to the γ -PGL and the 6PGA directly issued from the δ -PGL. Finally, peak 8 was assigned to $^{13}\text{C}_1$ of ethanol, and peak 9 to DMSO which served for the chemical shift calibration at 39 ppm. **7.2d:** Time evolution of the carbonyl region of the ^{13}C spectrum upon hyperpolarized glucose pulse. **7.2e:** superposition of a sum of the first 20 one-dimensional spectra of exp # 3, acquired in a typical DDNP experiment (black) and the reference spectra of a sample of unlabeled Acetate (blue); both experiments performed at same pH (7.2) and temperature (310 K) conditions.

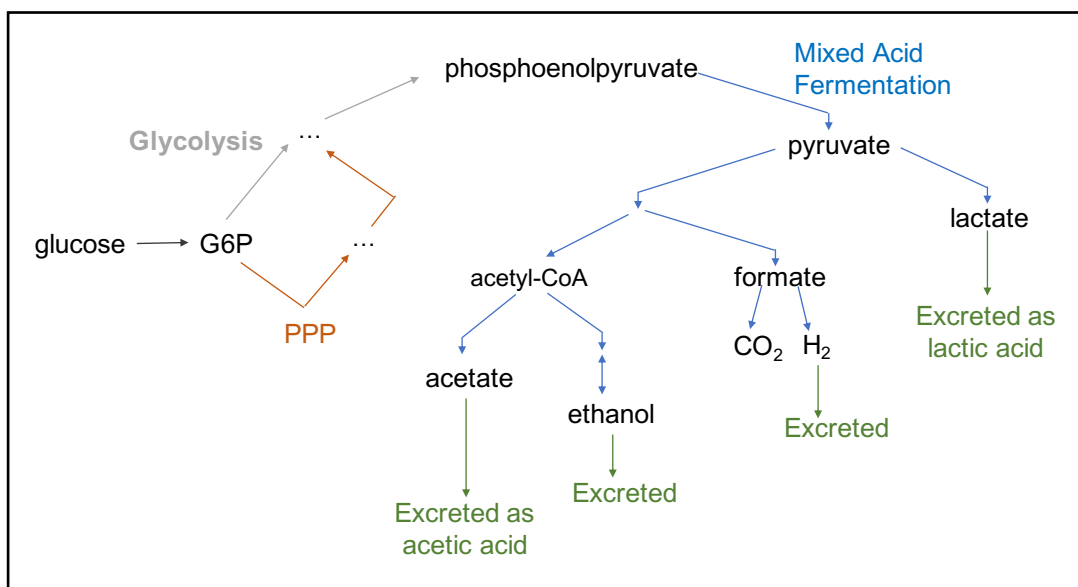


Figure 7.3: E. Coli K12 glucose metabolic pathways - Glycolysis feeds the Mixed Acid Fermentation pathway that leads to the production of multiple end chain metabolites. Only the metabolites of interest for the present study (lactate, formate, ethanol and acetate) - are indicated.[251]

indicating further evolution of the metabolite transformations beyond the DDNP experiment time window, i.e., on the time scale of minutes. One can additionally note that the same resonance peaks were observed in all of the experiments, thereby pointing to the overall repeatability of the experimental procedure. Assignments of lactate, acetate and formate in the DDNP and "post-DDNP" (NMR spectrum acquired in thermally polarized conditions immediately following the DDNP experiment) experiments were confirmed by comparison to reference ^{13}C spectra (figure 7.2e in the *Supplementary Information*).

The resonance doublet at ~ 182 ppm detected in the DDNP experiment was thus assigned to acetate, and the additional resonances appearing at ~ 184 ppm and ~ 171 ppm, in the "post-DNP" experiment, to the lactate doublet ($^1J_{CC}$) and the formate doublet ($^1J_{HC}$, no proton decoupling during the acquisition), respectively. This seemed to indicate that the production of lactate and formate by E. coli in our experiments occurred at a significantly later stage than acetate after the injection of hyperpolarized glucose. Finally, as ethanol was found to be also produced in the course of the DDNP experiment (Fig. 7.2c), it was inferred that acetate and ethanol were both produced at an earlier stage than lactate and formate. Note that resonance peaks were assigned based both on the knowledge of published chemi-

cal shifts, or available from databases[252] and of the glucose metabolic pathways that lead from its uptake by *E. coli* to the PPP, glycolysis, to various products of the mixed acid fermentation pathway. Indeed, the latter starts from phosphoenolpyruvate, produced through glycolysis, to yield lactate, formate, ethanol and acetate (for an extensive compilation of references on *E. coli* K12 metabolism, see ref. [253]). Note that neither CO₂ (125 ppm) nor HCO₃⁻ (161 ppm) were observed in our DDNP experiments. A schematic summary is depicted in Figure 7.3.

The remaining metabolite resonance observed in the carbonyl region of the ¹³C spectrum (~ 174 ppm) during the DDNP experiment matches that of the ¹³C₁ resonance of the δ -phosphogluconolactone (δ -PGL),[33] and the ¹J_{cc} = 43 Hz is identical to the one observed on a DDNP spectrum of δ -PGL enzymatically produced from glucose, and observed independently. This assignment is supported by the presence of a triplet corresponding to δ (¹³C₂) \approx 80 ppm) of δ -PGL with again ¹J_{cc} = 43Hz. The remaining δ -PGL resonances are buried under the glucose ¹³C₂₋₅ signals. However, the presence of δ -PGL in our experiments was rather surprising, as the latter is expected to be transformed into 6-phosphogluconic acid through the action of the 6-phosphogluconolactonase (6PGL) in the oxPPP.[254] Indeed, in the DDNP experiments performed by Meier and coworkers on *E. coli*, no δ -PGL could be observed in K12 strain whereas its accumulation was demonstrated on BL21 cells that lack the *pgl* gene encoding 6-phosphogluconolactonase. [245] However, it has been shown that a tenfold increase of δ -PGL production can be induced in K12 *E. coli* cells by a glucose pulse[255] . Such a fast increase of δ -PGL production could explain the early and transient accumulation of δ -PGL resonances in our experiments. Additional arguments supporting the presence of δ -PGL in the obtained DDNP spectra will be discussed below.

7.3.1 The decay rates of the α/β -glucose anomeric signals are markers of the cellular metabolic response to a glucose pulse

In an attempt to probe the metabolic state of the cells, we analyzed the kinetics of the decay of the DDNP-enhanced NMR signals of the injected glucose – the primary substrate in

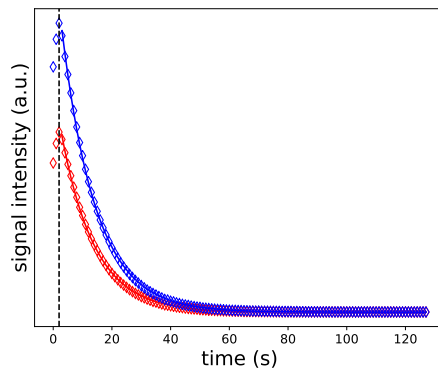


Figure 7.4: Typical $^{13}\text{C}_1$ signal evolution of the β (blue) and α (red) anomers of glucose (experiment 3 in Table 7.1, $\text{OD}_{600} = 1$). Experimental measurements (diamonds) acquired after complete injection of the hyperpolarized glucose sample (vertical dotted line) are fitted to an exponential (continuous line)

our experiments. Glucose is present in the extracellular medium only and absent from the cytosol, as it is phosphorylated upon cell intake, during transport through the cytoplasmic membrane, to yield glucose-6-phosphate (G6P).[256, 257] In addition, glucose signals are by far the most intense ones in these experiments and strategies targeting G6P were impeded by weak signal amplitudes. The (intracellular) G6P resonances were undetectable, and the doublet of $^{13}\text{C}_6$ was not observed (~ 63.5 ppm).

We investigated the possibility to use the observed decay rates of the extracellular α - and β -Glc signals as indicators of their relative uptake by the cells, and as markers of the cell metabolic response to a sudden excess of glucose, *given the growth (therefore metabolic) state* in which they were prepared. In all experiment, the $^{13}\text{C}_1$ signal intensities of both anomers exhibited clear exponential decays with time (see Fig. 7.4), consistent with the assumption of a pseudo first-order kinetic model of glucose uptake. The decay rates are the sum of the $^{13}\text{C}_1$ relaxation rate r_α (r_β) and α - (β -) glucose uptake rate k_α by *E. coli*: $r_{\alpha,\beta} + k_{\alpha,\beta}$. The longitudinal magnetization M_α of the $^{13}\text{C}_1$ of the α anomer therefore evolves with time as:

$$\frac{dM_\alpha(t)}{dt} = -r_\alpha M_\alpha(t) - k_\alpha M_\alpha(t) \quad (7.1)$$

(with a similar expression for M_β). The time evolution of the NMR signal is therefore:

$$S_\alpha(t) = \text{const} \times \cos^{n-1}(\theta) M_{z0,\alpha} e^{-(r_\alpha + k_\alpha)t} \times \sin(\theta) \quad (7.2)$$

where $M_{z0,\alpha}$ is the initial $^{13}\text{C}_1$ glucose magnetization, $cnst$ is a constant characteristic of the spectrometer, n is the number of experiments performed at time t , and θ is the read pulse flip angle. In order to study the anomeric uptake ratio in each experiment, we computed and fitted the signal ratio of glucose anomers with the following expression :

$$\frac{S_{\alpha}(t)}{S_{\beta}(t)} = \frac{M_{z0,\alpha}}{M_{z0,\beta}} e^{(-r_{\alpha}-k_{\alpha}+r_{\beta}+k_{\beta})t}, \quad (7.3)$$

from which the differences $(r_{\beta} + k_{\beta}) - (r_{\alpha} + k_{\alpha})$ between the global decay rates $r_{\alpha,\beta} + k_{\alpha,\beta}$ of the α and β $^{13}\text{C}_1$ signals, were extracted. These decay rates were then compared to a reference experiment performed on a sample of hyperpolarized glucose, in the absence of cells, giving access to the difference $r_{\beta} - r_{\alpha}$. The difference of the time constants obtained in an experiment performed in the presence of *E. coli* and the reference thus provided the anomeric differential uptake rates of glucose by the cells, $k_{\beta} - k_{\alpha}$. Results are summarized in Figure 7.5. Interestingly, in our experiments, the ratios $\frac{S_{\alpha}(t)}{S_{\beta}(t)}$ were linear in time in all experiments, indicating that the defined pseudo-first order kinetics of glucose uptake can be also analysed as a zero order, linear kinetics. The linear behaviour simply means that the approximation $e^x \sim 1 + x$ may also be used in our experiments.

It is seen that in experiments 1 to 3 (see Table 7.1), when cells are in early exponential phase and harvested at $\text{OD}_{600} \leq 1$, the difference $k_{\alpha} - k_{\beta}$ exhibits positive values. In contrast, in experiments #4-#8, where cells were grown to higher densities, with OD_{600} in the range 1.4 – 2.8 (late exponential or stationary phase, and possibly subject to an applied external stress, such as in experiment 8), lower, negative, differential anomeric glucose uptake rates $k_{\alpha} - k_{\beta}$ were consistently observed. Thus, when compared to experiments 1-3, these results suggest that the cell uptake of β -Glc is favored when cells are grown to higher cell densities, indicating significant changes in the glucose metabolism upon sudden exposure to a glucose excess. Thus, these experiments seemed to allow for the direct observation, in real-time, of the distinct roles of the α - and β - glucose anomers in the metabolism of *E. coli*.

The above discussion relies implicitly on the assumption that the different time evolu-

tions of the glucose anomers inside the cell can be monitored through the observation of the *extracellular* signal of glucose, and obey first order kinetics. This hypothesis implies that the uptake of glucose, which includes its transfer to the intracellular medium through the outer and cytoplasmic membranes, can be modeled as a simple first order kinetic process. This is supported by known facts of glucose uptake mechanism. Indeed, the diffusion of glucose through the outer membrane into the periplasmic space is a passive process that takes place through channels formed by the specialized, transmembrane porin proteins.[258, 259] It is then internalized into the cytoplasm of *E. coli* through the cytoplasmic membrane by an active mechanism involving the phosphoenolpyruvate:sugar Phospho-Transferase System (PTS).[256, 257] The PTS comprises an integral protein part and a soluble protein that combine their actions to simultaneously transfer α - and β - glucose anomers through the cytoplasmic membrane and phosphorylate them to yield intracellular G6P. In the perspective of our analysis, the crucial point is that this transfer is also known to have anomeric selectivity, which has been observed by NMR.[72] It has been suggested that glucose uptake by the PTS could be modeled by a two-site model where each site shows specificity towards a single anomer.[30] Moreover, as also shown in the latter reference, the approximation of a steady-state glucose:protein complex was made and, as cytosolic phosphate concentration was assumed constant, the irreversible phosphorylation step was modeled as a first-order kinetics.

The results of our analysis can be interpreted in the perspective of the relative metabolic fluxes of G6P towards the glycolysis and of the pentose phosphate pathway (PPP). Indeed, a number of studies have shown that glycolysis and the PPP are anomer selective.[260] Thus, the yeast glucose-6-phosphate dehydrogenase (G6PDH), the first enzyme of the PPP that transforms glucose-6-phosphate into δ -phosphogluconolactone has β -glucose specificity.[74] A direct proof of this result was shown recently, in more physiological conditions, using DDNP.[226] Such a specificity has also been demonstrated in such diverse organisms as human erythrocytes[261] and *Pseudomonas fluorescens*. [262] Alternatively, the first enzyme of the glycolysis pathway, the yeast glucose-fructose isomerase (PG-isomerase), has

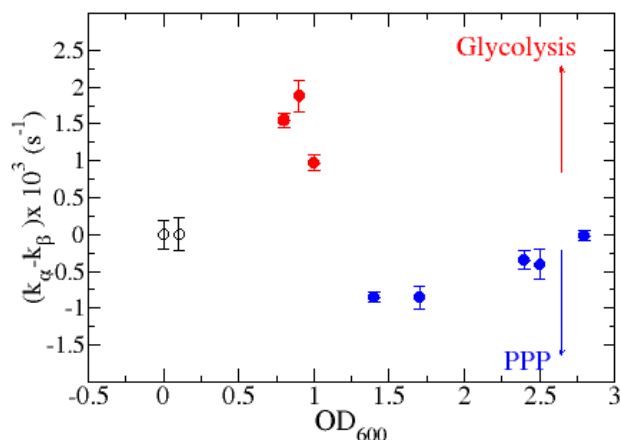


Figure 7.5: Uptake rate differences of glucose anomers extracted from experiments performed on cells grown to various OD stages. In red, values indicate larger α anomer uptake, and in blue, larger β anomeric consumption by the cell. Black empty circles indicate values obtained from two reference experiments. Values cluster in two clearly visible groups, according to $OD_{600} \leq \sim 1$ and $OD_{600} \geq \sim 1.5$. Error bars result from a Monte Carlo estimation.

an anomeric selectivity towards the α anomer of G6P.[74, 263] In the light of these facts, our observations suggest that the first key enzymes of the phosphoglucose metabolism in *E. coli*, G6PDH and PG-isomerase, also verify the properties evidenced in other species. The differential rates $k_{\alpha} - k_{\beta}$ obtained from the $^{13}\text{C}_1$ glucose signals, due to the substrate selectivity of these enzymes, therefore provide information on the relative consumption of both anomers by the cells, and indirectly inform on the relative activities of glycolysis and the PPP upon the applied glucose pulse.

These experiments exploit the large extra-cellular DDNP-polarized glucose signal to monitor the response to *E. coli* cells prepared following a well-codified protocol, to a dynamic perturbation achieved by the sudden injection of glucose. A number of studies have focused on the cell response to a single and sudden excess of glucose,[255] or to repetitive "feast-famine" cycles.[264] Such studies suggest that *E. coli* responds to glucose pulses by a large increase of the PPP flux, as would be needed to match the NADPH needs for cell growth.[255]. Thus, following the previous assumption, our *in vivo* DDNP studies point to the fact that the metabolic response to a glucose pulse induces a rerouting of the metabolic fluxes towards the PPP. In addition, higher cell densities are believed [265] to create anaero-

bic conditions and significant metabolic modifications. Hence, our results show consistency with recent findings that show metabolic flux rerouting of *E. coli* towards the PPP at later growth states, i.e., at higher ODs.[264]. Thus, information extracted from our experiments may also be relevant to the metabolic conditions of the cells prior to the DDNP experiment.

7.3.2 Quantitative kinetic analysis of metabolite signals

The time-resolved analysis of DDNP experiments is necessarily an empirical approach where the cell is treated as a "black box", and the output (metabolite) signal is obtained from the input (the substrate) through a transfer function that describes the combined effects of several metabolic pathways. Because of their weak intensities, with typical maximum signal-to-noise ratios on the order of $\approx 2 - 3$ only (see Fig. 7.6), a kinetic analysis could be performed for a pair of signals only, which, as mentioned above, were tentatively assigned to acetate and δ -PGL.

In all of our experiments, these signals were observed at very early times (~ 1 s after the beginning of the experiment, when the injection of the hyperpolarized solution is complete), attesting for their fast production by the cells. This observation is consistent with recent studies that suggest an immediate response of the cells to glucose pulses.[266] Moreover, their metabolism was assumed to be "saturated" by the very large glucose amount brought by the pulse during the time course of these experiments. Since the experiments are per-

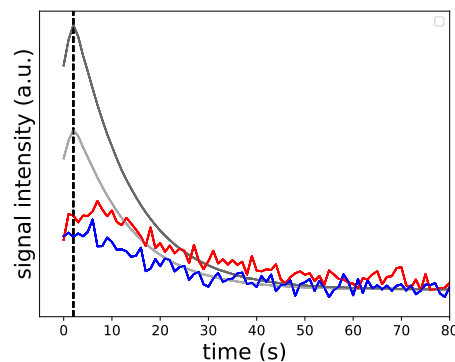


Figure 7.6: Signal evolution of $^{13}\text{C}_1$ for α and β anomers of glucose (in gray) compared to the signal evolution of Acetate (in red) and δ -PGL (in blue) multiplied by a factor of 200.

formed in a large excess of glucose and assuming that the cells are readily functioning at

full capacity, a simple kind of zero-order kinetic model, in which the production rate of the compound is independent of the concentration of the substrate, was implemented. The evolution of the z magnetization of a product, say, P_1 , thus writes:

$$\frac{dM_{zP_1}}{dt} = k_1 M_{z0,G} e^{-\rho_{P_1} t} - r_{P_1} M_{zP_1}(t) \quad (7.4)$$

In this equation, $M_{z0,G} = I_0 \times P_0$ is the initial glucose magnetization where I_0 is the concentration of hyperpolarized glucose, which is assumed constant during the DDNP experiment, P_0 is the initial glucose polarization, and r_{P_1} is the relaxation rate of the product. ρ_{P_1} represents an effective spin relaxation rate that accounts for the spin depolarization during transfer from the initially hyperpolarized glucose to the product, and k_1 is the kinetic constant of the overall process that transforms the hyperpolarized extracellular glucose into a product. From Eq. 7.4 one has:

$$M_{zP_1}(t) = k_1 I_0 P_0 \frac{e^{-r_{P_1} t} - e^{-\rho_{P_1} t}}{\rho_{P_1} - r_{P_1}}, \quad (7.5)$$

so that the NMR signal of the product is:

$$S_{P_1}(t) \propto k_1 I_0 P_0 \frac{e^{-r_{P_1} t} - e^{-\rho_{P_1} t}}{\rho_{P_1} - r_{P_1}} \times \cos^{n-1} \theta \times \sin(\theta), \quad (7.6)$$

where θ is the (constant) read pulse flip angle and n is the number of pulses performed at time t . Eq. 7.6 involves three parameters that define the evolution of the signal: r_{1P} , ρ_1 and $K_1 = \text{const} \times k I_0 P_0 \sin(\theta)$. The variations with time of the ^{13}C resonance peaks ($P_1 = \text{acetate}$ and $P_2 = \delta\text{-PGL}$) at 182 and 174 ppm were thus fitted to the model of Eq. 7.5. Experimental buildup curves of these signals and the associated fits are depicted in Figure 7.7. However, because of too weak signals, only four out of the eight experiments of table 7.1 were amenable to this quantitative analysis (experiments nb. 2, 3, 4, 7). It is clear from the model used that the values of the kinetic constants cannot be compared between different experiments. This is due to the fact that the absolute kinetics, i.e., the production

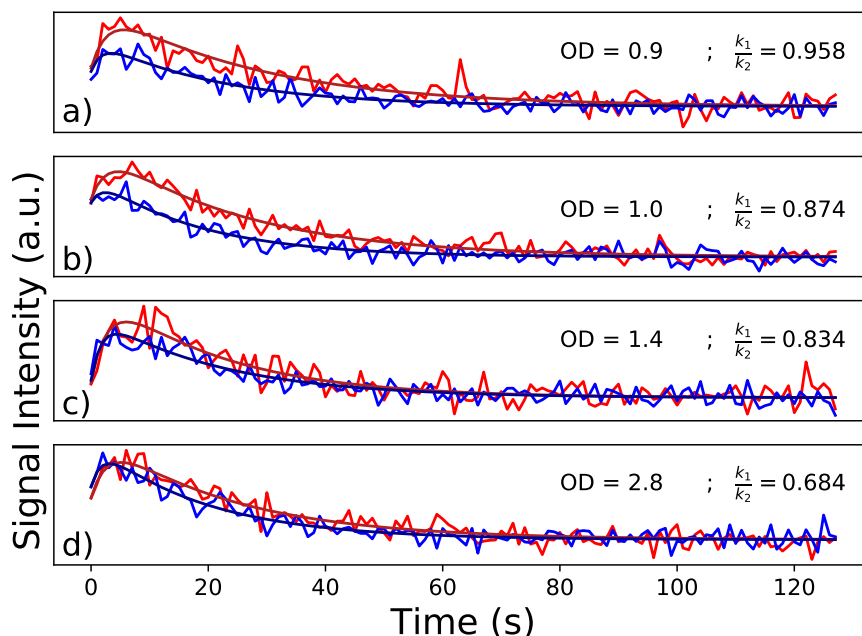


Figure 7.7: Variation of the metabolite signals with time. Experiments were performed on *E. coli* harvested at different stages of the culture growth, and characterized by their respective $OD_{600} = 0.9, 1.0, 1.4$ and 2.8 , respectively (from a) to d)). The associated ratios k_1/k_2 of the buildup rates of both monitored metabolites are indicated in the figure.

rate of the metabolites in the sample, cannot be disentangled from the absolute substrate concentration in the sample, which varies from one DDNP experiment to the other. However, following Eq. 7.6, the ratio of the kinetic rate constants of both products P_1 and P_2 , $\frac{k_{p1}}{k_{p2}}$, can be extracted from a single experiment, since the variation of glucose concentration is the same for both products. Although for experiments # 2, 3, 4, 7 the signals could be analyzed, the major source of error for the kinetic study remains the weak signal to noise ratio of the product's resonances. Hence, the significance of the buildup rate ratio $\frac{k_{p1}}{k_{p2}}$ of these metabolites was tested by a Monte Carlo (MC) simulation where the experimental uncertainty was estimated from the noise rmsd. Our analysis shows that this ratio varies significantly between experiments (Fig. 7.8a), and that $\frac{k_{p1}}{k_{p2}}$ seems to strongly correlate with the stage at which the bacteria were harvested from the culture medium, as monitored by its OD_{600} . This is shown in Fig. 7.8b. As discussed above, the signal at 182 ppm was assigned to the $^{13}\text{C}_1$ of acetate, whilst the peak located at 174 ppm was typical of the $^{13}\text{C}_1$ resonance of δ -PGL that is produced by oxidation of the G6P. However, one would expect

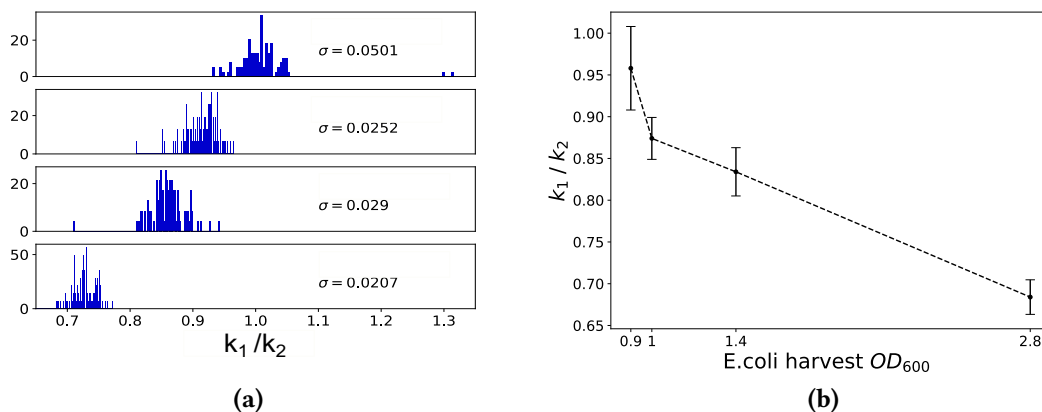


Figure 7.8: (7.8a): ratios of the kinetic parameters k_1/k_2 for (experiments 2, 3, 4, 7, from top to bottom). The parameter distributions were estimated using Monte Carlo simulations with simulated detection noise. The histogram shown in this plot results from 100 iterations; (7.8b): plot of kinetic parameter ratios as a function of the OD_{600} of the E.coli culture at harvest time. On the other experiments of table 7.1, signal intensities were too weak to be analyzed quantitatively by model of Eq. 7.6

to mainly observe 6-phosphogluconate (6PGA) instead, produced upon enzymatic hydrolyzation of δ -PGL by 6PGL. Note that a very weak signal at the chemical shift of 6PGA (~ 179.5 ppm) could be identified, as well as another one, hardly distinguishable from noise, at the expected chemical shift of γ -PGL (~ 178 ppm) was observed (see Fig. 7.2e).[33, 226]

In their work, Meier *et al.*[245] performed similar DDNP experiments on both BL21 and the K12 strains of E. coli. The genomes of these cell strains differ slightly, but with notable consequences for the case at hand, as BL21 cells, in contrast to K12, do not express the *ybhE* (*pgl*) gene encoding 6PGL. These authors clearly showed in DDNP experiments, that in the former strain, δ -PGL accumulated, whereas in the latter, 6PGA was readily observable, and δ -PGL remained undetected.

In the light of that work, the presence of δ -PGL signal in the ^{13}C DDNP spectra presented in the present study was rather puzzling. However, several contextual aspects of the present work seem particularly relevant to interpret our data:

- *The cells, at the beginning of the DDNP experiment, are in a partially anaerobic state.* This is attested by the early production of acetate, seconds after the mixing with the hyperpolarized glucose solution, as well as ethanol, both detected during the DDNP

experiment. Note, that formate and lactate were observed only several minutes later.

- *The DDNP experiment probes the metabolic response of cells prepared in a defined array of growth states to a glucose pulse, rather than the normal response of the metabolic state itself*- The sudden influx of (hyperpolarized) glucose perturbs the metabolic equilibrium, to which the cells oppose by a post-transcriptional response. Indeed, the production of the mixed-acid fermentation metabolites appear in the first seconds after injection. This delay is much shorter than the time needed for the implementation of enzyme synthesis by the cell, which is on the order of minutes.[267] Therefore, the observed metabolic response of *E. coli* relies on an enzyme content already present in the cells.
- *Recent studies that focused on the investigation of the metabolic phenotypes* of several *E. coli* strains under aerobic and anaerobic conditions showed the high variability of the metabolic fluxes in a number of basic pathways in the cell, including glycolysis, the PPP, the TCA cycle and mixed acid fermentation.[268] In particular, these authors have confirmed that the PGL flux (δ -PGL \rightarrow 6PGA reaction) in BL21 cells was zero. This is expected, as the BL21 *E. coli* strain lacks the *pgl* (or *ybhE*) gene. However, surprisingly, it was also reported that, whilst K12 cells (which have the *pgl* gene) exhibited a significant PGL flux in aerobic conditions, this dramatically decreased under anaerobic conditions to a similar value.
- Together, these elements suggest that at the time of dissolution, cells are in an anaerobic state where the 6PGL flux is too low to transform the rapidly produced δ -PGL into 6PGA, leading to a transient, weak, and very early accumulation of the former. The fact that this signal is absent from the post DDNP spectra attests for the efficient - but slower - response of the cell to the glucose pulse by enzyme synthesis.

Besides, the simultaneous production of hyperpolarized formate and acetate in reference [245] contrasts with our experiments that showed an early production of hyperpolarized acetate, whilst formate was only identified at a later stage, in the "post DDNP", thermally

polarized, spectrum acquired minutes after the DDNP experiments. Such differences may originate from different culture conditions, which can lead to highly different metabolic cell states. In this respect, it is noteworthy that, as shown in ref. [265] the measured OD_{600} value, which is the commonly used criterion to assess the growth state of the cells, only poorly correlates with their physiological state, which may not be reproducible for $OD_{600} \geq 0.3$. For these reasons, variations between experimental protocols that do not permit exact control of the metabolic state of the cells may also contribute to explain the apparent discrepancies between similar experiments.

The technique was able to provide valuable metabolic information through comparison of the *real-time* kinetics of both α -glucose and β -glucose uptake. The analyses of these experiments allowed us to relate the relative glucose uptake of each anomer by *E. coli* to the relative activities of glycolysis and the Pentose Phosphate Pathway (PPP) in the cell. Thus, the routing of glucose towards either of these two metabolic pathways of *E. coli* K12 when the cells are subject to a glucose pulse was shown to correlate well with the growth stage of the cells, as assessed by their OD_{600} (optical density at 600 nm).

We have shown that, in the absence of any available reference signals, the metabolite decay rate differences or ratios within a single experiment could be used as makers of the metabolic response of the cells to a single glucose pulse. Although a biological description was attempted, the major objective of this method is to empirically determine the correlations between the values of the previously defined markers and the metabolic state of *E. coli*.

Conclusion

The main goal of the work presented here was to achieve quantitative kinetic studies of metabolic reactions and pathways. Kinetic rates had therefore to be extracted from the resulting NMR data. During this work, based on the existing DDNP approach, we adapted strategies aiming at characterizing kinetic reactions having various degrees of complexity. These kinetic analyses involved finding normalization strategies of the different signal intensities in each experiment; simultaneous fitting of multiple experiments to better constrain model parameters; devising strategies to identify possible markers of the metabolic response. Limitations due to either technicalities of DDNP or the system complexity were identified and solutions to overcome them were proposed, both for *in vitro* observations of selected metabolic reactions and *in cellulo* "global" monitoring of the metabolism on living cells.

***In vitro* kinetic studies by DDNP**

In order to try and characterize *in vitro* enzymatic reactions of the first steps of the oxPPP, DDNP experiments were performed with changing the activity of one of the enzymes of the cascade, and by simultaneously analyzing of the experiments. Simultaneous fitting of the data of both experiments allowed to better constrain the model and to determine plausible values for several parameters. However, some remained undetermined, which Modeling DDNP studies of a complex reaction pathway required simplifying assumptions and approximations. Moreover, fitted enzyme activities showed inconsistencies, the origin of which was not unambiguously determined. These may be due, among others, to the use

of an oversimplified kinetic model. These limitations point to the necessity to improve the technique, but also to issues that are not specific of DDNP, rather to parameter estimation and data fitting in general.

A simplifying strategy was based on the direct use of $[U-^{13}C, U-^2H]G6P$ to study the kinetics of the G6P dehydrogenase. This involved the optimization of the purification procedure of enzymatically produced labelled G6P. DDNP experiments using different G6PDH activities, which allowed for the determination of the model parameters. In particular, the obtained values for the relaxation and the anomerization rates were also consistent with independent measurements. In particular, the anomerization rate of G6P was extracted from the data. To our knowledge, the value of the anomeric rates $\alpha \leftrightarrow \beta$ is scarcely documented once [75].

Reducing the complexity of the reaction network involved made its analysis easier, and opens the way to more complex modeling of the reaction mechanisms, including the cofactor concentration, for instance, sources of metabolic regulation.

In cell kinetic studies by DDNP

In principle, DDNP provides a unique means to monitor metabolic reactions in the cell in real time. The difficulty to extract quantitative kinetic parameters from the observed data still remains a challenge. In our *E. coli* experiments, we were able to relate the changes of the metabolic response of the cells changes to the growth phase of the cells. The study relied on the comparative *real-time* kinetics of both α - and β -glucose uptake. The analyses of these experiments allowed us to relate the relative glucose uptake of each anomer by *E. coli* to the relative changes of activities of glycolysis and the Pentose Phosphate Pathway (PPP) in the cell. Thus, the routing of glucose towards either of these two metabolic pathways of *E. coli* K12 was shown to correlate well with the growth stage of the cells, as assessed by their OD_{600} (optical density at 600 nm). Alternatively, the analysis of the compared real-time evolution of a couple of glucose metabolites showed that these provide an intrinsic marker of the glucose metabolic response to the sudden (hyperpolarized) glucose exposure.

Again, the signal evolution of two products in multiple experiments was fitted together and markers of metabolic states were defined out of extracted kinetic parameters.

This analysis is based on the comparison of kinetic rate ratios extracted from different experiments. These quantities are not affected by possible fluctuations of the polarization levels or polarization losses during the dissolution or injection stages, from experiment to experiment. This approach, a limited set of experiments (< 10), therefore suggests the possibility to perform comparative studies of kinetics on cells, and may provide a way to increase the reliability of the DDNP method as a time-resolved, quantitative technique. Preliminary developments of this in-cell approach to different substrates and cellular systems are shown in an appendices [Appendix B](#) and [Appendix C](#) of this manuscript. exemple

Appendix A

DNP mechanisms

The different polarization transfer mechanisms in DNP rely on the dipolar interactions between electrons and nuclear spins. Here we introduce the interactions related to DNP polarization transfer from electron to nuclear-spins. Additionally, a brief description of the DNP mechanisms will be given, focusing mainly in TM mechanism.

A.1 Dipolar interactions and spectral diffusion

In typical DNP samples, the distances between electrons are so large that their spatial wave functions do not overlap, so that Fermi-contact interactions can be neglected. In the dipolar interaction for two electron spins, the magnetic moment of a spin S induces a magnetic field $\mathbf{B}_S(\mathbf{r})$ at position \mathbf{r}'_S of S' , expressed as [269]:

$$\mathbf{B}_S(\mathbf{r}) = -\frac{\mu_0}{4\pi} \left(\frac{\boldsymbol{\mu}_S}{r^3} - 3\frac{(\boldsymbol{\mu}_S \cdot \mathbf{r})\mathbf{r}}{r^5} \right) = -\frac{\mu_0}{4\pi} \hbar\gamma_S \left(\frac{\mathbf{S}}{r^3} - 3\frac{(\mathbf{S} \cdot \mathbf{r})\mathbf{r}}{r^5} \right) \quad (\text{A.1})$$

where $\mathbf{r} = \mathbf{r}_S - \mathbf{r}'_{S'}$, is the vector that connects the two particle positions so that $r = |\mathbf{r}|$ is the distance between them, $\mu_0 = 4\pi \times 10^{-7}$ is the permeability of the vacuum. The electron-electron dipolar Hamiltonian is thus:

$$\mathcal{H}_{SS'} = -\mathbf{B}_S \cdot \boldsymbol{\mu}_{S'} = -\hbar\gamma_S \mathbf{B}_S \cdot \mathbf{S}' = \hbar\mathbf{S} \cdot \mathbf{D} \cdot \mathbf{S}' \quad (\text{A.2})$$

with:

$$\mathbf{D} = \frac{\mu_0}{4\pi} \hbar \gamma_S^2 \left(\frac{1}{r^3} - 3 \frac{\mathbf{r}\mathbf{r}}{r^5} \right) \quad (\text{A.3})$$

where \mathbf{D} is the electron-electron dipolar operator. Note that DNP experiments are performed in solid samples so that nuclear inter-spin distances are fixed and so \mathbf{r}_I and \mathbf{r}'_I positions can be defined. Similarly, the dipolar Hamiltonian for the nuclear spins is:

$$\mathcal{H}_{II'} = -\mathbf{B}_I \cdot \boldsymbol{\mu}_{I'} = -\hbar \gamma_S \mathbf{B}_I \cdot \mathbf{I}' = \hbar \mathbf{I} \cdot \mathbf{C} \cdot \mathbf{I}' \quad (\text{A.4})$$

where,

$$\mathbf{C} = \frac{\mu_0}{4\pi} \hbar \gamma_I^2 \left(\frac{1}{r^3} - 3 \frac{\mathbf{r}\mathbf{r}}{r^5} \right) \quad (\text{A.5})$$

is the operator for the nuclei-nuclei dipolar interaction, where the tensor $\mathbf{r}\mathbf{r}$ is :

$$\mathbf{r}\mathbf{r} = \begin{pmatrix} r^2 - 3xx & -3xy & -3xz \\ -3yx & r^2 - 3yy & -3yz \\ -3zx & -3zy & r^2 - 3zz \end{pmatrix} \quad (\text{A.6})$$

so that:

$$\mathbf{D} = \frac{\mu_0}{4\pi} \frac{\hbar \gamma_S^2}{r^5} \begin{pmatrix} r^2 - 3xx & -3xy & -3xz \\ -3yx & r^2 - 3yy & -3yz \\ -3zx & -3zy & r^2 - 3zz \end{pmatrix} = \begin{pmatrix} D_{xx} & D_{xy} & D_{xz} \\ D_{yx} & D_{yy} & D_{yz} \\ D_{zx} & D_{zy} & D_{zz} \end{pmatrix} \quad (\text{A.7})$$

and similarly for \mathbf{C} .

A.1.0.1 Spectral diffusion

Dipolar coupling between spins can induce flip-flop transitions that propagate throughout the spin ensemble and is responsible for spectral diffusion, of major importance for several DNP processes. For nuclear spins, $\mathcal{H}_{II'}$ permits the transport of polarization among nuclei in the sample, whereas for the electron spin system, efficient spectral diffusion increases the diffusion of μ -wave saturation, of crucial importance for thermal mixing mechanism that

will be introduced below.

To better understand the transitions induced by spectral diffusion, $\mathcal{H}_{SS'}$ is expressed in terms of the step operators $S_{\pm} = S_x \pm iS_y$ and $I_{\pm} = I_x \pm iI_y$. For an isolated pair of spins, we have:

$$\begin{aligned} \mathcal{H}_{SS'} = \hbar [& D_{zz} S_z S'_z + \frac{1}{2} D_{z+}^* (S_z S'_+ + S_+ S'_z) + \frac{1}{2} D_{z+} (S_z S'_- + S_- S'_z) \\ & + \frac{1}{4} (D_{++}^* S_+ S'_+ + D_{++} S_- S'_-) + \frac{1}{4} D_{+-} (S_- S'_+ + S_- S'_-)] \end{aligned} \quad (\text{A.8})$$

where the notations $D_{z+} = D_{zx} + iD_{zy} = D_{z-}^*$, $D_{++} = D_{xx} - D_{yy} + 2iD_{xy} = D_{--}^*$, and $D_{+-} = D_{xx} + D_{yy} = -D_{zz}$ have been introduced. Only the terms containing S_{\pm} and S'_{\pm} in this Hamiltonian induce transitions. The Hamiltonian defining the system of two dipolarly-coupled electron spins has also to consider Zeeman interactions and is therefore:

$$\mathcal{H} = \mathcal{L}_S + \mathcal{L}_{S'} + \mathcal{H}_{SS'} = \hbar [\omega_{0S} (S_z + S'_z) + \mathbf{S} \cdot \mathbf{D} \cdot \mathbf{S}'] \quad (\text{A.9})$$

where the first two terms represent the Zeeman interactions for spins S and S' . The dipolar hamiltonian $\mathcal{H}_{SS'}$ induces transitions between the 4 perturbed eigenstates of the two-spin system S, S' with the energy values displayed in table A.1. According to perturbation theory

$ m_S, m'_{S'}\rangle$	
$ -\frac{1}{2}, -\frac{1}{2}\rangle$	$\omega_{0S} + \frac{1}{4} D_{zz}$
$ +\frac{1}{2}, -\frac{1}{2}\rangle$	$-\frac{1}{4} D_{zz}$
$ -\frac{1}{2}, +\frac{1}{2}\rangle$	$-\frac{1}{4} D_{zz}$
$ +\frac{1}{2}, +\frac{1}{2}\rangle$	$-\omega_{0S} + \frac{1}{4} D_{zz}$

Table A.1: Eigenvalues (right) of the eigenstates (left), of the dipolarly coupled system of electron spins S and S' .

only the parts of the hamiltonian that do not induce a change of the total magnetic number contribute to the splitting of the energy levels, to first order. One may therefore neglect in eq. A.10 the transitions at $\hbar\omega_{0S}$ or $2\hbar\omega_{0S}$, and retain only transitions between $|+\frac{1}{2}, -\frac{1}{2}\rangle$ and $|-\frac{1}{2}, +\frac{1}{2}\rangle$. These flip-flop transitions also allow for the spin diffusion, in multiple spin

systems. The resulting secular Hamiltonian is thus:

$$\mathcal{H} = \mathcal{L}_S + \mathcal{L}_{S'} + \mathcal{H}_{SS'} = \hbar[\omega_{0S}S_z + \omega_{0S'}S'_z + D_{zz}S_zS'_z + \frac{1}{4}D_{+-}(S_+S'_- + S_-S'_+)] \quad (\text{A.10})$$

The Hamiltonian in equation A.10 can be further simplified by ignoring the term $D_{zz}^{ij}S_z^iS_z^j$ (with the change of notations $S \rightarrow S^i$ and $S' \rightarrow S^j$) which merely shifts the different energy levels without inducing transitions:

$$\mathcal{H} = \hbar[\omega_S^iS_z^i + \omega_S^jS_z^j + \frac{1}{4}D_{+-}(S_+^iS_-^j + S_-^iS_+^j)] \quad (\text{A.11})$$

The matrix representation of this Hamiltonian is :

$$\mathcal{H} = \frac{1}{2}\hbar \begin{pmatrix} \omega_S^i + \omega_S^j & 0 & 0 & 0 \\ 0 & \omega_S^i - \omega_S^j & D_{+-}^{ij} & 0 \\ 0 & D_{+-}^{ij} & -(\omega_S^i - \omega_S^j) & 0 \\ 0 & 0 & 0 & -(\omega_S^i + \omega_S^j) \end{pmatrix} \quad (\text{A.12})$$

When we described how was constituted the EPR line for a given radical, we talked about "homogeneous broadening" which induced fluctuation of ω_S in time, in a range of Δ_h . Since the fluctuations of ω_S^i and ω_S^j are not correlated the difference $\omega_S^i - \omega_S^j$ (appearing in the diagonal terms of the matrix) also fluctuates. The total fluctuation is composed by the convolution of ω_S^i 's and ω_S^j 's individual fluctuations and has a width Δ_{SS} . Additionally, the intensities of the non-diagonal terms in A.12 depend on the coupling of the electron with one single particle, the second electron, and is normally less intense than the convoluted fluctuations of ω_S^i and ω_S^j in the range Δ_{SS} . Thus it may be assumed that $\frac{1}{4}\hbar D_{+-}^{ij} \ll \Delta_{SS}$, which means that the dipolar interaction can produce a flip-flop transition if the fluctuations of the field are more intense than the interaction itself. As shown in [187], the flip-flop transitions are much more more likely more likely if the difference between ω_S^j and ω_S^i is smaller than Δ_h , hence expressing the conservation of energy.

In conclusion, spectral diffusion is a process that relies on flip-flop transitions that are

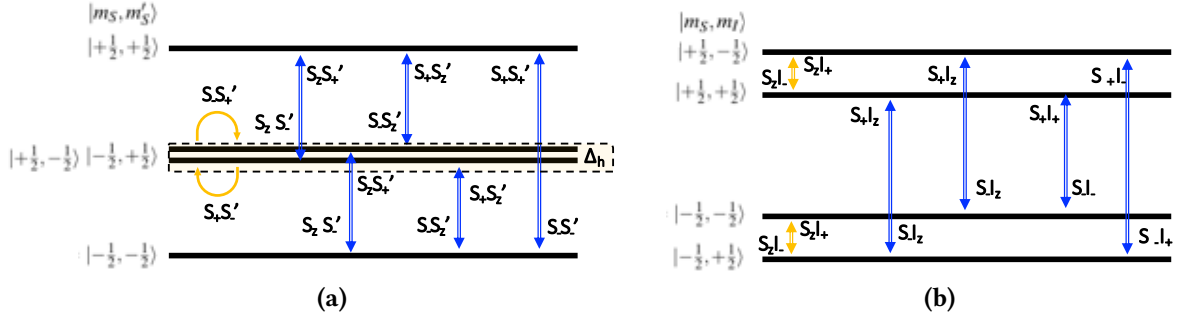


Figure A.1: Diagram of the transitions induced by dipolar couplings. **a)** Electron dipolar interaction, for a system of two electrons where $|\omega_S - \omega'_S| \leq \Delta_h$, allowed transitions are represented in yellow. **b)** Hyperfine interaction where the transitions in yellow are allowed if $\omega_{0I} \sim \Delta_h$

allowed even without μ -wave irradiation. Spectral diffusion couples a spin to a neighboring one and induces transitions of electrons with close precession frequencies, in the range Δ_{SS} .

A.1.0.2 Hyperfine coupling

The coupling between nuclei and electrons is due to the hyperfine or super-hyperfine interactions. As mentioned above, Fermi-type interactions are neglected, and so the associated Hamiltonian writes:

$$\mathcal{H}_{SI} = -\mathbf{B}_S \cdot \boldsymbol{\mu}_I = -\hbar \gamma_I \mathbf{B}_S \cdot \mathbf{I} = \hbar \mathbf{S} \cdot \mathbf{A} \cdot \mathbf{I} \quad (\text{A.13})$$

$$\mathbf{A} = \frac{\mu_0}{4\pi} \hbar \gamma_I \gamma_S \left(\frac{1}{r^3} - 3 \frac{\mathbf{r}\mathbf{r}}{r^5} \right) \quad (\text{A.14})$$

where $\mathbf{r} = \mathbf{r}_S - \mathbf{r}_I$, is the inter-spin distance.

After including the Zeeman interactions and using the secular approximation, the hyperfine Hamiltonian simplifies to:

$$\mathcal{H} = \mathcal{L}_S + \mathcal{L}_I + \mathcal{H}_{SI} = \hbar [\omega_{0S} S_z + -\omega_{0I} I_z + A_{zz} S_z I_z + \frac{1}{2} A_{z-} S_z I_+ + \frac{1}{2} A_{z+} S_z I_-] \quad (\text{A.15})$$

The two rightmost terms on the Hamiltonian contain the step operators I_{\pm} that are responsible for transitions of the type $|m_I\rangle = |-\frac{1}{2}\rangle \iff |+\frac{1}{2}\rangle$, in orange in figure A.1b. These transitions require amounts of energy in the order of $\hbar \omega_{0I}$ that are typically three orders of magnitude smaller than $\hbar \omega_{0S}$. The energy is provided by the hyperfine interaction, which

can match the nuclear Zeeman energy under particular conditions, for more information see ???. Hence, in order to increase the rate of transitions between nuclear Zeeman levels we need to introduce a supplementary source of energy. As a matter of fact, the combined effect of μ -wave irradiation and the hyperfine interaction could induce such transitions. Moreover, as we will see in the next section, the introduction of a third electronic spin to the system can also increase the rate at which transitions are induced between the nuclear Zeeman levels.

In order to describe the complete set of interactions governing DNP process, we need to group all the previously introduced interactions and the μ -wave irradiation. Hence, we define a Hamiltonian considering Spectral diffusion, hyperfine and super-hyperfine interactions, and μ -wave irradiation and we obtain:

$$\mathcal{H} = \mathcal{L}_S + \mathcal{L}_I + \mathcal{H}_m + \mathcal{H}_{SI} + \mathcal{H}_{SS'} + \mathcal{H}_{II'} \quad (\text{A.16})$$

This Hamiltonian contains all possible interactions involved in DNP transfer. However, the polarization process depends on various factors, such as the nature of the radical, the composition of the sample, and on different thermodynamic parameters. Depending on the sample, the different interactions cooperate giving raise to different DNP mechanisms.

A.1.1 Solid Effect

Of the various DNP mechanisms, the 'Solid Effect' (SE), described in 1957, represents the first DNP theory able to account for hyperpolarization experiments [270], [271], [272]. We only briefly present this mechanism, a simplified diagram of which is depicted in figure A.2. It relies on a μ -wave irradiation that is tuned at $\omega_m = |\omega_S - \omega_I|$ frequency and induces simultaneous spin flips of an electron and the nuclear spin to which it is coupled. Hence, when the irradiation is tuned at the good frequency the combined effort of the μ -wave irradiation and the hyperfine coupling induce the simultaneous flip of the electron and the nuclear spin.

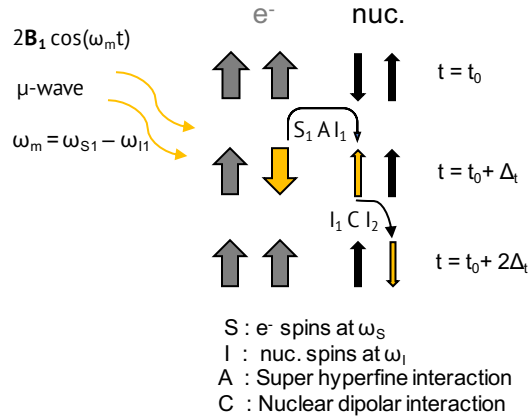


Figure A.2: SE mechanism. At t_0 , the sample is at equilibrium with electrons almost fully polarized (99%). When the μ -wave irradiation starts (at $t_0 + \Delta_t$), both the interaction of an electron with the μ -wave field and the super hyperfine coupling, produce the simultaneous flip-flop of a coupled electron and nuclear spins. Subsequently, the spin flip is diffused to the rest of the nuclear spin population by nuclear dipolar interactions (i.e. nuclear spectral diffusion). Then, the electron spins relax and the process starts again. The efficient polarization transfer of this process depends strongly on the μ -wave irradiation frequency to match SE conditions.

Since the electron spin-lattice relaxation time is much shorter than the one of the nucleus, the electron spin returns to its lower energy state in a short time and can thus polarize another nucleus and so on. Additionally, the polarization can be diffused throughout the rest of the nuclear spin population by nuclear spin diffusion, see figure A.2.

The solid effect depends strongly on the irradiation frequency of the μ -wave. If the condition $\omega_m \approx \omega_S - \omega_{0I}$ is met, the solid effect induces a flip-flop transition (electron spin flip, nuclear spin flop), whereas if $\omega_m \approx \omega_S + \omega_{0I}$, the solid effect induces flip-flip transitions. Finally, in case $\omega_m \approx \omega_S$ the EPR line at ω_m but no nuclear spin transition is induced.

Other DNP mechanisms involve three-spin processes, two electronic and one nuclear spin, those mechanisms are said to rely on triple spin flips, notably Cross Effect (CE) and Thermal Mixing (TM). The difference between these mechanisms is still a subject of discussion. However, some principal features specific to TM have been identified and will be described above.

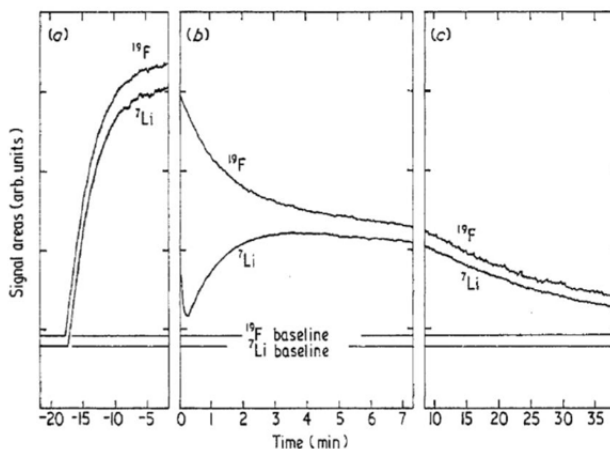


Figure A.3: Figure from M. Goldman and coworkers publication [196]. Figure taken from [196]. NMR signal evolution of lithium and fluorine nuclei in a DNP sample. At time 0 μ -wave irradiation is stopped and ^7Li NMR signal is saturated. The signal evolution is monitored and shows that there is a polarization transfer from ^{19}F to ^7Li causing a build-up of ^7Li NMR signal after saturation. Eventually both signals decay following longitudinal relaxation.

A.2 Thermal Mixing mechanism

In 1973, Goldman and co-workers [196] studied the transfer of polarization between two different nuclear spin systems present in a sample during a DNP experiment. The experiment consisted on hyperpolarizing crystals of lithium fluoride to monitor the time evolution of the NMR signals of lithium and fluorines. At some point (time 0 in figure A.3), the μ -wave irradiation was stopped and one of the NMR signals was saturated. Following the saturation of the lithium resonance, a build-up was observed in parallel with the fluorine signal decay (figure A.3). This was explained in thermodynamic terms as the existence of a thermal contact between lithium and fluorine energy spin reservoirs that allowed polarization flowing between them. The associated DNP mechanism was hence termed Thermal Mixing in analogy with thermodynamics.

A.2.1 Triple spin flips

The elementary process involved in thermal mixing is the coupling between two electron spins S^j , S^i and one nuclear spin I . This coupling can induce a transition of a nuclear spin, thereby transferring electron spin polarization to nuclei. Such a process is termed a triple

$ m_S^i, m_S^j, m_I\rangle$	
$ +\frac{1}{2}, +\frac{1}{2}, -\frac{1}{2}\rangle$	$\omega_{++-} = +\frac{1}{2}(\omega_S^j - \omega_S^i) + \frac{1}{2}\omega_{0I}$
$ +\frac{1}{2}, +\frac{1}{2}, +\frac{1}{2}\rangle$	$\omega_{+++} = +\frac{1}{2}(\omega_S^j - \omega_S^i) - \frac{1}{2}\omega_{0I}$
$ +\frac{1}{2}, -\frac{1}{2}, -\frac{1}{2}\rangle$	$\omega_{+--} = +\frac{1}{2}(\omega_S^j - \omega_S^i) + \frac{1}{2}\omega_{0I}$
$ +\frac{1}{2}, -\frac{1}{2}, +\frac{1}{2}\rangle$	$\omega_{+-+} = +\frac{1}{2}(\omega_S^j - \omega_S^i) - \frac{1}{2}\omega_{0I}$
$ -\frac{1}{2}, +\frac{1}{2}, -\frac{1}{2}\rangle$	$\omega_{-+-} = -\frac{1}{2}(\omega_S^j - \omega_S^i) + \frac{1}{2}\omega_{0I}$
$ -\frac{1}{2}, +\frac{1}{2}, +\frac{1}{2}\rangle$	$\omega_{-++} = -\frac{1}{2}(\omega_S^j - \omega_S^i) - \frac{1}{2}\omega_{0I}$
$ -\frac{1}{2}, -\frac{1}{2}, -\frac{1}{2}\rangle$	$\omega_{---} = -\frac{1}{2}(\omega_S^j - \omega_S^i) + \frac{1}{2}\omega_{0I}$
$ -\frac{1}{2}, -\frac{1}{2}, +\frac{1}{2}\rangle$	$\omega_{--+} = -\frac{1}{2}(\omega_S^j - \omega_S^i) - \frac{1}{2}\omega_{0I}$

Table A.2: Eigenvalues (right) of the different eigenstates (left). States given for the triple spin flip system (two electron spins one nuclear spin).

spin flip. The relevant hamiltonian for the description of three-spin processes is:

$$\mathcal{H} = \hbar[\omega_S^i S_z^i + \omega_S^j S_z^j - \omega_{0I} I_z + \frac{1}{4}D_{+-}(S_+^i S_-^j + S_-^i S_+^j) + \frac{1}{2}(A_{z-} S_z^i I_+ + A_{z+} S_z^i I_-)] \quad (\text{A.17})$$

which, in the interaction representation with respect to the electron spin S^j gives:

$$\mathcal{H} = \hbar[(\omega_S^i - \omega_S^j) S_z^i - \omega_{0I} I_z + \frac{1}{4}D_{+-}(S_+^i S_-^j + S_-^i S_+^j) + \frac{1}{2}(A_{z-} S_z^i I_+ + A_{z+} S_z^i I_-)] \quad (\text{A.18})$$

The energy level for every state of this Hamiltonian are displayed in table A.2. The matrix can be split into three blocks:

$$\begin{aligned} & \frac{1}{2}\hbar \begin{pmatrix} (\omega_S^j - \omega_S^i) + \omega_{0I} & -\frac{1}{2}A_{z-} \\ -\frac{1}{2}A_{z+} & (\omega_S^j - \omega_S^i) - \omega_{0I} \end{pmatrix} \\ & \frac{1}{2}\hbar \begin{pmatrix} (\omega_S^j - \omega_S^i) + \omega_{0I} & \frac{1}{2}A_{z+} & \frac{1}{2}D_{+-} & 0 \\ \frac{1}{2}A_{z-} & (\omega_S^j - \omega_S^i) - \omega_{0I} & 0 & \frac{1}{2}D_{+-} \\ \frac{1}{2}D_{+-} & 0 & -(\omega_S^j - \omega_S^i) + \omega_{0I} & -\frac{1}{2}A_{z+} \\ 0 & \frac{1}{2}D_{+-} & -\frac{1}{2}A_{z-} & -(\omega_S^j - \omega_S^i) - \omega_{0I} \end{pmatrix} \\ & \frac{1}{2}\hbar \begin{pmatrix} -(\omega_S^j - \omega_S^i) + \omega_{0I} & -\frac{1}{2}A_{z-} \\ -\frac{1}{2}A_{z+} & -(\omega_S^j - \omega_S^i) - \omega_{0I} \end{pmatrix} \end{aligned} \quad (\text{A.19})$$

For both of the two 2×2 submatrices, the energy difference between the diagonal terms is $\pm \hbar \omega_{0I}$. On the other hand, the 4×4 matrix can provide such a compensation if the condition $(\omega_S^j - \omega_S^i) = \pm \omega_{0I}$ is met. However, a third spin, the second electron, is necessary in this case. Such, a triple spin flip can occur if $\omega_S^j \approx \omega_S^i - \omega_{0I}$, or if, $\omega_S^j \approx \omega_S^i + \omega_{0I}$. Also, remember that, ω_S^i and ω_S^j fluctuate in time in a range of Δ_h . Hence, the energy of dipolar coupling between the two electrons needs to match the nuclear Larmor frequency, in a range up to Δ_h . There are two different kinds of transitions related to the non diagonal terms of this matrix:

- The first case, $\omega_S^j \approx \omega_S^i - \omega_{0I}$ of transition produces a triple spin flip and allows the thermal mixing to happen. The terms proportional to $S_+^i I_+$ and to $S_-^i I_-$ induces the transitions and its related to the hyperfine interaction.
- The second case happens when $\omega_S^j \approx \omega_S^i + \omega_{0I}$. In this case the terms proportional to $S_+^i I_-$ and $S_-^i I_+$ produce the triple spin flip.

There is a third possible transition that does not induce triple spin flips but only an electronic flip-flop transitions. When $\omega_S^j \approx \omega_S^i$, the term $\frac{1}{2} D_{+-} (S_+^i + S_-^i)$ induces this electronic transitions. This is related only to the dipolar interaction between electrons.

A.2.1.1 Cross effect

The Cross Effect (CE) was first introduced by Kessenikh and coworkers in 1963 [193] and has been largely studied and discussed since [192, 194, 186]. A discussion of the difference between CE mechanisms and TM is beyond the scope of this manuscript. However, some descriptions have given a hint on what might define the efficiency of both CE and TM.

CE relies on the saturation of the allowed triple spin flip transitions by the μ -wave irradiation that rely on the condition $\Delta_{EPR} \leq \omega_{0I}$. The latter implies that CE (as for triple spin flips mechanisms in general) depends on the width of the EPR line [195]. Thus, when the inhomogeneous linewidth Δ_{EPR} is such that $\omega_{0I} < \Delta_{EPR}$, CE becomes an efficient DNP mechanism. As a matter of fact, the transitions in CE come from the saturation produced by the μ -wave

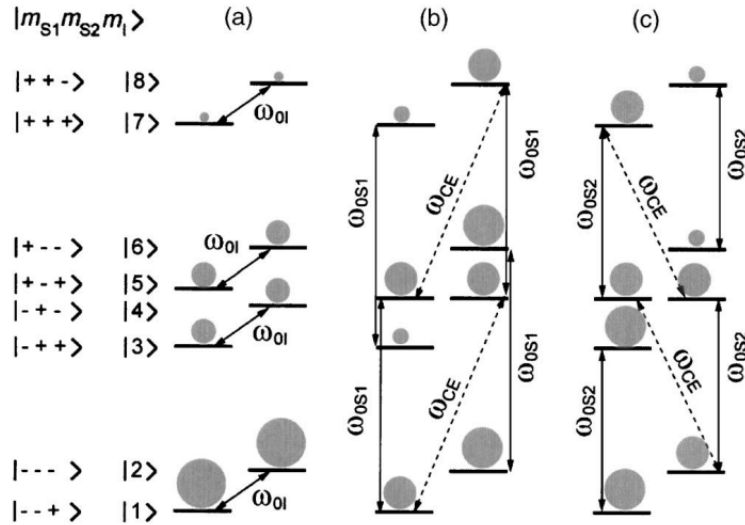


Figure A.4: Figure taken from [195]. **a** Population distribution for a conventional three spin system. **b** Population distribution for a system matching CE conditions, μ -wave irradiation saturates the transition for the first electron producing a nuclear negative polarization. **c** μ -wave irradiation saturates, the transition for the second electron

irradiation of the electron transitions. The saturation changes the populations in each level which, depending on the saturated transition, can produce positive or negative polarization [195]. The systems have nevertheless to fulfill the condition $|\omega_S^i - \omega_S^j| = \omega_I$ [192][195], as depicted in figure A.4. The μ -wave saturation is at the origin of CE, a system with low spectral diffusion is thus more adapted for CE mechanism since the saturation is not diffused throughout the EPR spectrum .

On the other hand, for TM, the mechanism depends on efficient spectral diffusion. In this mechanism, the saturation of the μ -wave is diffused through the population of spins until the triple spin flip conditions are matched ($(\omega_S^j - \omega_S^i) = \pm \omega_{0I}$). Although in TM, the μ -wave is also at the origin of the DNP enhancement, the process of coupling electrons and nuclei depends on the efficiency of spectral diffusion. The manifestation of an out of equilibrium hyperpolarized state depends on the spectral diffusion being faster than the relaxation of the nuclear hyperpolarization with the lattice. This will be further discussed in the next section.

The triple spin flips transitions are depicted in figure A.5. On the left hand side of the figure (reproduced from chapter 6.1.3 of [187]), μ -wave irradiation saturates an electron transition

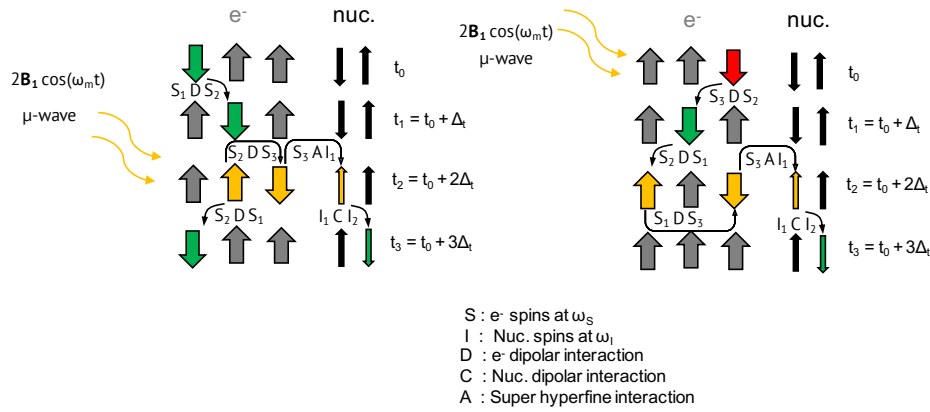


Figure A.5: Two different cartoons depicting the TM mechanism in different contexts. The green arrows represent the spins flipped by conventional spectral diffusion and the yellow arrows are the triple spin flips. On the left side, the triple spin flip is directly induced by the μ -wave irradiation at t_2 . The hyperpolarization is then transferred to the other nuclear spins by nuclear spin diffusion. Electron spin diffusion keeps flipping electron spins through the entire EPR line (if the EPR line is continuous). One of the features of TM is that it does not depend on the μ -wave irradiation frequency. On the right side, we have an example in which the μ -wave irradiation saturates a frequency of the EPR line (flipping the electron spin in red) at time t_0 . Then, spectral diffusion flips subsequent electron spins until matching triple spin flip conditions at time t_2 ($\omega_{I1} = \omega_{S1} - \omega_{S3}$).

that triggers directly the triple spin flip. On the right hand side, μ -wave irradiation saturates the electron spin system at a particular frequency, after spectral diffusion $|\omega_S^i - \omega_S^j| = \omega_{I0}$ condition is matched. Although the left side displays spectral diffusion (and can also occur in TM conditions), the direct irradiation of the electron spins involved in the triple spin flip corresponds more to CE scheme. μ -wave irradiation frequency can be set to saturate different transitions depicted in figure A.4.

A.2.2 Spin temperature exchange and μ -wave irradiation

In a publication entitled "Spin Temperature", by A. Abragam and W. G. Proctor,[200] the concept of spin temperature was discussed. Its formalism is fundamental for the understanding of DNP phenomena among others. In section 2 of the review, [189], Abragam and M. Goldman state that "The basic hypothesis in spin-temperature theory is that the evolution of an isolated system of a large number of interacting spins leads to a state of equilibrium characterised by a temperature, i.e. a Boltzmann distribution of the populations of its various energy levels." It was also claimed later on, that the concept of spin temperature is only meaningful if the process exciting spins out of equilibrium is faster than the spin-lattice re-

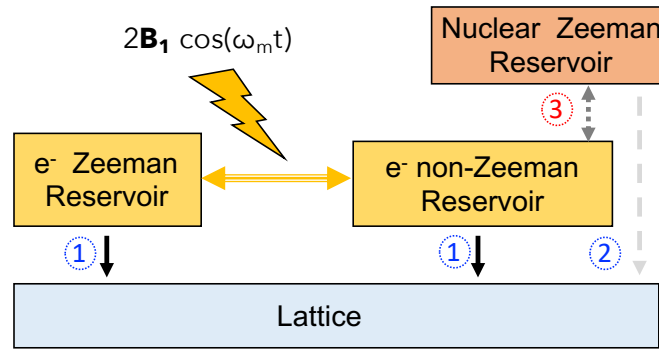


Figure A.6: Scheme depicting the heat exchanges between the different reservoirs of energy involved in TM context under μ -wave irradiation. The main nuclear relaxation source comes from the coupling with the electron spins that also relax through spin-lattice relaxation (1). The direct nuclear spin-lattice relaxation is not an efficient process (2). Tiplle spin flips couple the electron non-Zeeman reservoir and the nuclear Zeeman reservoir due to the dipolar and hyperfine interactions between the different electron and nuclear spins. The μ -wave irradiation cools down the electron non-Zeeman reservoir and creates a contact between the electron Zeeman and the electron non-Zeeman reservoirs (yellow arrow). Due to the coupling, the microwave cools down the nuclear Zeeman reservoir indirectly. If TM is efficient the invers spin temperature of both the nuclear Zeeman, and electron non-Zeeman reservoirs will homogenize . This last phenomenon is responsible for the hyperpolarization of the nuclear spin systems.

laxation [189]. In this scenario, a process affecting the population difference of the different energy levels produces a variation in spin temperature. Hence, the spin temperature can be defined in terms of the polarization of the spin system. Yet if the polarization can be determined by a Boltzmann distribution, the system can be considered at equilibrium and so, spin-temperature and lattice temperature are equal. Indeed, the first requirement for TM is that mutual interactions must lead to establishing a local stationary state in a time short with respect to the spin-lattice relaxation time [189]. In this case, there may exist a spin temperature T_S different from the lattice temperature T_L .

In the thermal mixing picture, several energy reservoirs are typically defined. Thus, for the electron spin system the *Electron Zeeman reservoir* is defined, to which is associated a temperature T_Z . The rest of the energy, contributed by the other interactions defines a second temperature for the system and constitutes the *Electron Non-Zeeman* reservoir, with its temperature T_{NZ} . In addition, a nuclear Zeeman reservoir is defined.

Note that for the electron-spin system, in the absence of μ -wave irradiation, the major energy contribution comes from the Electron Zeeman reservoir, which therefore determines the spin temperature, in this case, the lattice temperature. Several descriptions of

TM have been proposed in the literature to describe the behavior of electron and nuclear polarization under μ -wave irradiation in particular conditions, such as high-temperature approximation [273] or strong μ – wave irradiation [197]. More recent work, inspired by the previous descriptions, has tried to describe systems under less constrained conditions, beyond high-temperature approximation [202], or under partial saturation of the μ -wave irradiation [198]. The final objective is to give a description of the TM mechanism in order to predict the evolution of the polarization in DNP systems.

If spectral diffusion is fast enough for a local equilibrium to establish, the electron spin polarization can be determined in function of two spin temperatures $\alpha = \hbar/k_B T_Z$ and $\beta_{NZ} = \hbar/k_B T_{NZ}$, the inverse electron Zeeman temperature, and the inverse electron non-Zeeman temperature respectively [273][189]. It has been discussed how triple spin flips create a contact between $\beta_I = \hbar/k_B T_I$, the inverse spin temperature for nuclear spins, and β_{NZ} , [189][188][198]. It can be shown that in TM conditions, when the thermal mixing process is very fast compared with all other relaxation mechanisms involved in the DNP processes, after reaching local equilibrium spin temperatures tend to $\beta_I = \beta_{NZ}$. The previous phenomenon is related to the energy conservation rules for triple spin flips, $\omega_s^j \approx \omega_s^i + \omega_{0I}$ and $\omega_s^j \approx \omega_s^i - \omega_{0I}$ introduced in the previous section, as demonstrated in [188] and [187].

The DNP process originates on the μ -wave irradiation which adds energy to the electron spin system. The dipolar coupling between electron spins distributes the energy to both the electron Zeeman reservoir and the electron non-Zeeman reservoir. This energy contribution produces a heating of the electron Zeeman reservoir while the electron non-Zeeman reservoir cools down. Triple spin flips create a contact between the electron non-Zeeman reservoir and the nuclear Zeeman reservoir, which is cooled down as well. Hence, the nuclear spins are polarized. as described in chapter 8 of [187]

As a matter of fact, you can express the inverse spin temperature of your electron spin system with the previous assumption:

$$\omega_S \beta(\omega_S) = \omega_0 \alpha + (\omega_0 - \omega_S) \beta_{NZ} \quad (\text{A.20})$$

Where ω_S is the resonance frequency of a given spin, and ω_0 is the frequency at the center of gravity of your EPR spectrum. In [188], the development of the previous expression gives:

$$P_S(\omega_S) = \tanh\left(\frac{1}{2}(\omega_0\alpha + (\omega_0 - \omega_S)\beta_{NZ})\right) \quad (\text{A.21})$$

Where we can see the contribution of the electron non-Zeeman and electron Zeeman reservoirs. It is important to remind that ω_S is affected by the homogeneous broadening and so, it fluctuates inside Δ_h . With the objective of predicting the evolution of the polarization under μ -wave irradiation, multiple theories have described the evolution of the spin temperatures (α and β_{NZ}) using approximations related to the intensity of the μ -wave and the efficiency of the triple spin flips. As reviewed in *T. Wenckebach 2017*, if an intense μ -wave irradiation is considered we have:

$$\alpha = -\frac{\omega_m - \omega_0}{\omega_0}\beta_{NZ} \quad (\text{A.22})$$

Which, inserted in equation A.21, in a frame rotating at the μ -wave's frequency, gives:

$$P_S(\omega_S) = \tanh\left(\frac{1}{2}(\omega_S - \omega_m)\beta_{NZ}\right) \quad (\text{A.23})$$

And so, with the μ -wave irradiation you can define the polarization of the electron spin system with a single inverse spin temperature β_{NZ} . Additionally, since triple spin flips homogenize the nuclear Zeeman and the electron non-Zeeman reservoirs' temperature, we got that:

$$P_I = \tanh\left(\frac{1}{2}\omega_{0I}\beta_{NZ}\right) \quad (\text{A.24})$$

This conclusion reproduces Borgini's expression of P_I in [197] which is pertinent since we do not consider the ratio between the number of nuclear spins and the number of saturated electron spins (like proposed in [198]) and therefore we describe a system under strong μ -wave irradiation. For the different spin systems, reaching the lattice temperature depends on a series of relaxation mechanisms. Electron spins relaxation with the lattice follows a process that affects all electron spins at the same rate $\frac{1}{T_{1S}}$. The relaxation process homog-

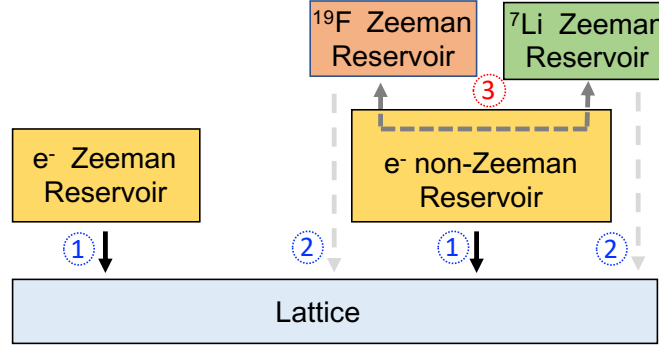


Figure A.7: Reservoirs of energy involved in the heat exchange between the different spin systems for the Goldman and coworkers experiment (performed in [196]). 1 and 2 correspond to the spin-lattice relaxation processes. It is important to precise that nuclear spin-lattice relaxation (2) is a very slow process, the main source of nuclear relaxation is due to the interaction with the electrons and the fluctuating field (introduce in previous paragraphs). In 3 we got the indirect contact between the different nuclear Zeeman reservoirs. The exchange of spin temperature is faster than the relaxation processes producing the transfer of polarization from one nucleus to the other. Eventually, the lattice pumps enough energy for the system to get to equilibrium and reach, for the different spin systems, the lattice temperature.

enizes the spin temperature of the electrons with $\beta_L = \hbar/k_B T_L$. The evolution of electrons polarization follows:

$$\frac{\partial P_S}{\partial t} = \frac{1}{T_{1S}} [P_S - P_L] \quad (\text{A.25})$$

Where, as expected, P_L is the polarization given by the Boltzman distribution. In the case of nuclear spins the coupling with electron spins is the major source of relaxation, their direct lattice-relaxation process is too slow ($1/T_{1I}$ many times smaller then $1/T_{1S}$). Multiple relaxation mechanisms are fundamental for the complete understanding of DNP and NMR in general, however their complexity makes them not to be detailed in this manuscript. Some minor descriptions will be given in chapters to come. For the moment we only precise that the main source of nuclear relaxation comes from their dipolar coupling with the electron spins, which relax directly with the lattice.

We saw that through TM β_{NZ} and β_I homogenize. If there are multiple nuclear species all nuclear Zeeman reservoirs can homogenize their spin temperature with the electron non-Zeeman reservoir [187]. When the triple spin flip process is efficient, i.e. the spin temperature exchange is faster than the electron spin-lattice relaxation, TM produces a transfer of spin temperature between multiple nuclear Zeeman reservoirs. This effect is at the origin

of the polarization transfer seen in Goldman and coworkers' experiments (in figure A.3). A cartoon depicting the exchange between the reservoirs is presented in figure A.7. The indirect contact responsible for the polarization transfer between nuclear reservoirs is represented by the arrow in 3.

Multiple of the mechanisms that have been presented can occur simultaneously in the same sample. However, we can use the efficiency of the spin temperature transfer between different nuclear species to evaluate the predominance of TM.

A.3 Characterizing TM via cross-talk between spin reservoirs

During my masters internship directed by Dennis Kurzbach, a method to evaluate the actual contribution of TM to DNP in a given sample was developed. The objective was to use the fact that the contact between the nuclear Zeeman and the electron non-Zeeman reservoirs tends to equalize the spin temperature of both reservoirs in TM conditions, hence, if the polarization transfer takes place on a time scale that is faster than the nuclear relaxation rate. In such conditions, if different types of nuclei are present in the sample, heat can flow spontaneously from one nuclear reservoir to another via the non-Zeeman electron reservoir. Therefore, under TM, polarization transfers between different nuclear species are expected to follow the simple laws of heat propagation as shown in the experiments of [196] and depicted in figure A.3. In practice, however, DNP often results from a combination of different mechanisms that may be difficult to disentangle. In order to determine if TM is the predominant DNP mechanism we performed experiments on samples containing different nuclear species. The samples for the different experiments contained protons $I = {}^1\text{H}$ and a second nuclei $I' = {}^2\text{H}$, ${}^{13}\text{C}$, or ${}^{31}\text{P}$, depending on the experiment.

Two complementary experiments were performed: (A) the polarization buildup curves

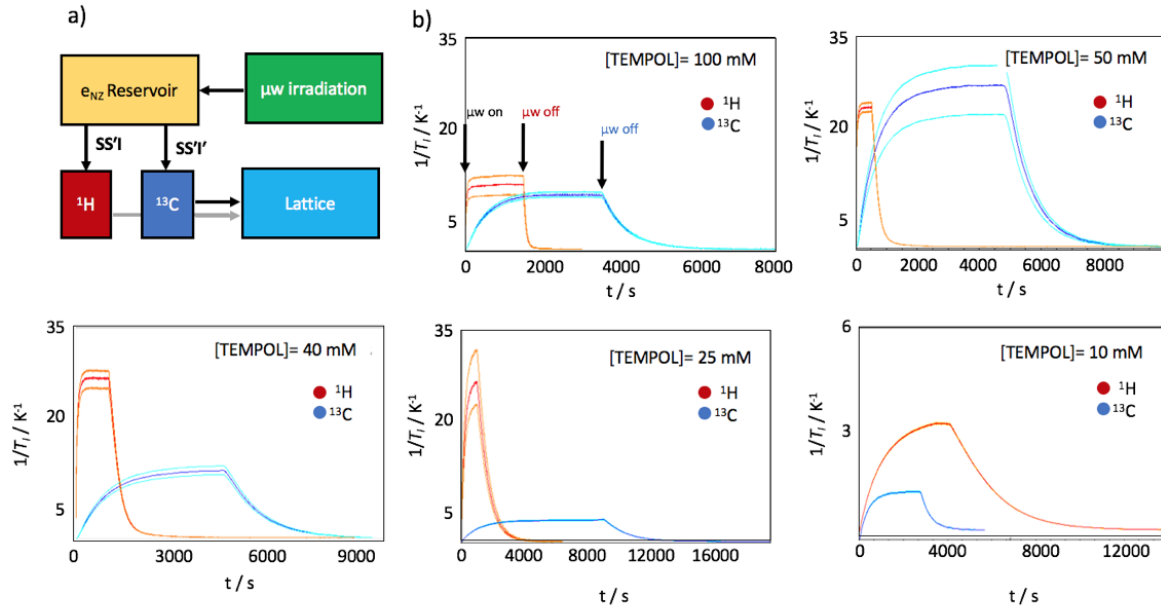


Figure A.8: **a)** Energy reservoirs involved in experiment A that monitors the build-up of the polarizations $P(I = ^1H)$ and $P(I' = ^{13}C)$ after switching on the saturation of the EPR spectrum by microwaves (μw), and their decay after interruption of the μw irradiation. The μw irradiation cools down the non-Zeeman dipolar electron reservoir e_{NZ} ; as a result, the 1H and ^{13}C spins are polarized simultaneously via heat exchange between the reservoirs. Nuclear relaxation proceeds via dissipation of energy to the lattice. **b)** DNP build-up curves and decay of polarizations after switching off the (μw)-field (at the delays indicated exemplarily for 1H and ^{13}C in the panel of 100 mM TEMPOL) for a sample containing $I = ^1H$ and $I' = ^{13}C$ nuclei. The polarizations are expressed in terms of inverse spin temperatures, $1/T_I$. Traces shown in lighter color indicate the ranges of experimental errors.

of both nuclei were monitored under microwave irradiation, then their return to thermal equilibrium after switching off the microwave irradiation was observed; (B) we reproduced the experiment proposed [196] (see figure ??) and initially performed on single crystals of lithium fluoride, and applied it to amorphous samples that are used in current DNP applications. In the latter experiment, two different nuclei were simultaneously hyperpolarized ($I = ^1H$, and $I' = ^2H$, ^{13}C or ^{31}P). After reaching the maximum stationary polarization, one of the nuclei was saturated by means of RF pulses, and the time-evolution of polarizations $P(I)$ and $P(I')$ were observed. For A and B experiments, we used the nitroxide radical TEMPOL which is characterized by a broad inhomogeneous EPR line (ca. 0.5 GHz). The TEMPOL concentration was varied in the range of 10 – 100 mM.

A.3.0.1 Reaching a common spin temperature

The first test consisted in verifying that both nuclear Zeeman reservoirs (for I and I') reached a common spin temperature. Figure A.8a displays schematically the flow of spin order in experiment A. Through μ -wave irradiation, the non-Zeeman dipolar electronic (e_{NZ}) energy levels are polarized, thus cooling down the corresponding heat reservoir. Consequently, triple spin flips tend to equalize the e_{NZ} spin temperature and the nuclear spin temperature of both ^1H (SS'I flips) and ^{13}C (SS'I' flips) reservoirs. After switching off the μw irradiation, both nuclear polarizations $P(^1\text{H})$ and $P(^{13}\text{C})$ decay and equilibrate at the lattice temperature. Typical DNP build-up curves of these nuclear spin polarizations and their subsequent decays, obtained for different concentrations of TEMPOL, are shown in figure A.8b for sample 2.

Results shown in figure A.8b for $I=^1\text{H}$ and $I'=^{13}\text{C}$ indicate that, for TEMPOL concentrations above 50 mM, both nuclei converge to a common spin temperature after the initial build-up. In contrast, at lower radical concentrations (10-40 mM), the ^{13}C spin temperature is significantly higher than the proton one, thus indicating that TM is not the dominant mechanism since the condition above is not fulfilled anymore.

The fact that TM no longer dominates at low radical concentrations originates from reduced spectral diffusion, as the average distance between radicals increases. When electron spectral diffusion slows down due to decreasing flip-flop probabilities, the electron spins cannot be treated anymore using thermodynamic concepts. The rate of triple-spin flips decreases dramatically and becomes lower than the relaxation rates of the different spin species, leading to the breakdown of the thermodynamic description of DNP.

A.3.0.2 Heat transfer between the nuclear Zeeman reservoirs

We can evaluate the presence of triple-spin flips at different radical concentrations by experiment B, schematically depicted in figure A.9a. Triple spin flips offer a mechanism through which the transfer of polarization, i.e., of heat from one nuclear reservoir to another via the e_{NZ} reservoir, can take place. Hence, a spontaneous heat flow from a warmer to a colder

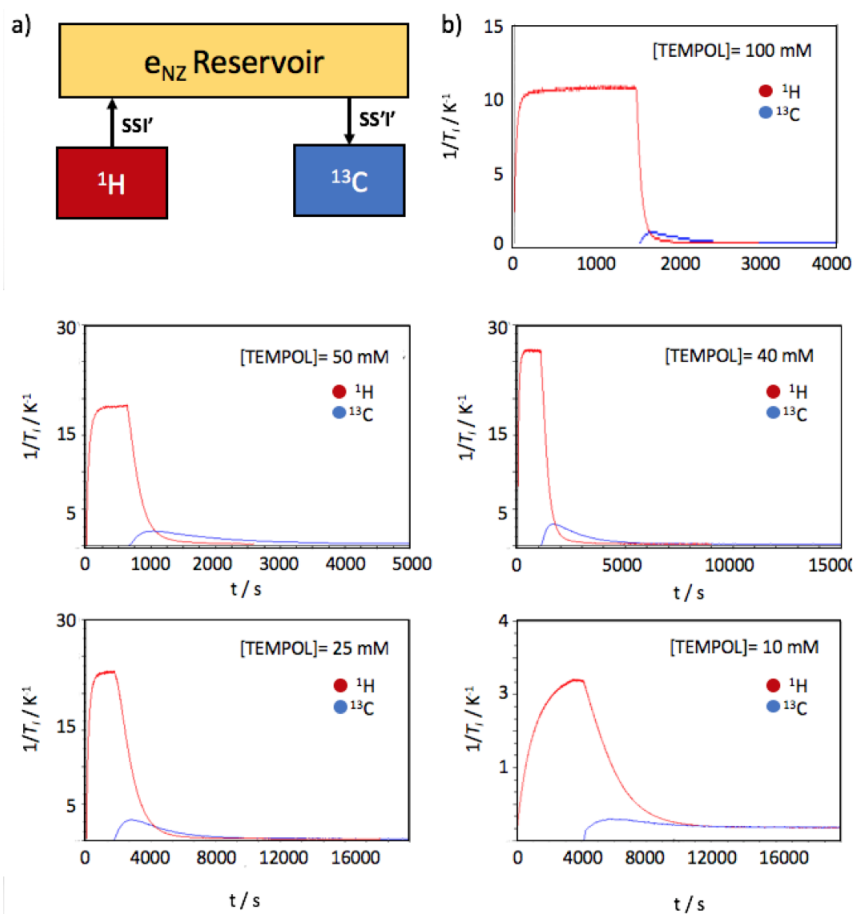


Figure A.9: a) Energy reservoirs involved in experiment B that monitors the transfer between the polarizations $P(I = ^1\text{H})$ and $P(I' = ^{13}\text{C})$ after the interruption of the μw irradiation and saturation of either I or I' nuclear reservoirs. Via triple spins flips, the polarization flows from ^1H to the non-Zeeman dipolar electron reservoir, and is then transferred to ^{13}C spins via $SS'I'$ triple spin flips. These processes are accompanied by relaxation to the lattice (omitted in the flow diagram.) b) Time evolution of the inverse nuclear spin temperature $1/T_I$. First, a polarization $P(I = ^1\text{H})$ is generated by DNP. Subsequently, after the μw irradiation is interrupted, the ^{13}C spins are saturated and a spontaneous flow of polarization from ^1H to ^{13}C reservoirs is observed. Spontaneous transfer of heat from the ^1H to ^{13}C reservoir is indicative of triple spin flips $SS'I$ and $SS'I'$.

spin reservoir attests for the presence of triple-spin flips. Through our experimental setup, we could observe the transfer of polarization from ^1H to ^{13}C , i.e., as the ^1H reservoir heats up, the ^{13}C reservoir cools down. When the rate of triple spin flips is high, the two nuclear and the e_{NZ} reservoirs reach a common spin temperature before they relax to the equilibrium temperature. This is exactly what is observed in figure A.9b between 40 and 100 mM where the ^{13}C polarization of sample 2 reaches a maximum when the temperatures of the two nuclear reservoirs become equal (the time traces cross). To our surprise, the transfer of polarization between the two nuclear reservoirs is not entirely suppressed even at a radi-

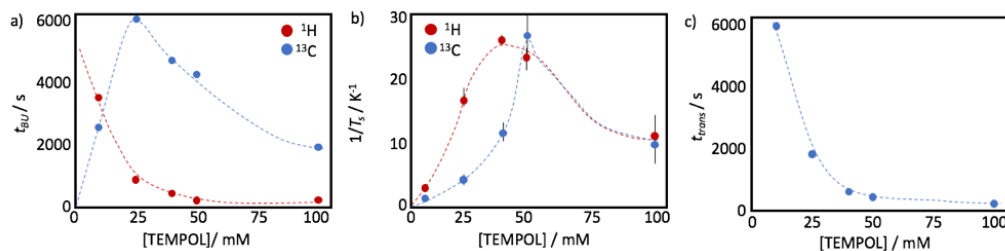


Figure A.10: **a)** Characteristic build-up times, t_{BU} for $P(^1\text{H})$ and $P(^{13}\text{C})$ polarizations at different TEMPOL concentrations, obtained by fitting experimental build-up curves to mono-exponential functions. At low radical concentrations, the build-up of $P(^{13}\text{C})$ is faster than the build-up of $P(^1\text{H})$, indicating a change of the dominant DNP regime (see text for details). **b)** Dependence of the inverse steady-state spin temperatures $1/T_I(^1\text{H})$ and $1/T_I(^{13}\text{C})$ as a function of the radical concentration. At a TEMPOL concentration of 50 mM these inverse spin temperatures are similar within experimental error, indicating that TM is predominant, while below 40 mM this is no longer the case. **c)** Characteristic polarization transfer times from $P(^1\text{H})$ to $P(^{13}\text{C})$ obtained by fitting the first part of the ^{13}C time dependence in experiment B to mono-exponential build-up functions. The dashed lines are to guide the eye.

cal concentration as low as 10 mM. Thus, even though the signature features of a common spin temperature and an efficient heat transfer are not fulfilled, we observe triple spin flips, indicating a non-TM regime with a reduced rate of such transitions.

At TEMPOL concentrations of 50 mM or above all characteristic features of TM, are observed, while at lower concentrations the nuclear reservoirs do not reach a common spin temperature and the heat transfer is inefficient despite the occurrence of triple spin flips. The characteristic build-up times and steady-state spin temperatures at the end of the build-up (experiment A) as well as the transfer times (characteristic cooling times of the ^{13}C reservoir in experiment B) are summarized in figure A.10. Note that heat transfer becomes faster with increasing radical concentration (figure A.10c), thereby confirming the dependence of the triple spin flip rate on the TEMPOL concentration.

In conclusion, combining experiments A and B yields a strategy for the determination of TM contributions to DNP, corresponding to the limiting case where the spin temperatures of all spin reservoirs tend to a common value T_I for $t \rightarrow \infty$ due to triple spin flips and the spontaneous heat transfer between different reservoirs. This strategy allows one to assess the presence of the TM regime, understood as a situation where a common nuclear spin temperature emerges from a spontaneous heat flow, through triple spin flip transitions. We want to stress that the sole occurrence of triple spin flips, or of spontaneous heat transfer, is

not indicative of strict and predominant TM, if the spin temperatures of the different nuclei in the system do not converge. Moreover, it can be stated that TM is the dominant mechanism at high TEMPOL concentrations (≥ 50 mM) at 4.2 K and 6.7 T, while for lower TEMPOL concentrations (≤ 40 mM) the spin temperatures of the different reservoirs tend to different values. From the experimental point of view, it is important to note that the lowest ^{13}C spin temperature can be reached at TEMPOL concentrations of 50 mM due to low ^1H spin temperatures and the dominance of TM. Yet, even lower ^1H temperatures can be reached at a lower TEMPOL concentration of 40 mM because favorable saturation factors[274][199]. This information is crucial for users who cannot rely on cross-polarization techniques. In this situation TM-DNP can be a remedy, since it not only allows one to hyperpolarize protons, but also homogenizes their spin temperatures with various other nuclei potentially increasing the final achievable hyperpolarization level.

Appendix B

Pyruvate into Ecoli ATCC and 2,4-DNP

The methodology introduced in the last chapter can be extended to a wide range of organisms and substrates. The principal conditions for this methodology to be applied are:

- The organism has to survive the mechanical shock produced in the injection of the dissolved DNP sample.
- The relaxation times of the substrates have to be long enough for the metabolic process to be observed.
- The substrate has to be internalized and metabolized by the organism.

Although glucose has a fundamental role in metabolism, its T_1 is shorter than other metabolites containing carbonyl groups. As a matter of fact, multiple in cell DDNP studies use Pyruvate due to its C_1 particularly small relaxation rate. Additionally, pyruvate is a metabolite that is commonly uptaken and metabolized by most living organisms since it plays a central role in multiple metabolic pathways (see [subsubsection 1.1.1.1](#)). Hence, for methodological development we chose pyruvate as substrate to perform our first in cell DDNP experiments.

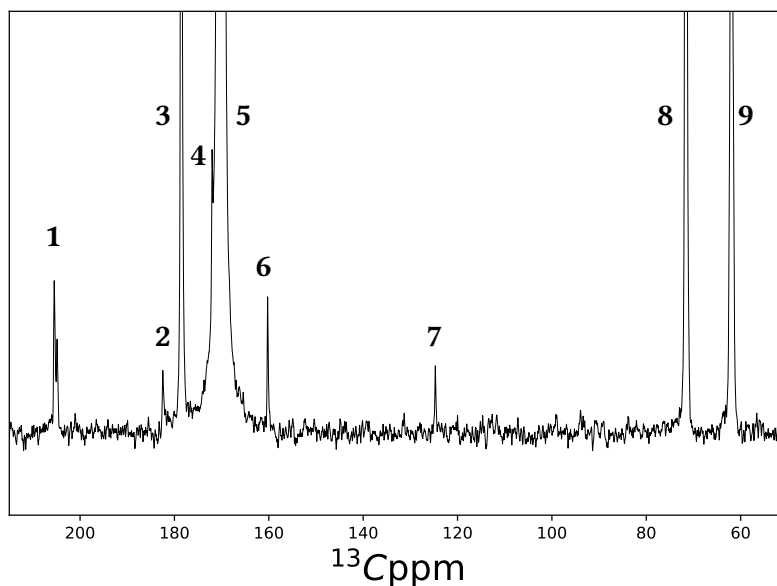


Figure B.1: Superposition of the first 25 scans of the injection of hyperpolarized [^{13}C]pyruvate into a suspension of *E.coli*. In this spectrum, resonances 1 and 5 are C_2 and C_1 of pyruvate respectively, 2 is acetate's C_1 , 3 is pyruvate hydrate's C_1 , 4 formate, 6 HCO_3^- or bicarbonate, 7 CO_2 and 8 and 9 are glycerol's C_1 and C_2 , 3 respectively.

B.0.1 Experiment n^o 1, no cell treatment

The culture of *E.coli* ATCC followed the same standard steps than the ones presented in [section 7.2](#). Using lysogeny broth as medium, bacteria precultures were grown overnight. Cultures were then inoculated into 50 mL of LB and grown to $OD_{600} = 0.9$. After reaching desired growth, cells were harvested by centrifugation at 3500 G-force for 10 minute, washed in PBS 1x buffer and resuspended in 1 mL of PBS 1x buffer pH = 7.2 inside a 10 mm NMR tube instants before the DDNP experiment.

The DNP sample for pyruvate had been previously optimized in our laboratory, it is composed of a mixture of H_2O , D_2O , and Glycerol- d_8 at 10:40:50% in volume respectively. This mixture was prepared with a stock solution of D_2O at 200 mM TEMPOL, to obtain a final concentration of 50mM TEMPOL. $^{13}\text{C}_1$ -pyruvate was added to the final solution to reach a concentration of 1.5 M. The hyperpolarization of $^{13}\text{C}_1$ -pyruvate was obtained with a CP sequence for approx. 45 min under μ -wave irradiation at 187.9 GHz with a orwer of

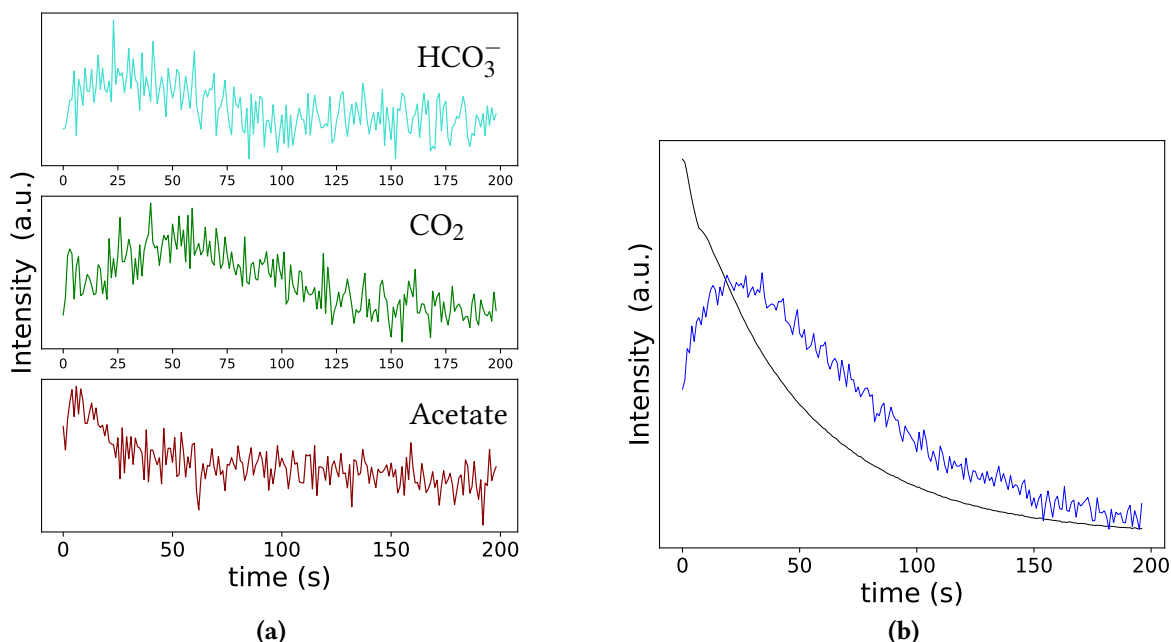


Figure B.2: Signal evolution of the different metabolites observed in pyruvate metabolism by *e.coli*. **B.2a** Products of pyruvate metabolism, HCO_3^- in top, CO_2 in the middle and acetate in the bottom, all end products of the citric acid fermentation pathway. For all products the SNR is very low, kinetics can not be analyzed. **B.2b** Spontaneous hydration of pyruvate. Pyruvate C_1 in black, pyruvate hydrate in blue, signal is multiplied, $\times 50$.

350 mW. The μ -wave irradiation was modulated with a saw-tooth function over a range of 100 MHz with a modulation frequency of 1 or 2 kHz.

To transfer the sample, 5 mL of PBS 1x at pH = 7.2 were inserted in the dissolution box, heated at 403 K and pressurized at 10.5 bar. The mixing of the hyperpolarized solution with the *E.coli* suspension is done in a 10 mm NMR tube, inside a 10mm BBO probe. Only 1^H decoupling was performed by means of a WALTZ16 pulse sequence. The results presented in this section consist on ^{13}C pseudo 2D experiments with a 1 s time interval between scans using 10° read pulses. Resulting FID's were treated following the same steps than for the previous chapter.

The resulting pseudo-2D spectrum displayed signals of the hyperpolarized substrate and of different products of *e.coli*'s metabolism. The cells seem to be metabolizing the injected pyruvate, this experiment was the first successful in cell DDNP experiment of our team. A projection of the first 25 scans is displayed in figure B.1. The peak were assigned by compar-

ison with literature and by the knowledge of the species involved in pyruvate's metabolism by *E.coli*. After integration of the different resonance, the time evolution of each metabolite's signal was reconstructed. The results are displayed in figure B.2. Although different products can be identified, the signal to noise ratio is very weak. Any kinetic analysis would be hardly affected by the noise. However, some comments can be given. The results suggests an early production of formate and acetate, both end chain products of acetyl-CoA (see figure 7.3). The former is eventually degraded into CO_2 and subsequently produces bicarbonate. Accelerated excretion of bicarbonate can also reflect and imbalance in the acid/base conditions of the solution due to excretion of acetic acid, lactic acid, etc... .

B.0.2 Experiment n°2, addition of 2,4-dinitrophenol

A second experiment was performed with pyruvate into *E.coli*. The aim was to increase the signal to noise ratio of the products. Since it had been previously optimized, the DNP sample was conserved (from last experiment). The different DNP related parameters were also conserved (μ -wave frequency etc..). The bacteria, on the other hand, followed a different treatment. After reaching desired growth $OD_{600} = 1.1$, 2,4-dinitrophenol (2,4-DNP) was added to the culture medium to reach a concentration of 1.5 mM, 30 min before dissolution experiment. Subsequently, cells were harvested by centrifugation at 3500 G-force for 10 minute, washed in PBS 1x buffer and resuspended in 1 mL of PBS 1x buffer pH = 7.2 containing also 1.5 mM of 2,4-dinitrophenol. The 1 mL resuspension was inserted inside a 10 mm NMR tube instants before the DDNP experiment.

The new experiment also displayed proof of metabolism. In figure B.3a we have the superposition of the first 20 1D-spectra. The resonances observed in the spectra evidence a different metabolic behaviour from the obtained in the first experiment with pyruvate. The increment of the acetate resonance's signal suggest that the production of acetate is enhanced. On the other hand, the production of format seems to diminish and its resonance's decreased signal seems to be covered by pyruvate C_{11} signal. Adittionally, we see the ap-

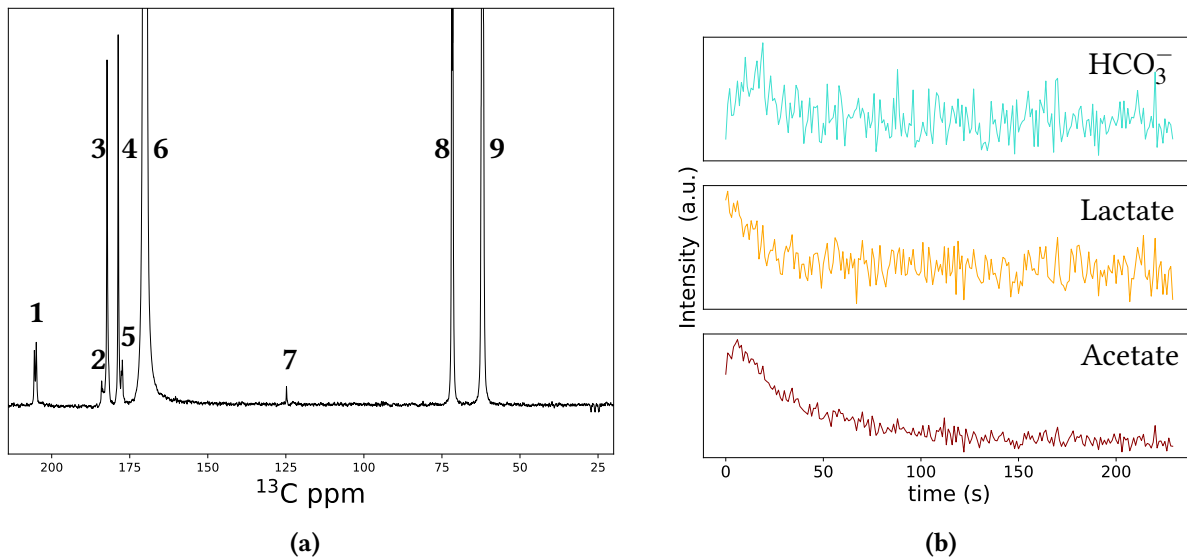


Figure B.3: B.3a Superposition of the first 20 scans of the injection of hyperpolarized [^{13}C]pyruvate into a suspension of *E.coli* previously treated with 2,4-DNP for 30 min. In this spectrum, resonances 1 and 6 are C_2 and C_1 of pyruvate respectively, 2 is lactate's C_1 , 3 is acetate's C_1 , 4 pyruvate hydrate's C_1 , 5, 7 CO_2 and, 8 and 9 are glycerol's C_1 and $\text{C}_{2,3}$ respectively.??

partition of 2 new resonances assigned to lactate and CO_2 is still being produced which confirms formate's production, however we cannot see its conversion into HCO_3^- , probably related to a lower hyperpolarized signal of CO_2 that relaxes before producing HCO_3^- . In the first experiment, the maximum of CO_2 was obtained around 25 s after the start of the dissolution. In this second experiment with 2,4-DNP, the maximum of CO_2 is obtained around 16 s after start. The same effect is observed for acetate's production for which the maximum is obtained approximately 4 s before in experiment 2. The production processes of both CO_2 (and so formate) and Acetate seems to accelerate in presence of 2,4-DNP. Addition of 2,4-DNP, also seems to enhance lactate's production. The latter can be originated by an enhanced in pyruvate metabolism in the same hypoxic conditions of experiment 1. Conditions at the origin of lactate production, see ??.

2,4-DNP is an uncoupler of oxidative phosphorylation which are compounds able to produce a proton transport across biological membranes. The latter has an impact on nutrient transport, ATP synthesis, and other endergonic reactions at the cell membrane [275]. Addition of 2,4-DNP to cellular medium has shown to affect metabolism (strongly diminishing

production of ATP) and increasing the efflux of multiple metabolic products such as acetate [276]. The enhanced metabolism towards acetate production and efflux might be at the origin of acetate resonance's signal increase in experiment 2. Different studies have shown how the uptake of some carbon sources is reduced in the presence of 2,4-DNP [275]. However, it has been proven that the inhibitory effects of 2,4-DNP on substrate uptake are not related to inhibition of the transmembrane transport but to the regulations of metabolism due to lack of ATP production (and so, low glycolytic rate). Glucose consumption has been shown to slow down in the presence of 2,4-DNP [276]. An effect of 2,4-DNP compound on pyruvate uptake has also been observed. Previous research has shown how pyruvate uptake is dependent on the pH gradient across the membrane [277]. In this work, they claim that the proton transport through membrane produced by 2,4-DNP reduces the pH gradient in a limit in which pyruvate transport can get completely inhibited. Our results are not necessarily in contradiction, the pulse of pyruvate create a metabolic shock with an enhanced efflux of acetic and lactic acid. The pH variation of the medium affects the gradient across the membrane that can be at origin of an enhanced pyruvate uptake. Our results qualitatively show that, the pulse of hyperpolarized pyruvate enhances the production of acetate and lactate for cells grown with 2,4-DNP. The substrate is thus being uptaken by the cells in presence of 2,4-DNP and the metabolism towards acid fermentation seems to be accelerated. Although, for *E.coli* K12, glucose metabolism has been shown to slow down by addition of 2,4-DNP [276], in our experimental conditions, 2,4-DNP seemed to enhance acetate and lactate production with pyruvate as substrate.

Appendix C

Glucose into Macrophages

Most of prokaryotic cells have a double membrane separating the inside from the external environment. The double membrane can help the organism resist mechanical shocks. Multiple cellular systems without this double membrane would not be able to resist the shock during DDNP's injection with our experimental setup. However, we were able to perform DDNP experiments on eucariotik cell systems. In this section we want to present experiments performed on eukaryotic cells aiming to observe macrophages metabolism of glucose. Macrophages are highly versatile cells with a range of functions depending on their location and activation status. Between the different functions of macrophages are, anti-bacterial and anti-tumor activity, secretion of a wide variety of regulatory peptide factors, prostanoids, and enzymes. The activation of macrophages has been shown to be dependent on the carbon sources and oxygenation [278]. As a matter of fact, glucose is a critical component in the proinflammatory response of macrophages[279]. Other research has shown the major role of oxygenation and metabolic regulation in macrophage's antitumor activity [280]. This cellular system is a very interesting subject of study that has recently been focused by oncology research[280]. The first experiments that we performed on macrophages focused on the study of glucose metabolism. The results presented here are preliminary work, no quantitative kinetic analysis has yet been performed on this system. However, some features of macrophage's metabolism can already be observed.

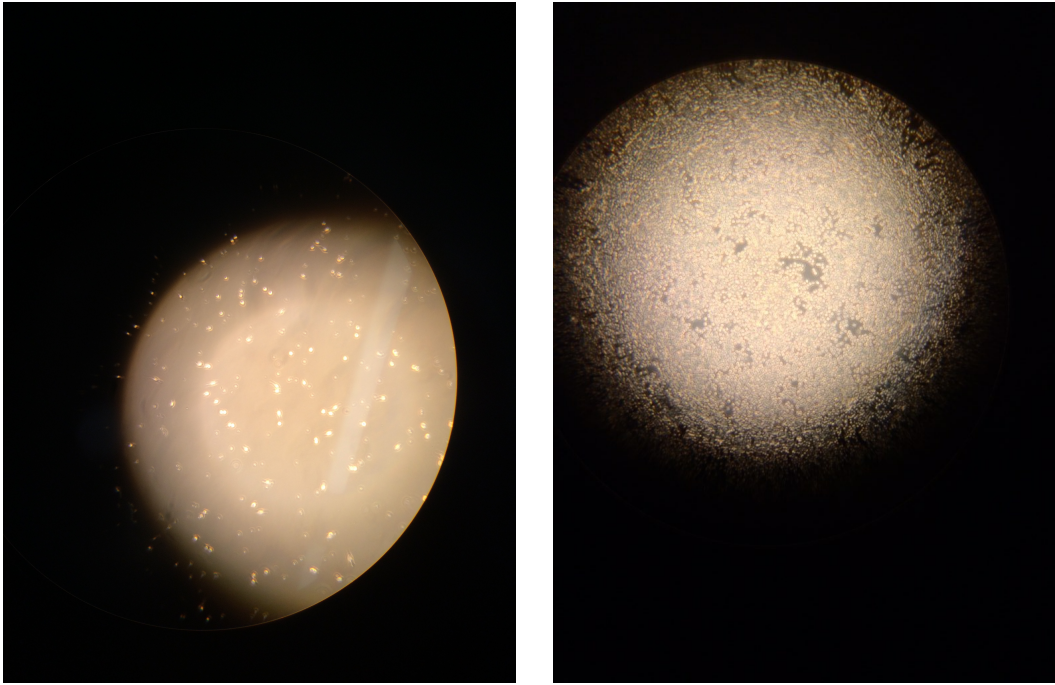


Figure C.1: Pictures of the observation of RAW culture with microscope. In the left cells are in low confluency conditions, in the right, cells are at high confluency conditions.

C.0.1 Cell culture and DDNP setup

All the studies were performed using macrophages from mouse, RAW 267 bought from ATCC. The vials containing the cells were stored in liquid nitrogen at -150°C . From the opening of the vials all operations were done in the cell-culture room, in complete aseptic conditions. For the first use the vials were thawed until liquefaction on a water bath at 37°C and subsequently decontaminated with ethanol 70%. The content of the vials was transferred to a falcon containing 9 mL of warm (37°C) culture medium. The ~ 10 mL solution was centrifuged at 125 g for 7 min and supernatants were discarded. Cells were then resuspended in 1 mL of warm culture medium prior to transfer to the culture flask (T75 for adherent cells). Flasks were filled with 14 mL of culture medium and set in the incubator during the procedure. Cells were finally resuspended in the culture flasks to reach a final volume of 15 mL. We used DMEM + 10% FBS as culture medium. Viability of cells was monitored every day by cell counting, the medium was renewed every two days. Pictures of low and high confluency (x5 as many cells) are displayed in figure ???. The process from cell's inoculation to high confluency state takes between 2 and 3 days. Before the dissolu-

tion experiment, cells were scratched from the culture flasks with a cell scraper, without addition of trypsin, and centrifuged at 125 g for 7 min. Cells were subsequently washed with HEPES 100 mM and resuspended into 0.5 mL of HEPES 100 mM in the 10 mm NMR tube, instants prior to the dissolution experiment. For the DNP experiments different cell amounts were used (from 1 to 8 flasks depending on the experiment), with all cell systems at high confluency conditions.

For the experiments with macrophages, the DNP sample were prepared with a mixture of 10:35:55% in volume of H₂O, deuterated DMSO and D₂O respectively. The mixture was prepared with a stock solution of D₂O at 200 mM TEMPOL to reach 40 mM TEMPOL concentration. [U-¹³C, U-²H]-glucose was added to the solution to have a final concentration of 1 M. The DNP sample consisted on 75 μ L of the previously described solution, inserted in a sample-holder and placed in the bath of liquid helium. Hyperpolarization was achieved by means of a CP sequence, see [subsubsection 4.2.3.2](#). The sample was set at 1.27 K under μ -wave irradiation at 187900 MHz and 350 mW. The dissolved sample was pushed with 5 ml of D₂O warmed at \sim 140°C.

NMR experiments consisted on series of 1D detections with 1 s time interval using read excitation pulses of 10°. All NMR spectra were recorded with simultaneous ¹H and ²H decoupling, achieved using a WALTZ16 pulse sequence[159]. The obtained FID's were apodized using a 5 Hz exponential window, and zero filling was applied prior to Fourier transformation. Processing of the NMR data was performed using the NMRPipe software [231].

C.0.2 Glucose metabolism in macrophages

The experiments with which we obtain the preliminary results presented in this section had to be further optimized. The resulting data sets have the first scans damaged by saturation and so results are displayed after enough hyperpolarization has relaxed, thus the first 12 1D spectra were lost. However, the different DDNP experiments on macrophages still showed

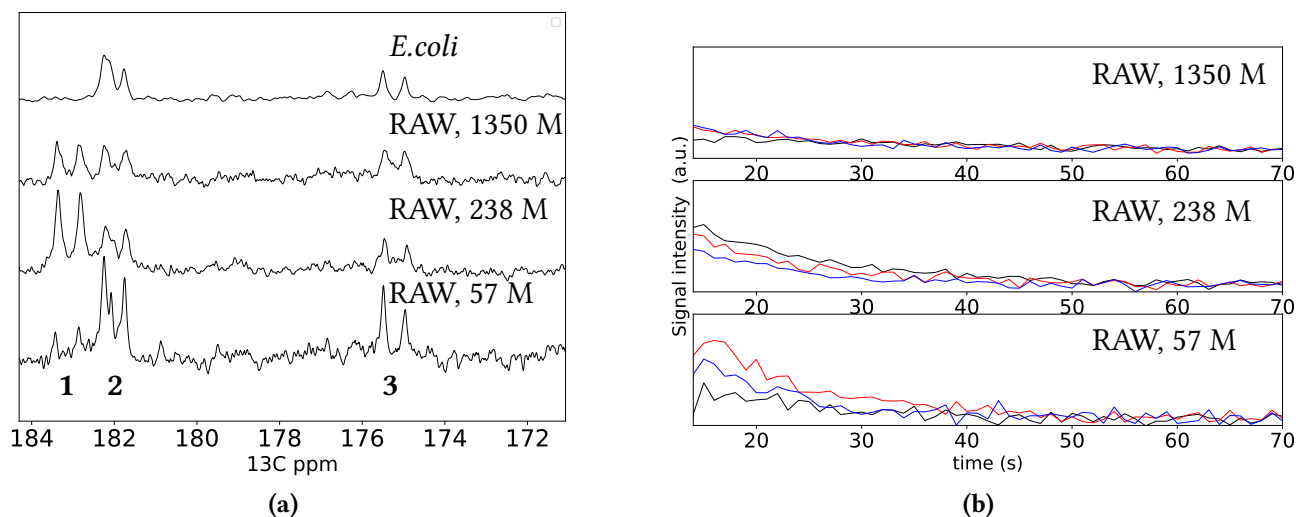


Figure C.2: C.2a Superposition of the first 20 scans of the DDNP experiments performed on macrophages at different cell concentrations. First line from top to bottom is an experiment with *E.coli* K12 at $\text{OD}_{600}=1$ to compare the produced and observable metabolites for different cellular systems. 1 lactate, 2 acetate, 3 δ -PGL. C.2b Integrated resonances to reconstruct the signal evolution of the different metabolites. In black lactate, in red acetate and in blue δ -PGL. Signal evolution displayed after scan $n^\circ 8$.

proof of metabolism. In figure C.2a are displayed the superposition of the first 20 1D spectra (after saturation at scan $n^\circ 12$) for experiments done with cells at different concentrations. The peak assignment for acetate and lactate was done by means of bibliographic research [134]. In this preliminary work the third doublet is assigned provisionally to δ -PGL. However, further investigation has to be done. Acetate and δ PGL resonances observed in the experiments with macrophages are also observed in the experiments on *E.coli*. The observation of δ -PGL could be explained by the pulse of glucose during the dissolution experiment, which has been previously documented to cause a 10 fold increase of δ -PGL's production in other cellular systems [255].

The cell cultures used in all experiments were prepared at the same growth phase, high confluency. Since we varied the cellular concentration for different experiments, the confluency is expected to evolve differently in each experiment during the minutes between harvesting and dissolution. In figure C.2a, a variation of the relative intensities of lactate and acetate doublets can be observed. This variation seems to depend on the concentration of cells. As a matter of fact, for the two experiments with 57 and 238 M of cells, the

production of acetate and lactate seems to inverse. This effect can be explained by the intensification of hypoxic conditions when there is a 4-fold increase of cell's concentration. Lactate production is enhanced to supply the NADH needed for the glycolytic process to continue (see ??). It has been demonstrated that macrophages adapt very fast to hypoxic conditions [281], which explains the fast variation of the metabolic response in our observations. The experiment performed with 1350 M of cells represents a ~ 20 fold increase of cellular concentration. The metabolism shows similar signal intensities for both acetate and lactate productions.

The lost of data due to miss-calibration of the experiments limit the kinetic analysis of these results. For the moment no further analysis will be done. The experiments have to be optimized and repeated. Never the less, observing changes in metabolism related to hypoxic conditions are a very interesting result. As a matter of fact, recent studies have related hypoxic conditions and lactate accumulation to the development of a pro-tumor phenotype in macrophages. The key role of lactate accumulation in cancer was shown to be related to the anaerobic glycolysis enhanced during the accumulation of macrophages around tumors [280]. Characterizing metabolic phases for macrophages is of central interest to determine their action on damaged or inflamed tissues with low levels of oxygenation (malignant tumors, dermal wounds, etc...).

Bibliography

- [1] David L. Nelson and Michael M. Cox. Principles of Biochemistry. Lehninger, 2013.
- [2] H. A. Krebs. The pasteur effect and the relations between respiration and fermentation. Essays Biochem, 8:1–34, 1972.
- [3] L. Pasteur. Expériences et vues nouvelles sur la nature des fermentations. Comp. Rend. Acad. Sci., 52:1260–1264, 1861.
- [4] E. Buchner. Alkoholische gährung ohne hefezellen. Ber. deut. chem. Ges., 30:117–124, 1897.
- [5] Antoine Lavoisier. Oeuvre. Mémoires de chimie et de physique, volume 2. 1770.
- [6] Robert V. Macalister. Nutritive sweetners made from starch. Advances in Carbohydrate Chemistry and Biochemistry, 36:7885–7891, 2003.
- [7] W. Kühne. Ueber den sehpurpur. Untersuch. Physiol. Institut. Univ. Heidelberg, 1:15–104, 1877.
- [8] FC Bing. The history of the word 'metabolism'. Journal of the History of Medicine and Allied Sciences, 1971.
- [9] Mitchell A. Lazar and Morris J. Birnbaum. De-meaning of metabolism. Science, 336:1651–1652, 2012.
- [10] Theodor Schwann. Mikroskopische untersuchungen ueber die uebadnstimmung in da struktur und dan wachstum da thiae und pflanzen. GE Reimer, 1839.

- [11] Graham Lusk. History of metabolism, 1922.
- [12] O. Fiehn. Metabolomics – the link between genotypes and phenotypes. 2002.
- [13] M. E. Smith and J. H. Strange. The surface of nanoparticle silicon as studied by solid-state nmr. Meas. Sci. Technol., 7:449, 1996.
- [14] M. E. Smith and J. H. Strange. Nmr spectroscopy in glass science: A review of the elements. Materials, 11:476, 2018.
- [15] N.A. Matwiyoff and T.E.Needham. Carbon-13 nmr spectroscopy of red blood cell suspensions. Biochemical and Biophysical Research Communications, 49:1158–1164, 1972.
- [16] R. T. Eakin, L. O. Morgan, C. T. Gregg, and N. A. Matwiyoff. Carbon-13 nuclear magnetic resonance spectroscopy of living cells and their metabolism of a specifically labeled ¹³C substrate. Biochemical and Biophysical Research Communications, 28:259–264, 1972.
- [17] J.L. Markley, D.H. Meadows, and O. Jardetzky. Nuclear magnetic resonance studies of helix-coil transitions in polyamino acids. J. Mol. Biol., 27:2535, 1967.
- [18] SJ Angyal and GS Bethell. Conformational analysis in carbohydrate chemistry. iii. the ¹³C nmr spectra of the hexuloses, 1976.
- [19] JS Leigh M Cohn. Magnetic resonance investigations of ternary complexes of enzyme–metal–substrate. Nature, 193:1037–1040, 1962.
- [20] O. Jardetzky and C.J. Jardetzky. Proton magnetic resonance spectra of amino acids. J. Biol. Chem., 233:383, 1958.
- [21] Asao Nakamura and Oleg Jardetzky. Systematic analysis of chemical shifts in the nuclear magnetic resonance spectra of peptide chains, i. glycine-containing dipeptides. Proc. Natl. Acad. Sci, 58:2212–2219, 1967.

- [22] K. Ugurbil S. Ogawa SM. Cohen R.G. Shulman, T.R. Brown and J.A. den Hollander. Cellular applications of ^{31}P and ^{13}C nuclear magnetic resonance. Science, 206:160–166, 1979.
- [23] Ofer Kaplan Jesus Ruiz-Cabello Jack S. Cohen, Jerzy W. Jaroszewski and Steven W. Collier”. A history of biological applications of nmr spectroscopy. Progress in Nuclear Magnetic, 28:53–85, 1995.
- [24] P. J. Seeley G. K. Radda. Recent studies on cellular metabolism by nuclear magnetic resonance. Annual Review of Physiology, 41:749–769, 1979.
- [25] J. R. Bales, J. D. Bell, J. K. Nicholson, P. J. Sadler and J. A. Timbrell, R. D. Hughes, P. N. Bennett, and R. Williams. Metabolic profiling of body fluids by proton nmr: Self-poisoning episodes with paracetamol (acetaminophen). Magnetic Resonance in Medicine, 6:300–306, 1988.
- [26] Raftery D. Gowda G., editor. volume 2037. Holt, Rinehardt and Winston, Humana, New York, NY., 2019.
- [27] Cynthia K. Larive, Gregory A. Barding, Jr., and Meredith M. Dinges. Nmr spectroscopy for metabolomics and metabolic profiling. Anal. Chem., 87:133–146, 2015.
- [28] Wolfgang Wiechert, Michael Möllney, Sören Petersen, and Albert A. de Graaf. A universal framework for ^{13}C metabolic flux analysis. Advan. Enzyme Regul., 3:256–283, 2001.
- [29] Thomas Gurley Andrey A. Gurinov Peter M. Tolstoy Ilya G. Shenderovich Nikolay Yu. Gorobets, Sergey A. Yermolayev and Nicholas E. Leadbeater. Difference between ^1H nmr signals of primary amide protons as a simple spectral index of the amide intramolecular hydrogen bond strength. Journal of Physical Organic Chemistry, 25:287–295, 2012.
- [30] Stig Benthin, Jens Nielsen, and John Villadsen. Anomeric specificity of glucose uptake systems in *Lactococcus cremoris*, *Escherichia coli* and *Saccharomyces cerevisiae*:

- Mechanism, kinetics, and implications. Biotechnology and Bioengineering, 40:137–146, 1992.
- [31] Michael Dauner, Tazio Storni, and Uwe Sauer. Bacillus subtilis metabolism and energetics in carbon-limited and excess-carbon chemostat culture. Journal of Bacteriology, 183:7308–7317, 2001.
- [32] Wolfgang Wiechert. 13c metabolic flux analysis. Metabolic Engineering, 3:195–206, 2001.
- [33] E. Miclet, V. Stoven, Paul A. M. Michels, Frederic R. Opperdoes, J.-Y. Lallemand, and F. Duffieux. Nmr spectroscopic analysis of the first two steps of the pentose-phosphate pathway elucidates the role of 6-phosphogluconolactonase. J. Biol. Chem., 276:34840–34846, 2001.
- [34] Helena Kovacs, Detlef Moskau, and Manfred Spraul. Cryogenically cooled probes—a leap in nmr technology. Progress in Nuclear Magnetic Resonance Spectroscopy, 46:131–155, 2005.
- [35] Harald Schwalbe. Editorial: New 1.2 ghz nmr spectrometers— new horizons? Angewandte Chemie, 56:10252–10253, 2017.
- [36] K. D. Atkinson M. J. Cowley P. I. P. Elliott S. B. Duckett G. G. R. Green I. G. Khazal J. Lopez-Serrano D. C. Williamson R. W. Adams, J. A. Aguilar. Reversible interactions with para-hydrogen enhance nmr sensitivity by polarization transfer. Science, 323:1708 – 1711, 2009.
- [37] C. Hilty D. E. Wemmer A. Pines L. Schröder, T. J. Lowery. Molecular imaging using a targeted magnetic resonance hyperpolarized biosensor. Science, 314:446 – 449, 2006.
- [38] J. H. Ardenkjaer-Larsen, B. Fridlund, A. Gram, G. Hansson, L. Hansson, M. H. Lerche, R. Servin, M. Thaning, and K. Golman. Increase in signal-to-noise ratio of > 10,000 times in liquid-state nmr. Proc. Natl. Acad. Sci. U. S. A., 100:10158–10163, 2003.

- [39] Pernille R. Jensen Mathilde H. Lerche, Magnus KarlssonJan H. Ardenkjær-Larsen. Targeted metabolomics with quantitative dissolution dynamic nuclear polarization. pages 385–393. Holt, Rinehardt and Winston.
- [40] Quentin Chappuis, Jonas Milani, Basile Vuichoud, Aurélien Bornet, Alvar D. Gossert, Geoffrey Bodenhausen, and Sami Jannin. Hyperpolarized water to study protein–ligand interactions. *J. Phys. Chem. Lett.*, 6:1674–1678, 2015.
- [41] Dennis Kurzbach, Estel Canet, Andrea G. Flamm, Aditya Jhajharia, Emmanuelle M. M. Weber, Robert Konrat, and Geoffrey Bodenhausen. Investigation of intrinsically disordered proteins through exchange with hyperpolarized water. *Angew. Chem. Int.*, 56:389–392, 2017.
- [42] Vesselin Z. Miloushev, Kristin L. Granlund, Rostislav Boltyanskiy, Serge K. Lyashchenko, Lisa M. DeAngelis, Ingo K. Mellinghoff, Cameron W. Brennan, Vivian Tabar, T. Jonathan Yang, Andrei I. Holodny, Ramon E. Sosa, YanWei W. Guo, Albert P. Chen, James Tropp, Fraser Robb, and Kayvan R. Keshari. Metabolic imaging of the human brain with hyperpolarized ^{13}C pyruvate demonstrates ^{13}C lactate production in brain tumor patients. *Cancer Res*, 78:3755–60, 2018.
- [43] Klaes Golman and J. Stefan Petersson. Metabolic imaging and other applications of hyperpolarized ^{13}C . *Acad Radiol*, 13:932–942, 2006.
- [44] Fabian Jähnig, Grzegorz Kwiatkowski, and Matthias Ernst. Conceptual and instrumental progress in dissolution dnp. *Journal of Magnetic Resonance*, 264:22–24, 2016.
- [45] Jan Henrik Ardenkjaer-Larsen. On the present and future of dissolution-dnp. *Journal of Magnetic Resonance*, 264:3–12, 2016.
- [46] Sami Jannin, Jean-Nicolas Dumez, Patrick Giraudeau, and Dennis Kurzbach. Application and methodology of dissolution dynamic nuclear polarization in physical, chemical and biological contexts. *Journal of Magnetic Resonance*, 305:41–50, 2019.

- [47] Arnaud Comment. Dissolution dnp for in vivo preclinical studies. Journal of Magnetic Resonance, 264:39– 48, 2016.
- [48] Lynette Smyth Steven Reynolds Simon P. Robinson Caroline J. Springer Martin O. Leach Geoffrey S. Payne Yann Jamin, Cristina Gabellieri and Thomas R. Eykyn. Hyperpolarized¹³C magnetic resonance detection of carboxypeptidase g2 activity. Magnetic Resonance in Medicine, 62:1300 –1304, 2009.
- [49] S. Bowen and C. Hilty. Time-resolved dynamic nuclear polarization enhanced nmr spectroscopy. Mol. BioSyst., 47:5235–5237, 2008.
- [50] Emeric Miclet, Daniel Abergel, Aurélien Bornet, Jonas Milan, Sami Jannin, and Geoffrey Bodenhausen. Toward quantitative measurements of enzyme kinetics by dissolution dynamic nuclear polarization. J. Phys. Chem. Lett., 19:3290–3295, 2014.
- [51] T. Harris, H. Degani, and L. Frydman. Hyperpolarized ¹³C nmr studies of glucose metabolism in living breast cancer cell cultures. NMR in Biomedicine, 2013.
- [52] Hyla Allouche-Arnona, Yonatan Hovavb, Lanette Friesen-Waldnerc, Jacob Sosnaa, J. Moshe Gomoria, and Shimon Vegaband Rachel Katz-Brull. Quantification of rate constants for successive enzymatic reactions with dnp hyperpolarized mr. NMR Biomed., 27:656–662, 2014.
- [53] Lucio Frydman Talia Harris, Galit Eliyah and Hadassa Degani. Kinetics of hyperpolarized ¹³C₁-pyruvate transport and metabolism in living human breast cancer cells. PNAS, 106:18131–18136, 2009.
- [54] Ardenkjær-Larsen JH, Bowen S, Petersen JR, Rybalko O, Vinding MS, Ullisch M, and Nielsen NC. Cryogen-free dissolution dynamic nuclear polarization polarizer operating at 3.35 t, 6.70 t and 10.1 t. Magnetic Resonance in Medicine, 81:2184–2194, 2019.
- [55] By Keith and N. Frayn. Metabolic Regulation: A human perspective. Portland Press LTD, 1996.

- [56] Jan Sapp. The prokaryote-eukaryote dichotomy: Meanings and mythology. Microbiology and Molecular Biology Reviews, 69:292–305, 2005.
- [57] Ulrich Warskulat, Andrea Reinen, Susanne Grether-Beck, Jean Krutmann, and Dieter Häussinger. The osmolyte strategy of normal human keratinocytes in maintaining cell homeostasis. Journal of Investigative Dermatology, 123:516–521, 2004.
- [58] D Zilberstein, V Agmon, S Schuldiner, and E Padan. Escherichia coli intracellular ph, membrane potential, and cell growth. Journal of Bacteriology, 158:246–252, 1984.
- [59] Walter B. Cannon. Organization for physiological homeostasis. Physiological Reviews, 9:399–431, 1929.
- [60] Monica H. Wei Eileen White Jared E. Toettcher Joshua D. Rabinowitz Lukas Bahati Tanner, Alexander G. Goglia. Four key steps control glycolytic flux in mammalian cells. Cell Systems, 7:1–14, 2018.
- [61] Robert C. Stanton. Glucose-6-phosphate dehydrogenase, nadph, and cell survival. IUBMB Life, 64:362–369, 2012.
- [62] D. P. Clark. The fermentation pathways of escherichia coli. FEMS Microbiol. Rev., 5:223–234, 1989.
- [63] S.G. Oliver, M.K. Winson, D.B. Kell, and F. Baganz. Systematic functional analysis of the yeast genome. Trends Biotechnol., 16:373–378, 1998.
- [64] Marta Cascante and Silvia Marin. Metabolomics and fluxomics approaches. Essays in Biochemistry, 45:67–81, 2008.
- [65] R.A. Harris. Encyclopedia of Biological Chemistry. 2013.
- [66] B.L. Horecker. The Roots of Modern Biochemistry. 1988.
- [67] T. F. Ryan E. L. Tatum A. Lwoff, C. B. Van Niel. Nomenclature of nutritional types of microorganisms. Cold Spring Harbor Symposia on Quantitative Biology, 11:302–303, 1946.

- [68] William C. Plaxton. The organization and regulation of plant glycolysis. Annual Review of Plant Physiology and Plant Molecular Biology, 47:185–214, 1946.
- [69] Peter J. Roach. Glycogen and its metabolism. Curr. Mol. Med., 2:101–120, 2002.
- [70] J. L. Ivy, M. C. Lee, J.T. Brozinick Jr, and M. J. Reed. Muscle glycogen storage after different amounts of carbohydrate ingestion. Trends Biotechnol., 65:2018–2023, 1988.
- [71] I. S. Hunter and H. L. Kornberg. Glucose-transport of escherichia coli growing in glucose-limited continuous culture. Biochem. J., 178:97–101, 1979.
- [72] J.A. Den Hollander P. Glynn K. Ugurbil, T.R. Brown and R. G. Shulman. High-resolution ^{13}C nuclear magnetic resonance studies of glucose metabolism in escherichia coli. Proc. Natl. Acad. Sci. USA, 75(1):3742–3746, 1978.
- [73] Adelfo Escalante, Ania Salinas Cervantes, Guillermo Gosset, and Francisco Bolívar. Current knowledge of the escherichia coli phosphoenolpyruvate–carbohydrate phosphotransferase system: peculiarities of regulation and impact on growth and product formation. Appl Microbiol Biotechnol, 94:1483–1494, 2012.
- [74] M. Salas, E. Vinuela, and A. Sols. Spontaneous and enzymatically catalyzed anomerization of glucose-6-phosphate and anomeric specificity of related enzymes. J. Biol. Chem., 240:561–586, 1965.
- [75] R. S. Balaban and J. A. Ferreti. Rates of enzyme-catalyzed exchange determined by twodimensional nmr: A study of glucose 6-phosphate anomerization and isomerization. PNAS, 80:1241–1245, 1983.
- [76] Maria V. Liberti and Jason W. Locasale. The warburg effect: How does it benefit cancer cells? Trends Biochem. Sci., 41:211–218, 2016.
- [77] Jacky L. Snoep Dan Nilsson Peter R. Jensen Brian J. Koebmann, Hans V. Westerhoff. The glycolytic flux in escherichia coli is controlled by the demand for atp. Biochemische Zeitschrift, 14:3909–3916, 2002.

- [78] Negelein E Warburg O, Posener K. Ueber den stoffwechsel der tumoren. Biochemische Zeitschrift, 152:319–344, 1924.
- [79] Sophia Y. Lunt and Matthew G. Vander Heiden. Aerobic glycolysis: Meeting the metabolic requirements of cell proliferation. Annual Review of Cell and Developmental Biology, 27:441–464, 2011.
- [80] J. L. Snoep M. R. de Graef, S. Alexeeva and M. J. Teixeira de Mattos. The steady-state internal redox state (nadh/nad) reflects the external redox state and is correlated with catabolic adaptation in escherichia coli. J. Bacteriol., 181:2351–2357, 1999.
- [81] W. J. Ingledew and R. K. Poole. The respiratory chains of escherichia coli. I T Microbiol. Rev., 48:222–271, 1984.
- [82]
- [83] Nicholas J Kruger and Antje von Schaeweny. The oxidative pentose phosphate pathway: structure and organisation. Current Opinion in Plant Biology, 6:236–246, 2003.
- [84] P Kotter H Juhnke, B Krems and Entian KD. Mutants that show increased sensitivity to hydrogen peroxide reveal an important role for the pentose-phosphate pathway in protection of yeast against oxidative stress. Mol. Gen. Genet., 252:456–464, 1996.
- [85] H. E. Neuhaus M. J. Emes. Non photosynthetic metabolism in plastids. FPlant Mol Biol, 51:111–140, 2000.
- [86] D. Estwick R. S. Gaskin and R. Peddi. G6pd deficiency: its role in the high prevalence of hypertension and diabetes mellitus. Ethn.Dis., 11:749–754, 2001.
- [87] Christopher B. Newgard. Metabolomics and Metabolic Diseases: Where Do We Stand? Cell Metabolism, 25(10):43–56, 2017.
- [88] Jeffrey R. Idle and Frank J. Gonzalez. Metabolomics. Cell metabolism, 6:348–351, 2007.

- [89] S.G. Oliver, M.K. Winson, and D.B. Kell F.Baganz. Systematic functional analysis of the yeast genome. Analyst, 16:373–378, 1998.
- [90] Mark P.Sawicki, Ghassan Samara, Michael Hurwitz, and Edward Passaro Jr. Human genome project. The American Journal of Surgery, 165:258–264, 1993.
- [91] Paul McGettigan. Transcriptomics in the rna-seq era. Current Opinion in Chemical Biology, 17:4–11, 2013.
- [92] Mike Tyers and Matthias Mann. From genomics to proteomics. Nature, 422:193–197, 2003.
- [93] Villas-Bôas S.G., Mas S., Åkesson M., and Smedsgaard J. Nielsen J. Mass spectrometry in metabolome analysis. Mass Spectrom. Rev., 24:613–646, 2005.
- [94] W.B. Dunn, N.J.C. Bailey, and H.E. Johnson. Measuring the metabolome: current analytical technologies. Analyst, 130:606–625, 2005.
- [95] K. Dettmer, P.A. Aronov, and B.D. Hammock. Mass spectrometry-based metabolomics. Mass Spectrom. Rev., 26:51–78, 2007.
- [96] Tomoyoshi Soga, Yoshiaki Ohashi, Yuki Ueno, Hisako Naraoka, Masaru Tomita, and Takaaki Nishioka. Quantitative metabolome analysis using capillary electrophoresis mass spectrometry. Journal of Proteome Research, 2:488–494, 2003.
- [97] Marc S. Sabatine, Emerson Liu, David A. Morrow, Eric Heller, Robert McCarroll, Roger Wiegand, Gabriel F. Berriz, Frederick P. Roth, , and Robert E. Gerszten. Metabolomic identification of novel biomarkers of myocardial ischemia. R. E. Circulation, 112:3868–3875, 2005.
- [98] Basem Kanawati Dimitrios Tziotis Rainer Lehmann Sara Forcisi, Franco Moritz and Philippe Schmitt-Kopplin. Liquid chromatography–mass spectrometry in metabolomics research: Mass analyzers in ultra high pressure liquid chromatography coupling. Journal of ChromatographyA, 1292:51–65, 2013.

- [99] Eva Maria Lenz and Ian D. Wilson. Analytical strategies in metabonomics. Journal of Proteome Research, 6:443–458, 2007.
- [100] Marie Brown Joshua D. Knowles Steve O’Hagan, Warwick B. Dunn and Douglas B. Kell. Closed-loop, multiobjective optimization of analytical instrumentation: Gas chromatography time-of-flight mass spectrometry of the metabolomes of human serum and of yeast fermentations. Anal. Chem., 77:290–303, 2005.
- [101] Jun Yang, Guowang Xu, Yufang Zheng, Hongwei Kong, Chang Wang, Xinjie Zhao, and Tao Pang. Strategy for metabonomics research based on high-performance liquid chromatography and liquid chromatography coupled with tandem mass spectrometry. Journal of Chromatography A, 1084:214–221, 2005.
- [102] By Wilfried and editor = Taylor Francis group year = 2006 M.A. Niessen, title = Liquid Chromatography-Mass Spectrometry.
- [103] Chang Wang, Hongwei Kong, Yufeng Guan, Jun Yang, Jianren Gu, Shengli Yang, , and Guowang Xu. Plasma phospholipid metabolic profiling and biomarkers of type 2 diabetes mellitus based on high-performance liquid chromatography/electrospray mass spectrometry and multivariate statistical analysis. Anal. Chem., 77:4108–4116, 2005.
- [104] R.A. Wallingford and A.G. Ewing. Capillary electrophoresis. Advances in Chromatography, 29:1–76, 1989.
- [105] Bernhard Michalke. Potential and limitations of capillary electrophoresis inductively coupled plasma mass spectrometry. J. Anal. At. Spectrom., 14:1297–1302, 1999.
- [106] Corte L, Antonielli L, Roscini L, Fatichenti F, and Cardinali G. Influence of cell parameters in fourier transform infrared spectroscopy analysis of whole yeast cells. Analyst, 136:2339–2349, 2011.
- [107] Maria Grazia Volpe, Susan Costantini, Elena Coccia, and Lucia Parrillo Marina Paolucci. Evaluation of metabolic changes induced by polyphenols in the cray-

- fish *astacus leptodactylus* by metabolomics using fourier transformed infrared spectroscopy. Journal of Biosciences, 43:585–596, 2018.
- [108] Laura Corte, Matteo Tiecco, Luca Roscini, Sergio De Vincenzi, Claudia Colabella, Raimondo Germani, Carlo Tascini, and Gianluigi Cardinali. Ftir metabolomic fingerprint reveals different modes of action exerted by structural variants of n-alkyltropinium bromide surfactants on *escherichia coli* and *listeria innocua* cells. PLOS ONE, 10:e0115275, 2014.
- [109] Matthew J Baker, Júlio Trevisan, Paul Bassan, Rohit Bhargava, Holly J Butler, Konrad M Dorling, Peter R Fielden, Simon W Fogarty, Nigel J Fullwood, Kelly A Heys, Caryn Hughes, Peter Lasch, Pierre L Martin-Hirsch, Blessing Obinaju, Ganesh D Sockalingum, Josep Sulé-Suso, Rebecca J Strong, Michael J Walsh, Bayden R Wood, and Peter Gardner Francis L Martin. Using fourier transform ir spectroscopy to analyze biological materials. Nature Protocols, 9:1771–1791, 2014.
- [110] Wishart DS, Tzur D, Knox C, and et al. Hmdb: the human metabolome database. Nucleic Acids Res., 35:D521–6, 2007.
- [111] Abdul-Hamid Emwas, Raja Roy, Ryan T. McKay, Leonardo Tenori, Edoardo Saccenti, G. A. Nagana Gowda, Daniel Raftery, Fatimah Alahmari, Lukasz Jaremko, Mariusz Jaremko, and David S. Wishart. Nmr spectroscopy for metabolomics research. Metabolites, 9:10.3390, 2019.
- [112] Iman Tavassoly, Joseph Goldfarb, and Ravi Iyengar. Systems biology primer: the basic methods and approaches. Essays in Biochemistry, page EBC20180003, 2018.
- [113] Wolfram Weckwerth. Metabolomics in systems biology. Annual Review of Plant Biology, 54:669–689, 2007.
- [114] * Miguel A. Aon and Sonia Cortassa. Systems biology of the fluxome. Processes, 3:607–618, 2015.

- [115] L. Agius. The physiological role of glucokinase binding and translocation in hepatocytes. Advan. Enzyme Regul., 38:303–331, 1998.
- [116] Silvia MARIN, W.N. Paul LEE, Sara BASSILIAN, Shu LIM, Laszlo G. BOROS and Josep J. CENTELLES, Josep Maria FERNANDEZ-NOVELL and Joan J. GUINOVART, and Marta CASCANTE. Dynamic profiling of the glucose metabolic network in fasted rat hepatocytes using [1,2-¹³C₂]glucose. Biochem. J., 381:287–294, 2004.
- [117] Charles C. McDonald and William Dale. Phillips. Manifestations of the tertiary structures of proteins in high-frequency nuclear magnetic resonance. J. Am. Chem. Soc., 24:6332–6341, 1967.
- [118] J.L. Jungnickel and J.W. Forbes. Quantitative measurement of hydrogen types by integrated nuclear magnetic resonance intensities. Anal. Chem., 35:938–942, 1963.
- [119] D.P. Hollis. Quantitative analysis of aspirin, phenacetin, and caffeine mixtures by nuclear magnetic resonance spectrometry. Anal. Chem., 35:1682–1684, 1963.
- [120] Patrick Giraudeau. Challenges and perspectives in quantitative nmr. Magn. Reson. Chem., 55:61–69, 2017.
- [121] H. Jancke F. Malz. Validation of quantitative nmr. Journal of Pharmaceutical and Biomedical Analysis, 38:813–823, 2005.
- [122] Ulrik Holzgrabe, Bernd W.K. Diehl, and Iwona Wawer. Nmr spectroscopy in pharmacy. Journal of Pharmaceutical and Biomedical Analysis, 17:557–616, 1998.
- [123] László G. Boros, Marta Cascante, and Wai-Nang Paul Lee. Metabolic profiling of cell growth and death in cancer: applications in drug discovery. Drug Discovery Today, 7:364–372, 2002.
- [124] F. Wei, K. Furuhata, M. Koda, F. Hu, R. Kato, T. Miyakawa, and M. Tanokura. ¹³C nmr-based metabolomics for the classification of green coffee beans according to variety and origin. J. Agric. Food Chem., 60:10118–10125, 2012.

- [125] I.J. Colquhoun P.S. Belton and B.P. Hills. Applications of nmr to food science. Annual Reports on NMR Spectroscopy, 26:1–53, 1993.
- [126] Flaminia Cesare Marincola, Antonio Noto, Pierluigi Caboni, Alessandra Reali, Luigi Barberini, Milena Lussu, Federica Murgia, Maria Laura Santoru, and Luigi Atzori⁵ Vassilios Fanos. A metabolomic study of preterm human and formula milk by high resolution nmr and gc/ms analysis: preliminary results. The Journal of Maternal-Fetal and Neonatal Medicine, 25:62–67, 2012.
- [127] W. B. Dunn, D. I. Broadhurst, H. J. Atherton, R. Goodacre, and J. L. Griffin. A metabolomic study of preterm human and formula milk by high resolution nmr and gc/ms analysis: preliminary results. Chemical Society Reviews, 40:387–426, 2011.
- [128] Patrick Giraudeau. Nmr-based metabolomics and fluxomics: developments and future prospects. Analyst, Royal Society of Chemistry, page 10.1039/D0AN00142B, 2020.
- [129] Alessia Vignoli, Gaia Meoni Dr. Veronica Ghini, Cristina Licari, Dr. Panteleimon G. Takis, Leonardo Tenori, Paola Turano, and Claudio Luchinat. High-throughput metabolomics by 1d nmr. Angew.Chem. Int. Ed., 58:968–994, 2019.
- [130] Silas G. Villas-Bôasm, Sandrine Mas, Mats Åkesson, Jørn Smedsgaard, and Jens Nielsen. Mass spectrometry in metabolome analysis. Mass Spectrometry Reviews, 24:613–646, 2005.
- [131] Jie Hao, Manuel Liebeke, William Astle, Maria De Iorio, Jacob G Bundy, and Timothy M D Ebbels. Bayesian deconvolution and quantification of metabolites in complex 1d nmr spectra using batman. Nature Protocols, 9:1416–1427, 2014.
- [132] Zach Serber, Adrian T. Keatinge-Clay, Richard Ledwidge, Alexander E. Kelly, Susan M. Miller, and Volker Dötsch. High-resolution macromolecular nmr spectroscopy inside living cells. J. Am. Chem. Soc., 123:2446–2447, 2001.
- [133] Susanne D. Riegel and Garrett M. Leskowitz. Benchtop nmr spectrometers in academic teaching. Trends in Analytical Chemistry, page 10.1016, 2016.

- [134] Craig R. Malloy, Elizabeth Maher, Isaac Marin-Valencia, Bruce Mickey, Ralph J. De Berardinis, and A. Dean Sherry. Carbon-13 nuclear magnetic resonance for analysis of metabolic pathways. Cambridge University Press, pages 415–445, 2013.
- [135] T. R. Brown and S. Ogawa. 31p nuclear magnetic resonance kinetic measurements on adenylate kinas. Proc. natn. Acad. Sci, 74:3627–3631, 1977.
- [136] Charles H. Cunningham, Justin Y.C. Lau, Albert P. Chen, Benjamin J. Geraghty, William J. Perks, Idan Roifman, Graham A. Wright, and Kim A. Connelly. 19f nmr metabolomics for the elucidation of microbial degradation pathways of fluorophenols. Circulation Research, 119:1177–1182, 2016.
- [137] Laura Castañar. Pure shift 1h nmr: what is next? Magnetic Resonance in Chemistry, 55:47–53, 2016.
- [138] Liladhar Paudel, Ralph W. Adams, Pter Kirly, Juan A. Aguilar, Mohammadali Foroozandeh, Matthew J. Cliff, Mathias Nilsson, Pter Sndor, Jonathan P. Waltho, and Gareth A. Morris. Simultaneously enhancing spectral resolution and sensitivity in heteronuclear correlation nmr spectroscopy. Angew. Chem., 125:11830–11833, 2013.
- [139] Jéréémy Marchand, Estelle Martineau, Yann Guitton, Gaud Dervilly-Pinel, and Patrick Giraudeau. Multidimensional nmr approaches towards highly resolved, sensitive and high-throughput quantitative metabolomics. Current Opinion in Biotechnology, 43:49–55, 2016.
- [140] Baptiste Féraud, Bernadette Govaerts, Michel Verleysen, and Pascal de Tullio. Statistical treatment of 2d nmr cosy spectra in metabolomics: data preparation and clustering-based evaluation of the metabolomic informative content and comparison with 1h-nmr. Metabolomics, 11:1756–1768, 2015.
- [141] Wolfram Gronwald, Matthias S. Klein, Hannelore Kaspar, Stephan R. Fagerer, Nadine Nürnberger, Katja Dettmer, Thomas Bertsch, and Peter J. Oefner. Urinary metabolite quantification employing 2d nmr spectroscopy. Anal. Chem., 2008:9288–9297, 2008.

- [142] Maryam Tabatabaei Anaraki, Daniel H. Lysak, Ronald Soong, Myrna J. Simpson, Manfred Spraul, Wolfgang Bermel, Hermann Heumann, Marcel Gundy, Holger Boenischd, and André J. Simpson. Nmr assignment of the in vivo daphnia magna metabolome. Analyst, 145:5787–5800, 2020.
- [143] Justine Leenders, Benita Percival Martin Grootveld, Miles Gibson, Federico Casanova, and Philippe B. Wilson. Low-field and benchtop nmr. Journal of Magnetic Resonance, 306:27–35, 2019.
- [144] Justine Leenders, Benita Percival Martin Grootveld, Miles Gibson, Federico Casanova, and Philippe B. Wilson. Benchtop low-frequency 60 mhz nmr analysis of urine: A comparative metabolomics investigation. Trends in Analytical Chemistry, 10:155, 2020.
- [145] B. M. Goodson. Nuclear magnetic resonance of laser-polarized noble gases in molecules, materials, and organisms. J. Magn. Reson., 155:157–216, 2002.
- [146] W. Proctor A. Abragam. C.R. Hebd. Seances Acad. Sci. 246,2253-2256, (1958).
- [147] Orla Teahan, Simon Gamble, Elaine Holmes, Jonathan Waxman, Jeremy K. Nicholson, Charlotte Bevan, and Hector C. Keun. Impact of analytical bias in metabonomic studies of human blood serum and plasma. Anal. Chem., 78:4307–4318, 2006.
- [148] Kirstin Feussner and Ivo Feussner. Ex vivo metabolomics: A powerful approach for functional gene annotation. Trends Plant Sci, 25:829–830, 2020.
- [149] Iola F. Duarte, Silvia O. Diaz, and Ana M. Gil. Nmr metabolomics of human blood and urine in disease research. Journal of Pharmaceutical and Biomedical Analysis, 93:17–26, 2014.
- [150] R.K. Gupta, A.G.Redfield, and M. Cohn. Nmr double resonance study of azidoferricytochrome. C. Biochem. Biophys. Res. Commun, 273:6981–6986, 1970.

- [151] H. L. Johnson D. W. Thomas M. Ellis L. Cary J. I. Degraw. Application of ^{13}C -nmr spectroscopy to in vitro analysis of enzyme kinetics. Journal of Pharmaceutical Sciences, 6:1660–1662, 1977.
- [152] D. H. Buttlair B.D. Rao and M. Cohn. ^{31}P nmr studies of the arginine kinase reaction. equilibrium constants and exchange rates at stoichiometric enzyme concentration. Journal of Biological Chemistry, 251:6981–6986, 1976.
- [153] Kai Tittmann, Ralph Golbik, Kathrin Uhlemann, Ludmila Khailova, Gunter Schneider, Frank Jordan Mulchand Patel, David M. Chipman, Ronald G. Duggleby, and Gerhard Hubner. Nmr analysis of covalent intermediates in thiamin diphosphate enzymes. Biochemistry, 42:7885–7891, 2003.
- [154] Teresa W-M. Fan, Andrew N. Lane, and Richard M. Higashi. Stable isotope resolved metabolomics studies in ex vivo tissue slices. Bio Protoc, 6:e1730, 2016.
- [155] Stephanie Deprez, Brian C Sweatman, Susan C. Connor, John N. Haselden, and Catherine J. Waterfiel. Optimisation of collection, storage and preparation of rat plasma for ^1H nmr spectroscopic analysis in toxicology studies to determine inherent variation in biochemical profiles. Journal of Pharmaceutical and Biomedical Analysis, 30:1297–1310, 2002.
- [156] Eun Ran Kim, Hyuk Nam Kwon, Hoonsik Nam, Jae J. Kim, Sunghyouk Park, and Young-Ho Kim. Urine-nmr metabolomics for screening of advanced colorectal adenoma and early stage colorectal cancer. Scientific Reports, 9:4786, 2019.
- [157] Joana Pinto, M. Rosario M. Domingues, Eulalia Galhano, Cristina Pita, Maria do Ceu Almeida, Isabel M. Carreira, and Ana M. Gil. Human plasma stability during handling and storage: impact on nmr metabolomics. Analyst, 139:1168, 2014.
- [158] Trixi von Schlippenbach, Peter J. Oefner, and Wolfram Gronwald. Systematic evaluation of non-uniform sampling parameters in the targeted analysis of urine metabolites by ^1H , ^2D nmr spectroscopy. Scientific Reports, 2018:4249, 2014.

- [159] Tom Frenkiel A. J. Shaka, James Keeler and Ray Freeman. An improved sequence for broadband decoupling: Waltz-16. Journal of magnetic resonance, 52:335–338, 1983.
- [160] Natalie J. Serkova, Zachary Van Rheen, Meghan Tobias, Joshua E. Pitzer, and J. Erby Wilkinson. Utility of magnetic resonance imaging and nuclear magnetic resonance-based metabolomics for quantification of inflammatory lung injury. Am J Physiol Lung Cell Mol Physiol, 296:L152–L161, 2008.
- [161] Parker JC and Townsley MI. Evaluation of lung injury in rats and mic. Am J Physiol Lung Cell Mol Physiol, 286:L231–L246, 2004.
- [162] Charles H. Cunningham, Justin Y.C. Lau, Albert P. Chen, Benjamin J. Geraghty, William J. Perks, Idan Roifman, Graham A. Wright, and Kim A. Connelly. Hyperpolarized ^{13}C metabolic mri of the human heart. Circulation Research, 119:1177–1182, 2016.
- [163] G. Navon, S. Ogawa, R. G. Shulman, and T. Yamane. ^{31}P nuclear magnetic resonance studies of ehrlich ascites tumor cells. Proc. Natl. Acad. Sci., 74:87–91, 1977.
- [164] Jumpei Hamatsu, Daniel O’Donovan, Takashi Tanaka, Takahiro Shirai, Yuichiro Hourai, Tsutomu Mikawa, Teppei Ikeya, Masaki Mishima, Wayne Boucher, Brian O. Smith, Ernest D. Laue, Masahiro Shirakawa, and Yutaka Ito. High-resolution heteronuclear multidimensional nmr of proteins in living insect cells using a baculovirus protein expression system. Journal of the American Chemical Society, 135:1688–1691, 2013.
- [165] T. Bezabeh, M. R. A. Mowat, L. Jarolim, A. H. Greenberg, and I. C. P. Smith. Detection of drug-induced apoptosis and necrosis in human cervical carcinoma cells using ^1H nmr spectroscopy. Cell Death Differentiation, 8:219–224, 2001.
- [166] William T. Evanochko, Thian C. Ng, and Jerry D. GLICKS. Application of in vivo nmr spectroscopy to cancer. Magnetic Resonance in Medicine, 1:508–534, 1984.

- [167] M. P. Gamcsik, K. K. Millis, and O. M. Colvin. Noninvasive detection of elevated glutathione levels in mcf-7 cells resistant to 4-hydroperoxycyclophosphamide. Cancer Res., 55:2012–2016, 1995.
- [168] Anthony Mancuso, Susan T. Sharfstein, Sean N. Tucker, Douglas S. Clark, and Harvey W. Blanch. Examination of primary metabolic pathways in a murine hybridoma with carbon-13 nuclear magnetic resonance spectroscopy. Biotechnology and Bioengineering, 44:563–585, 1994.
- [169] Maryam Tabatabaei Anaraki, Rudraksha Dutta Majumdar, Nicole Wagner, Ronald Soong, Vera Kovacevic, Eric Reiner, Satyendra Bhavsar, Xavier Ortiz Almirall, Daniel Lane, Myrna J. Simpson, Hermann Heumann, Sebastian Schmidt, and André J. Simpson. Development and application of a low volume flow system for solution-state in vivo nmr. Anal. Chem., 90:7912–7921, 2018.
- [170] Steve Y. Rhieu, Aaron A. Urbas, Daniel W. Bearden, John P. Marino, Katrice A. Lipka, and Vytas Reipa. Probing the intracellular glutathione redox potential by in-cell nmr spectroscopy. Angew. Chem., 126:457–460, 2014.
- [171] K Ugurbil, D L Guernsey, T R Brown, P Glynn, N Tobkes, and I S Edelman. 31p nmr studies of intact anchorage-dependent mouse embryo fibroblasts. Proc. Natl. Acad. Sci. U.S.A., 78:4843–7, 1981.
- [172] David L.Foxall, Jack S.Cohen, and James B.Mitchell. Continuous perfusion of mammalian cells embedded in agarose gel threads. Experimental Cell Research, 154:521–529, 1984.
- [173] Michael H. Melner, Stephen T. Sawyer, William T. Evanochko, Thian C. Ng, Jerry D. Glickson, and David Puett. Phosphorus-31 nuclear magnetic resonance analysis of epidermal growth factor action in a-431 human epidermoid carcinoma cells and sv-40 virus transformed mouse fibroblasts. Biochemistry, 22:2039–2042, 1983.

- [174] N.A. Matwiyoff and T.E. Needham. Carbon-13 nmr spectroscopy of red blood cell suspensions. Biochemical and Biophysical Research Communications, 49:1158–1164, 1972.
- [175] Philipp Selenko, Zach Serber, Bedrick Gadea, Joan Ruderman, and Gerhard Wagner. Quantitative nmr analysis of the protein g b1 domain in xenopus laevis egg extracts and intact oocytes. PNAS, 103:11904–11909, 2006.
- [176] David S Burz, Kaushik Dutta, David Cowburn, and Alexander Shekhtman. In-cell nmr for protein-protein interactions (stint-nmr). Nature Protocols, 1:146–152, 2006.
- [177] A. Overhauser. Polarization of nuclei in metals. Phys. Rev., 1:411–415, 1953.
- [178] Jan H. Ardenkjær-Larsen, Björn Fridlund, Andreas Gram, Georg Hansson, Lennart Hansson, Mathilde H. Lerche, Rolf Servin, Mikkel Thaning, , and Klaes Golman. Increase in signal-to-noise ratio of > 10,000 times in liquid-state nmr. PNAS, 100:10158–10163, 2003.
- [179] A.W. Barb, S.K. Hekmatyar, J.N. Glushka, and J.H. Prestegard. Probing alanine transaminase catalysis with hyperpolarized ^{13}C -pyruvate. J. Magn. Res., 228:59–65, 2010.
- [180] Sebastian Meier, Magnus Karlsson, Pernille R. Jensen, Mathilde H. Lerche, and Jens Ø. Duus. Metabolic pathway visualization in living yeast by dnp-nmr. Molecular Biosystems, 7:2834–2836, 2011.
- [181] Mathilde H. Lerche, Sebastian Meier, Pernille R. Jensen, Herbert Baumann, Bent O. Petersen, Magnus Karlsson, Jens Ø. Duus, Jan, and H. Ardenkjær-Larsen. Study of molecular interactions with ^{13}C dnp-nmr. Journal of Magnetic Resonance, 203:52–56, 2010.
- [182] Basile Vuichoud, Jonas Milani, Aurélien Bornet, Roberto Melzi, Sami Jannin, and Geoffrey Bodenhausen. Hyperpolarization of deuterated metabolites via remote

- cross-polarization and dissolution dynamic nuclear polarization. J. Phys. Chem. B, 118:1411–1415, 2014.
- [183] Talia Harris, Christian Bretschneider, and Lucio Frydman. Dissolution dnp nmr with solvent mixtures: Substrate concentration and radical extraction. Journal of Magnetic Resonance, 211:96–100, 2011.
- [184] Steven Reynolds, Adriana Bucur, Michael Port, Tooba Alizadeh, Samira M.Kazan, Gillian M.Tozer, and Martyn N.J.Paley. A system for accurate and automated injection of hyperpolarized substrate with minimal dead time and scalable volumes over a large range. Journal of Magnetic Resonance, 239:1–8, 2014.
- [185] Tian Chenga, Mor Mishkovsky, Jessica A. M. Bastiaansen, Olivier Ouarid, Ben van den Brandt Patrick Hautle, Paul Tordo, and Arnaud Comment. Automated transfer and injection of hyperpolarized molecules with polarization measurement prior to in vivo nmr. NMR Biomed., 26:1582–1588, 2013.
- [186] T. Wenckebach. Dynamic nuclear polarization via the cross effect and thermal mixing: A. the role of triple spin flips. Journal of Magnetic Resonance, 299:124–134, 2019.
- [187] T. Wenckebach. Essentials of Dynamic Nuclear Polarization. Sprindrift Publications, (2016).
- [188] W.T. Wenckebach. Spectral diffusion and dynamic nuclear polarization: beyond the high temperature approximation. Journal of Magnetic Resonance, 284:104–114, 2017.
- [189] A. Abragam and M. Goldman. Principles of dynamic nuclear polarisation. Rep. Prog. Phys. 41, 1978.
- [190] T. Wenckebach. Appl. Magn. Reson. Sci. 34, 227-235, (2008).
- [191] A. Abragam. Principles of nuclear magnetism. Oxford University Press, 1961.

- [192] Daphna Shimon, Yonatan Hovav, Ilia Kaminker, Akiva Feintuch, Daniella Goldfarb, and Shimon Vega. Simultaneous dnp enhancements of ^1H and ^{13}C nuclei: theory and experiments. Phys. Chem. Chem. Phys., 17:11868, 2015.
- [193] A. A. Manenkov, A. V. Kessenikh, V. I. Lushchikov and Y. V. Taran. Proton polarization in irradiated polyethylenes. Sov. Phys. Solid State, 5:321, 1963.
- [194] D. S. Wollan. Dynamic nuclear polarization with an inhomogeneously broadened esr line. i. theory. Phys. Rev. B, 13:3671, 1976.
- [195] Thorsten Maly, Galia T. Debelouchina, Vikram S. Bajaj, Kan-Nian Hu, Chan-Gyu Joo, Melody L. Mak-Jurkauskas, Jagadishwar R. Sirigiri, Patrick C. A. van der Wel, Judith Herzfeld, Richard J. Temkin, and Robert G. Griffin. Dynamic nuclear polarization at high magnetic fields. J. Chem. Phys., 128, 2008.
- [196] V. Bouffard, S.F.J. Cox and M. Goldman. The coupling of two nuclear Zeeman reservoirs by the electronic spin-spin reservoir. J. Phys. C: Solid State Phys., 6, 1973.
- [197] M. Borghini. Spin temperature model of dynamic nuclear polarization using free radicals. Phys. Rev. Lett., 20:419–421, 1968.
- [198] Sami Jannin, Arnaud Comment, and J. J. van der Klink. Dynamic nuclear polarization by thermal mixing under partial saturation. Appl Magn Reson, 43:59–68, 2012.
- [199] S. C. Serra, A. Rosso, and F. Tedoldi. On the role of electron-nucleus contact and microwave saturation in thermal mixing dnp. Phys. Chem. Chem. Phys., 15:84168428, 2013.
- [200] W. Proctor and A. Abragam. Spin temperature. Physical Review, 109:1441–1458, 1958.
- [201] Ilia Kamnicker, Hui Zhang, Suchada Rajca, Andrzej Rajca, Alisa Leavesley, Sheetal Jain and Songi Han. Maximizing nmr signal per unit time by facilitating the e-e-n cross effect dnp rate †. Phys. Chem. Chem. Phys., 20:27646–27657, 2019.

- [202] W. T. Wenckebach. Dynamic nuclear polarization via I mixing: beyond the high temperature approximation. J. Magn. Res., 277:68–78, 2017.
- [203] Mathieu Baudin, Basile Vuichoud, Aurélien Bornet, Geoffrey Bodenhausen, and Sami Jannin. A cryogen-consumption-free system for dynamic nuclear polarization at 9.4 t. Journal of Magnetic Resonance, 294:115–121, 2018.
- [204] N. Clarke J. Urbahn D. Anderson J.H. Ardenkjaer-Larsen, A.M. Leach and T.W. Skloss. Dynamic nuclear polarization polarizer for sterile use intent. NMR Biomed., 24(8):927–932, 2011.
- [205] C. Parish Q. Wang A. Kiswandhi, P. Niedbalski and L. Lumata. Assembly and performance of a 6.4 t cryogen-free dynamic nuclear polarization system. Magn. Reson. Chem., 55(9):846–852, 2017.
- [206] Herv8 Vezin Ghislaine Frebourg Daniel Abergel Geoffrey Bodenhausen Emmanuelle M. M. Weber, Giuseppe Sicoli and Dennis Kurzbach. Sample ripening through nanophase separation influences the performance of dynamic nuclear polarization. Angew. Chem. Int. Ed., 17:5171 –5175., 2018.
- [207] Daniel Lee Vincent Maurel Serge Gambarelli Michel Bardet Sabine Hediger Anne-Laure Barra Gaël De Paëpe Hiroki Takahashi, Carlos Fernández-de-Alba. Optimization of an absolute sensitivity in a glassy matrix during dnp-enhanced multidimensional solid-state nmr experiments. Journal of Magnetic Resonance, 239:91–99, 2014.
- [208] Alexey S. Kiryutin, Bogdan A. Rodin, Alexandra V. Yurkovskaya, Konstantin L. Ivanov, Dennis Kurzbach, Sami Jannin, David Guarin, Daniel Abergele, and Geoffrey Bodenhausen. Transport of hyperpolarized samples in dissolution-dnp experiments. Phys. Chem. Chem. Phys., 21:13696, 2019.
- [209] Arthur C. Pinon, Andrea Capozzi, and Jan Henrik Ardenkjær-Larsen. Hyperpolarized water through dissolution dynamic nuclear polarization with uv-generated radicals. Communications Chemistry, 3, 2020.

- [210] Guido Pintacuda Hartmut Oschkinat Kristaps Jaudzems, Tatyana Polenova and Anne Lesage. Dnp nmr of biomolecular assemblies. Journal of Structural Biology, 206:90–98, 2018.
- [211] D Guarin et al. Characterizing thermal mixing dynamic nuclear polarization via cross-talk between spin reservoirs. J. Phys. Chem. Lett., 8, 5531-5536, 2017.
- [212] Jonas Milani, Basile Vuichoud, Aurélien Bornet, Pascal Miéville, Roger Mottier, Sami Jannin, and Geoffrey Bodenhausen. Review of Scientific Instruments, 86:024101, 2015.
- [213] Hsueh-Ying Chen and Christian Hilty. Implementation and characterization of flow injection in dissolution dnp-nmr. Chem. Phys. Chem, 16:2646–2652, 2015.
- [214] Corinna Dietrich, Julia Wissel, Jannik Knoche, Oliver Lorenz, and Jörg Matysik. Simple device for dissolution and sample transfer for applications in spin-hyperpolarization. Molecular Physics, 117:2772–2776, 2018.
- [215] Michael Batel, Marcin Krajewski, Kilian Weiss, Oliver With, Alexander Däpp, Andreas Hunkeler, Martin Gimersky, Klaas P. Pruessmann, Peter Boesiger, Beat H. Meier, Sebastian Kozerke, and Matthias Erns. A multi-sample 94 ghz dissolution dynamic-nuclear-polarization system. Journal of Magnetic Resonance, 214:166–174, 2012.
- [216] T. Harris, O.Szekely, , and L. Frydman. On the potential of hyperpolarized water in biomolecular nmr studies. J. Phys. Chem. B., 118:33281–3290, 2014.
- [217] Jihyun Kim, Mengxiao Liu, and Christian Hilty. Modeling of polarization transfer kinetics in protein hydration using hyperpolarized water. J. Phys. Chem. B., 121:6492–6498, 2017.
- [218] Sami Jannin, Aurélien Bornet, Sonia Colombo, and Geoffrey Bodenhausen. Low-temperature cross polarization in view of enhancing dissolution dynamic nuclear polarization in nmr. Chemical Physics Letters, 517:234–236, 2011.

- [219] Lucio Frydman, Tali Scherf, and Adonis Lupulescu. The acquisition of multidimensional nmr spectra within a single scan. PNAS, 99:15858–15862, 2002.
- [220] Dennis Kurzbach, Carine van Heijenoort, Daniel Abergel, and Jean-Nicolas Dumez. Single-scan ^{13}C diffusion-ordered nmr spectroscopy of dnp hyperpolarised substrates. Chem.–Eur. J., 23:16722–16727, 2017.
- [221] Patrick Giraudeau, Yoav Shrot, and Lucio Frydman. Multiple ultrafast, broadband 2d nmr spectra of hyperpolarized natural products. J. Am. Chem. Soc., 131:13902–13903, 2009.
- [222] S. R. Hartmann and E. L. Hahn. Nuclear double resonance in the rotating. Chemical Physics Letters, 128:2042–2053, 1962.
- [223] Dmitry Shishmarev Alan J. Wright Tiago B. Rodrigues Giuseppe Pileio Gabriele Stevanato Kevin M. Brindle Philip W. Kuchel. Sub-minute kinetics of human red cell fumarase: 1h spin-echo nmr spectroscopy and ^{13}C rapid-dissolution dynamic nuclear polarization. NMR in Biomedicine, 31:e3870, 2018.
- [224] Hyla Allouche-Arnon, Yonatan Hovav, Lanette Friesen-Waldner, Jacob Sosna, J. Moshe Gomori, Shimon Vega, and Rachel Katz-Brull. Quantification of rate constants for successive enzymatic reactions with dnp hyperpolarized mr. NMR Biomed., 27:656–662, 2014.
- [225] Sivaranjan Uppala, Ayelet Gamliel, Gal Sapir, Jacob Sosna, J. Moshe Gomori, and Rachel Katz-Brull. Observation of glucose-6-phosphate anomeric exchange in real-time using ddnp hyperpolarised nmr. RSC Adv., 10:41197, 2020.
- [226] Aude Sadet, Emmanuelle M. M. Weber, Aditya Jhajharia, Dennis Kurzbach, Geoffrey Bodenhausen, Emeric Miclet, and Daniel Abergel. Rates of chemical reactions embedded in a metabolic network by dissolution dynamic nuclear polarisation nmr. Chem. Eur. J., 24:5456–5461, 2018.

- [227] P. G. Pentchev J. M. Bailey, P. H. Fishman. Studies on mutarotases ii. investigations of possible rate-limiting anomerizations in glucose metabolism. J. Biol. Chem., 243:4827–4831, 1968.
- [228] Storn R. and K. Price. Differential evolution - a simple and efficient heuristic for global optimization over continuous spaces. Journal of Global Optimization, 11:341 – 359, 1997.
- [229] Aude Sadet. Etudes de cinétiques enzymatiques par polarisation dynamique nucléaire avec dissolution (D-DNP) : application à l'étape oxydative de la voie des pentoses phosphates (PPP). PhD thesis, Ecole Normale Supérieure, 2018.
- [230] S.G. Prapulla and N.G. Karanth. Encyclopedia of Food Microbiology. 2014.
- [231] F. Delaglio, S. Grzesiek, G.W. Vuister, G. Zhu, J. Pfeifer, and A. Bax. Nmrpipe: A multidimensional spectral processing system based on unix pipes. J. Biomol. NMR, 6:277–293, 1995.
- [232] J. Jonathan Helmus and Christopher P. Jaroniec. Nmrplug: An open source python package for the analysis of multidimensional nmr data. J. Biomol NMR, 55(4):355–367, April 2013.
- [233] Naglis Malys Matthew G.S. Norris. What is the true enzyme kinetics in the biological system? an investigation of macromolecular crowding effect upon enzyme kinetics of glucose-6-phosphate dehydrogenase. Biochemical and Biophysical Research Communications, 405:388–392, 2011.
- [234] Sarah J. Nelson, John Kurhanewicz, Daniel B. Vigneron, Peder E. Z. Larson, Andrea L. Harzstark, Marcus Ferrone, Mark van Criekinge, Jose W. Chang, Robert Bok, Ilwoo Park, Galen Reed, Lucas Carvajal, Eric J. Small, Pamela Munster, Vivian K. Weinberg, Jan Henrik Ardenkjaer-Larsen, Albert P. Chen, Ralph E. Hurd, Liv-Ingrid Odegaardstuen, Fraser J. Robb, James Tropp, and Jonathan A. Murray. Metabolic imag-

- ing of patients with prostate cancer using hyperpolarized [1-13c]pyruvate. Magnetic Resonance in Chemistry, 5:198ra108, 2013.
- [235] Klaes Golman, Rene ' in 't Zandt, and Mikkel Thaning. Real-time metabolic imaging. PNAS, 13:11270–11275, 2006.
- [236] Sebastian Meier, Pernille R. Jensen, and Jens Ø. Duus. Real-time detection of central carbon metabolism in living escherichia coli and its response to perturbations. FEBS Letters, 585:3133–3138, 2011.
- [237] Mathilde H. Lerche, Pernille Rose Jensen, Magnus Karlsson, and Sebastian Meier. Nmr insights into the inner workings of living cells. Analytical Chemistry, 87:119–132, 2014.
- [238] Yael Adler-Levy, Atara Nardi-Schreiber, Talia Harris, David Shaul, Sivaranjan Uppala, Gal Sapir, Naama Lev-Cohain, Jacob Sosna, Shraga Nahum Goldberg, J. Moshe Gommori, and Rachel Katz-Brull. In-cell determination of lactate dehydrogenase activity in a luminal breast cancer model – ex vivo investigation of excised xenograft tumor slices using ddnp hyperpolarized [1-13c]pyruvate. Nat Rev Immunol., 19:2090, 2019.
- [239] S. Khan Hekmatyara Roberto Docampob You Zhuoa, Ciro D. Cordeirob and James H. Prestegard. Dynamic nuclear polarization facilitates monitoring of pyruvate metabolism in trypanosoma brucei. J Biol Chem., 292(44):18161–18168, 2017.
- [240] Kayvan R. Keshari, Renuka Sriram, Mark Van Criekeing, David M. Wilson, Zhen J. Wang, Daniel B. Vigneron, Donna M. Peehl, and John Kurhanewicz. Metabolic reprogramming and validation of hyperpolarized 13c lactate as a prostate cancer biomarker using a human prostate tissue slice culture bioreactor. The Prostate, 73:1171–1181, 2013.
- [241] Jack J. Miller, Angus Z. Lau, Per Mose Nielsen, Giles McMullen-Klein, Andrew J. Lewis, Nichlas Riise Jespersen, Vicky Ball, Ferdia A. Gallagher, Carolyn A. Carr,

- Christoffer Laustsen, Hans Erik Bøtker, Damian J. Tyler, and Marie A. Schroeder. Hyperpolarized [1,4-¹³C₂]fumarate enables magnetic resonance-based imaging of myocardial necrosis. Am Coll Cardiol Cardiovasc Imaging, 11:1594–1606, 2018.
- [242] Ferdia A. Gallagher, Mikko I. Kettunen, Sam E. Day, De-En Hu, Jan Henrik Ardenkjær-Larsen, René in 't Zandt, Pernille R. Jensen, Magnus Karlsson, Klaes Golman, Mathilde H. Lerche, and Kevin M. Brindle. Magnetic resonance imaging of pH in vivo using hyperpolarized ¹³C-labelled bicarbonate. Am Coll Cardiol Cardiovasc Imaging, 11:1594–1606, 2018.
- [243] I.Park, P.E.Z. Larson, J.W. Gordon, L. Carvajal, H.-Y. Chen, R.Bok, M. Van Criekinge, M. Ferrone, J.B. Slater, D. Xu, John Kurhanewicz, Daniel B. Vigneron, Susan Chang, and Sarah J Nelson. Development of methods and feasibility of using hyperpolarized carbon-13 imaging data for evaluating brain metabolism in patient studies. Magn. Reson. Med., 80:864–873, 2018.
- [244] Renuka Sriram, Jinny Sun, Javier Villanueva-Meyer, Christopher Mutch, Justin De Los Santos, Jason Peters, David E. Korenchan, Kiel Neumann, Mark Van Criekinge, John Kurhanewicz, Oren Rosenberg, David Wilson, and Michael A. Ohliger. Detection of bacteria-specific metabolism using hyperpolarized [2-¹³C] pyruvate. CS Infect, 8:797–805, 2018.
- [245] Sebastian Meier, Pernille R. Jensen, and Jens Ø. Duus. Direct observation of metabolic differences in living escherichia coli strains k-12 and bl21. ChemBioChem, 13:308–310, 2012.
- [246] Mengxiao Liu and Christian Hilty. Metabolic measurements of non-permeating compounds in live cells using hyperpolarized nmr. Analytical Chemistry, 90:1217–1222, 2017.
- [247] Renuka Sriram, Julia Nguyen, Justin DeLos Santos, Linda Nguyen, Jinny Sun, Seth Vigneron, Mark Van Criekinge, John Kurhanewicz, and John D. MacKenzie. Molec-

- ular detection of inflammation in cell models using hyperpolarized ^{13}C -pyruvate. Theranostics, 8:3400–3407, 2018.
- [248] Piotr Dzien, Anne Fages, Ghil Jona, Kevin M. Brindle, Markus Schwaiger, and Lucio Frydman. Following metabolism in living microorganisms by hyperpolarized ^1H nmr. J. Am. Chem. Soc., 138:12278–12286, 2016.
- [249] Ferdia A. Gallagher, Mikko I. Kettunen, De-En Hua, Pernille R. Jensen, René in 't Zand, Magnus Karlsson, Anna Gisselsson, Sarah K. Nelson, Timothy H. Witney, Sarah E. Bohndiek, Georg Hansson, Torben Peitersen, Mathilde H. Lerche, and Kevin M. Brindle. Production of hyperpolarized $[1,4-^{13}\text{C}_2]$ malate from $[1,4-^{13}\text{C}_2]$ fumarate is a marker of cell necrosis and treatment response in tumors. PNAS, 106:19801–19806, 2009.
- [250] Aurélien Bornet, Jonas Milani, Basile Vuichoud, Angel J. Perez Linde, Geoffrey Bodenhausen, and Sami Jannin. Microwave frequency modulation to enhance dissolution dynamic nuclear polarization. Chem. Phys. Lett., 602:63–67, 2014.
- [251] Andreas H. Förster and Johannes Gescher. Metabolic engineering of *Escherichia coli* for production of mixed-acid fermentation end products. Front. Bioeng. Biotechnol., 10:3389, (2014).
- [252] A.C. Guo, T. Jewison, M. Wilson, Y. Liu, C. Knox, Y. Djoumbou, P. Lo, R. Mandal, R. Krishnamurthy, and D.S. Wishart. Ecmdb: the *E. coli* metabolome database. Nucleic Acids Res., 41:D625–30, 2013.
- [253] Ingrid M. Keseler, Amanda Mackie, Alberto Santos-Zavaleta, Richard Billington, César Bonavides-Martínez, Ron Caspi, Carol Fulcher, Socorro Gama-Castro, Anamika Kothari, Markus Krummenacker, Mario Latendresse, Luis Muñoz-Rascado, Quang Ong, Suzanne Paley, Martin Peralta-Gil, Pallavi Subhraveti, David A. Velázquez-Ramírez, Daniel Weaver, Julio Collado-Vides, Ian Paulsen, and Peter D. Karp. The

- ecocyc database: reflecting new knowledge about escherichia coli k-12. Nucleic Acids Research, page D543–D550, (2017).
- [254] Donald Voet and Judith G. Voet. Biochemistry, second edition. Wiley, 1995.
- [255] Hilal Taymaz-Nikerel, Walter M. van Gulik, and Joseph J. Heijnen. Escherichia coli responds with a rapid and large change in growth rate upon a shift from glucose-limited to glucose-excess conditions. Metabolic Engineering, 13:307–318, 2011.
- [256] Guillermo Gosset. Improvement of Escherichia coli production strains by modification of the phosphoenolpyruvate:sugar phosphotransferase system. Microbial Cell Factories, 4:14, 2005.
- [257] Josef Deutscher, Christof Francke, and Pieter W. Postma. How phosphotransferase system-related protein phosphorylation regulates carbohydrate metabolism in bacteria. Microbiology and Molecular Biology Reviews, 70:939–1031, 2007.
- [258] Hiroshi Nikaido and Taiji Nakae. The outer membrane of gram-negative bacteria. volume 20 of Advances in Microbial Physiology, pages 163 – 250. Academic Press, 1980.
- [259] Muriel Masi, Mathias Winterhalter, and Jean-Marie Pagès. Outer Membrane Porins, pages 79–123. Springer International Publishing, Cham, 2019.
- [260] Bernd Wurster and Benno Hess. Anomeric specificity of enzymes of d-glucose metabolism. FEBS Lett., 40:S112–S118, 1974.
- [261] J.E. Smith and E. Beutler. Proc. Soc. Exptl. Biol. Med., 122:617–673, 1966.
- [262] Dieter Lessmann, Karl-Ludwig Schimz, and Gerhart Kurz. D-glucose-6-phosphatedehydrogenase (entner-doudoroff enzyme) from pseudomonas fluorescens - purification, properties and regulation. Eur. J. Biochem., 1975.

- [263] Francois Kayser, Monique Biesemans, Rudolph Willem, Francine Malaisse-Lagae, and Wily J. Malaisse. Does phosphoglucosomerase display anomeric specificity or selectivity towards α -D-glucose-6-phosphate? Biochemical Journal, 295:607–609, 1993.
- [264] Lian He, Yu Xiu, J. Andrew Jones, Edward E.K. Baidoo, Jay D. Keasling, Yinjie J. Tang, and Mattheos A.G. Koffas. Deciphering flux adjustments of engineered e. coli cells during fermentation with changing growth conditions. Metabolic Engineering, 39:247–256, 2017.
- [265] Guennadi Sezonov, Danièle Joseleau-Petit, and Richard D’Ari. Escherichia coli physiology in luria-bertani broth. Journal of Bacteriology, 189:8746–8749, 2007.
- [266] Eleni Vasilakou, Mark C. M. van Loosdrecht, and S. Aljoscha Wahl. Escherichia coli metabolism under short-term repetitive substrate dynamics: adaptation and trade-offs. Microbial Cell Factories, 19:116–137, 2020.
- [267] G.N. Stephanopoulos, A.A. Aristidou, and J. Nielsen. Metabolic engineering. Principles and methodologies. San Diego: Academic Press, (1998).
- [268] Jonathan M. Monk, Anna Koza, Miguel A. Campodonico, Daniel Machado, Jose Miguel Seoane, Bernhard O. Palsson, Markus J. Herrgard, and Adam M. Feist. Multi-omics quantification of species variation of escherichia coli links molecular features with strain phenotypes. Cell Systems, 3:238–251, 2016.
- [269] D.J. Griffiths. Introduction to Electrodynamics. Prentice Hall, (1999).
- [270] C. D. Jeffries. Polarization of nuclei by resonance saturation in paramagnetic crystals. Phys. Rev., 106:164–, 1957.
- [271] M. Abraham R. W. Kedzie and C. D. Jeffries. Paramagnetic resonance hyperfine structure of ^{141}Ce and ^{147}Nd . Phys. Rev., 106:165–166, 1957.
- [272] O. S. Leifson and C. D. Jeffries. Dynamic polarization of nuclei by electron-nuclear dipolar coupling in crystals. Phys. Rev., 122:1781, 1961.

- [273] B. N. Provotorov. Magnetic resonance saturation in crystals, soviet physics. JETP, 14:1126–1132, 1962.
- [274] T. A. Siaw, M. Fehr, A. Lund, A. Latimer, S. A. Walker, D. T. Edwards, and S.I. Han. Effect of electron spin dynamics on solid- state dynamic nuclear polarization performance. Phys. Chem. Chem. Phys, 16:1869418706, 2014.
- [275] Daniel J. Gage and Frederick C. Neidhardt. Adaptation of escherichia coli to the uncoupler of oxidative phosphorylation 2,4-dinitrophenol. Journal of bacteriology, 175:7105–7108, 1993.
- [276] Pieter W. Postma, Oense M. Neyssel, and Ronald Van Ree. Glucose transport in salmonella typhimurium and escherichia coli. Eur. J. Biochem., 123:113–119, 1982.
- [277] T. Ogino, Y. Arata, , and S. Fujiwara. Proton correlation nuclear magnetic resonance study of metabolic regulations and pyruvate transport in anaerobic escherichia coli cells"1. Biochemistry, 19:3684–3691, 1980.
- [278] David M. Mosser and Justin P. Edwards. Exploring the full spectrum of macrophage activation. Nat Rev Immunol., 8:958–969, 2008.
- [279] Alex J. Freemerman, Amy R. Johnson‡, Gina N. Sacks, J. Justin Milner, Erin L. Kirk, Melissa A. Troester, Andrew N. Macintyre, Pankuri Goraksha-Hicks, Jeffery C. Rathmell, and Liza Makowskis. Metabolic reprogramming of macrophages. Nat Rev Immunol., 189:7884–7896, 2014.
- [280] Lionel B. Ivashkiv. The hypoxia–lactate axis tempers inflammation. Nat Rev Immunol., pages doi:10.1038/s41577–019–0259–8, 2019.
- [281] J. S. Lewis, J. A. Lee, J. C. E. Underwood, A. L. Harris, and C. E. Lewis. Macrophage responses to hypoxia: relevance to disease mechanisms. Journal of Leukocyte Biology, 66:889–900, 1999.